

Electronic Thesis and Dissertation Repository

4-14-2021 12:00 PM

Machine Learning Prediction of Structural Response for Reinforced Concrete Members under Blast Loading

Monjee Almustafa, *The University of Western Ontario*

Supervisor: Nehdi Moncef, *The University of Western Ontario*

A thesis submitted in partial fulfillment of the requirements for the Master of Engineering Science degree in Civil and Environmental Engineering

© Monjee Almustafa 2021

Follow this and additional works at: <https://ir.lib.uwo.ca/etd>



Part of the [Structural Engineering Commons](#)

Recommended Citation

Almustafa, Monjee, "Machine Learning Prediction of Structural Response for Reinforced Concrete Members under Blast Loading" (2021). *Electronic Thesis and Dissertation Repository*. 7745.
<https://ir.lib.uwo.ca/etd/7745>

This Dissertation/Thesis is brought to you for free and open access by Scholarship@Western. It has been accepted for inclusion in Electronic Thesis and Dissertation Repository by an authorized administrator of Scholarship@Western. For more information, please contact wlsadmin@uwo.ca.

Abstract

With increasing accidental and intentional explosions and blast events inflicting life loss and economic damage to civil infrastructure, greater attention is given to the analysis and design of blast-resistant structures. Accordingly, this thesis introduces state-of-the-art machine learning models dedicated to predicting the structural behavior of various reinforced concrete (RC) members under blast loading, including slabs, columns, and beams. Moreover, extended prediction models were developed for RC members that employ fiber-reinforced polymer (FRP) retrofitting and steel fiber-reinforced concrete as blast mitigation strategies. For each model, extensive validation was conducted through statistical performance measures and comparisons to existing prediction methods. Additionally, feature importance analyses were performed to investigate the extent to which each proposed model captured its respective application. Overall, the developed prediction models achieved accurate and computationally efficient performance for the complex application of blast-loaded structures.

Keywords

Blast loading; Reinforced concrete; Column; Beam; Fiber-reinforced polymer; Steel fiber; Machine learning; Random Forests; Gradient boosted regression trees; Gaussian process regression.

Summary for Lay Audience

In the event of an accidental or intentional explosion, reinforced concrete structures are highly susceptible to structural damage that may lead to severe consequences for both the structure and its occupants. Therefore, appropriate analysis and design considerations should be adopted to provide a desired level of protection. A part of this procedure is to accurately predict the response of structural members to different blast loading scenarios. Current simplified response prediction approaches are laborious and produce limited responses, whereas more detailed approaches require competent skills in finite element modeling and are computationally intensive.

To expand the state-of-the-art in predictive modeling for structures under blast loading, this thesis explores the use of machine learning methods towards developing more simplified and flexible approaches. Throughout the thesis, structural behavior prediction models were developed for reinforced concrete (RC) members including slabs, columns, and beams exposed to blast loading. The performance of each model was thoroughly investigated and found to be competitive with existing approaches. The use of machine learning for developing behavior prediction models was also extended to complex members which considered strategies for mitigating blast-induced damage. These include RC slabs with fiber-reinforced polymer surface retrofits and RC beams designed incorporating steel fibers. The resulting extensions showed that the adoption of ML methods was highly effective in considering exceedingly complicated design considerations. Overall, the proposed models throughout this thesis provided a simplified, accurate, and time-efficient approach for structural blast applications. With the expressed convenience and applicability of these models, further future developments of these models are encouraged.

Co-Authorship Statement

The present thesis has been structured according to the regulation of integrated-article format stipulated by the School of Graduate and Postdoctoral Studies (SGPS) at Western University. The third, fourth, fifth, sixth, and seventh chapters have been submitted for publication to peer-reviewed journals. All data analysis, formal investigation, and writing were carried out by the candidate under the guidance and supervision of Professor Moncef L. Nehdi.

Almustafa, M. K., & Nehdi, M. L. (2020). Machine learning model for predicting structural response of RC slabs exposed to blast loading. *Engineering Structures*, 221, 111109, 12 p.

Almustafa, M. K., & Nehdi, M. L. (2021). Machine Learning model for predicting structural response of RC columns subjected to blast loading. *International Journal of Impact Engineering*. (In review).

Almustafa, M. K., & Nehdi, M. L. (2021). Hybrid machine learning model for predicting structural response of reinforced concrete beams under blast loading. *International Journal of Impact Engineering*. (In review).

Almustafa, M. K., & Nehdi, M. L. (2021). Machine learning prediction of structural response for FRP retrofitted RC slabs subjected to blast loading. *Engineering Structures*. (In review).

Almustafa, M. K., & Nehdi, M. L. (2021). Machine learning prediction of structural response for steel fiber-reinforced concrete beams subjected to far-field blast loading. *Cement and Concrete Composites*. (In review).

Dedication

To:

My dearest mother, Dalal Awida
My wisest father, Khaled Almustafa
My supportive brothers, Mohamed and Jaffar

Acknowledgement

Above all else, I would like to thank God for providing me with the path of knowledge, the patience to learn, and the strength to persist throughout my degree.

I would like to gratefully express my appreciation to my supervisor Professor Moncef L. Nehdi for granting me the opportunity of pursuing a Master's degree and providing me with endless support and guidance throughout the program. I would also like to thank him for his ongoing encouragement that always led me to explore new fields.

I would like to thank my dearest and oldest friends Mohammed Tatary, Ali Tatary, Ayman ElSha'ar, and Yamin Shayah for keeping me focused and always pushing me to achieve greater lengths. I would also like to thank my undergraduate research supervisor Professor Yasser Ibrahim for investing time and effort early on in my studies, which contributed to my achievements throughout graduate school.

I am ever so grateful to my brother and roommate, Mohamed, for encouraging me throughout every sleepless night and celebrating every success along the way. I would also like to thank him for his optimistic companionship throughout the unanticipated surprises of the past year. There was no one else I would rather have been quarantined with.

Lastly, I would like to express my deepest appreciation and gratitude to my family for their love, encouragement, and support throughout my academic career. I would like to thank my mother for her patience and for always checking up on me. Your morning phone calls would always ease my hardships. I would also like to thank my father for always knowing what to say and being by my side, especially throughout the early days. Without them, I could not have imagined myself reaching the finish line.

Table of Contents

Abstract.....	ii
Summary for Lay Audience.....	iii
Co-Authorship Statement.....	iv
Dedication.....	v
Acknowledgement.....	vi
Table of Contents.....	vii
List of Tables.....	xiii
List of Figures.....	xv
List of Abbreviations.....	xviii
Chapter 1.....	1
1 Introduction.....	1
1.1 Background.....	1
1.2 Research need and objectives.....	5
1.3 Original contributions.....	6
1.4 Thesis structure.....	7
1.5 Chapter references.....	9
Chapter 2.....	10
2 Literature Review.....	10
2.1 Blast phenomenon.....	10
2.1.1 Blast wave parameters.....	12
2.1.2 Unconfined explosions.....	17
2.2 Existing modeling methods.....	23
2.2.1 Equivalent dynamic SDOF models.....	23
2.2.2 Numerical models.....	25

2.3	Previous research on RC members under blast loads	27
2.3.1	General	27
2.3.2	Reinforced concrete slabs	28
2.3.3	Reinforced concrete columns.....	29
2.3.4	Reinforced concrete beams	30
2.4	Structural blast mitigation strategies.....	31
2.4.1	General.....	31
2.4.2	External FRP retrofitting for RC slabs.....	32
2.4.3	Steel fiber incorporation in RC beams	34
2.5	Machine learning in structural engineering	36
2.5.1	General.....	36
2.5.2	Recent studies	36
2.6	Chapter references	38
Chapter 3.....		43
3	Machine learning model for predicting structural Response of RC slabs exposed to blast loading	43
3.1	Introduction and background	43
3.2	Machine learning in civil engineering	45
3.3	Data collection and description.....	46
3.4	Model development	50
3.4.1	Preliminary assessment of regression models.....	50
3.4.2	Random Forests algorithm	51
3.4.3	Hybrid classification-regression Random Forests algorithm.....	53
3.4.4	Model overview	53
3.5	Results and discussion	56
3.5.1	Performance measures of the ML model	56

3.5.2	Comparative study of ML model to alternative models	59
3.5.3	Results of PFI for input features	61
3.5.4	Comparative study of PFI values to existing parametric studies	63
3.6	Analysis of model discrepancies.....	68
3.6.1	Variations between numerical and experimental methods	68
3.6.2	Variations in blast load characteristics	70
3.6.3	Variations unique to the present dataset	71
3.6.4	Suggestion for improved ML model and its practical applications	72
3.7	Conclusions.....	72
3.8	Chapter references	73
Chapter 4.....		79
4	Machine learning model for predicting structural response of RC columns subjected to blast loading	79
4.1	Introduction.....	79
4.2	Data collection and description.....	81
4.2.1	Feature description.....	82
4.3	Model development	83
4.3.1	Gradient boosted regression trees	84
4.3.2	Random Forests and feature importance.....	85
4.3.3	Performance measure	86
4.4	Results and discussion	87
4.4.1	Model validation through performance criteria	88
4.4.2	Model validation through comparisons of existing methods	90
4.4.3	Feature importance analysis of near-field and far-field blast	94
4.4.4	Importance measure of column parameters	95
4.4.5	Axial load ratio	98

4.4.6	Importance measure of blast parameters.....	100
4.5	Practical implementation and model improvement considerations	103
4.5.1	Model improvement through added features	103
4.5.2	Practical usage in accordance with code and future model development.....	104
4.6	Conclusions.....	105
4.7	Chapter references	106
Chapter 5	110
5	Hybrid machine learning model for predicting structural response of RC beams under blast loading	110
5.1	Introduction and background	110
5.2	Model development	113
5.2.1	Hybrid gradient-boosted regression trees	113
5.2.2	Performance measures and cross-validation.....	115
5.3	Data collection and description.....	118
5.3.1	Feature descriptions	118
5.3.2	Displacement prediction model	118
5.3.3	Failure mode and cracking pattern classification model.....	119
5.4	Displacement prediction model	122
5.4.1	Model validation through performance criteria	122
5.4.2	Model validation through comparisons with existing methods	124
5.4.3	Model validation through feature importance.....	129
5.5	Failure mode and cracking pattern classification model.....	137
5.5.1	Model validation through performance criteria	137
5.6	Implicit feature learning and elimination of modeling complexities	142
5.6.1	Dynamic increase factors	142
5.6.2	Constitutive material models	143

5.6.3	Practical implementation	144
5.7	Conclusions.....	145
5.8	Chapter references	146
Chapter 6	150
150		
6	Machine learning prediction for structural response of FRP retrofitted RC slabs subjected to blast loading	150
6.1	Introduction and background	150
6.2	Data collection and description.....	153
6.2.1	Feature description.....	153
6.2.2	Experimental and numerical data.....	154
6.2.3	Synthetic data.....	156
6.3	Model development and assessment.....	159
6.3.1	Gaussian process regression	159
6.3.2	Performance criteria and cross-validation	161
6.3.3	Feature importance using Interaction Test.....	162
6.4	Displacement behavior prediction model	163
6.4.1	Model validation through performance criteria	163
6.4.2	Model Validation through comparisons of existing methods	166
6.4.3	Model validation through feature importance.....	168
6.5	Practical implementation and recommendations	175
6.5.1	Prediction model for displacement	175
6.5.2	Dataset discrepancies	175
6.6	Conclusions.....	176
6.7	Chapter references	177
Chapter 7	180

7	Machine learning prediction of structural response for steel fiber-reinforced concrete beams subjected to far-field blast loading	180
7.1	Introduction and background	180
7.2	Model development	183
7.2.1	Gaussian process regression	183
7.2.2	Generative adversarial networks.....	186
7.2.3	Statistical performance measures.....	187
7.3	Data collection	188
7.3.1	Description of shock wave simulation device	188
7.3.2	Data from UOST and feature description	189
7.3.3	Data from CTGAN	192
7.4	Results and discussion of model validation	193
7.4.1	Evaluation of model performance.....	193
7.4.2	Implicit application considerations	197
7.4.3	Comparisons to existing prediction methods	201
7.5	Parametric analysis	204
7.6	Conclusions.....	211
7.7	Chapter references	212
	Chapter 8.....	216
8	Conclusions and future research	216
8.1	Summary and conclusions	216
8.2	Future research.....	222
	Curriculum Vitae	224

List of Tables

Table 3-1. Mean, standard deviation, and range of model features	48
Table 3-2. MATLAB Regression Learner and Random Forest results.	51
Table 3-3. Summary of learner comparison.	58
Table 3-4. Comparisons of hybrid RF model to alternative models.	60
Table 3-5. PFI values of permuted features.	62
Table 3-6. Effect of reflected impulse on maximum displacement.	64
Table 3-7. Effect of scaled distance on maximum displacement.	64
Table 3-8. Effect of slab thickness on maximum displacement.	66
Table 3-9. Effect of reinforcement ratio on maximum displacement.	67
Table 3-10. Effect of compressive strength on maximum displacement.	67
Table 4-1. Mean, standard deviation, and range of model features.	82
Table 4-2. Comparisons of the GBRT model to alternative models for near-field and far-field blast scenarios	92
Table 5-1. Data statistics for displacement prediction dataset.	120
Table 5-2. Data statistics for failure mode and crack pattern classification dataset.	120
Table 5-3. Average percentage of predictions within different error bounds respective of the dataset	123
Table 5-4. Comparisons of ML model to alternative models for NSC beams.	126
Table 5-5. Comparisons of ML model to alternative models for HSC beams.	128
Table 5-6. Effect of reflected pressure.	132

Table 5-7. Effect of reflected impulse.	132
Table 5-8. Effect of steel yield strength.	133
Table 5-9. Effect of concrete compressive strength.	133
Table 5-10. Effect of tension reinforcement ratio.	135
Table 5-11. Effect of compression reinforcement ratio.	136
Table 5-12. Effect of stirrup spacing.	136
Table 5-13. Precision and recall for each class and overall model.	139
Table 6-1. Mean, count, standard deviation, and range of features for real data.	155
Table 6-2. Mean, count, standard deviation, and range of features for synthetic data.	158
Table 6-3. Performance metrics for various model considerations.	164
Table 6-4. Percent and number of data points within each error bound for various considerations of training data and cross-validation.	166
Table 6-5. Comparison of displacement prediction model and analytical methods.	168
Table 7-1. Steel fiber properties.	182
Table 7-2. Average shock wave parameters produced by UOST Facility.	190
Table 7-3. Statistics of real data.	190
Table 7-4. Statistics of synthetic data.	192
Table 7-5. Performance measures for alternative model considerations.	194
Table 7-6. Comparisons between the ML model and alternative prediction models.	202

List of Figures

Figure 1-1. Bombing of the Alfred P. Murrah Building	1
Figure 1-2. Bombing of the Ufundi Building.	2
Figure 1-3. Damage resulting from the explosion at the Port of Beirut.	3
Figure 2-1. Pressure-time profile of a shock wave.	11
Figure 2-2. Reflected pressure factor for different angles of incidence [3].	16
Figure 2-3. Free air burst explosion on a structure.	17
Figure 2-4. Positive-phase shockwave parameters for a free air burst explosion [3].	18
Figure 2-5. Air burst explosion on a structure.	19
Figure 2-6. Reflected pressures for varying scaled heights and angle of incidence [3].	20
Figure 2-7. Surface burst explosion on a structure.	21
Figure 2-8. Positive-phase shockwave parameters for a surface burst explosion [3].	22
Figure 2-9. Shock-wave interaction and resulting pressure distribution on target structural member.	27
Figure 3-1. Distribution plots of features and output.	49
Figure 3-2. Scatter plots of normalized features.	50
Figure 3-3. Diagram of regression and classification Random Forests.	52
Figure 3-4. Actual versus predicted responses with a 40% error bound.	58
Figure 3-5. Comparison between actual and predicted responses.	59
Figure 4-1. Distribution plots of features and output.	83
Figure 4-2. Stage-wise learning process of the gradient boosted regression trees algorithm.	84

Figure 4-3. Actual versus predicted responses with a 20% error bound.	89
Figure 4-4. Actual versus predicted responses with a 20% error bound.	90
Figure 4-5. Feature importance estimates for selected features in near-field and far-field blasts.	95
Figure 4-6. Effect of longitudinal reinforcement ratio on maximum displacement where Z has units of $m/kg^{1/3}$	96
Figure 4-7. Effect of transverse reinforcement ratio on maximum displacement where Z has units of $m/kg^{1/3}$	98
Figure 4-8. Effect of axial load ratio on maximum displacement where Z has units of $m/kg^{1/3}$	99
Figure 4-9. Effect of scaled distance on maximum displacement.	101
Figure 4-10. Effect of reflected impulse from changing charge weights on maximum displacement where Z has units of $m/kg^{1/3}$	102
Figure 5-1. Confusion matrix representation for multi-class classification problems.	117
Figure 5-2. Histograms of features and output for displacement prediction dataset.	121
Figure 5-3. Histograms of features and output for classification dataset.	121
Figure 5-4. Actual versus predicted responses with a 20% error bound considering 10-fold CV.	123
Figure 5-5. Actual versus predicted responses with a 20% error bound considering LOO CV.	124
Figure 5-6. Feature importance estimates for selected features of the displacement prediction model.	130
Figure 5-7. Multi-class confusion matrix for classification model.	138

Figure 5-8. Feature importance estimates for selected features of the classification model.	141
Figure 6-1. Configurations of FRP retrofit layers considered in the dataset.	153
Figure 6-2. Distribution of features for real data.	155
Figure 6-3. General workflow of a generative adversarial network.	156
Figure 6-4. Distribution of features for synthetic data.....	158
Figure 6-5. Actual versus prediction response plots for different model considerations.	165
Figure 6-6. Actual response versus predicted scatter plot with error bounds.	166
Figure 6-7. Feature importance estimates for FRP retrofitted slabs and conventional slabs.	169
Figure 7-1. Distribution of features for real data.	191
Figure 7-2. Distribution of features for synthetic data.....	193
Figure 7-3. Actual versus prediction response plots for different model considerations.	195
Figure 7-4. Actual versus prediction scatter plot with 10% and 20% error bounds.	196
Figure 7-5. Taylor Diagram representing model comparisons for Sets A-G.....	204
Figure 7-6. Effect of fiber parameters on maximum displacement of SFRC beams with NSR.	205
Figure 7-7. Effect of fiber parameters on maximum displacement of UHPFRC beams with NSR.....	207
Figure 7-8. The effect of fiber parameters on UHPFRC beams with HSR.	210

List of Abbreviations

AFRP	Aramid fiber-reinforced polymer
ANFO	Ammonium nitrate - fuel oil
CDIF	Compression dynamic increase factor
CFRP	Carbon fiber-reinforced polymer
CTGAN	Conditional tabular generative adversarial network
CV	Cross-validation
DIF	Dynamic increase factor
FRP	Fiber-reinforced polymer
GBRT	Gradient boosted regression trees
GFRP	Glass fiber-reinforced polymer
GP	Gaussian process
GPR	Gaussian process regression
HGSO	Henry gas solubility optimization
HSC	High strength concrete
HSFRC	High strength fiber-reinforced concrete
HSR	High strength reinforcement
LOO CV	Leave-one-out cross-validation
MAE	Mean absolute error
MAPE	Mean absolute percent error

ML	Machine learning
MSE	Mean squared error
NSC	Normal strength concrete
NSR	Normal strength reinforcement
PFI	Permutation feature importance
RC	Reinforced concrete
RF	Random forests
SDOF	Single degree of freedom
SFRC	Steel fiber-reinforced concrete
TDIF	Tension dynamic increase factor
TGAN	Tabular generative adversarial network
TNT	Trinitrotoluene
UHPC	Ultra-high-performance concrete
UHPFRC	Ultra-high-performance fiber-reinforced concrete
UOST	University of Ottawa shock tube
VE _{cv}	Variance explained by cross validation

Chapter 1

1 Introduction

1.1 Background

Numerous past events of explosions causing severe structural damage have demonstrated that buildings are far from immune to such overwhelming loading conditions. One of the most devastating examples of such events is the bombing of the Alfred P. Murrah Federal Building in Oklahoma in 1996. The explosion resulted from 3000 kg of ammonium nitrate and fuel oil (ANFO) causing 168 deaths and injuring another 680 individuals. The destruction sustained by the blast is illustrated in **Figure 1-1** in which critical localized damages can be observed.



Figure 1-1. Bombing of the Alfred P. Murrah Building.

Another disturbing event of structural blast loading is the bombing of the Ufundi Building at the US Embassy in Kenya in 1998 where the explosive was generated from 900 kg of trinitrotoluene (TNT) and ANFO. The blast inflicted 213 deaths and over 4000 injured individuals. Additionally, the structural damage caused by the explosion brought about the total collapse of the building, as depicted in **Figure 1-2**.

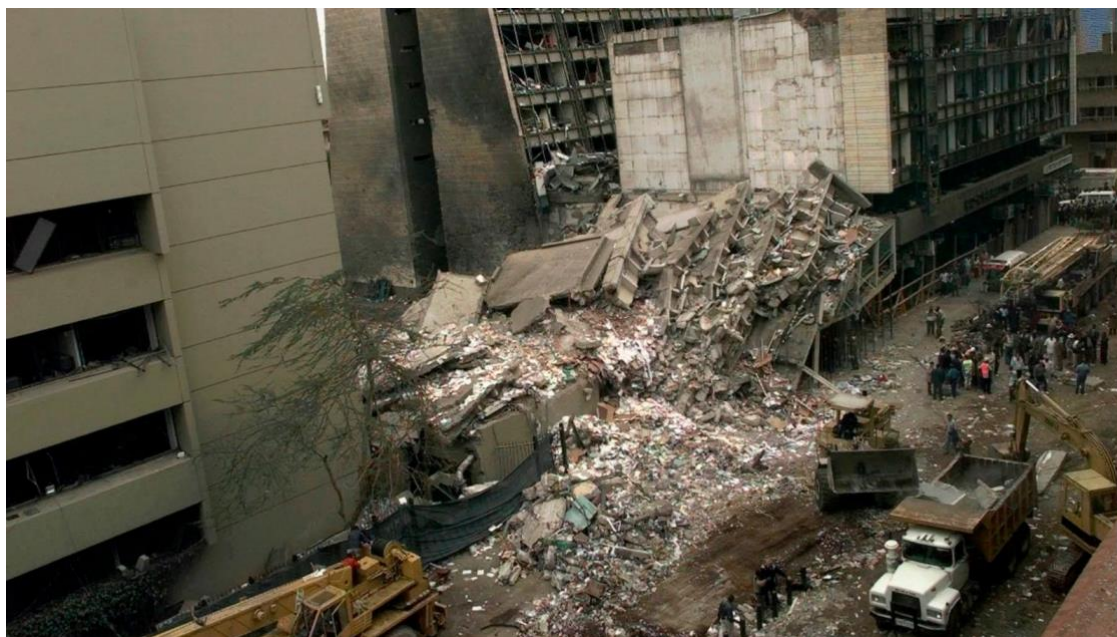


Figure 1-2. Bombing of the Ufundi Building.

Only recently in 2020, the Port of Beirut in Lebanon was exposed to one of the largest accidental explosions in the world produced from nearly 2700 tons of ammonium nitrate that had ignited within a materials facility. In the aftermath of the blast, 215 deaths and over 7500 wounded individuals were accounted for. Also, the applied pressure caused by the blast induced damage to over 6000 surrounding buildings in which most of the structural damage was witnessed throughout steel structure warehouses closest to the blast, as can be observed in **Figure 1-3**. The different events of structural blast loading presented herein highlight the importance of considering effective measures of blast-resistant design in modern day building and infrastructure developments.



Figure 1-3. Damage resulting from the explosion at the Port of Beirut.

With the increasing development of structures in densely populated communities, there exists growing demand for implementing protective measures against accidental or intentional explosions. Considering the associated risks of such events, the proactive development of resilient infrastructures to mitigate structural vulnerabilities has been continuously investigated.

Existing studies of blast-resistant design for reinforced concrete (RC) structures have been mostly concerned with the local and global behaviors of individual structural elements. This may be attributed to the nature of blast loading, which is more inclined to inflict extreme local building damage, as opposed to inducing global behaviors of an entire structure. Towards this notion, experimental studies have investigated the individual response of RC slabs, columns, and beams through their resulting displacements, cracking patterns, and failure modes considering varying element detailing [1]. Moreover, available design codes require specific response limits that consider the behavior of single structural components under varying magnitudes of blast loading [2]. Thus, in several cases, the analysis of buildings exposed to such loading may be sufficiently conducted on an element-wise basis.

Two primary response prediction methods are utilized to analyze the behavior of structural elements subjected to blast loading. The first is a simplified dynamic single degree of freedom (SDOF) model, which implements a dynamic equation of motion with assumptions for the equivalent mass, loading, and stiffness of an element. This approach is also dependent on assuming a deformed shape based on a flexural response mode. Additionally, a resistance function derived from an element's section analysis may be incorporated, which can account for an element's static and dynamic material properties [3]. Although further modifications to the approach may be implemented to achieve more accurate responses, the structural response produced from this approach is limited to an element's maximum displacement. As a result, further responses or analyses such as crack analysis, spalling analysis, or failure mode prediction would require more advanced methods [4].

An alternative and more detailed modeling approach consists of using numerical methods. Using advanced material properties, accurate blast load implementations, and accurate element representations, numerical models can capture a range of both local and global behaviors for the complex application of blast-loaded elements. However, competent modeling efforts, availability of material models, and a profound understanding of the application are pertinent to the development of reliable numerical models. Moreover, this method is associated with significant computational demand and substantial duration of run-time [5]. The limitations or complexities presented by each method are sufficiently apparent when analyzing conventional RC elements.

When more advanced materials are introduced as a means of blast mitigation strategy for RC elements, an increase in modeling complexity is also observed. Two commonly adopted strategies of blast mitigation are the use of fiber-reinforced polymers (FRP) retrofits and the incorporation of steel fibers in concrete mixtures. The application of FRP retrofitted RC elements has demonstrated favorable blast resistant characteristics through increased energy absorption and reduced fragmentation. Additionally, this technique may be applied on both developing and existing structures, while also being convenient in transporting, handling, and applying [6]. Conversely, the inclusion of steel fibers in RC elements offers an inherent increase in ductility to a naturally brittle material, while

contributing to improved shear and flexural capacities. When subjected to blast loading, steel fiber-reinforced concrete (SFRC) elements demonstrate significantly enhanced blast resistance by mitigating displacements, crack development, and shear failure modes [7].

Using simplified SDOF models for maximum displacement predictions of blast loaded FRP retrofitted RC elements [8] or SFRC elements demonstrated relatively acceptable performance but is a highly involved approach. Moreover, limitations of existing SFRC material models have been observed to noticeably affect the accuracy of SDOF predictions [9]. Similarly, SDOF models are incapable of being expanded to identify more detailed responses attributed to these advanced materials. Such responses would entail their qualitative failure modes, as well as the quantitative local degree of damage [6,10]. Conversely, the use of numerical methods for modeling advanced material behaviors are highly efficient yet are further characterized by the aforementioned complexities of implementation. With the reported limits and sophistications of existing prediction methods, considerations for a simplified and accurate approach that can encompass multiple responses would contribute to the state-of-the-art of blast engineering modeling.

A field of study that has gained remarkable influence across various disciplines over the past few years is Machine Learning (ML). The inspiration for such interdisciplinary studies has been fueled by innovation as well as its flexibility and compatibility. In more recent years, the integration of ML in civil engineering has seen significant growth throughout branches of structural analysis, structural health monitoring, and construction materials science [11]. The advancements in civil engineering resulting from ML implementations provide a strong motivation towards its adoption.

1.2 Research need and objectives

With the apparent complexities and limitations associated with existing response prediction methods for blast-loaded RC elements, there is need for investigating alternative methods of modeling such applications. Thus, the objective of this thesis is to investigate the applicability of ML methods in developing reliable and time-efficient models for predicting

the behavior of various structural elements under blast loading. The different ML models considered for conventional elements are maximum displacement prediction models for RC slabs, columns, and beams. Additionally, a cracking pattern and failure mode classification model was investigated for RC beams. When considering elements with advanced materials, maximum displacement prediction models were also studied for FRP retrofitted RC slabs and SFRC beams.

The relatively wide scope of research presented acts towards setting a strong precedent for the integration of ML in the complex and sensitive field of blast engineering. Efforts towards this outcome are expressed partly by demonstrating the performance of global and local behavior of conventional RC elements, and partly by demonstrating the capability of extending such performance towards advanced material variations and additional structural responses.

1.3 Original contributions

The current study investigates the potential of developing modern ML models to predict the structural response of RC elements under blast loading as a simplified, accurate, and time-efficient alternative to existing prediction methods. The contributions of this study consist of the following:

1. Introducing, for the first time, a comprehensive integration of machine learning methods in the field of structural blast design as a novel approach for member response predictions.
2. Identifying and compiling consistent application datasets from the existing literature for multiple structural elements under blast loading.
3. Developing independent maximum displacement prediction models for RC slabs, columns, and beams subjected to blast loading using ML methods.

4. Conducting a comprehensive investigation of the relative importance of application parameters for RC slabs, columns, and beams under blast loading, considering extensive parameter ranges and validated by existing experimental results.
5. Developing a failure mode and cracking pattern classification model for normal-strength and high-strength RC beams subjected to varying blast load magnitudes.
6. Developing a displacement prediction model for FRP retrofitted RC slabs subjected to blast loading and investigating the effects of slab and fiber parameters compared to non-retrofitted RC slabs.
7. Developing a displacement prediction model for SFRC beams of varying strengths subjected to far-field blast loading and conducting a critical parametric study of the effects of different steel fiber types and fiber contents on blast resistance.

1.4 Thesis structure

This thesis has been structured in compliance with the integrated-article format as per the guidelines and regulations of the School of Graduate and Postdoctoral Studies (SGPS) at Western University. The thesis comprises eight chapters, which focus on the development, validation, and evaluation of ML models to predict the response of various RC elements under blast loading. They are as follows:

Chapter 1 briefly describes the background of the current application, the dedicated scope of research, and the original contributions emanating from the present work.

Chapter 2 provides an overall perspective of the blast phenomenon, details of existing approaches in modeling the structural behavior under blast loading, and the different parameters considered for each RC element based on previous experimental studies. An overview of structural blast mitigation techniques is also presented with respect to existing studies. Lastly, recent advancements of ML methods in structural engineering are reported.

Chapter 3 discusses the details of the maximum displacement prediction model of RC slabs under blast loading. It includes the sources of data collection, discussion on the hybrid classification-regression random forests algorithm, and discussion on the feature importance analysis validated by experimental data. Model prediction comparisons to existing analytical and numerical models are also reported.

Chapter 4 reports the details of the maximum displacement prediction model of RC columns under blast loading. Discussions on the sources of data collection, gradient boosted regression trees algorithm, and feature importance analysis validated by experimental data are provided. An analysis of the effects of column parameters under near-field and far-field blast loading is also conducted and prediction comparisons to existing models are presented.

Chapter 5 discusses the details of the maximum displacement prediction model as well as the crack pattern and failure mode classification model of RC beams under blast loading. Descriptions of the sources of data collection, a hybrid gradient boosted regression trees algorithm, and feature importance analysis validated by experiment are reported. Prediction comparisons to existing analytical and numerical models are also provided.

Chapter 6 describes the development of the maximum displacement prediction model of FRP retrofitted RC slabs subjected to blast loading. Details on the source of data collection, gaussian process regression implementation, and feature importance analysis validated by experimental data are reported. Prediction comparisons to existing models are also provided.

Chapter 7 provides the details of the maximum displacement prediction model of SFRC beams of varying strengths under blast loading. A discussion on the data collection process and gaussian process regression implementation is provided. Also, comparisons with respect to existing prediction methods are given. A critical parametric study on the effect of steel fiber parameters on blast resistance is also conducted.

Chapter 8 summarizes the results of the developed models and sets forth recommendations for their improvement. Extensions of the current study are elaborated for future research.

1.5 Chapter references

- [1] Hao, H. (2015). Predictions of structural response to dynamic loads of different loading rates. *International Journal of Protective Structures*, 6, 585-605.
- [2] Canadian Standards Association. (2012). Design and assessment of buildings subjected to blast loads, CSA S850-12.
- [3] USA Department of Defense. Structures to Resist the Effect of Accidental Explosions Unified Facilities Criteria (UFC) 3-340-02. Department of Defense; 2008.
- [4] Zhang, C., & Mousavi, A. A. (2020). Blast loads induced responses of RC structural members: State-of-the-art review. *Composites Part B: Engineering*, 108066.
- [5] Hao, H., Hao, Y., Li, J., & Chen, W. (2016). Review of the current practices in blast-resistant analysis and design of concrete structures. *Advances in Structural Engineering*, 19(8), 1193-1223.
- [6] Goswami, A., & Adhikary, S. D. (2019). Retrofitting materials for enhanced blast performance of Structures: Recent advancement and challenges ahead. *Construction and Building Materials*, 204, 224-243.
- [7] Soufeiani, L., Raman, S. N., Jumaat, M. Z. B., Alengaram, U. J., Ghadyani, G., & Mendis, P. (2016). Influences of the volume fraction and shape of steel fibers on fiber-reinforced concrete subjected to dynamic loading—A review. *Engineering Structures*, 124, 405-417.
- [8] Jacques, E. (2011). *Blast retrofit of reinforced concrete walls and slabs* (Master's thesis, Université d'Ottawa/University of Ottawa).
- [9] Castonguay, S. (2017). *Performance of Steel Fiber-Reinforced Concrete Beams Under Shock Tube Induced Blast Loading* (Master's thesis, Université d'Ottawa/University of Ottawa).
- [10] Yang, L., Lin, X., Li, H., & Gravina, R. J. (2019). A new constitutive model for steel fibre reinforced concrete subjected to dynamic loads. *Composite Structures*, 221, 110849.
- [11] Salehi, H., & Burgueño, R. (2018). Emerging artificial intelligence methods in structural engineering. *Engineering structures*, 171, 170-189.

Chapter 2

2 Literature Review

2.1 Blast phenomenon

When an explosive material is detonated, it instantaneously generates extremely high temperatures and pressure. The gas surrounding the material is consequently compressed and expands radially from the source. As it expands, the compressed air forms a shock wave front, also known as a blast wave, with considerable pressure, which decays as it covers a larger volume. Moreover, as the initial air expansion occurs and forms the positive pressure wave, a vacuum is created at the center of the detonation region. The resulting vacuum region creates a negative pressure wave that expands with the positive wave while trailing behind it. In terms of pressure magnitudes, the positive pressure wave is significantly greater than its negative counterpart, which is often disregarded in structural analysis. Additionally, the positive pressure shock wave is characterized by a positive phase duration, which is considerably less than the corresponding negative phase duration.

If the positive pressure shock wave expands without interacting with any surfaces, the wave front pressure will eventually decay until it reaches a value below atmospheric pressure before reclaiming equilibrium [1]. A graphical representation of the pressure-time history of an idealized shock wave is shown in **Figure 2-1**. However, in the case where the initial shock wave (or incident wave) interacts with a surface, the pressure wave front reflects and produces an applied reflected pressure. The resulting reflected pressure is significantly greater than the initial shock wave pressure due to the air particles being compressed at the surface, leading to an increase in pressure [2].

The different types of blast waves may be classified with respect to the setting in which detonation occurs and are labeled as confined or unconfined explosions. A confined explosion is formed when material detonation is initiated within an enclosed space or

structure. This type of explosion produces blast waves that are significantly amplified with the occurrence of reflected waves on nearby surfaces. Based on the degree of confinement, a build-up of quasi-static gas pressure and temperature is produced and possesses a duration longer than the initial shock wave. The different degrees of confinement are fully vented, partially confined, or fully confined in which gas pressure build-up increases with confinement. Conversely, the second type of blast wave is produced from unconfined explosions, which are characterized by the height of detonation from the ground and labeled as free-air burst explosions, air burst explosions, and surface burst explosions [3]. The current thesis primarily deals with unconfined explosions, which are discussed in detail in subsequent sections.

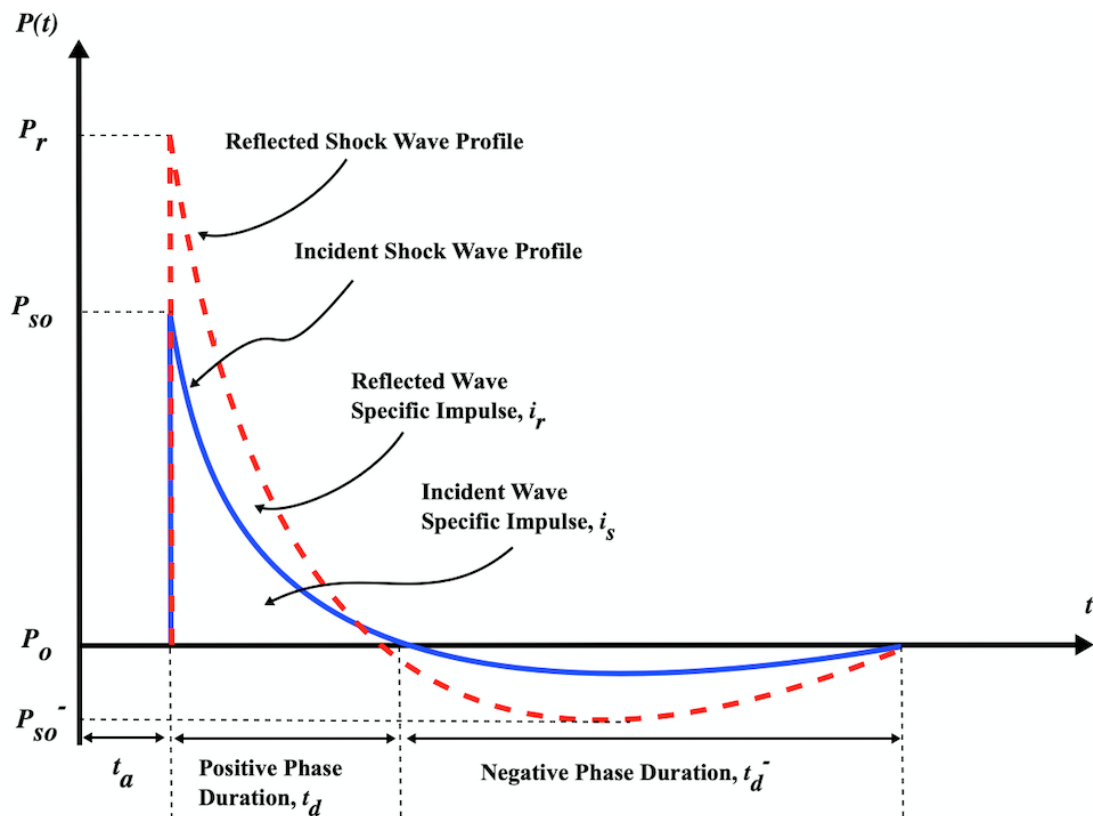


Figure 2-1. Pressure-time profile of a shock wave.

2.1.1 Blast wave parameters

The two primary components that affect the parameters of a blast wave are the weight of the explosive charge, W , and its standoff distance, R . Using the cube-root scaling law, a relationship between the two components and a scaled distance, Z , is presented in Eq. (1). This relationship was proposed by Hopkinson in 1915 after it was observed that two explosions of varying weights produced the same effect for some common scaled distance [4]. Furthermore, the use of scaling laws allows for the investigation of large-scale blasts using proportionate small-scale charge weights and standoff distances [5]. The implementation of a scaled distance has been conveniently used to form pertinent relationships between a blast's charge weight and standoff distance with numerous blast parameters, as will be described within this section. It should be noted that the charge weight, W , is often taken in terms of TNT, in which weights of alternative explosive materials are converted with respect to their corresponding TNT equivalence.

$$Z = \frac{R}{W^{1/3}} \quad (1)$$

The idealized pressure-time history of a shock wave presented in **Figure 2-1** is a meaningful representation of both the behavior of a shock wave, as well as its parameters. As shown in the figure, P_o , P_{so} , and P_{so}^- are the ambient atmospheric pressure, peak positive overpressure, and peak negative overpressure, respectively. Similarly, the quantities of the positive phase duration and the negative phase duration are denoted as t_d and t_d^- , respectively. Throughout this thesis, direct investigations were conducted only with respect to the positive phase of blast loading, while considerations for the negative phase were disregarded. The positive phase pressure profile can be represented by the modified Friedlander equation given in Eq. (2) [6], where b is a waveform parameter that characterizes the decaying pressure and is empirically obtained as a function of the scaled distance [7].

$$P(t) = P_o + P_{so} \left(1 + \frac{t}{t_d}\right) e^{-\frac{bt}{t_d}} \quad (2)$$

In addition to the parameters observed from the pressure-time history, two additional parameters that are used to characterize a blast wave are its positive-phase specific impulse, i_s , and its negative-phase specific impulse, i_s^- which are quantified as the area under each respective curve. The values of i_s may be taken as the integration of the positive pressure over the positive phase duration, as shown in Eq. (3), where t_a is the blast's time of arrival.

$$i_s = \int_{t_a}^{t_a+t_d} P(t) dt \quad (3)$$

To obtain the appropriate pressure profile considering a given charge weight and standoff distance, the quantities of P_{so} and t_d are required. In determining the peak positive overpressure, various researchers have proposed appropriate formulations as a function of the scaled distance. By analyzing the differential equations of gas motion, Brode developed an analytical expression with respect to different ranges of scaled distance, which are presented in Eq. (4) with the pressure units in bar scaled distances given as $m/kg^{1/3}$ [9].

$$P_{so} = \frac{6.7}{Z^3} + 1 \quad (P_{so} > 10 \text{ bar}) \quad (4a)$$

$$P_{so} = \frac{0.975}{Z} + \frac{1.455}{Z^2} + \frac{5.85}{Z^3} - 0.019 \quad (0.1 < P_{so} < 10 \text{ bar}) \quad (4b)$$

Similarly, Henrych proposed expressions for peak positive overpressures following the similarity ratio formula based on experimental data and considering free-field air explosions for varying ranges of scaled distances [10]. These expressions are shown in Eq. (5) with pressures given in bar and scaled distances in $m/kg^{1/3}$.

$$P_{so} = \frac{14.072}{Z} + \frac{5.540}{Z^2} - \frac{0.357}{Z^3} + \frac{0.00625}{Z^4} \quad (0.05 < Z < 0.3) \quad (5a)$$

$$P_{so} = \frac{6.194}{Z} - \frac{0.326}{Z^2} + \frac{2.132}{Z^3} \quad (0.3 < Z < 1) \quad (5b)$$

$$P_{so} = \frac{0.662}{Z} + \frac{4.05}{Z^2} + \frac{3.228}{Z^3} \quad (1 < Z < 10) \quad (5c)$$

A computationally efficient formula was proposed by Kinney and Grahm [7] based on a chemical explosive of 1 kg TNT considering scaled distance values between 0.1 and 20 $m/kg^{1/3}$ with pressure units in bar, as presented in Eq. (6).

$$P_{so} = \frac{808P_o \left[1 + \left(\frac{Z}{4.5}\right)^2\right]}{\left\{\left[1 + \left(\frac{Z}{0.048}\right)^2\right]\left[1 + \left(\frac{Z}{0.32}\right)^2\right]\left[1 + \left(\frac{Z}{1.35}\right)^2\right]\right\}^{0.5}} \quad (6)$$

Another expression based on explosion data analysis was proposed by Sadovskiy and is given by Eq. (7) with pressure units in MPa [10].

$$P_{so} = 0.085 \left(\frac{W^{1/3}}{R}\right) + 0.3 \left(\frac{W^{1/3}}{R}\right)^2 + 0.8 \left(\frac{W^{1/3}}{R}\right)^3 \quad (7)$$

The same authors have also proposed different empirical expressions to determine the positive phase duration of a blast wave as functions of the scaled distance, standoff distance, and charge weight. The corresponding expressions of Henrych [9], Kinney and Graham [7], and Sadovskiy [10] are presented in Eqs. (8) - (10), respectively.

$$t_d = e^{(-2.75 + 0.27 \log Z) + \log W^{1/3}} \quad (8)$$

$$t_d = \frac{980W^{1/3} \left[1 + \left(\frac{Z}{0.54}\right)^{10}\right]}{\left[1 + \left(\frac{Z}{0.02}\right)^3\right]\left[1 + \left(\frac{Z}{0.74}\right)^6\right]\left[1 + \left(\frac{Z}{6.9}\right)^2\right]^{0.5}} \quad (9)$$

$$t_d = 1.2 \sqrt[6]{W} \sqrt{R} \quad (10)$$

Empirical expressions for the positive-phase specific impulse have also been extensively developed and are collected in [11], but the underlying impulse derivation shown in Eq. (3) is well-established, nonetheless. Although the literature includes an extensive effort for developing empirical expressions for peak positive overpressures, the application of blast wave and structure interactions is heavily dominated by magnitudes of the reflected pressures. It has previously been stated that pressures of reflected blast waves are several times greater than the pressure of its incident wave. As a result, an analytical equation to express reflected pressure as a function of peak positive overpressure was derived from the conservation of momentum and energy by Rankine and Hugoniot [2] as given by Eq. (11).

$$P_r = 2P_{so} + (\gamma + 1)q_s \quad (11)$$

The constant γ is the specific heat ratio of a real gas and q_s is the dynamic pressure expressed as Eq. (12), where ρ_s is the density of air and u_s is the particle velocity behind the shock wave front.

$$q_s = \frac{1}{2} \rho_s u_s^2 \quad (12)$$

The expression for the wave front velocity is presented in Eq. (13), where a_o is the speed of sound in ambient conditions.

$$u_s = \frac{a_o P_{so}}{\gamma P_o} \left[1 + \left[\frac{\gamma+1}{2\gamma} \right] \frac{P_{so}}{P_o} \right]^{-0.5} \quad (13)$$

When choosing the γ value for air equal to 1.4 and substituting Eqs. (12) and (13) in Eq. (11), the final expression is given in Eq. (14).

$$P_r = 2P_{so} \left[\frac{7P_o + 4P_{so}}{7P_o + P_{so}} \right] \quad (14)$$

Based on this expression, it can be observed that in the case of a very small theoretical incident overpressure, the reflected pressure reduces to a lower limit corresponding to twice the incident overpressure. Conversely, if the incident overpressure was considerably greater than the ambient pressure, then the expression indicates the reflected pressure can be up to eight times the incident overpressure. Although the theoretical ratio between the reflected and incident pressures, C_r , is shown to be between 2 and 8, actual recorded ratios have reached up to 12 due to effects of gas dissociation [2]. It should be noted that this expression assumes the reflected pressure is acting normal to a surface with an angle of incidence of zero.

In the case that the incident pressure is reflected with an angle of incidence, α , a chart provided by UFC 3-340-02 [3] may be adopted to compute the resulting reflected pressure. This is depicted in **Figure 2-2** which relates the ratio between the reflected and incident pressures, C_r , to the angle of incidence. Based on this chart, it can be observed that the value of C_r decreases as the angle of incidence deviates from being normal to the surface and reduces to a value of 1 when acting parallel to a surface. Additionally, a jump in

reflected pressure is observed for angles of incidence between 40 and 50 degrees. This phenomenon is a unique characteristic of air burst explosions and is described in the subsequent section.

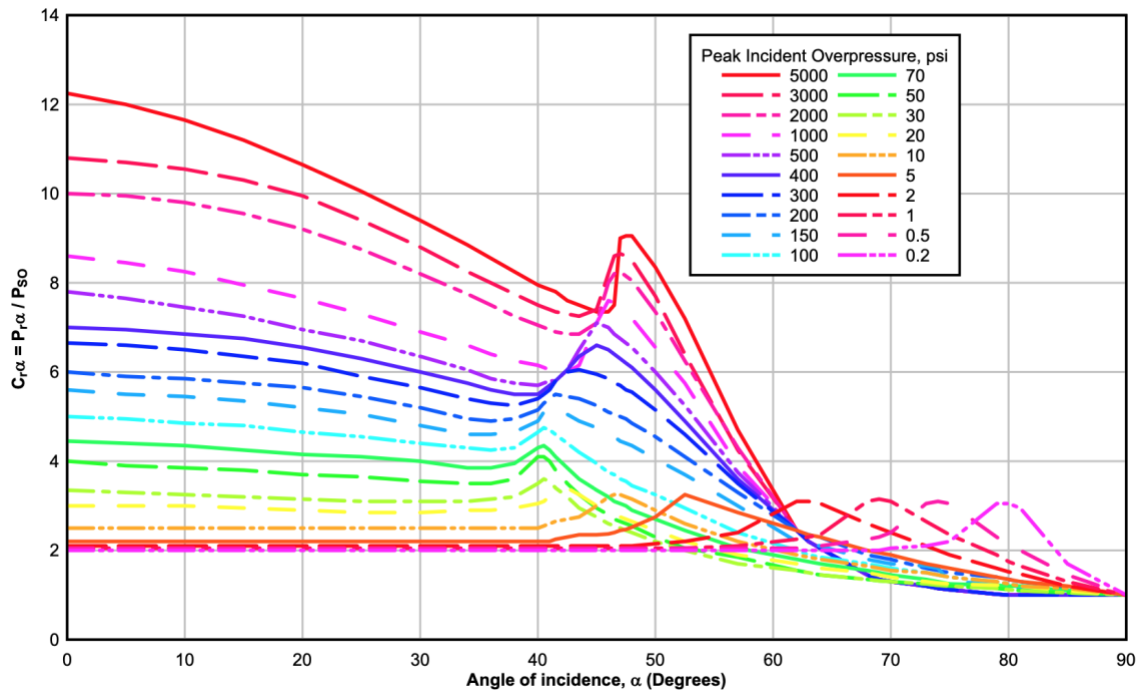


Figure 2-2. Reflected pressure factor for different angles of incidence [3].

Overall, it can be noted that analytical methods for computing positive incident overpressures and positive phase durations are readily available and may be used to characterize an expression for shock wave pressure-time histories. Furthermore, expressions for additional blast parameters such as positive-phase specific impulses and reflected pressures are also accessible. However, charts or graphical adaptations have been developed based on extensive experimental testing and may be used as an alternative to obtain multiple blast parameters. These charts conveniently present both positive phase and negative phase parameters as well as parameters pertaining to reflected blast waves as functions of the scaled distance. Moreover, independent charts are provided for blast waves occurring from free air burst explosions and surface burst explosions. The alternative types of unconfined explosions as well as their respective blast parameter charts are discussed in the subsequent section.

2.1.2 Unconfined explosions

The first type of unconfined explosions is free air burst explosions, which occur at a sufficient height above the ground, such that the resulting shock wave interacts with a target structure before reaching the ground. **Figure 2-3** depicts a typical free air burst explosion with a given charge weight and standoff distance. Upon interacting with the target structure, the incident waves reflect and apply an amplified pressure [2,3]. In addition to the parameters obtained through the empirical expressions in the previous sections, alternative critical parameters are graphically obtained using the chart in **Figure 2-4**, which is only compatible with free air burst explosions. As a function of the scaled distance, this chart provides the parameters of pressures, impulses, and durations of incident and reflected shock waves considering positive and negative phases. The chart also considers the wavelength and wave front velocity of the shock wave. When an angle of incidence greater than zero is considered, pressure values from **Figure 2-4** may be adapted using the chart shown in **Figure 2-2**.

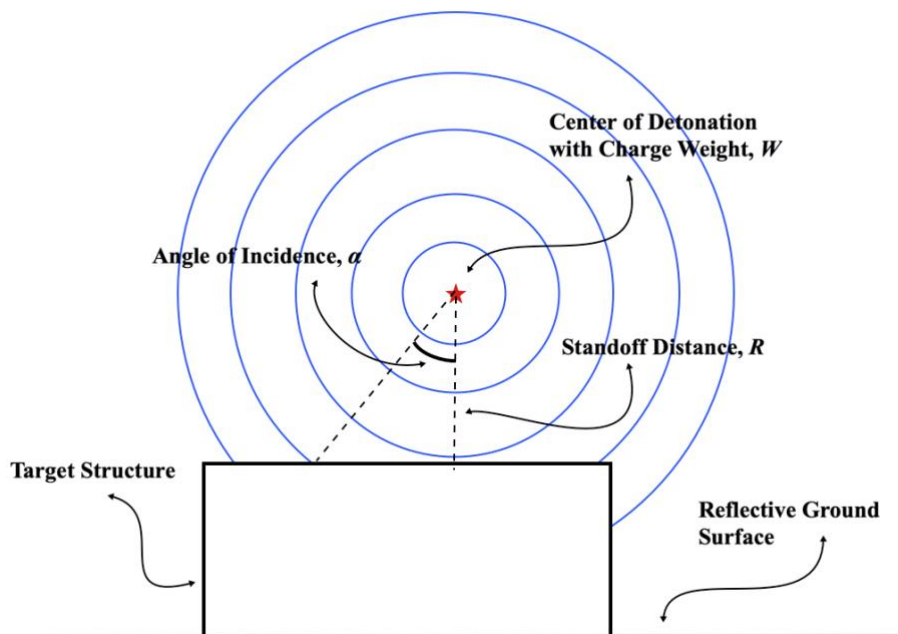


Figure 2-3. Free air burst explosion on a structure.

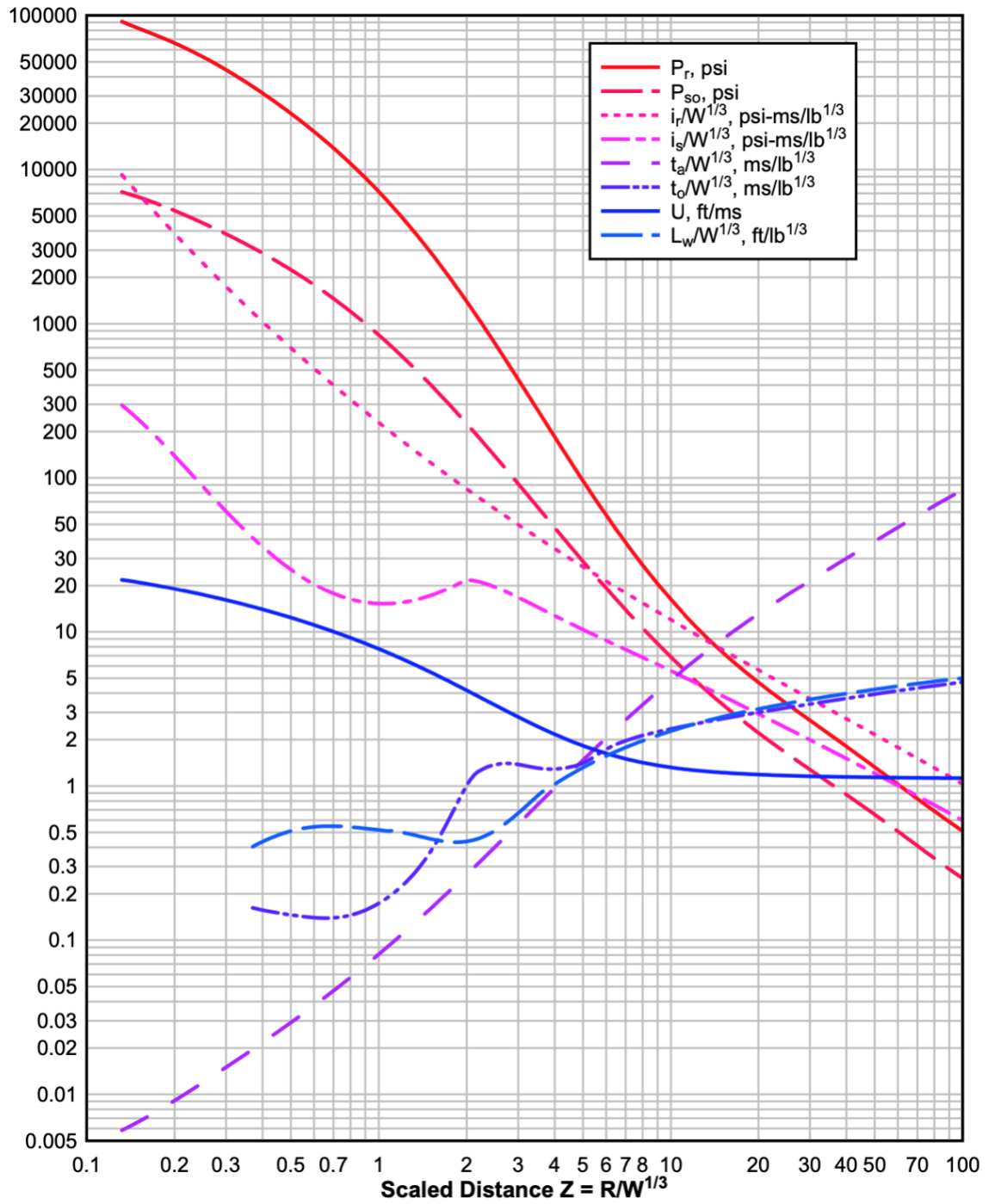


Figure 2-4. Positive-phase shockwave parameters for a free air burst explosion [3].

The second type of unconfined explosions is air burst explosions and occurs when a detonation is initiated at a distance above and away from a target, such that the incident wave interacts with the ground before reaching the target. As the incident wave approaches the ground, it generates a reflected pressure wave that travels outwards with an amplified pressure magnitude. As the shock waves propagate, the initial incident wave and the generated reflected wave interact and form a Mach front, which may be idealized as a plane wave front. The concept of an assumed plane wave is made based on the condition that the blast is at a sufficient scaled distance from the target structure. The point at which the incident wave, reflected wave, and Mach front meet is labeled as the triple point whose height increases with increasing distance from the blast source [2,3]. **Figure 2-5** depicts the formation of a Mach front resulting from an air burst explosion. It should be noted that the pressure profile for a Mach front resembles that of an incident pressure wave.

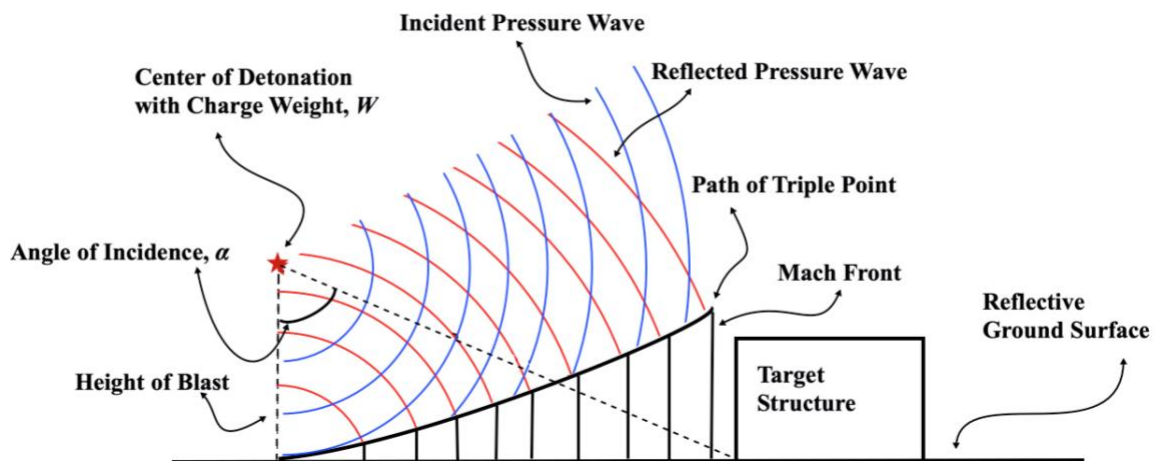


Figure 2-5. Air burst explosion on a structure.

Two noteworthy parameters of the air burst explosion are the blast height and angle of incidence. Smith and Hetherington [2] speculated that reflected pressures have a limiting angle of incidence value after which incident waves no longer create traditional reflections but instead form Mach reflections. This angle of incidence produces a reflected pressure (Mach pressure) greater than the reflected pressure produced at a zero angle of incidence. The aforementioned limiting angle of incidence varies with varying blast magnitudes but is found to be greater than 40 degrees. This is also observed in **Figure 2-2**, which depicts

the discrepancy (jump) in reflected pressure at angles of incidence greater than 40 degrees. Although direct blast parameters for air bursts cannot readily be obtained from **Figure 2-4**, an adaptive approach is used instead as proposed by [3]. For a given blast height (scaled by the charge weight) and angle of incidence, the blast's reflected pressure (P_{ra}) may be obtained using the chart in **Figure 2-6**. By inputting the resulting reflected pressure in **Figure 2-4** as the incident pressure ($P_{ra} = P_{so}$), an equivalent scaled distance value may be obtained, which is then used to acquire the remaining blast parameters. A similar approach is taken to identify the reflected impulse (i_{ra}) based on the blast height and angle of incidence using a similar chart in [3] and inputting it as the incident impulse, ($i_{ra} = i_s$), in **Figure 2-4**. It can also be observed from **Figure 2-6** that as the height of blast increases, the effect of reflected pressure variations with respect to varying angles of incidence becomes less apparent.

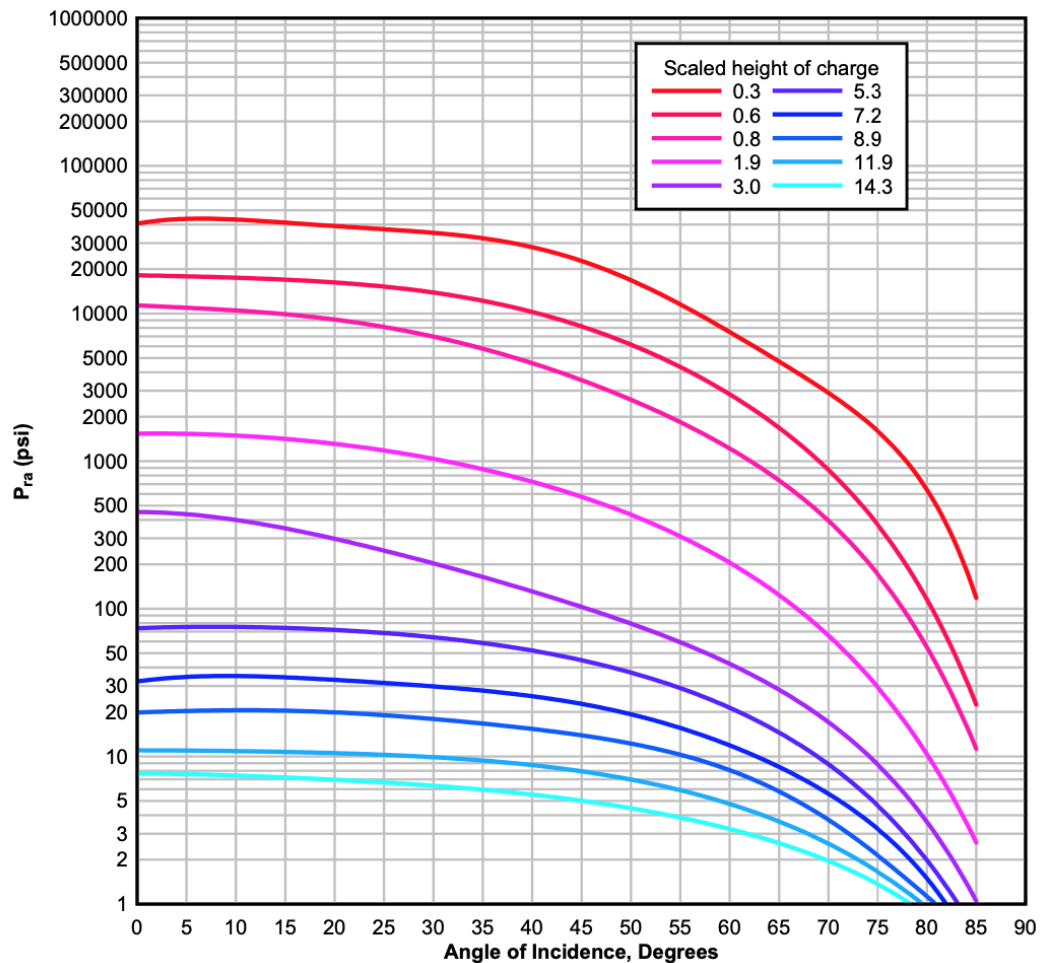


Figure 2-6. Reflected pressures for varying scaled heights and angle of incidence [3].

The third type of unconfined explosions is surface burst explosions, which occurs when a blast wave is initiated from or near a ground surface. Due to the proximity of the reflective ground surface, reflected waves are generated upon detonation and merge with the incident waves to form a single high-magnitude pressure wave at the point of detonation, as described in **Figure 2-7**. The development of the merged waves in surface bursts follows a similar concept as the Mach waves from air bursts but forms hemispherical waves with respect to the blast source. When the propagating waves of a surface burst reflect off a target structure, the blast loading may be idealized as a plane wave [2,3].

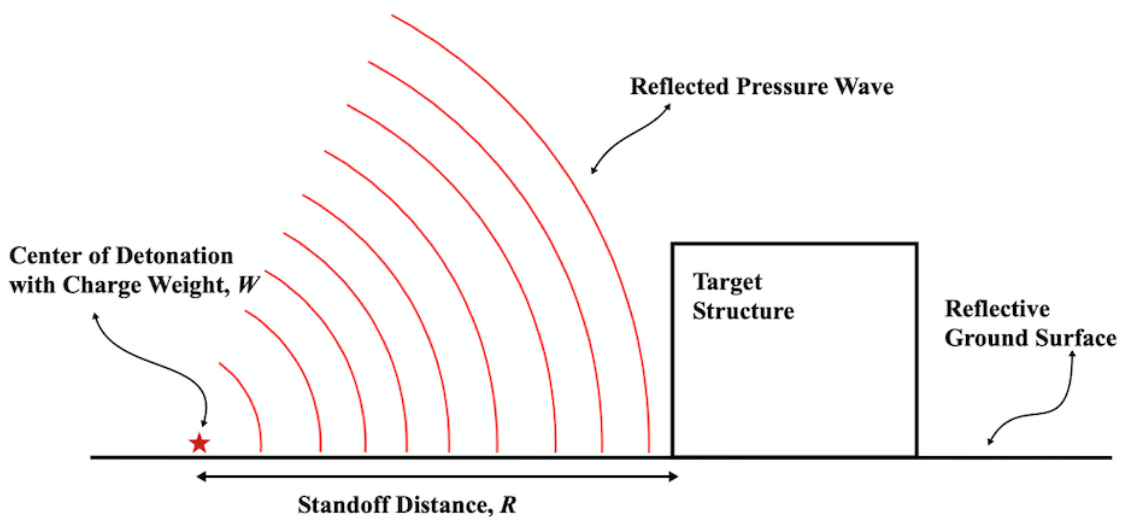


Figure 2-7. Surface burst explosion on a structure.

A similarity between surface bursts and free air bursts is that the generated blast waves are uniformly propagated albeit at different blast magnitudes. It has previously been demonstrated that the parameters for surface bursts correlate to free air burst parameters with an applied enhancement factor to the source charge weight (i.e. blast energy) [2]. When assuming a perfect ground reflection, an enhancement factor of 2 is taken, however, a more practical value of 1.8 is used due to energy dissipation during crater formation. Although this approach yields acceptable parameter values, a dedicated chart similar to **Figure 2-4** was developed for obtaining several positive phase surface burst parameters as a function of the scaled distance and is provided in **Figure 2-8** [3].

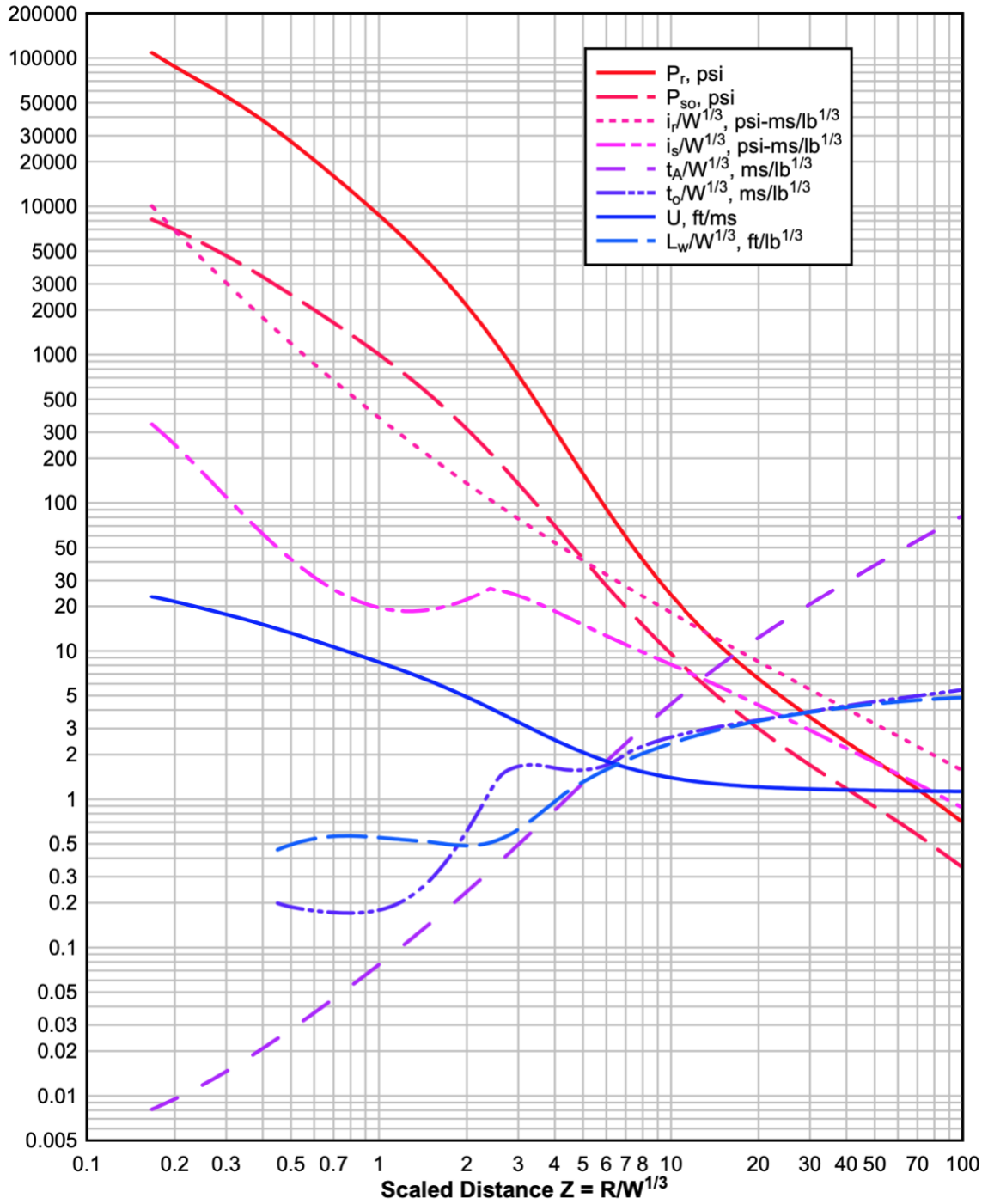


Figure 2-8. Positive-phase shockwave parameters for a surface burst explosion [3].

2.2 Existing modeling methods

2.2.1 Equivalent dynamic SDOF models

A single degree of freedom (SDOF) model is among the most implemented approaches in predicting the dynamic response of an element under blast loading. The dynamic equation of motion that characterizes a SDOF system is given in Eq. (15) where m , c , and K are the mass, damping coefficient, and stiffness with their terms of acceleration, velocity and displacement, respectively.

$$m\ddot{u} + c\dot{u} + Ku = F(t) \quad (15)$$

The damping term is often neglected due to the minor effect of damping forces in structural blast applications. Additionally, the stiffness term Ku is often replaced with a more general resistance function term, $R(u)$. Lastly, the force as a function of time, $F(t)$, may be replaced with a more compatible expression in terms of the reflected blast pressure over the applied area, $AP_r(t)$. The quantities shown in Eq. (15) may be acceptably taken as their actual values if the entire mass experiences a load that causes the system to move as a unit. However, in the case where motion varies along the length of a member, the resulting displacements would be produced with considerable error. For such a continuous system, the variable motion of a distributed mass under a distributed load may be ideally characterized by an infinite degree of freedom. However, this system may be conveniently represented by an equivalent SDOF through the introduction of transformation factors. The equivalent system can capture the dynamic response of a desired point with respect to an assumed deflected shape [2,3,12].

The three types of transformation factors are the load factor, K_L , mass factor, K_M , and stiffness factor, K_S , where each factor is derived through the total work done, kinetic energy, and strain energy, respectively. When considering an appropriate deflected shape, $\varphi(x)$, the equivalent load, mass, stiffness, and resistance expressions along a member are shown in Eqs. (16) – (19) [3,12].

$$F_{eq} = \int_0^L F(x)\varphi(x)dx \quad (16)$$

$$M_{eq} = \int_0^L M(x)\varphi^2(x)dx \quad (17)$$

$$K_{eq} = \int_0^L EI(x)[\varphi''(x)]^2 dx \quad (18)$$

$$R_{eq} = \int_0^L R(u)\varphi(x)dx \quad (19)$$

The ratio of each equivalent quantity to the corresponding actual quantity will produce each respective transformation factor as expressed in Eq. (20). It should be noted that the resistance transformation factor is very similar to the load transformation factor and can be considered the same [2].

$$K_L = \frac{F_{eq}}{F} ; K_M = \frac{M_{eq}}{M} ; K_S = \frac{K_{eq}}{K} ; K_R = K_L \quad (20)$$

By implementing these factors to the original SDOF equation in Eq. (15), an equivalent system may be developed. It is also worth mentioning that different factors may be derived with respect to varying deflected shapes that reflect the element's boundary conditions or loading. Lastly, since both the resistance term and the loading term in the SDOF equation use the load factor, K_L , a load-mass factor K_{LM} is introduced to simplify the expressions and is merely a ratio of the mass factor and load factor. The developed equivalent SDOF expression is presented in Eq. (21).

$$K_{LM}m\ddot{u} + R(u) = AP_r(t) \quad (21)$$

Although several methods may be used to solve the equivalent SDOF equation, a common approach is the average acceleration method, which employs an iterative numerical solution [2,12]. Using this method, values for acceleration, velocity, and displacement are computed at numerous small-time increments, Δt . Initially, the acceleration value at $t = 0$ is denoted as \ddot{u}_o and computed using the rearrangement of Eq. (21) in which both the displacement and velocity are zero ($u_o = \dot{u}_o = 0$). The loading value of $AP_r(t=0)$ and the resistance value of $R(u_o)$ are extracted from an assumed blast pressure profile and resistance function. Therefore, the formulation of the initial acceleration as well as its general form for every time step $t_i = t_{i-1} + \Delta t$ are shown in Eq. (22).

$$\ddot{u}_o = \frac{AP_r(0) - R(u_o)}{K_{LM}m} \quad ; \quad \ddot{u}_i = \frac{AP_r(t_i) - R(u_i)}{K_{LM}m} \quad (22)$$

For computing the velocity as a function of the average acceleration across a time step, the expression in Eq. (23) is used. Similarly, the corresponding displacement at every time step is computed using Eq. (24).

$$\dot{u}_i = \dot{u}_{i-1} + 1/2(\ddot{u}_i + \ddot{u}_{i-1})\Delta t \quad (23)$$

$$u_i = u_{i-1} + 1/2(\dot{u}_i + \dot{u}_{i-1})\Delta t \quad (24)$$

When computing the values of displacement and velocity for $t > 0$, the approach consists of a prediction pass and a correction pass. The prediction pass assumes $\ddot{u}_i = \ddot{u}_{i-1}$ in order to obtain the predicted velocity, \dot{u}_i , and displacement, u_i , values using Eqs. (23) and (24) and the corresponding resistance $R(u_i)$ from an appropriate resistance function. Afterwards, the acceleration, \ddot{u}_i , is computed using the predicted values and is then inputted in Eqs. (23) and (24) to compute the corrected velocity, \dot{u}_i , and displacement, u_i , at a given time t_i . Once the corrected values are computed, the time interval is updated and both passes are reiterated [3,13].

A notable feature of the equivalent SDOF model is its ability to account for more elastic and inelastic responses. This may be addressed through both the predefined resistance function of the element, as well as the derivation of the load-mass factor based on an inelastic deflected shape. Additionally, more detailed parameters pertaining to an element's static and dynamic material properties may be accounted for through the element's developed resistance function. Examples of such implementations can be found in various studies [14,15,16].

2.2.2 Numerical models

An alternative modeling method is the use of numerical simulations that can accurately capture significantly more complex structural behaviors under various blast loading scenarios. For the application of blast-loaded structures, commercial software such as LS-DYNA [17], ABAQUS [18], and ANSYS [19] are widely used in developing such

numerical models. Although several different modeling techniques exist to produce reliable results, two general approaches are briefly described herein.

The first approach employs a purely Lagrangian formulation in which only the structure is explicitly modeled, and the model's mesh deforms with the structure under loading. In this case, the blast loading is applied directly on the structure based on semi-empirical functions of blast parameters using the built-in CONWEP algorithm [20,21]. As a result, the explosive material, blast wave propagations, and fluid-structure interactions are not explicitly modeled. This leads to reduced computational demand but also produces less accurate responses when compared to more detailed approaches [5]. Furthermore, one of the drawbacks of the Lagrangian model is its susceptibility to mesh distortion at high strain-rates and large deformations. A means of mitigating mesh distortions is remeshing at various time-steps, which also leads to an increase in computational time [22]. Generally, this approach yields acceptable results for non-complex structures under moderate deformations.

The second approach uses a multi-material arbitrary Lagrangian-Eulerian (MMALE) formulation. The inclusion of the Eulerian formulation eliminates the event of mesh distortions of the Lagrangian formulation by implementing an overlapping fixed mesh through which the material deforms [23]. Moreover, the MMALE formulation allows for multiple materials to be defined for a single element and uses an interface tracking algorithm to track the different materials within an element [24]. This advantage can increase the flexibility and accuracy of the model. As opposed to the previous modeling approach, the MMALE formulation requires the explicit modeling of the explosive material, the air through which the blast propagates, as well as the structure. Moreover, the interaction between the resulting blast wave and the structure is accounted for throughout the model [21]. Details pertaining to each approach along with additional numerical modeling methods can be found in [5,21,25].

2.3 Previous research on RC members under blast loads

2.3.1 General

The primary response of a RC member is dependent on the positive phase blast load duration, t_d , with respect to its fundamental period of vibration, T . The ratio of these durations, t_d/T , can be used as an indication to the resulting structural behavior. When an explosive material is detonated directly on or near a surface, the resulting t_d/T ratio will be very small, and the corresponding structural response is governed by local damage modes of concrete crushing or spalling. Moreover, the applied loading is remarkably concentrated at the point of detonation. For greater ratios of t_d/T , the resulting structural behavior may exhibit either direct or diagonal shear responses. At such ratios, the detonation occurs at a distance far enough that an applied non-uniform loading is induced along the member in which the loading may be labeled as near-field. At relatively large t_d/T ratios due to distant detonations, the applied blast loading may be considered uniform and labeled as far-field in which the resulting structural response is primarily governed by flexural behavior [25, 26]. The contrasting pressure distributions of far-field and near-field loading can be observed in **Figure 2-9**.

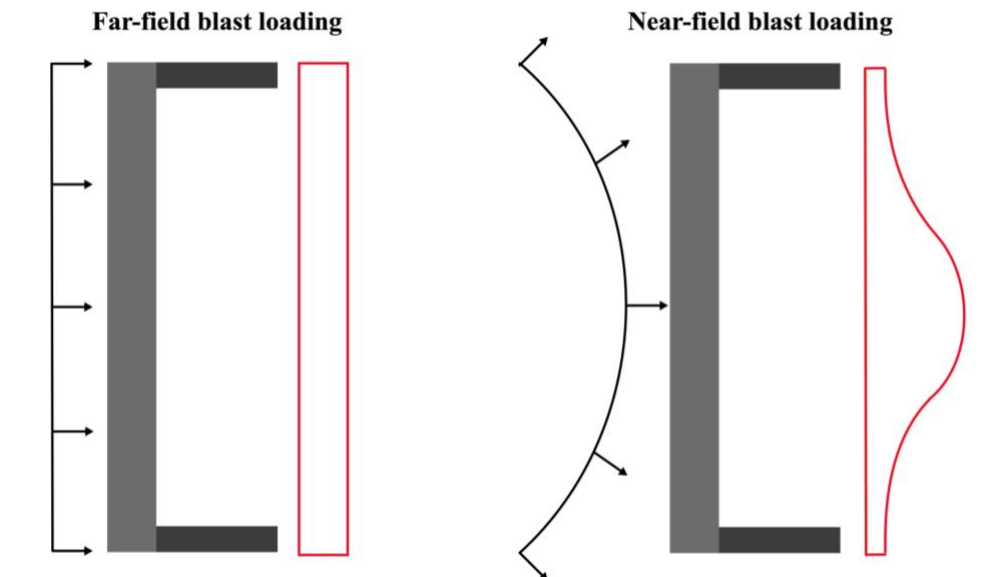


Figure 2-9. Shock-wave interaction and resulting pressure distribution on target structural member.

This generalized classification of behaviors with respect to varying blast load scenarios is applicable across RC slabs, columns, and beams. Throughout the thesis, both shear and flexural responses are investigated with a greater focus on the latter. The current section provides a discussion on each RC member through existing studies exploring their unique parameters and resulting behaviors.

2.3.2 Reinforced concrete slabs

An analytical study by Low and How [27] investigated the effects of slab thickness, reinforcement ratio, and boundary conditions of RC slabs under blast loading. An increased blast capacity was observed for greater slab thicknesses and reinforcement ratios. It was also reported that slabs having fixed boundary conditions were more susceptible to failure than simply supported slabs under greater blast magnitudes. Furthermore, Tai *et al.* [28] developed a numerical model using LS-DYNA to investigate RC slab parameters subjected to blast loading. When considering a large reinforcement ratio, the maximum displacement at the slab center was mitigated, but the damage at the supports increased with blast magnitude. Conversely, slabs with lower reinforcement ratios produced greater maximum displacements while showing little or no damage at the supports. It was posited that the slab's structural response was altered from bending failure to shear failure with increasing reinforcement ratio and at high magnitudes of blast loading.

A more recent numerical study by Lin *et al.* [29] implemented LS-DYNA to analyze the effect of slab thickness and reinforcement ratio of RC slabs under blast loading. It was reported that increasing the slab thickness had a remarkable effect on reducing maximum displacements. The influence of the reinforcement ratio was also observed to improve the blast capacity of RC slabs but having a lower effect than the slab thickness.

A limited experimental study investigated the effects of concrete compressive strength and steel yield strength in RC slabs under blast loading [30]. A blast load simulation device was used to load four one-way RC slabs. It was observed that both parameters contributed to mitigating maximum displacements with a greater influence reported from an increase in compressive strength.

Furthermore, Yao *et al.* [31] implemented both experimental testing and numerical modeling in analyzing RC slabs under blast loading. During both implementations, two major observations were reported. First, an increase in reinforcement ratio resulted in a reduced maximum displacement, which is consistent with previously reported studies. Secondly, the magnitude of localized spalling damage was reduced with an increase in the reinforcement ratio.

2.3.3 Reinforced concrete columns

Astarlioglu *et al.* [32] performed an analytical study to investigate various features of RC columns under blast loading. It was observed from numerous comparisons that an increase in the axial load resulted in greater capacity of columns to resist shear failure under intense magnitudes of loading. Moreover, an increase in the longitudinal reinforcement ratio produced a positive effect in reducing maximum displacements for all ranges of loading. It was also noted that a tension membrane behavior was exhibited in columns under greater axial loads, which deterred its post-blast axial load carrying capacity.

An extensive experimental investigation was conducted by Braimah and Siba [33] using an explosive material in which the effects of column detailing on high magnitude blast loading were studied. It was observed that increasing the transverse reinforcement improved the concrete confinement and led to improved blast performance. The study also reported that for lower blast magnitudes, an increase in the axial load improved the column's stiffness against loading, whereas the opposite was observed at greater magnitudes of loading. This was reportedly due to crushing in the compression zone as the column underwent lateral displacements and led to a reduction in stiffness.

Moreover, a numerical model using LS-DYNA was developed by Kyei and Braimah [34] as an extension of the work [33] to further investigate the response of conventionally and seismically detailed RC columns subjected to blast loading. The effect of transverse reinforcement ratio was reported to be relatively insignificant at lower degrees of blast loading but was more pronounced at greater blast magnitudes. Conversely, for all magnitudes of loading, an increase in axial load resulted in greater blast resistance.

However, the effect of axial loading was found to have a limiting influence at larger axial loads, which resulted in an adverse response.

In evaluating the behavior of blast-loaded RC columns, Bao and Li [35] conducted a comprehensive evaluation using numerical models in LS-DYNA and considered multiple application parameters. The influence of axial load was shown to improve the column's capacity when having sufficient confinement and under low blast magnitudes. This conclusion is consistent with previously reported findings. Similarly, an increase in longitudinal reinforcement ratios generally resulted in an increase in a column's performance. However, it was also observed that when longitudinal reinforcement exceeded a certain limit, the column's flexural resistance may exceed its shear resistance, thus resulting in a shear failure for poorly confined columns. When assessing the effect of the transverse reinforcement ratio, it was found that increased ratios allowed for a greater blast capacity, while significantly influencing the resulting failure mode.

2.3.4 Reinforced concrete beams

An experimental study by Li *et al.* [36] evaluated the behavior of RC beams under blast loading using a blast simulation device. The study consisted of numerous test specimens and the effects of several application parameters were investigated. When considering the effect of the longitudinal reinforcement ratio, a mitigated maximum displacement was observed at higher ratios, but the resulting element failure was consequently more critical than that observed at lower ratios. Moreover, the influence of the transverse reinforcement ratio showed a remarkable contribution towards resisting brittle shear failure modes, while having a relatively minimal effect on reducing maximum displacements. It was also reported that an increase in the concrete compressive strength produced a minor effect on both the maximum displacement and resulting failure mode.

An evaluation of RC beams under high magnitude blast loads was experimentally conducted by Yao *et al.* [37] using an explosive material. It was reported that an increase in the transverse reinforcement ratio produced a notable reduction in the maximum displacement and contributed to mitigating local damages. The local damage included damage to the concrete core, as well as damage through concrete spall radius and depth.

Furthermore, Liu *et al.* [38] experimentally investigated the degree of damage to RC beams under various weights of explosive materials. Considering similar beam configurations, the variations in element damage due to different blast magnitudes consisted of large tensile cracking or compressive crushing due to flexural behavior, local concrete spalling, or a combination of both.

In a more recent study, Rao *et al.* [39] performed an experimental investigation on RC beams under high-intensity cylindrical charge weights. A subsequent numerical model was developed using ANSYS based on experimental validation and the effect of longitudinal reinforcement was analyzed. It was observed that an increase in the ratio led to an increase in blast performance through reducing the maximum and residual displacements. It was also qualitatively reported that when lower and intermediate ratios were used, the beam exhibited flexural-shear behavior, while a direct shear response was observed at very high reinforcement ratios. These findings are consistent with previously stated observations.

2.4 Structural blast mitigation strategies

2.4.1 General

With the escalation in both intentional and accidental blast events on infrastructures, the availability of feasible and effective implementations towards reducing risks has become increasingly pertinent. One of the most reliable approaches to significantly reduce blast-related structural damage is to increase the event's potential standoff distances. This may be achieved through the deployment of barriers or perimeters surrounding the structure [40]. However, this approach is highly inapplicable in populated or urban regions where the available space is limited. Thus, structural blast-mitigation strategies have resorted to focusing on element-specific modifications. These strategies fall under two major categories being design or retrofit [41]. Design strategies consider the implementation of efficient composite members such as concrete-filled steel tube components, prestressed components, or components built with advanced fiber-reinforced concrete mixtures. Such strategies are effective for newly developed structures, which consider protective measures. On the other hand, the use of retrofitting strategies may be adapted to both new

and existing structures. These strategies consider attaching or fitting innovative materials such as fiber-reinforced polymer (FRP) sheets, or metal cladding on structural members [41]. Despite the remarkable blast resistant contribution of such strategies, existing design codes have yet to provide dedicated guidance on their widespread applications [42]. The two blast-mitigation strategies, along with their element-specific application, that have been considered in this thesis are the use of external FRP retrofitting for RC slabs and the incorporation of steel fibers in RC beams. Therefore, the current section provides a brief description of each approach's advantages and disadvantages, along with discussions on their parameters through existing studies. Moreover, the details of blast-mitigation techniques for conventional RC members discussed in this section sets the underlying importance and motivation towards the development of Chapters 6 and 7 of this thesis.

2.4.2 External FRP retrofitting for RC slabs

The different types of materials considered throughout existing studies on FRP retrofitting are carbon fiber (CFRP), glass fiber (GFRP), and aramid fiber (AFRP) reinforced polymers. During application, these materials are in the form of sheets or strips that are either bonded to a member's surface or wrapped around it. The surface bonding process requires competent workmanship and is often achieved using a polymer resin [43]. Furthermore, the installation of FRP retrofits may be applied to consider multiple orientations to resist loading based on the type of member and may also consist of several independent layers.

The major advantage of using FRP retrofitting stems from the material's remarkable tensile resistance that is imparted to an adjoining RC member. Extended features include improvements to flexural strength, energy absorption, and inherent material durability. A secondary advantage of having an external cover on a RC member is the reduction in fragmentation and flying debris caused by blast loading [43]. Conversely, FRP retrofitted members are susceptible to debonding under extreme loading. To counter such a response, the FRP material is "anchored" into the member [44]. Another unfavorable response of the significant gain in flexural strength is a consequent change in the failure mode from pure bending to flexural-shear, which calls for additional attention to be directed to the

element's shear capacity [41]. Lastly, for FRP retrofitted slabs and panels, a “rebounding” response occurs upon reaching the maximum displacement, which leads to significant damage. Although costly, the mitigation of such unfavorable responses may be achieved by implementing FRP retrofitting on either side of the element [14]. The following studies report on the behavior of FRP retrofitted slabs exposed to blast loading.

Tanapornraweekit *et al.* [45] conducted a thorough experimental study on the effect of different FRP retrofitting materials and layout schemes. Both CFRP and GFRP sheets were used in the study considering one-sided single layer, two-sided single layer, and two-sided double layer schemes. Compared against a non-retrofitted slab under the same magnitude of loading, a one-sided single layer GFRP retrofitted slab could reduce maximum displacement and prevent concrete spalling. However, it was reported that the retrofitted slab exhibited strong rebounding, which resulted in significant damage and displacement on the slab's loading face. When considering the two-sided single layer scheme with GFRP sheets, a greater improvement to displacement control was observed. The effect of element rebounding was eliminated, and the element's behavior was reportedly characterized by elastic oscillations. Under a second independent blast load, the retrofitted slab remained sufficiently capable of resisting loading without reaching failure. The third loading event involved a two-sided double layer scheme to study the effect of multiple layering, where each side consisted of a GFRP layer and a CFRP layer. Under the same two blast magnitudes as the previous single-layer double sided scheme, the double layer scheme resulted in slightly improved blast-resistant performance. Overall, it was concluded that FRP retrofitting was successful for blast-mitigation in which a double-sided scheme provided most favorable results with the implementation of double layering offering only marginal improvements.

A recent study by Maazon *et al.* [46] investigated the effect of CFRP strips on the blast resistance of RC slabs. The different layout schemes considered one, two, and four strips on a single side and two strips on either side of the slab. It was reported that the application CFRP strips on the slab significantly improved blast performance when compared to a non-retrofitted slab. When comparing the resulting maximum displacements between the single sided retrofitting schemes, it was observed that an increase in strips provided only minor

improvements. Moreover, the rebounding deflection was measured for the two-strip and four-strip layouts and was found to be greater with an increase in strips. Thus, a double sided two-strip scheme was tested and resulted in the successful mitigation of rebound deflection. These results are effectively consistent with previous studies.

To conduct a more flexible investigation of FRP-retrofitted slabs, Kong *et al.* [47] performed a comprehensive numerical study using LS-DYNA. The notable features evaluated in the study were the FRP material type, the number of layers, and the bond strength to the RC slab surface. For the materials of CFRP, GFRP, and AFRP, the performance of FRP retrofitting was observed to correlate directly to the material's tensile strength. This led to CFRP exhibiting the highest blast performance followed by AFRP then GFRP. Moreover, the effect of FRP layers was studied considering up to five layers. It was reported that using two layers provided minor contribution to improving the blast capacity as opposed to one layer, whereas three or more layers resulted in relatively insignificant improvements. Lastly, when considering different bond strengths in the range of commercially available resins, the consequent behaviors presented very similar results implying a marginal effect.

2.4.3 Steel fiber incorporation in RC beams

Traditional concrete is well characterized by very low tensile resistance and brittle failure modes. The use of steel fiber-reinforced concrete (SFRC) is one of the most effective approaches in controlling the member behavior and even more so under blast loading. Steel fibers in concrete introduce improved shear, flexural, and tensile strengths, while leading to ductile response. Another advantage of SFRC is its ability to mitigate cracking by means of fiber bridging. When subjected to blast loading, SFRC members exhibit reliable aptitude in mitigating concrete fragmentation, debris, and spalling. Moreover, the inclusion of steel fibers strongly contributes to a shift of the failure mode from brittle shear to flexural [48]. The limitations of this approach are primarily due to issues relating to the distribution of fibers within the concrete mixture. In some cases, the selection of the fiber size or dosage in the concrete mixture may affect fiber distribution, alignment, and concrete flowability [49]. Lastly, it should be noted that even minimal fiber incorporation has resulted in

noteworthy improvements in concrete behavior, which further supports the cost-effectiveness of this approach [41]. Several studies on the behavior of SFRC beams and their parameters under blast loading are presented herein.

Magnusson and Hansson [50] conducted an experimental investigation on the effect of fiber reinforcement in various RC beams. The two types of RC beams considered were high-strength reinforced concrete (HSRC) beams and high-strength steel fiber-reinforced concrete (HSRFRC) beams having a volumetric fiber content of 2.4%. Under intermediate and lower magnitudes of blast loading, it was reported that the HSRFRC beams exhibited fewer cracks and reduced maximum deflections. When subjected to higher magnitudes of loading, the HSRC beams suffered brittle shear failure, whereas their fiber-reinforced alternatives incurred a flexural failure mechanism. It was thus concluded that the use of steel fibers successfully improved the blast capacity of RC beams.

In a more recent experimental investigation, Lee *et al.* [51] used a blast simulation device to test SFRC beams under repeated blasts considering fiber contents of 0.5% and 1%. Fiber-reinforced beams without stirrups were able to mitigate displacements and cracks as opposed to conventional RC beams. Moreover, SFRC beams could withstand more blasts than RC beams before reaching shear failure, while an increased capacity was observed at higher fiber content. Similarly, for beams having stirrups, the incorporation of steel fibers contributed to improved blast performance and greater capacity to resist repeated blasts, while reaching flexural failure.

Using a similar blast simulation device, a more thorough investigation of SFRC beams was conducted by Castonguay [16] and considered various fiber types with fiber volumes of 0.5%, 0.75%, 1% and 1.5%. Consistent with the previous study, the use of steel fibers successfully contributed to increasing the beam's blast capacity. It was also reported that the use of steel fibers may be used to completely replace stirrups in RC beams owing to the observed enhancement in shear resistance. Lastly, the SFRC beams exhibited an excellent ability in reducing blast fragments.

2.5 Machine learning in structural engineering

2.5.1 General

When considering the available obstacles, uncertainties, and difficulties across the field of civil engineering, a means of overcoming such widespread hurdles based on simplified and data-driven methods is highly prevalent. This has motivated a multitude of studies to investigate the extent to which engineers can integrate machine learning (ML) methods throughout various disciplines of the field [52]. The flexibility of such methods may be adopted in applications of design, analysis, decision making, health monitoring, material testing, and construction management. Moreover, the underlying development of ML does not rely on the theories, proofs, and principles that heavily make up such applications, but instead attempts to “learn” or identify the correlations among the parameters that characterize each application. Although this can lead to “black-box” types of models, such methods have the potential to convert a highly complex application to a simplified input-output relationship. However, it should be noted that with the increased usage of ML methods in civil engineering applications, notable efforts have been made to adapt practical empirical formulations from ML models to eliminate unknown prediction mechanisms [53,54]. The use of ML methods in structural engineering has therefore gained popularity. The following section describes some examples of implementations for ML in structural engineering conducted in 2020.

2.5.2 Recent studies

Tran *et al.* [53] developed a comprehensive dataset on the axial compression capacity of circular concrete-filled steel tube columns using ABAQUS and consisting of 768 data points. Considering multiple instances, the numerical model was validated against existing experimental studies before generating a large number dataset of the application. An artificial neural network (ANN) algorithm was used to develop the ML model, which produced remarkable performance through measures of root mean squared error (*RMSE*), mean absolute percent error (*MAPE*) and coefficient of determination (R^2), yielding values

of 150.36 kN, 0.46%, and 99.9%, respectively. The predictions of the developed model were compared to four different design code formulas and were found to outperform them.

Zhou *et al.* [54] considered the application of interfacial bond strength between FRP and concrete. A well-rounded dataset was compiled from the existing literature consisting of 969 data points and considering the parameters of the concrete compressive strength, concrete width, FRP elastic modulus, FRP thickness, FRP width and FRP bond length. Furthermore, an ANN algorithm was adopted in developing the ML prediction model and resulted in an R^2 of 92.8%. They also compiled twenty existing empirical prediction formulas of the application that have been developed since 2000. When compared to the existing models, the ANN model produced superior performance, while being developed considering a greater range of parameters.

Charalampakisa *et al.* [55] studied the application of predicting the fundamental period of vibration for masonry infilled RC frame structures. Considering the parameters of structure height, bay length, wall opening ratio, and masonry wall stiffness, a set of 4026 data points were obtained from the literature. Both M5rules decision trees and ANN algorithms were considered in the development of the ML model in which both achieved R^2 values of 99.9%.

Marani *et al.* [56] investigated the application of concrete compressive strength for ultra-high-performance concrete. A total of 810 data points was accumulated from the existing literature considering fifteen application parameters. Furthermore, a Tabular Generative Adversarial Networks (TGAN) algorithm was implemented as a means of generating synthetic data for improved ML model development. Towards developing the ML model, the algorithms of Random Forests (RF), Extra Trees (ET), and Gradient boosted Regression Trees (GBRT) were considered in the study. The optimal resulting performance measures were observed in the GBRT model yielding a mean absolute error (MAE), $RMSE$, and R^2 of 6.72, 8.41, and 95%, respectively.

2.6 Chapter references

- [1] Dusenberry, D. O. (Ed.). (2010). *Handbook for blast resistant design of buildings*. John Wiley & Sons.
- [2] Hetherington, J., & Smith, P. (2014). *Blast and ballistic loading of structures*. CRC Press.
- [3] US Department of Defense. (2008). Structures to resist the effects of accidental explosions. *UFC 3-340-02*.
- [4] Esparza, E. D. (1986). Blast measurements and equivalency for spherical charges at small scaled distances. *International Journal of Impact Engineering*, 4(1), 23-40.
- [5] Shirbhate, P. A., & Goel, M. D. (2020). A Critical Review of Blast Wave Parameters and Approaches for Blast Load Mitigation. *Archives of Computational Methods in Engineering*, 1-18.
- [6] Dewey, J. M. (2010). The shape of the blast wave: studies of the Friedlander equation. In *21st international symposium on military aspects of blast and shock, Israel*.
- [7] Kinney GF, Graham KJ (1985) Explosive shocks in air. Springer, Berlin.
- [8] Brode, H. L. (1955). Numerical solutions of spherical blast waves. *Journal of Applied physics*, 26(6), 766-775.
- [9] Henrych, J., & Major, R. (1979). *The dynamics of explosion and its use* (Vol. 569). Amsterdam: Elsevier.
- [10] Sadovskiy, M. A. (2004). Mechanical effects of air shockwaves from explosions according to experiments. *Sadovskiy MA Selected works: Geophysics and physics of explosion*. Nauka Press, Moscow.
- [11] Goel, M. D., Matsagar, V. A., Gupta, A. K., & Marburg, S. (2012). Review of Blast Wave Parameters. *Defence Science Journal*, 62(5), 300-306.
- [12] Biggs, J.M. (1964) "Introduction to Structural Dynamics" McGraw-Hill Inc., New York.
- [13] Hughes, T. J. (2012). *The finite element method: linear static and dynamic finite element analysis*. Courier Corporation.
- [14] Jacques, E. (2011). *Blast retrofit of reinforced concrete walls and slabs* (Master's Thesis, Université d'Ottawa/University of Ottawa).

- [15] Lloyd, A. E. W. (2015). *Blast retrofit of reinforced concrete columns* (Master's Thesis, Université d'Ottawa/University of Ottawa).
- [16] Castonguay, S. (2017). *Performance of Steel Fiber-Reinforced Concrete Beams Under Shock Tube Induced Blast Loading* (Master's Thesis, Université d'Ottawa/University of Ottawa).
- [17] LS-DYNA, Keyword User's Manual V971, CA: Livermore Software Technology Corporation (LSTC), Livermore, California, ed, 2015.
- [18] ABAQUS (2016) ABAQUS analysis user's manual. Version 2016. Dassault Systemes Simulia Corp.
- [19] Canonsburg, P. A. (2013). ANSYS Workbench User's Guide. *ANSYS Inc.*
- [20] Trajkovski, J., Kunc, R., Perenda, J., & Prebil, I. (2014). Minimum mesh design criteria for blast wave development and structural response-MMAL method. *Latin American Journal of Solids and Structures*, 11(11), 1999-2017.
- [21] Tabatabaei, Z. S., & Volz, J. S. (2012, June). A comparison between three different blast methods in LS-DYNA: LBE, MM-ALE, Coupling of LBE and MM-ALE. In *12th International LS-DYNA Users Conference* (pp. 1-10).
- [22] Souli, M., Bouamoul, A., & Nguyen-Dang, T. V. (2012). ALE formulation with explosive mass scaling for blast loading: experimental and numerical investigation. *Computer Modeling in Engineering and Sciences*, 86(5), 469-486.
- [23] Børvik, T., Hanssen, A. G., Langseth, M., & Olovsson, L. (2009). Response of structures to planar blast loads—A finite element engineering approach. *Computers & Structures*, 87(9-10), 507-520.
- [24] Dua, A., & Braimah, A. (2016). State-of-the-art in near-field and contact explosion effects on reinforced concrete columns.
- [25] Hao, H. (2015). Predictions of structural response to dynamic loads of different loading rates. *International Journal of Protective Structures*, 6, 585-605.
- [26] Zhang, C., & Mousavi, A. A. (2020). Blast loads induced responses of RC structural members: State-of-the-art review. *Composites Part B: Engineering*, 108066.
- [27] Low, H. Y., & Hao, H. (2001). Reliability analysis of reinforced concrete slabs under explosive loading. *Structural safety*, 23(2), 157-178.
- [28] Tai, Y. S., Chu, T. L., Hu, H. T., & Wu, J. Y. (2011). Dynamic response of a reinforced concrete slab subjected to air blast load. *Theoretical and applied fracture mechanics*, 56(3), 140-147.

- [29] Lin, X., Zhang, Y. X., & Hazell, P. J. (2014). Modelling the response of reinforced concrete panels under blast loading. *Materials & Design (1980-2015)*, 56, 620-628.
- [30] Thiagarajan, G., Kadambi, A. V., Robert, S., & Johnson, C. F. (2015). Experimental and finite element analysis of doubly reinforced concrete slabs subjected to blast loads. *International Journal of Impact Engineering*, 75, 162-173.
- [31] Yao, S., Zhang, D., Chen, X., Lu, F., & Wang, W. (2016). Experimental and numerical study on the dynamic response of RC slabs under blast loading. *Engineering Failure Analysis*, 66, 120-129.
- [32] Astarlioglu, S., Krauthammer, T., Morency, D., & Tran, T. P. (2013). Behavior of reinforced concrete columns under combined effects of axial and blast-induced transverse loads. *Engineering Structures*, 55, 26-34.
- [33] Braimah, A., & Siba, F. (2018). Near-field explosion effects on reinforced concrete columns: an experimental investigation. *Canadian Journal of Civil Engineering*, 45(4), 289-303.
- [34] Kyei, C., & Braimah, A. (2017). Effects of transverse reinforcement spacing on the response of reinforced concrete columns subjected to blast loading. *Engineering Structures*, 142, 148-164.
- [35] Bao, X., & Li, B. (2010). Residual strength of blast damaged reinforced concrete columns. *International journal of impact engineering*, 37(3), 295-308.
- [36] Li, Y., Algassem, O., & Aoude, H. (2018). Response of high-strength reinforced concrete beams under shock-tube induced blast loading. *Construction and Building Materials*, 189, 420-437.
- [37] Yao, S. J., Zhang, D., Lu, F. Y., Wang, W., & Chen, X. G. (2016). Damage features and dynamic response of RC beams under blast. *Engineering Failure Analysis*, 62, 103-111.
- [38] Liu, Y., Yan, J. B., & Huang, F. L. (2018). Behavior of reinforced concrete beams and columns subjected to blast loading. *Defence Technology*, 14(5), 550-559.
- [39] Rao, B., Chen, L., Fang, Q., Hong, J., Liu, Z. X., & Xiang, H. B. (2018). Dynamic responses of reinforced concrete beams under double-end-initiated close-in explosion. *Defence Technology*, 14(5), 527-539.
- [40] Chipley, M. (2003). *Reference Manual to Mitigate Potential Terrorist Attacks Against Buildings: Providing Protection to People and Building*. Federal Emergency Management Agency.

- [41] Draganić, H., Gazić, G., & Varevac, D. (2019). Experimental investigation of design and retrofit methods for blast load mitigation—A state-of-the-art review. *Engineering Structures*, *190*, 189-209.
- [42] CSA S850-12. (2012). S850-12 Design and assessment of buildings subjected to blast loads. *Mississauga, ON, Canada: Canadian Standards Association*.
- [43] Pichandi, S., Rana, S., Oliveira, D., & Figueiro, R. (2013). Fibrous and composite materials for blast protection of structural elements—A state-of-the-art review. *Journal of Reinforced plastics and composites*, *32*(19), 1477-1500.
- [44] Orton, S. L., Chiarito, V. P., Minor, J. K., & Coleman, T. G. (2014). Experimental testing of CFRP-strengthened reinforced concrete slab elements loaded by close-in blast. *Journal of Structural Engineering*, *140*(2), 04013060.
- [45] Tanapornraweekit, G., Haritos, N., & Mendis, P. (2011). Behavior of FRP-RC slabs under multiple independent air blasts. *Journal of Performance of Constructed Facilities*, *25*(5), 433-440.
- [46] Maazoun, A., Belkassem, B., Reymen, B., Matthys, S., Vantomme, J., & Lecomte, D. (2018). Blast response of RC slabs with externally bonded reinforcement: Experimental and analytical verification. *Composite Structures*, *200*, 246-257.
- [47] Kong, X., Qi, X., Gu, Y., Lawan, I. A., & Qu, Y. (2018). Numerical evaluation of blast resistance of RC slab strengthened with AFRP. *Construction and Building Materials*, *178*, 244-253.
- [48] Soufeiani, L., Raman, S. N., Jumaat, M. Z. B., Alengaram, U. J., Ghadyani, G., & Mendis, P. (2016). Influences of the volume fraction and shape of steel fibers on fiber-reinforced concrete subjected to dynamic loading—A review. *Engineering Structures*, *124*, 405-417.
- [49] Yoo, D. Y., & Banthia, N. (2017). Mechanical and structural behaviors of ultra-high-performance fiber-reinforced concrete subjected to impact and blast. *Construction and building materials*, *149*, 416-431.
- [50] Magnusson J and Hansson H .(2000). High Performance Concrete Beams Subjected to Shock Waves from Air Blast. Swedish Defense Research Agency (FOI), Tumba, FOA-R--OO-01586-311-SE.
- [51] Lee, J. Y., Shin, H. O., Yoo, D. Y., & Yoon, Y. S. (2018). Structural response of steel-fiber-reinforced concrete beams under various loading rates. *Engineering Structures*, *156*, 271-283.
- [52] Salehi, H., & Burgueño, R. (2018). Emerging artificial intelligence methods in structural engineering. *Engineering structures*, *171*, 170-189.

- [53] Tran, V. L., Thai, D. K., & Nguyen, D. D. (2020). Practical artificial neural network tool for predicting the axial compression capacity of circular concrete-filled steel tube columns with ultra-high-strength concrete. *Thin-Walled Structures*, 151, 106720.
- [54] Zhou, Y., Zheng, S., Huang, Z., Sui, L., & Chen, Y. (2020). Explicit neural network model for predicting FRP-concrete interfacial bond strength based on a large database. *Composite Structures*, 240, 111998.
- [55] Marani, A., Jamali, A., & Nehdi, M. L. (2020). Predicting Ultra-High-Performance Concrete Compressive Strength Using Tabular Generative Adversarial Networks. *Materials*, 13(21), 4757.

Chapter 3

3 Machine learning model for predicting structural Response of RC slabs exposed to blast loading

3.1 Introduction and background

When an explosive event occurs, whether due to accidents or caused by intentional detonation, it can generate an enormous amount of pressure that can cause irreparable damage to the surrounding structures while threatening the lives of their occupants. Therefore, structural mitigation strategies are required to reduce the implications of such events. Recent research has been conducted to investigate different approaches for modeling the overall damage in structural components exposed to blast loading. Thiagarajan *et al.* [1] studied the response of high-strength and normal-strength concrete slabs reinforced with steel and vanadium bars exposed to blast loading. To numerically model the slabs and loading scheme, they used the non-linear finite element software LS-DYNA considering both the Winfrith Concrete Model (WCM) and the Concrete Damage Model Release 3 (CDMR3). They also used a Blast Load Simulator to apply dynamic loading to the studied slabs to obtain experimental results emulating actual blast events. The differences of peak deflections between numerical model predictions and experimental results were 5.9%-37.5% using the WCM and 0%-35.6% using the CDMR3 with 25.4 mm mesh size, and 10.4%-58.8% using the WCM and 2.3%-68.6% using the CDMR3 with 12.5 mm mesh size. The results of the numerical model were thus considered reasonably good for predicting maximum deflections.

Similarly, Mao *et al.* [2] studied the performance of ultra-high-performance fiber-reinforced concrete (UHPFRC) slabs subjected to close-in blasts. A numerical model was developed to simulate the event using LS-DYNA considering the Karagozian & Case (K&C) concrete model, while field blast tests were also conducted. UHPFRC slabs were found to have greater resistance to blast loading, and the numerical model showed

reasonable peak deflection prediction accuracy showing differences of peak deflections between the numerical model and experimental results of 0%-66% considering slabs with 2%, 4%, and 6% fiber volume.

In addition to developing an experimentally-validated numerical model to study the behavior of reinforced concrete slabs under blast loading, Zhao *et al.* [3] also developed an empirical equation to calculate the peak displacement of a conventional reinforced concrete (RC) slab with fixed parameters as a function of the slab thickness, h , and the blast scaled distance, Z . The empirical formula was found to have a prediction error of 1.9% but was limited within the range of $40 \text{ mm} < h < 60 \text{ mm}$ and $0.218 \text{ m/kg}^{1/3} < Z < 0.517 \text{ m/kg}^{1/3}$. Based on such previous studies, there is evidence that using finite element modeling for modeling structural elements subjected to blast loading is associated with several limitations including mesh size sensitivity, constitutive models and other simplifying assumptions [1, 2].

Furthermore, analytical approaches for predicting the behavior of structures exposed to blast loading have been explored [4, 20, 21]. For instance, Maazoun *et al.* [4] studied the efficiency of using externally bonded reinforcements of carbon fiber reinforced polymer (CFRP) on RC slabs exposed to blast loading. Their results showed that using CFRP significantly improved the flexural capacity and stiffness of the RC slabs. A simplified single degree of freedom (SDOF) approach was adopted to predict the maximum displacements of the slabs. The results of the analytical approach were tested against experimental results and showed excellent accuracy in predicting maximum displacements, with only 2%-14% differences.

Additionally, Oesterle [21] used a Frangible Panel Wall Analysis (FWPA) code, which applies a multiple degree of freedom (MDOF) model, to predict the impulse and peak mid-span displacement of wall panels exposed to blast loading. The FPWA was compared to experimental data and was found to predict both impulse and displacement with very good accuracy having displacement differences between experimental and analytical models of 0.6%-22.7%

Existing prediction approaches such as numerical methods require a competent background

in computer modeling as well as extensive modeling effort and computational cost. Similarly, analytical models are dependent on assumptions based on the complex understanding of the application. Hence, in the present chapter, a machine learning model is developed to predict the maximum displacement of RC slabs subjected to blast loading requiring much less computational time, effort, and complexity of implementation. The dataset used for the model, the learning algorithm adopted, and the selection of features are described below. The results of the model predictions are discussed through measures of the coefficient of determination, R^2 , goodness-of-prediction, VE_{cv} , mean absolute error (MAE), and compared to results of alternative models found in the literature. Moreover, the effect of each input feature on the output is measured through permutation feature analysis along with comparisons of feature importance with existing parametric studies. Furthermore, a detailed analysis of the model's discrepancies is discussed and an approach for an improved model is proposed.

3.2 Machine learning in civil engineering

Machine learning (ML) is the use of programmed algorithms to optimize a performance standard based on previously accumulated data. Essentially, the act of learning involves training an algorithm using existing data (pairs of inputs and outputs), and having the trained algorithm provide an efficient inference. A machine learning model can also be used to recognize and extract important relationships between inputs and outputs. By allowing a model to learn about an application through relevant data, it can arrive at an inference without being explicitly programmed [5]. The use of machine learning has gained popularity across several disciplines. In a survey conducted by Kish [6], state-of-the-art research in machine learning has been listed in the fields of engineering, mathematics, medicine, neuroscience, and public health among others. The survey shows that the amount of research being conducted in machine learning has been increasing rapidly since 2015.

In the field of civil and infrastructure engineering, using machine learning has proven to be effective in several recent applications. For instance, Cao *et al.* [7] compared the performance of three types of ensemble machine learning models to predict the unit price

bids of highway resurfacing using a dataset collected from over 1400 projects considering 57 features. The proposed model was found to provide accurate cost forecast. Spencer Jr. *et al.* [8] presented an overview of recent developments in the use of computer vision in monitoring and inspecting civil infrastructure through non-contact methods. The inspection applications consisted of characterizing local and global visible damage, detecting changes from a reference image, and recognizing structural components, whereas the monitoring aspects consisted of both static applications such as the static measurement of displacement and strain, and dynamic applications such as displacement measurements for modal analysis. Moreover, a study comparing different machine learning models for predicting concrete compressive strength was reported by Chopra *et al.* [9]. They investigated the predictive accuracy of using decision tree, random forests, and neural networks. It was found that neural networks had the highest accuracy followed by random forests in predicting concrete compressive strength. Such applications have shown reliable advancements in the field of civil engineering through machine learning.

3.3 Data collection and description

The database used in this chapter was compiled from numerous research articles across several journals in addition to research theses, which specifically studied the behavior and mitigation techniques of RC slabs exposed to blast loading. Data was retrieved from both results of experimental programs and numerical models validated by experiments. Only consistent data among all the studied articles and theses was included. Whenever required information was missing, it was obtained from the appropriate authors through personal correspondence. When this was not feasible, incomplete data was discounted from the database.

Experimental investigations exploring blast loading applications require sensitive instrumentation to measure the responses of structural components [10, 17]. It also requires extreme precaution to be undertaken upon setting up detonations near structures, as well as in detonating the charge. Unlike computer simulations, experimental studies are associated with high costs, and thus tend to be limited in scope and in repetitions of experiments. A

typical experimental setup for slabs exposed to blast loading consists of the slab specimen, a steel support frame, an explosive charge, and instrumentation for data acquisition. The slab specimen is clamped on to the support frame and may act in the form of a simple, pinned, or fixed support in two opposite sides of the slab to simulate one-way bending or all four sides to simulate two-way bending. The slab specimen is then equipped with the relevant instrumentation such as Linear Variable Displacement Transducers (LVDT), pressure transducers, strain gauges (previously installed in specimen), and accelerometers to capture separate responses. Afterwards, an explosive charge is positioned with the desired standoff distance above the specimen and detonated to induce a spherical shockwave acting on the slab, during which relevant data to the blast's parameters and specimen's response are recorded [15, 16, 18, 23]. A total of 22 data points [10-15, 23] were taken from articles and theses that have collected experimental data on RC slabs exposed to blast loading.

Devices such as the Blast Load Simulator [19] or the Blast Simulator [21] generate and apply pressure on a specimen like that of a detonated charge. This method reduces risk, cost, and mitigates potential damage to instrumentation, while it can be conducted in laboratory facilities to obtain near-identical results. However, these devices do not explicitly provide the equivalent blast weight, blast distance, or scaled distance being simulated. Oesterle [21] presented a method to use blast parameters obtained from blast simulations for extracting the equivalent scaled distance of blasts through charts provided by the TM5-1300 [14]. This method was adopted to extract the equivalent scaled distances of the simulated blasts from articles and theses that used such devices. Overall, 26 data points [1, 19-21] were collected from articles and theses that utilized these devices on RC slabs.

The use of finite element modeling (FEM) software to simulate blast load applications has been shown to provide relatively good predictions of structural behavior. Using FEM eliminates cautionary and monetary aspects related to blast loading, and it allows for a great deal of flexibility in modeling, while offering a wide range of detailed analyses. A total of 102 points [22-29] were collected from articles that used FEM, validated by experiments, for applications of RC slabs exposed to blast loading. The sources from which

data was collected contained information on several nonconventional RC slabs, such as those with external retrofits, fiber-reinforced concretes, or novel rebar orientation, but also included conventional RC slabs as control or reference specimens. The database used in the present chapter was created considering only conventional RC slabs. It should also be noted that both one-way and two-way slabs were considered in the dataset in which 84 were one-way slabs and 66 were two-way slabs. The dataset also considered the slab's boundary conditions in which 70 slabs were simply supported, 75 slabs were fixed, and 5 slabs were simply supported on one end and fixed on the other end.

Table 3-1. Mean, standard deviation, and range of model features

Notation	Feature/Output	Mean/Count	Standard Deviation	Range/Categories
X1	Length (m)	1.85	0.91	0.75 – 3.6
X2	Width (m)	1.4	0.818	0.44 - 3
X3	Thickness (m)	0.109	0.046	0.03 - 0.305
X4	Concrete compressive strength (MPa)	51.13	35.89	16 - 140
X5	Steel yield strength (MPa)	450.9	105.2	235 - 630
X6	Steel reinforcement ratio	0.0117	0.0086	0 - 0.0612
X7	Scaled distance (m/kg ^{1/3})	2.15	3.58	0.345 - 25.4
X8	Reflected Impulse (MPa-msec)	2.82	2.86	0.0247 - 7.71
X9	One-way / Two-way	84 / 66	-	2
X10	Simple / Fixed / Simple-Fixed	70 / 75 / 5	-	3
Y	Maximum displacement (mm)	33.38	32.16	0.6 - 140

The parameters that effect the behavior of RC slabs under blast loading include the slab type and dimensions, the quantities and properties of materials used, and the parameters of the blast. These aspects were common among nearly all the studies associated with the dataset. Eight of the features were based on continuous (quantitative) data and two of the features were based on categorical data. Therefore, the features considered in this chapter

are the length, width, and thickness of the slab, concrete compressive strength, reinforcing steel yield strength, steel reinforcement ratio, the blast's scaled distance, the blast's reflected impulse, type of slab, and slab support. Every data point collected consisted of all ten features without any missing information, with every data point being unique to the dataset. Additional features could have been considered, however the availability of information that was consistent across the entire dataset was relatively limited and presented through these ten features. **Table 3-1** lists the mean or count, standard deviation, and range/categories of each input feature. **Figures 3-1** and **3-2** display the distributions of the continuous features and output, as well as the scatter plot of the relationship of each normalized feature with the normalized output, respectively. The statistics provided for the categorical features are simply the frequency of each category and the number of categories provided in **Table 3-1**.

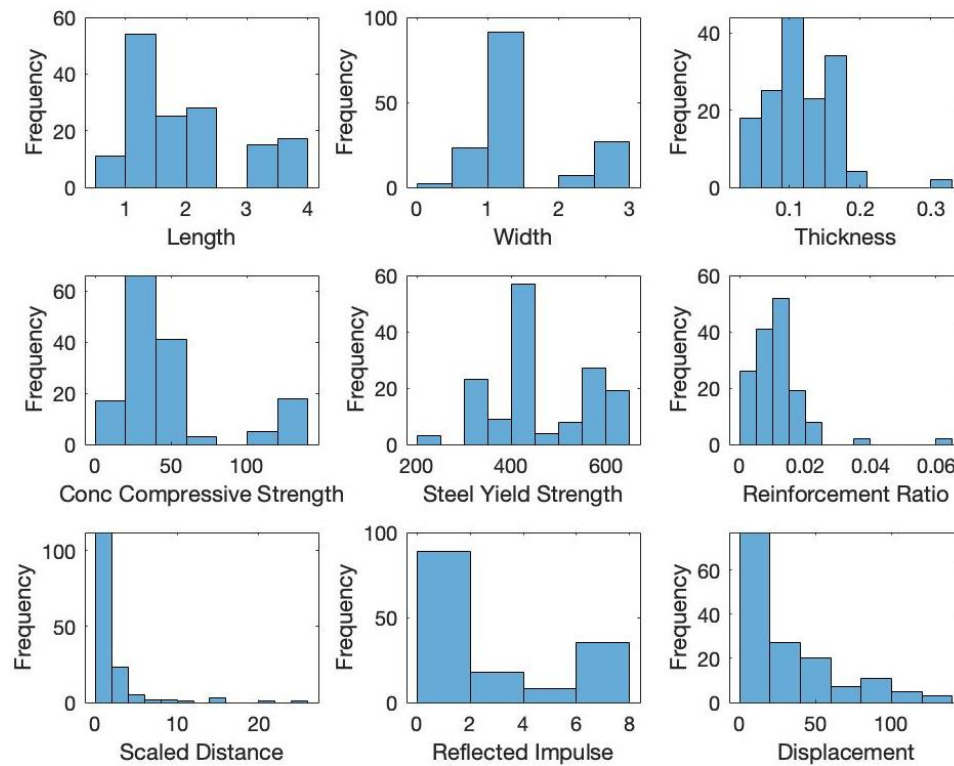


Figure 3-1. Distribution plots of features and output.

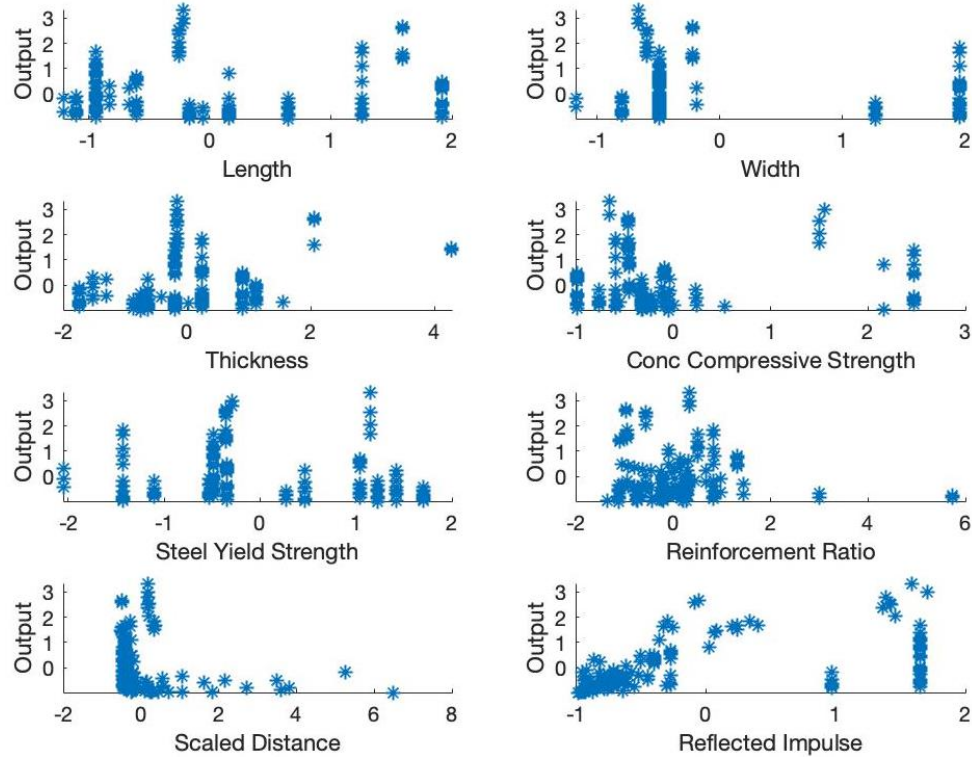


Figure 3-2. Scatter plots of normalized features.

3.4 Model development

3.4.1 Preliminary assessment of regression models

To identify which regression learning algorithm was best suited for the dataset, a preliminary analysis was conducted in which several learning algorithms were tested using the MATLAB Regression Learner (MRL) as well as the Random Forests algorithm coded using MATLAB [30]. The assessed models in the MRL consisted of linear regression models, regression trees, support vector machines (SVM), and ensembles of trees. A k-fold cross-validation of 10 folds was applied to all models. Also, each model retained its default settings and parameters, while comparisons were done based on the resulting mean absolute errors and R^2 . The preliminary analysis of the models was only based on the eight continuous features due to the limitation of the MRL to include categorical data. **Table 3-2** lists the models tested along with their performance measures. The MRL is a convenient method of thoroughly investigating several learning algorithms for a dataset, however, in

this study it was only used to gain a general overview of the performance of several models after which a more detailed approach was executed. Based on the results, the random forests model achieved the highest performance in both MAE and R^2 followed by the ensemble model of boosted trees with the remaining models showing less suitable performances with respect to the given dataset. In addition to the random forests model having the highest performance, it is also favorable due to being nonparametric and its ability to prevent overfitting.

Table 3-2. MATLAB Regression Learner and Random Forest results.

Regression Models	Mean Absolute Error	R^2
Linear Regression	21.41	0.26
Regression Tree, fine	8.88	0.83
Linear SVM	21.4	0.2
Quadratic SVM	13.85	0.42
Cubic SVM	12.1	-0.06
Ensemble, bagged trees	12.4	0.73
Ensemble, boosted trees	8.14	0.86
Random Forest, regression	6.68	0.92

3.4.2 Random Forests algorithm

The use of the Random Forests (RF) algorithm for this application was motivated by the capabilities attributed to the algorithm. RF acts to reduce the variance of prediction while keeping low bias, which acts to provide an appropriate fit for the data. Furthermore, prediction performance is assessed through a type of cross-validation while the training step is occurring (which further acts to prevent overfitting) [32]. Among others, these qualities make the use of RF attractive for this application. It has also been shown in **Table 3-2** that other types of learning algorithms were less appropriate for the current application. The RF algorithm is essentially an ensemble of decision trees in which each tree is grown using a bootstrap (random) sample, with replacement, from the training set. At each node

of the tree, a randomly chosen subset of features is used to create the best partitioning. The training process continues until each point in the sample is assigned to a terminal node from previously partitioned nodes and is repeated until the desired number of trees have been grown. By creating trees from bootstrap samples, the created trees will generally be less correlated with each tree producing a prediction. In regression, the final prediction is the average of individual predictions. For classification, the final predicted class is the most common class among the individual predictions [31]. A depiction of the Random Forests algorithm for both regression and classification problems is given in **Figure 3-3**.

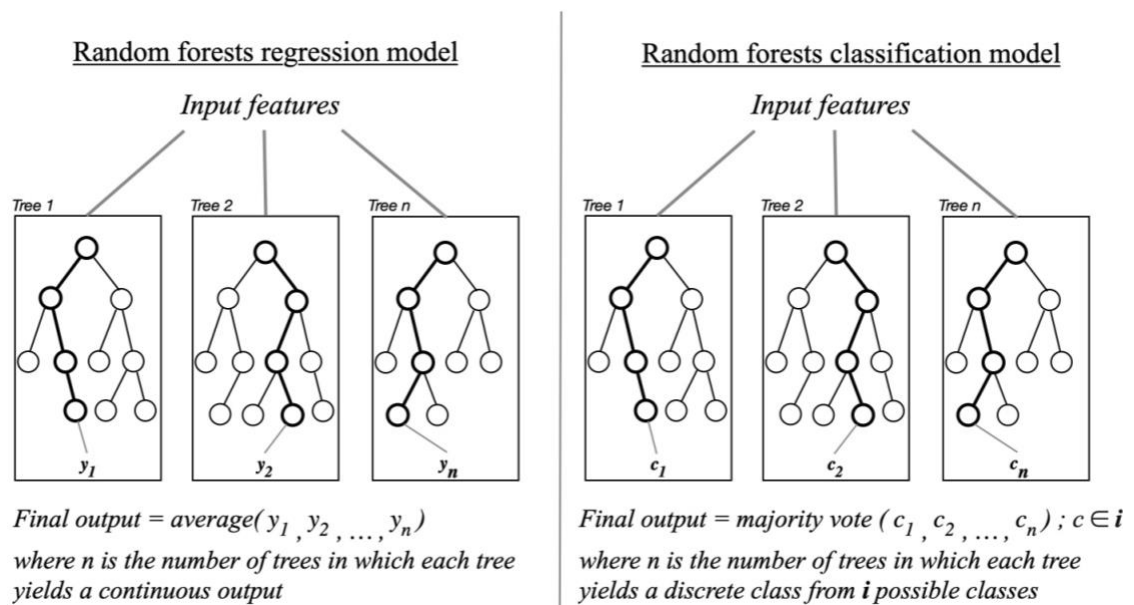


Figure 3-3. Diagram of regression and classification Random Forests.

The probability that a data point in the original data set is not chosen by a single tree's bootstrap sample is given by $(1-1/N)^N$, where N is the total number of data points in the training set. This expression approaches a limit of $1/e$, approximately 0.37, as N approaches infinity. Therefore, 37% of the data is not included in a single tree's bootstrap sample and is referred to as the out-of-bag data. It can also be understood that a single data point is not included in the bootstrap sample of 37% of the total number of trees. This out-of-bag data can be used by each tree to act as an internal validation set, resulting in a fair assessment of the RF prediction performance [33].

3.4.3 Hybrid classification-regression Random Forests algorithm

The use of Random Forests classification algorithms to make predictions on continuous datasets have been previously shown to yield accurate results [34,35]. The approach considers a continuous output variable to be discretized and treats the output as though it were a multi-class classification problem. Additionally, recent studies have explored the simultaneous use of both classification and regression algorithms to establish an effective machine learning model. Wang *et al.* [36] developed a hybrid classification-regression neural network for the application of model pose estimation. The model was found to mitigate errors caused by data imbalance while also yielding improved accuracy compared to previous models of the same application. Furthermore, Chen *et al.* [37] implemented joint classification and regression learning using neural networks for age predictions on social media. The model was shown to have better results when compared individual regression or classification models. In the current chapter, the use of a hybrid classification-regression approach using the Random Forests algorithm is considered. Through this approach, a regression model and classification model are trained independently while testing, validation, and performance measures are based on a robust linear fit of their predicted outputs.

3.4.4 Model overview

The RF model development, including training and testing, cross-validation, performance measures, feature importance analysis, and graphic representations, was carried out using MATLAB 2019a. The sections below provide further detail on each aspect of the model development.

3.4.4.1 Cross-validation

To develop a reliable model, training an algorithm on a dataset alone does not suffice. The model must also be validated by external data that was not included as part of the model development [38]. Therefore, cross-validation (CV) was implemented such that the dataset was divided into a training subset through which the model was trained, and a testing subset used to evaluate the model's performance. The division of training and testing subsets was based on k -fold CV where the data is divided into k equal subsets, such that for every subset

being tested, the remaining $k-1$ subsets were used to train the model. The training and testing cycle of k -fold CV was repeated until every subset was tested once, with performance measures computed through the testing subsets. This approach prompts a more robust conclusion [33]. A common value of folds for k -fold CV is 5 or 10 [39], therefore 10-fold CV was adopted herein. Additionally, before every run of dividing the data into training and testing subsets through CV, the dataset was randomly permuted such that no two runs have the same data points in the training and testing subsets, with every run computing a value of performance measures. The final performance measures were taken from the average of 100 repetitions for the purpose of stabilizing results and statistical assurance.

3.4.4.2 Selected performance measures

The performance of a prediction model is based on the difference between the actual values and the predicted values [40]. There are several different approaches to measuring a model's performance based on the nature of the data [40, 41]. The measures chosen for the current study are the mean absolute error (MAE), variance explained by cross validation (VE_{cv}), and coefficient of determination (R^2). The use of MAE is a common error metric in analyzing model performance [41-43]. The value of the MAE does not penalize the presence of outliers as heavily as the mean squared error or root mean squared error do, making it robust to outliers and equally sensitive to different frequency distribution of errors. MAE is given by:

$$MAE = \frac{1}{n} \sum_1^n |y_i - \hat{y}_i| \quad (1)$$

where \hat{y} is the predicted output, y is the actual output for every i th entry in the set, and where n is the number of items in the set [42]. By using the predicted values obtained through cross-validation, the measure of a model's prediction accuracy can also be represented using VE_{cv} , which is given by

$$VE_{cv} = \left(1 - \frac{\sum_1^n (y_{CVi} - \hat{y}_i)^2}{\sum_1^n (y_{CVi} - \bar{y})^2} \right) * 100\% \quad (2)$$

where \hat{y} is the predicted output, y_{cv} is the actual output for every i th entry in the validation (or testing) subset, \bar{y} is the mean of the actual values, and n is the number of items in the validation subset. It should also be noted that the value of VE_{cv} can be negative and has a maximum value of 100%, implying ideal accuracy [43-45].

A correlation between the actual outputs and the predicted outputs can be measured through the coefficient of determination, R^2 , also referred to as the goodness-of-fit or coefficient, given by

$$R^2 = \left(1 - \frac{\sum_1^n (y_i - \hat{y}_i)^2}{\sum_1^n (y_i - \bar{y})^2}\right) * 100\% \quad (3)$$

where \hat{y} is the predicted output, y is the actual output for every i th entry in the dataset, \bar{y} is the mean of the actual values, and n is the number of items in the dataset. The value of R^2 is always positive and ranges between 0 and 1 [43, 45]. Although R^2 has often been misinterpreted as a measure of accuracy, it is in fact a measure of correlation and is related to the fit of the data [43]. As mentioned in the previous section, the three performance measures discussed were computed for every repetition and averaged for the final values.

3.4.4.3 Permutation feature importance

In several applications, it is desirable to understand the effect that an input variable (or feature) has on an output variable. By implementing variable importance measures, investigated variables can be compared based on the degree to which they influence the output [46]. In random forests, a common variable importance measure used is permutation feature importance (*PFI*), which is both effective and easy to implement. *PFI* is based on the understanding that if there exists an association between an input variable X_i and an output Y , then by randomly permuting X_i and using it to predict Y , while keeping all other input variables non-permuted, the prediction accuracy will decrease significantly. The value of *PFI* for a single variable is given by the difference in error measures between the original accuracy and the accuracy resulting from having that variable randomly permuted [46-48]. All input features used in this chapter have been considered for *PFI* with the error measure being *MAE*. The closer the *PFI* value is to zero, the less impact it has on the output, while greater values of *PFI* signify a higher impact on the output [47]. Furthermore, the

approach of *PFI* may conveniently be implemented on several ML algorithm due to the simplicity of capturing the change in errors produced from permuting a feature. This assumes, however, that a given dataset is sufficiently capable of describing the variations of an applications features. Thus, in order to validate the *PFI* outcomes of the current model, experimental correlations were thoroughly investigated.

3.5 Results and discussion

This section applies the methodology outlined in the previous section and thoroughly presents and discusses the results of the ML model in five subsections: the first and second present the performance measures of the model and compare the predicted outputs to other predicted outputs of different models for the same application found in the literature; the third and fourth present the importance of each feature through their *PFI* values and relate the importance of each feature obtained from the ML model to parametric studies of the same features found in the literature. The final subsection discusses the model's discrepancies through several sources of variability and proposes an improved model.

3.5.1 Performance measures of the ML model

As shown in **Table 3-1**, the data of each feature can be considered widely spread given that the value of the standard deviation is relatively close to the mean value, as opposed to having a small standard deviation implying the data is clustered around the mean. This can also be observed in **Figure 3-1**, which also shows that none of the features follows a normal distribution. Additionally, the scatter plots in **Figure 3-2** show that there is no clearly defined relationship between each feature and the output. The work done by Tsanas and Xifara [34] indicated similar results for their data and suggested that traditional learning algorithms such as linear regression may be unable to accurately relate the input features to the output. Such plots therefore encourage the use of more sophisticated regression learning algorithms, such as RF. This suggestion agrees with the results obtained by the MRL shown in **Table 3-2**, which also indicates the inability of several learning algorithms to accurately predict the output.

The performance measures of the RF regression model resulted in a *MAE* value of 6.68 \pm 0.24 biased upward, a *VEcv* value of 85.5% \pm 7.4%, and an R^2 value of 92% \pm 0.9%, averaged from 100 repetitions with an input of 100 trees. Generally, *MAE* values are scale/unit dependent; therefore, only models prepared by the same dataset can be compared through *MAE*. Since this dataset was compiled by the authors and no other models have yet been developed, then comparisons to *MAE* can only currently be done with the values acquired by the MRL. With the results of the MRL in **Table 3-2**, RF outperformed the tested regression models in both *MAE* and R^2 . A summary of learner comparisons based on *MAE* are shown in **Table 3-3**. The RF regression model results compared to the MRL results only consider continuous features for the sake of valid comparison. When considering all the features, the RF regression model resulted in a *MAE* value of 6.51 \pm 0.23 biased upward, a *VEcv* value of 87.6% \pm 6.8%, and an R^2 value of 92.6% \pm 0.92%.

The performance measures of the hybrid classification-regression RF model resulted in a *MAE* value of 4.38 \pm 0.22 biased upward, a *VEcv* value of 94.4% \pm 3.5%, and an R^2 value of 96.2% \pm 0.6%. The results of the RF hybrid model are shown to be considerably greater than those of the RF regression model in all three performance measures. According to [43], the performance of a predictive model is considered to have good accuracy if *VEcv* is between 50% and 80%, and excellent accuracy if above 80%. The importance of accuracy is dependent on the type of application considered, and the resulting *VEcv* in this chapter is found to be highly acceptable for the given application. The R^2 representation of the hybrid model is presented through **Figure 3-4**, which displays the actual response versus predicted response plot. An ideal case would be if all the points fell on the line, implying that all predicted values are the same as the observed values. **Figure 3-4** shows the points scattered relatively close to the line, with minimal outliers scattered further from the line, indicating a good fit. The figure also includes a \pm 40% difference bounds that included 121 points. Furthermore, additional bounds were considered to report on the data points lying in certain ranges of difference bounds such that for \pm 30%, \pm 20%, \pm 10%, and \pm 5% bounds the number of points included within each bound were 108, 93, 72, and 42, respectively based on a total of 150 data points. Furthermore, **Figure 3-5** presents the comparison between actual and predicted responses. It can be observed that the predicted responses

had an overall good agreement with the actual responses but tended to slightly over-predict lower outlier values. Based on the results of the three performance measures, the comparisons shown in **Table 3-3**, as well as the prediction outputs in **Figures 3-4** and **3-5**, the current ML model is shown to provide acceptable results.

Table 3-3. Summary of learner comparison.

Learner	MAE	Difference (%)
Random Forests, regression	6.68	Base
Ensembles, boosted trees	8.14	21.8
Ensembles, bagged trees	12.4	85.6
Regression tree, fine	8.88	32.9
Linear SVM	21.4	220.4
Quadratic SVM	13.85	107.3
Cubic SVM	12.1	81.1
Linear Regression	21.41	220.5

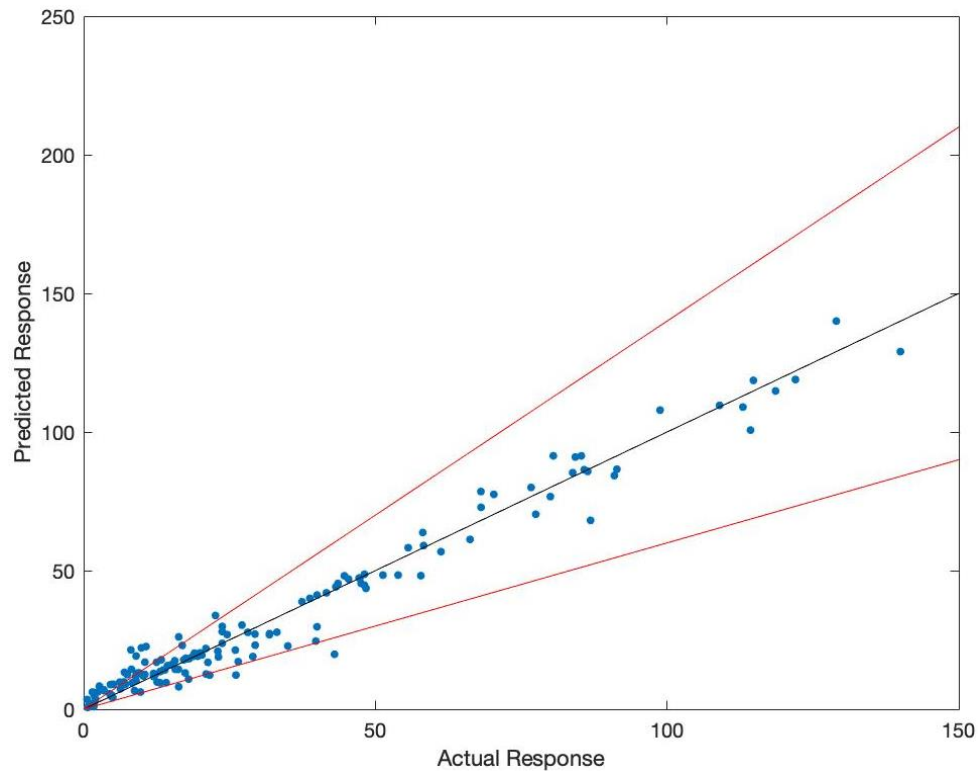


Figure 3-4. Actual versus predicted responses with a 40% error bound.

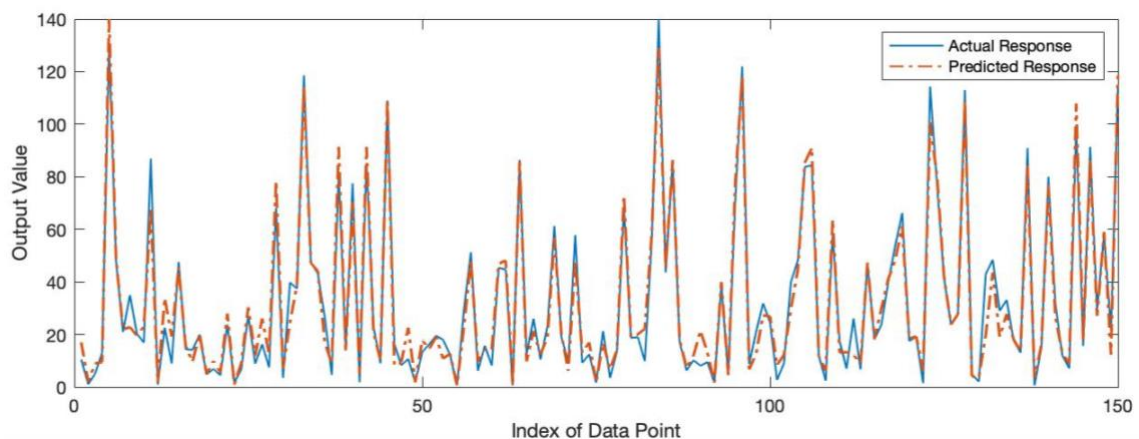


Figure 3-5. Comparison between actual and predicted responses.

3.5.2 Comparative study of ML model to alternative models

To further elaborate on the performance of the ML model, comparisons between different models predicting the maximum displacement of RC slabs to blast loading and the current model are shown in **Table 3-4**. The points in this Table were taken from studies that compared their model predictions to corresponding experimental results. Therefore, using such results as a baseline, the current model was compared to alternative models utilized for the same application.

The model details provided are the software, concrete model, and mesh size, or the analytical method. Additional details of each model and their results can be found at their respective reference. As stated in the previous section, the ML model tended to generally over-predict very few lower outlier values, which agrees with the current comparisons as shown through comparison numbers 10, 11, and 23 in **Table 3-4**. Additionally, the ML model has proven to outperform both software-based models and analytical models in most cases while in the remaining cases, the ML model's performance was lower than that of alternative models (comparison numbers 10, 15, 18, 19, 22, 23, 24, 25), but still providing acceptable predictions. In comparisons 10, 23, and 25, the ML model poorly predicted the actual value, and the reason for this lacking accuracy along with the reasons for the prediction discrepancies in the overall model are discussed in detail.

Table 3-4. Comparisons of hybrid RF model to alternative models.

Entry #	Source	Alternative Model Detail	Experimental result (mm)	Alt. Model Prediction (mm)	ML model prediction (mm)	Alt. Model Error (%)	ML Model Error (%)
1	[1]	LS-DYNA, WCM, 25.4mm mesh size	122	76	118.9	37.5	2.5
2		LS-DYNA, CDMR3, 25.4mm mesh size	122	101	118.9	16.7	2.5
3		LS-DYNA, WCM, 12.5mm mesh size	122	109	118.9	10.4	2.5
4		LS-DYNA, CDMR3, 12.5mm mesh size	122	180	118.9	47.5	2.5
5		LS-DYNA, WCM, 25.4mm mesh size	140	124	129	10.9	7.85
6		LS-DYNA, CDMR3, 25.4mm mesh size	140	121	129	12.7	7.85
7		LS-DYNA, WCM, 12.5mm mesh size	140	124	129	10.9	7.85
8		LS-DYNA, CDMR3, 12.5mm mesh size	140	180	129	29.1	7.85
9	[20]	Dynamic SDOF model	6.9	8.9	7.41	29	7.4
10		Dynamic SDOF model	0.6	0.35	3.5	41.6	483
11		Dynamic SDOF model	3.5	7.7	6.7	120	91.4
12		Dynamic SDOF model	6.7	11.4	9.1	70.1	35.8

13		Dynamic SDOF model	12.6	17	9.8	35	22.2
14	[21]	LS-DYNA, K&C,	80	66	76.7	17.5	4.1
15		LS-DYNA, K&C,	114.8	111.76	100.7	2.6	12.3
16		LS-DYNA, K&C,	118.6	114.3	114.8	3.6	3.2
17		LS-DYNA, K&C,	76.7	71.12	80	7.3	4.3
18		FPWA (MDOF model)	80	82.8	76.7	3.5	4.1
19		FPWA (MDOF model)	114.8	104.14	100.7	9.7	12.3
20		FPWA (MDOF model)	118.6	106.7	114.8	10	3.2
21		FPWA (MDOF model)	76.7	63.5	80	17.2	4.3
22		[23]	LS-DYNA, CDMR3, 3mm mesh size	9	8.4	12.3	6.6
23	LS-DYNA, CDMR3, 3mm mesh size		5.1	5.7	9	11.7	76.4
24	LS-DYNA, CDMR3, 3mm mesh size		23.1	21.3	20.3	7.8	12.1
25	LS-DYNA, CDMR3, 3mm mesh size		9.9	10.5	18.3	6.1	84.8

3.5.3 Results of PFI for input features

A thorough study of the impact of each feature was conducted through *PFI*. The *MAE* of ten different models were recorded to assess the mean absolute error of each model having a single feature permuted. Furthermore, a comparison between each of the ten models with

the original non-permuted model was made through *MAE*. **Table 3-5** presents the results of the ten models along with the comparisons of the original model. Greater values of *MAE* suggest a corresponding feature has a higher impact on the output, whereas *MAE* values closer to the original model's *MAE* has less of an impact on the output. The *PFI* values presented in the fourth column show that the ranking of feature importance based on *MAE* from highest to lowest impact is X8, X3, X7, X6, X4, X1, X2, X5, X10, X9. This ranking indicates that the features for which the output is most sensitive to are the blast impulse, blast scaled distance, the slab's thickness, and the slab's steel reinforcement ratio, followed by less sensitive features including the slab's length and width, with the least sensitive feature shown to be the concrete compressive strength and steel yield strength. Additionally, the two categorical features of slab type and slab support type were shown to have a very small impact on the output of the model when assessed through *PFI*. However, this may be due to the reduced effect of permutation for such features in which several data points may still retain their original categorical value even when permuted.

Table 3-5. PFI values of permuted features.

Permuted Feature	<i>MAE</i>	<i>PFI = MAE_{perm} - MAE_{orig}</i>
X1	4.78	0.4
X2	4.8	0.42
X3	5.68	1.3
X4	5.17	0.79
X5	4.69	0.31
X6	5.29	0.91
X7	5.43	1.05
X8	6.14	1.76
X9	4.57	0.19
X10	4.6	0.22

3.5.4 Comparative study of PFI values to existing parametric studies

To validate the results reported in the previous section, a comprehensive investigation of the relation between each feature and the output was performed based on several parametric studies found in the open literature. Afterwards, the impact of each feature was analyzed and compared to the results obtained from *PFI*. The investigated features, in which sufficient parametric studies were found, are the scaled distance, slab thickness, reinforcement ratio, concrete compressive strength, and steel yield strength. For the features of slab length, width, and steel yield strength, *PFI* values could not be compared to parametric studies due to insufficient information in the open literature relating to the effect of each parameter.

3.5.4.1 Effect of reflected impulse

A blast's reflected impulse is a function of the blast's reflected pressure and positive duration while also relating to the standoff distance and charge weight of the blast through a $R/W^{2/3}$ relation [14]. For near-field blasts having a scaled distance of less than $1.2 \text{ m/kg}^{1/3}$, the blast's duration becomes less than the time it takes to reach the maximum response of the structure, therefore the reflected impulse load becomes essential to assess the exposed structure [53].

Table 3-6 shows two sources of comparisons between the change in reflected impulse and the corresponding change in maximum displacement. For each source of comparison, all remaining parameters were kept constant aside from the analyzed parameter. This approach was also adopted in the subsequent subsections and additional information pertaining to each slab, as well as the model used for analysis, can be found at their respective sources. Based on **Table 3-6**, the rate at which the maximum displacement increases becomes significantly higher for greater values of impulse. This result coincides with the *PFI* values expressing the critical importance of this feature in the model.

Table 3-6. Effect of reflected impulse on maximum displacement.

Source	Reflected Impulse (kPa-ms)	Maximum Displacement (mm)	Change in Reflected Impulse	Corr. Change in Max Disp.
[21] a	103	4.83	Base	Base
	164	8.13	59.2%	68.3%
	232	15.11	125.2%	212.8%
	386	36.32	274.5%	652%
[21] b	103	1.65	Base	Base
	164	2.92	59.2%	79%
	232	4.19	125.2%	154.5%
	386	8.28	274.5%	401.8%
	563	14.86	446.6%	800.6%

Table 3-7. Effect of scaled distance on maximum displacement.

Source	Scaled Distance (m/kg ^{1/3})	Maximum Displacement (mm)	Change in Scaled Dist.	Corr. Change in Max Disp.
[22] a	0.756	4.6	Base	Base
	0.6	10.5	20.6%	128.3%
	0.524	16.9	30.8%	267.4%
[22] b	0.936	8.9	Base	Base
	0.782	12	16.5%	34.8%
	0.626	23	33.1%	158.4%
[49] a	1.48	4.14	Base	Base
	1.11	5.99	25%	44.7%
	0.59	26.92	60.1%	550.2%
[49] b	1.3	5.97	Base	Base
	0.97	9.51	25.4%	59.3%
	0.52	38.84	60%	550.6%
[50]	0.684	10	Base	Base
	0.592	15	13.4%	50%
	0.518	35	24.3%	250%

3.5.4.2 Effect of scaled blast distance

In the application of structural elements exposed to blast loading, the primary load that the structure withstands is the reflected pressure caused by the explosion. Based on the blast parameters provided by [14], the reflected pressure increases significantly as the scaled distance decreases. Moreover, the structural response of an element is also significantly affected by a change in scaled distance. **Table 3-7** lists several scaled distances with their corresponding output of maximum displacement, along with the change in maximum displacement resulting from the change in scaled distance.

The maximum displacement was shown to increase significantly with decreasing scaled blast distance, which is consistent in all five sources listed in **Table 3-7**. It should be noted that the scaled distance is the standoff blast distance divided by the cubic root of the charge weight. Therefore, changes in either the standoff distance or the charge weight will contribute to a change in the scaled distance. A set of three points were taken from each source in which the first point acts as a base of comparison for the second and third points. The rate at which the maximum displacement increased was significantly greater as the value of scaled distances approached smaller values, as shown in **Table 3-7**. The values of the corresponding changes of maximum displacement with respect to changing scaled distances reflect the high importance of this feature in the application.

3.5.4.3 Effect of slab thickness

The effect of slab thickness was analyzed through parametric studies listed in **Table 3-8**. Similarly, all points of comparison maintained constant parameters with varying slab thicknesses. It can be observed that decreasing the thickness of the slab considerably decreased its ability to resist deformation when subjected to blast loading. Also, for similar rates of change in thickness and blast impulse, the rate at which the maximum deformation changed was lower for changes in slab thickness. Therefore, the results of the *PFI* value for slab thickness being less than that of the blast impulse is strongly supported through this comparison.

Table 3-8. Effect of slab thickness on maximum displacement.

Source	Slab Thickness (mm)	Maximum Displacement (mm)	Change in Slab Thickness	Corr. Change in Max Disp.
[22]	200	8.4	Base	Base
	180	10.7	10%	27.4%
	150	22.6	25%	169%
[51]	600	9.6	Base	Base
	500	11.8	16.7%	23%
	400	14	33.3%	45.8%
[52] a	400	4.1	Base	Base
	300	6.9	25%	68.3%
	200	13.31	50%	224.6%
[52] b	400	20.92	Base	Base
	300	25.62	25%	22.5%
	200	36.7	50%	75.4%
[21]	355.6	10.41	Base	Base
	254	15.24	28.6%	46.4%
	152.4	27.7	57.1%	166.1%

3.5.4.4 Effect of reinforcement ratio

For similar changes in the value of the feature, the reinforcement ratio had lower corresponding changes to the maximum displacement than that of the slab thickness and the scaled distance, as shown in **Table 3-9**. Furthermore, the results in **Table 3-9** show that decreasing the reinforcement ratio, while keeping the remaining parameters constant, caused a relatively adequate increase of maximum displacement. The comparison of the effect of reinforcement ratio with respect to the effect of both scaled distance and slab thickness accurately followed the results obtained by *PFI*.

Table 3-9. Effect of reinforcement ratio on maximum displacement.

Source	Reinforcement Ratio	Maximum Displacement (mm)	Change in Reinforcement Ratio	Corr. Change in Max Disp.
[49] a	0.013	26.92	Base	Base
	0.00975	28.41	25%	5.5%
	0.0078	29.09	40%	8.1%
[49] b	0.013	38.84	Base	Base
	0.00975	43.3	25%	11.5%
	0.0078	47.24	40%	21.6%
[22]	0.0109	43.6	Base	Base
	0.00818	48.4	25%	11%
	0.00655	53.9	40%	23.6%
[21] a	0.0251	13.17	Base	Base
	0.01255	17.18	50%	30.4%
	0.00354	33.53	90%	154.6%
[21] b	0.0251	8.65	Base	Base
	0.01255	12.5	50%	44.5%
	0.00354	21.84	90%	152.5%

Table 3-10. Effect of compressive strength on maximum displacement.

Source	Compressive Strength (MPa)	Maximum Displacement (mm)	Change in Compressive Strength	Corr. Change in Max Disp.
[19] a	103.4	98.8	Base	Base
	34.5	109	66.63%	10.3%
[19] b	103.4	86.4	Base	Base
	34.5	91.4	66.63%	5.8%
[19] c	103.4	85.8	Base	Base
	34.5	80.5	66.63%	6.2%
[52] a	140	12.99	Base	Base
	35	13.31	75%	2.5%
[52] b	140	17.6	Base	Base
	35	18.1	75%	2.8%
[3]	60	7.8	Base	Base
	50	9.6	16.7%	23.1%
	30	14	50%	79.5%

3.5.4.5 Effect of concrete compressive strength

An increase in compressive strength corresponded to minor changes of maximum displacement, as shown in **Table 3-10**. Additionally, the rate of change for maximum displacement was much smaller than those of previously analyzed features. This shows how little compressive strength affected the output with respect to previous four features, especially considering that the rate of change for compressive strength was higher than that of the previously analyzed features. Such results agree with the *PFI* ranking in which the feature of compressive strength had a lower effect on impact on maximum displacement due to blast loading than the features previously discussed.

3.6 Analysis of model discrepancies

As shown in both **Figure 3-4** as well as **Table 3-4**, there are instances of large differences between the values of the predicted output and the actual output. This lack of model accuracy is attributed to the variations existing among the original data points and are summarized through the following aspects.

3.6.1 Variations between numerical and experimental methods

The methods of implementing the application of RC slabs exposed to blast loads featured in the dataset are composed of experimental, numerical, or blast simulation methods. Although numerical methods are efficient in imitating an equivalent experimental event, there are still aspects relating to the modeling parameters as well as the blast parameters that cause numerical results to deviate from experimental results.

For instance, there are several different constitutive material models to characterize the behavior of concrete under high strain rates in numerical methods. The results for two similar numerical models having different concrete material models may vary significantly while also differing from the experimental results [1,21,23,53].

Furthermore, numerical approaches such as LS-DYNA and ABAQUS, as well as the ConWep program, consider the shockwave parameters based on the semi-empirical charts

and relations provided by UFC-3-340 which are essentially high order polynomials based on the experimental programs conducted by Kingery & Pannill [54]. In several cases, the parameters obtained through numerical methods differ from the parameters recorded from experimental events [15-17].

Additionally, in numerical methods, the equations of state (EOS) used to represent the relation between pressure, volume, and internal energy (or any state variables) for each material are considered and are used to calculate the pressure throughout a mesh for every time step. These EOS are derived from thermodynamic relations while relying on experimental measurements with several EOS existing for both concrete as well as explosive materials [53]. Zhou et al [55] presented different concrete EOS for both tension and compression while comparing them to concrete EOS found in the literature in which considerable differences were shown. Baker et al [56] showed the error of two EOS for explosive materials tested against experimental data in which both EOS exhibited minor errors. Also, the EOS constants for several explosive materials are based on a cylinder of explosions confined by copper-like metal, which may show slightly different values for constants of alternative set-ups [53].

For RC subjected to blast loading, very high strain rates are achieved in which the strength of concrete increases significantly. To account for this increase in strength, a dynamic increase factor (DIF) is implemented and is a ratio of the concrete's dynamic to static strengths as a function of strain rate. Malvar & Crawford compared several DIF for concrete in tension from several sources and based different sets of experimental data found in the literature, different values of DIF were reached [57].

Another discerning aspect of numerical methods is the model's mesh size based on sensitivity analyses. For different sized mesh, the numerical model's assessment of peak pressures and reflected impulses are shown to vary [58, 59, 29]. Also, the extent of the structure's response considering different mesh sizes will also differ [1].

When considering the dataset used in the present chapter, there were 102 data points taken from numerical methods validated by experiment. The results of these data points may be varying from equivalent experimental results due to the five aspects discussed and will

therefore tend to exhibit minor variabilities with the remaining 48 experimental data points in the model. There will also exist inconsistencies among the 102 numerical data points due to different material models, mesh sizes, and modelling methods. However, even when considering such discrepancies of the dataset, the ML model was still able to perform very well.

3.6.2 Variations in blast load characteristics

In addition to the differences in the method used, there are also differences in the characteristics of the blast load. For free air bursts, the blast occurs above or adjacent to a structure in which the initial shockwave consists of only the incident wave travelling radially outwards with no augmentation. Conversely, surface bursts occur near or at the ground surface in which the initial shockwave is reflected by the ground, causing the reflected wave and the incident wave to form a strengthened initial wave acting outward in a hemispherical form. The blast parameters for a surface blast are found to be much greater than those of free air blasts for the same standoff distance and explosive weight [14]. Although this aspect of blast load exhibits large variations between both cases, the current dataset is primarily made up of free air bursts and therefore does not contain discrepancies caused by this blast characteristic. Another characteristic of blast loading consists of the range of scaled distance. Near-field blasts and far-field blasts exhibit different behaviors on a target surface and are characterized by scaled distances of less than or greater than $1.2 \text{ m/kg}^{1/3}$ [60]. The resulting blast load of near-field blasts is distributed nonuniformly in both space and time on a target surface while also subjecting the surface to a high temperature fireball, whereas far-field blasts act uniformly on a target surface while exceeding the proximity of a surface making the effect of the explosive fireball insignificant [53, 60]. In terms of the present dataset, there were a total of 95 near-field blasts and 55 far-field blasts. Also, among the far-field blasts there were 7 data points that were considered outliers having very large scaled distances and very small reflected impulses as compared to the remaining data points.

3.6.3 Variations unique to the present dataset

In cases where data points consisted of features being extreme outliers, the model would show poor prediction accuracy as presented in comparison 10 in **Table 3-4**. The cause of this was mostly dependent on the data point having the largest scaled distance and smallest reflected impulse, $25.4 \text{ m/kg}^{1/3}$ and 0.0247 MPa-ms , which were both extreme outliers of the features. To further elaborate on this, the features of scaled distance and reflected impulse were found to have among the greatest PFI values, causing them to have a very high impact on the model's prediction accuracy.

Also, considering the importance of the reinforcement ratio through PFI, the reinforcement ratio was only provided for one direction due to limitations of data availability. The given information on reinforcement is sufficient for one-way slabs but may affect data points of two-way slabs.

It can also be shown that providing additional features that are pertinent to the application may have a great effect on the overall performance of the model. For instance, the resulting performance measures of the existing model with the feature of reflected impulse eliminated result in a *MAE* value of 9.62, a *VE_{cv}* value of 52.46%, and an *R*² value of 77.29% while also requiring over 1000 repetitions of the model to stabilize results. This major change in performance suggests that missing relevant features for the existing model may lead to the loss of accuracy. However, the limit of features is based solely on the availability of data.

As previously stated, the differences between the actual values and predicted values are due to discrepancies that have been discussed in detail. The degree in which these discrepancies affect each predicted value is difficult to assess and would require a meticulous parametric study considering the effect of each major discrepancy individually. Also, by understanding the reasons that cause the model to underperform, an improved model may be achieved.

3.6.4 Suggestion for improved ML model and its practical applications

After quantifying the effect of major discrepancies, the effect of each feature's range and standard deviation should be analyzed to understand how these statistics affect the model's performance along with their relation to the importance of each feature. Based on the analyses of feature statistics and discrepancies, for both existing and additional features, a reliable dataset may be created. Also, the model should consider additional quantitative features such as reinforcement ratios for both directions of the slab as well as the blast's reflected pressure. In an ideal case, the dataset would be compiled through a dedicated blast program of numerous slab specimens, however this requires substantial cost and resources. An appropriate alternative would be to implement both numerical and experimental approaches together in which the numerical dataset would be verified in intervals by experimental data.

In terms of practical application, the improved dataset may be used to develop a ML model to identify if RC slabs conform with the design limits set forth by both ASCE 59-11 and CSA S850-12. The result obtained from the model would require an insignificant amount of time and minimal technical background to achieve an accurate result, after which a more detailed approach may be taken for further assessment. Additionally, the codes relate the design limit to the maximum allowable support rotation which may be related to the maximum displacement predicted by the model through simple calculations. Both codes state that the support rotation for flexural elements should not exceed 2° which keeps the element in a repairable state and assures life safety. For flexural elements designed for collapse prevention, the element suffers significant permanent damage while avoiding failure in which the maximum support rotation should not exceed 6° [60,61].

3.7 Conclusions

This chapter introduces a machine learning model to predict the maximum displacement of reinforced concrete slabs subjected to blast loading. A dataset of 150 points was compiled upon a thorough search through pertinent literature. The consistent dataset

included ten features, namely the length, width, and thickness of slab, concrete compressive strength, reinforcing steel yield strength, reinforcement ratio, blast scaled distance, blast reflected impulse, type of slab, and slab support along with one output: the maximum displacement.

The Random Forests algorithm along with k -fold cross-validation was used to develop the validated hybrid classification-regression RF model, which resulted in performance MAE value of 4.38 ± 0.22 , a VE_{cv} value of $94.4\% \pm 3.5\%$, and an R^2 value of $96.2\% \pm 0.6\%$. The learning model used was compared to several other learning models and exhibited superior performance measures, which affirms the effectiveness of Random Forests in complex applications. Additionally, the current developed model was compared to alternative models for the same application and was found to outperform them in some cases, while approaching reasonable results in other cases. A variable importance measure was conducted to assess the model's ability in recognizing the importance of each feature through permutation feature importance. The effect of each feature was appraised. Four of the features were compared to parametric studies found in the literature, which accurately reflected the results of the model's PFI values. Additionally, variations relating to the dataset, method of application, and blast characteristics were discussed and an improved ML model was proposed along with its practical application.

Overall, the machine learning model achieved good performance in terms of predicting maximum displacements of RC slabs exposed to blast loading. It also proved to be a strong contender against existing methods in modeling blast applications of structures and demonstrated excellent ability in identifying the effect of each input feature, while saving computational time and effort.

3.8 Chapter references

- [1] Thiagarajan, G., Kadambi, A. V., Robert, S., & Johnson, C. F. (2015). Experimental and finite element analysis of doubly reinforced concrete slabs subjected to blast loads. *International Journal of Impact Engineering*, 75, 162-173.

- [2] Mao, L., Barnett, S. J., Tyas, A., Warren, J., Schleyer, G. K., & Zaini, S. S. (2015). Response of small scale ultra-high performance fibre reinforced concrete slabs to blast loading. *Construction and building materials*, 93, 822-830.
- [3] Zhao, C., Wang, Q., Lu, X., & Wang, J. (2019). Numerical study on dynamic behaviors of NRC slabs in containment dome subjected to close-in blast loading. *Thin-Walled Structures*, 135, 269-284.
- [4] Maazoun, A., Belkassem, B., Reymen, B., Matthys, S., Vantomme, J., & Lecompte, D. (2018). Blast response of RC slabs with externally bonded reinforcement: Experimental and analytical verification. *Composite Structures*, 200, 246-257.
- [5] Ayodele, T. O. (2010). *Introduction to machine learning*. INTECH Open Access Publisher.
- [6] Kish, Adam. (2018). Survey of Machine Learning. 10.13140/RG.2.2.17066.47041.
- [7] Cao, Y., Ashuri, B., & Baek, M. (2018). Prediction of unit price bids of resurfacing highway projects through ensemble machine learning. *Journal of Computing in Civil Engineering*, 32(5), 04018043.
- [8] Spencer Jr, B. F., Hoskere, V., & Narazaki, Y. (2019). Advances in Computer Vision-Based Civil Infrastructure Inspection and Monitoring. *Engineering*.
- [9] Chopra, P., Sharma, R. K., Kumar, M., & Chopra, T. (2018). Comparison of machine learning techniques for the prediction of compressive strength of concrete. *Advances in Civil Engineering*, 2018.
- [10] Tolba, A. F. F. (2002). *Response of FRP-Retrofitted Reinforced concrete panels to Blast loading* (Doctoral dissertation, Carleton University).
- [11] Wang, W., Zhang, D., Lu, F., Wang, S. C., & Tang, F. (2012). Experimental study on scaling the explosion resistance of a one-way square reinforced concrete slab under a close-in blast loading. *International Journal of Impact Engineering*, 49, 158-164.
- [12] Mendonça, F., Urgessa, G., & Rocco, J. (2018). Experimental investigation of 50 MPa reinforced concrete slabs subjected to blast loading. *Ingeniería e Investigación*, 38(2), 27-33.
- [13] Feng, J., Zhou, Y., Wang, P., Wang, B., Zhou, J., Chen, H., ... & Jin, F. (2017). Experimental research on blast-resistance of one-way concrete slabs reinforced by BFRP bars under close-in explosion. *Engineering Structures*, 150, 550-561.

- [14] USA Department of Defense. (2008). "Structures to Resist the Effect of Accidental Explosions - Unified Facilities Criteria (UFC) 3-340-02", Department of Defense.
- [15] Wu, C., Oehlers, D. J., Rebstroth, M., Leach, J., & Whittaker, A. S. (2009). Blast testing of ultra-high performance fibre and FRP-retrofitted concrete slabs. *Engineering structures*, 31(9), 2060-2069.
- [16] Ha, J. H., Yi, N. H., Choi, J. K., & Kim, J. H. J. (2011). Experimental study on hybrid CFRP-PU strengthening effect on RC panels under blast loading. *Composite Structures*, 93(8), 2070-2082.
- [17] Razaqpur, A. G., Tolba, A., & Contestabile, E. (2007). Blast loading response of reinforced concrete panels reinforced with externally bonded GFRP laminates. *Composites Part B: Engineering*, 38(5-6), 535-546.
- [18] Li, J., Wu, C., & Hao, H. (2015). An experimental and numerical study of reinforced ultra-high performance concrete slabs under blast loads. *Materials & Design*, 82, 64-76.
- [19] Reynolds, K. A. (2015). *Experimental Behavior of High Strength Concrete Slabs Subjected to Shock Loading* (Doctoral dissertation).
- [20] Jacques, E. (2011). *Blast retrofit of reinforced concrete walls and slabs* (Doctoral dissertation, Université d'Ottawa/University of Ottawa).
- [21] Oesterle, M. G. (2009). *Blast simulator wall tests: experimental methods and mitigation strategies for reinforced concrete and concrete masonry* (Doctoral dissertation, UC San Diego).
- [22] Lin, X., Zhang, Y. X., & Hazell, P. J. (2014). Modelling the response of reinforced concrete panels under blast loading. *Materials & Design (1980-2015)*, 56, 620-628.
- [23] Yao, S., Zhang, D., Chen, X., Lu, F., & Wang, W. (2016). Experimental and numerical study on the dynamic response of RC slabs under blast loading. *Engineering Failure Analysis*, 66, 120-129.
- [24] Lin, X. (2018). Numerical simulation of blast responses of ultra-high performance fibre reinforced concrete panels with strain-rate effect. *Construction and Building Materials*, 176, 371-382.
- [25] Syed, Z. I., Raman, S. N., Ngo, T., Mendis, P., & Pham, T. (2018). The Failure Behaviour of Reinforced Concrete Panels Under Far-field and Near-field Blast Effects. In *Structures* (Vol. 14, pp. 220-229). Elsevier.
- [26] Du, H., & Li, Z. (2009). Numerical analysis of dynamic behavior of RC slabs under blast loading. *Transactions of Tianjin University*, 15(1), 61-64.

- [27] Abdel-Mooty, M., Alhayawei, S., & Issa, M. (2014). Numerical evaluation of the performance of two-way RC panels under blast loads. *Structures Under Shock and Impact SUSI XIII*, 13-25.
- [28] Jia, H., Yu, L., & Wu, G. (2014). Damage assessment of two-way bending RC slabs subjected to blast loadings. *The Scientific World Journal*, 2014.
- [29] Tai, Y. S., Chu, T. L., Hu, H. T., & Wu, J. Y. (2011). Dynamic response of a reinforced concrete slab subjected to air blast load. *Theoretical and applied fracture mechanics*, 56(3), 140-147.
- [30] MathWorks, (2019). *Statistics and Machine Learning Toolbox™: User's Guide (R2019a)*. Retrieved September 2, 2019 from https://www.mathworks.com/help/pdf_doc/stats/stats.pdf
- [31] Breiman, L. (2001). Random forests. *Machine learning*, 45(1), 5-32.
- [32] Svetnik, V., Liaw, A., Tong, C., Culberson, J. C., Sheridan, R. P., & Feuston, B. P. (2003). Random forest: a classification and regression tool for compound classification and QSAR modeling. *Journal of chemical information and computer sciences*, 43(6), 1947-1958.
- [33] Mitchell, J. B. (2014). *Machine learning methods in chemoinformatics*. Wiley Interdisciplinary Reviews: Computational Molecular Science, 4(5), 468-481.
- [34] Tsanas, A., & Xifara, A. (2012). Accurate quantitative estimation of energy performance of residential buildings using statistical machine learning tools. *Energy and Buildings*, 49, 560-567.
- [35] Tsanas, A., Little, M. A., McSharry, P. E., & Ramig, L. O. (2011). Nonlinear speech analysis algorithms mapped to a standard metric achieve clinically useful quantification of average Parkinson's disease symptom severity. *Journal of the royal society interface*, 8(59), 842-855.
- [36] Wang, Z., Li, W., Kao, Y., Zou, D., Wang, Q., Ahn, M., & Hong, S. (2018, July). HCR-Net: A Hybrid of Classification and Regression Network for Object Pose Estimation. In *IJCAI* (pp. 1014-1020).
- [37] Chen, J., Cheng, L., Yang, X., Liang, J., Quan, B., & Li, S. (2019, February). Joint learning with both classification and regression models for age prediction. In *Journal of Physics: Conference Series* (Vol. 1168, No. 3, p. 032016). IOP Publishing.
- [38] Tropsha, A., Gramatica, P., & Gombar, V. K. (2003). The importance of being earnest: validation is the absolute essential for successful application and interpretation of QSPR models. *QSAR & Combinatorial Science*, 22(1), 69-77.

- [39] T. Hastie, R. Tibshirani, J. Friedman J, The elements of statistical learning: data mining, inference, and prediction, (2009) New York, USA: 2nd edition, Springer.
- [40] Botchkarev, A. (2018). Evaluating performance of regression machine learning models using multiple error metrics in Azure Machine Learning Studio. *Available at SSRN 3177507*.
- [41] Shcherbakov, M. V., Brebels, A., Shcherbakova, N. L., Tyukov, A. P., Janovsky, T. A., & Kamaev, V. A. E. (2013). A survey of forecast error measures. *World Applied Sciences Journal*, 24(24), 171-176.
- [42] Willmott, C. J., & Matsuura, K. (2005). Advantages of the mean absolute error (MAE) over the root mean square error (RMSE) in assessing average model performance. *Climate research*, 30(1), 79-82.
- [43] Li, J. (2016). Assessing spatial predictive models in the environmental sciences: Accuracy measures, data variation and variance explained. *Environmental Modelling & Software*, 80, 1-8.
- [44] Li, J. (2019). A Critical Review of Spatial Predictive Modeling Process in Environmental Sciences with Reproducible Examples in R. *Applied Sciences*, 9(10), 2048.
- [45] Li, J. (2017). Assessing the accuracy of predictive models for numerical data: Not r nor r2, why not? Then what?. *PloS one*, 12(8), e0183250.
- [46] Strobl, C., Boulesteix, A. L., Kneib, T., Augustin, T., & Zeileis, A. (2008). Conditional variable importance for random forests. *BMC bioinformatics*, 9(1), 307.
- [47] Janitza, S., Strobl, C., & Boulesteix, A. L. (2013). An AUC-based permutation variable importance measure for random forests. *BMC bioinformatics*, 14(1), 119.
- [48] Gregorutti, B., Michel, B., & Saint-Pierre, P. (2017). Correlation and variable importance in random forests. *Statistics and Computing*, 27(3), 659-678.
- [49] Shuaib, M. M. N. (2014). *Numerical modeling of reinforced concrete slabs under blast loads* (Master's Thesis, University of Khartoum).
- [50] Wang, W., Zhang, D., Lu, F., Wang, S. C., & Tang, F. (2013). Experimental study and numerical simulation of the damage mode of a square reinforced concrete slab under close-in explosion. *Engineering Failure Analysis*, 27, 41-51.
- [51] Zhao, C., Wang, Q., Lu, X., & Wang, J. (2019). Numerical study on dynamic behaviors of NRC slabs in containment dome subjected to close-in blast loading. *Thin-Walled Structures*, 135, 269-284.

- [52] Abdel-Mooty, M., Alhayawei, S., & Issa, M. (2016). Performance of one-way reinforced concrete walls subjected to blast loads. *International Journal of Safety and Security Engineering*, 6(2), 406-417.
- [53] Dua, A., Braimah, A., & Kumar, M. (2018). Contact explosion response of reinforced concrete columns: experimental and validation of numerical model. In Paper presented at the 6th international disaster mitigation specialty conference, Fredericton, New Brunswick.
- [54] Kingery, C. N., & Pannill, B. F. (1964). Peak Overpressure Vs Scaled Distance for TNT Surface Bursts (Hemispherical Charges). US Army Armament Research and Development Center Aberdeen, MD.
- [55] Zhou, X. Q., Kuznetsov, V. A., Hao, H., & Waschl, J. (2008). Numerical prediction of concrete slab response to blast loading. *International Journal of Impact Engineering*, 35(10), 1186-1200.
- [56] Baker, E. L., Murphy, D., Stiel, L. I., & Wrobel, E. (2010). Theory and calibration of JWL and JWLb thermodynamic equations of state. *WIT Transactions on The Built Environment*, 113, 147-158.
- [57] Malvar, L. J., & Crawford, J. E. (1998). Dynamic increase factors for concrete. Naval Facilities Engineering Service Center Port Hueneme CA.
- [58] Huang, Y., Willford, M. R., & Schwer, L. E. (2012). Validation of LS-DYNA® MPM with blast experiments. In 12th International LS-DYNA Users Conference.
- [59] Codina, R., Ambrosini, D., & de Borbón, F. (2016). Experimental and numerical study of a RC member under a close-in blast loading. *Engineering Structures*, 127, 145-158.
- [60] ASCE. (2011). Blast protection of buildings: ASCE/SEI 59-11.
- [61] Canadian Standards Association. (2012). Design and assessment of buildings subjected to blast loads, CSA S850-12.

Chapter 4

4 Machine learning model for predicting structural response of RC columns subjected to blast loading

4.1 Introduction

Due to the risk of exposure to explosions and blast events, reinforced concrete (RC) structures are susceptible to severe magnitudes of damage that may result in considerable economic loss and casualties. Among the most vulnerable structural elements that could induce greatest damage, load-bearing columns are notable. Their sudden failure may trigger progressive partial or total collapse of the structure [1]. Therefore, improving the capability of predicting the structural behavior of columns subjected to blast loading would allow for more accurate proactive measures to be taken against such catastrophic events.

The current state-of-the-art in predicting the response of RC columns exposed to blast loading has shown the competence of both analytical and numerical models. For instance, Lloyd [1] conducted an experimental study using a shock tube to simulate blast loading on 14 unique RC columns in which the magnitude of shock waves produced was equivalent to far-field blasts. An analytical single degree of freedom (SDOF) model was used to predict the dynamic response of the columns and was compared to the experimental results through maximum displacement, with prediction errors ranging from 0.53-222% considering 24 comparisons. Using a similar experimental loading mechanism, Lloyd [2] tested RC columns with several retrofitting techniques, such as via fiber-reinforced polymer (FRP), transverse prestressing, and lateral bracing. A total of 16 unique columns were tested. The results were compared to an analytical SDOF model through maximum displacement at various heights along the column, and yielded prediction errors of 14.9-323% considering 10 comparisons of conventional columns only.

In an experimental study conducted by Kadhom [3], a similar shock tube system was used to simulate far-field blasts on 32 unique RC columns considering external FRP retrofits with various configurations. Two analytical SDOF models were used to predict the dynamic column behavior with and without considering the P -delta effect based on the applied axial load. When compared to the experimental results through maximum displacement, the model ignoring and considering the P -delta effect produced prediction errors of 32.1-51% and 3.5-25.2%, respectively.

Furthermore, Liu *et al* [4] conducted an experimental study on 11 RC columns subjected to near-field blasts of TNT. Their experimental results were compared to an improved SDOF model, which considered section and member analyses to develop nonlinear resistance functions. The comparison was made through maximum displacement and yielded prediction errors of 3.2-16.3%. A numerical model using LS-DYNA [5] considering smooth particle fluid dynamics was also developed and compared to the experimental values. This resulted in prediction errors of less than 5% considering 3 comparisons.

Additionally, Al-Bayti [6] developed a numerical model through LS-DYNA to investigate the response of RC columns against various magnitudes of blast loading based on numerous blast threat scenarios. The numerical model was shown to generate an error of 7.9% when compared to an experimental data point considering a 25 mm mesh size. Kyei [7] also implemented a numerical model using LS-DYNA to conduct analyses on RC columns subjected to near-field blast loading. The model was validated using limited experimental data through maximum displacement. It yielded a prediction error of 14% considering a 15 mm mesh size and 46.6 minutes of run time, and an error of 3% considering a 10 mm mesh and 361.7 minutes of run time. Similarly, a numerical model developed using LS-DYNA presented a prediction error of 9.3% considering a 30 mm mesh and 548 minutes of run time and an error of 1.7% considering a 15 mm mesh and 12000 minutes of run time for RC columns subjected to near-field blasts [8].

The literature discussed above indicates good accuracy, for both analytical and numerical models, in predicting the response of RC columns exposed to far-field and near-field blasts.

However, both approaches demand a strong understanding of the application to implement, while the numerical method further require a great deal of modeling effort and computational run time. A simplified machine learning (ML) model was introduced by Almustafa and Nehdi [9], which accurately predicted the maximum displacement of RC slabs subjected to blast loading, resulting in *MAE* of 4.38, *VE_{cv}* of 94.4%, and an *R*² of 96.2%, while also forming validated correlations between the influential parameters. The ML approach also eliminated the need for an in-depth understanding of the application, mitigated modeling complexity, and effectively reduced the computational time.

Therefore, the present chapter introduces a machine learning model to predict the response of RC columns subjected to both near-field and far-field blast loading. Tree-based ensemble algorithms were used to develop the model, which is validated through various statistical performance metrics, direct comparisons to existing models, and the ability of the model to recognize the importance of parameters for varying blast scenarios. Furthermore, a critical feature analysis was conducted to directly observe the variations in the effect of application parameters between near-field and far-field blast loading while being validated by existing studies. The limitations and future improvements of the proposed model were discussed, while presenting the model's practical implementation with respect to the limits set forth by guidelines of ASCE 59-11 [10] and CSA S850-12 [11].

4.2 Data collection and description

The dataset used to develop the prediction model was obtained from numerous papers and theses pertinent to RC columns subjected to blast loading, comprising a total of 420 data points. The source of the data includes experimental studies based on live blasts [4,12-15], experimental studies using shock tube simulated blasts [1-3], numerical methods validated by experiments [6-8,16,17], and analytical methods validated by experiments [4], producing 12, 29, 210, and 169 data points, respectively. All column specimens in the data set have fixed boundary conditions and conform to design standards in accordance with CSA-A23.3-04 [18]. Furthermore, the dataset contains both conventional and seismically

designed columns, while also consisting of near-field and far-field loading scenarios. It also takes into account the applied axial load and the height of detonation along the height of the column for near-field blasts. The mean, standard deviation, and range of the data are given in **Table 4-1**. The statistics presented show that the dataset covers a wide range of both column and blast parameters, which should allow for a holistic interpretation of the application. Also, the frequency distribution of each feature is presented in **Fig. 4-1**.

Table 4-1. Mean, standard deviation, and range of model features.

Feature/Output	Mean	Standard Deviation	Range
Length (mm)	303.26	64.48	150 – 450
Width (mm)	301.83	68.31	100 – 450
Height (mm)	3087.77	431.49	1700 – 4000
Concrete compressive strength (MPa)	34.69	9.79	27.6 – 120
Long steel yield strength (MPa)	413.51	32.15	400 – 571
Long steel reinforcement ratio	2.16	0.99	0.67 – 4.88
Tran steel yield strength (MPa)	423.6	50.84	400 – 604
Tran steel reinforcement ratio	1.298	0.742	0.19 – 3.04
Axial load ratio	0.24	0.226	0 – 0.8
Reflected Pressure (MPa)	19.92	24.84	0.013 – 118.76
Reflected Impulse (MPa-msec)	4.62	3.04	0.12 – 16.27
Blast height (mm)	1360.79	413.1	0 – 1830
Displacement height (mm)	1563.01	303.06	666 – 2540
Maximum displacement (mm)	44.55	38.98	2.42 – 169.8

4.2.1 Feature description

A total of thirteen (13) input features were determined to characterize RC columns subjected to blast loading. The features relating to the element are the column's length, width, height, concrete compressive strength, longitudinal steel yield strength, longitudinal steel reinforcement ratio, transverse steel yield strength, transverse steel volumetric reinforcement ratio, and the axial load ratio (ALR). The features relating to the blast are the reflected pressure, reflected impulse, height of the blast along the column, and height of the recorded maximum displacement. The volumetric reinforcement ratio was defined as the total volume of transverse steel over the total volume of the column. Also, the ALR

was taken as the applied axial load over the unfactored axial capacity of the column's cross-section, taking into account the capacity provided by the longitudinal steel. There were instances in the dataset where the height of the blast was different from the height of the recorded maximum displacement. Therefore, appropriate modifications to the blast parameters were considered with respect to its angle of incidence, as specified by UFC-3-340-02 [19]. All mentioned features were consistent among the entire dataset with no missing information. Also, the selection of these features was limited by the consistency of the available information throughout the literature.

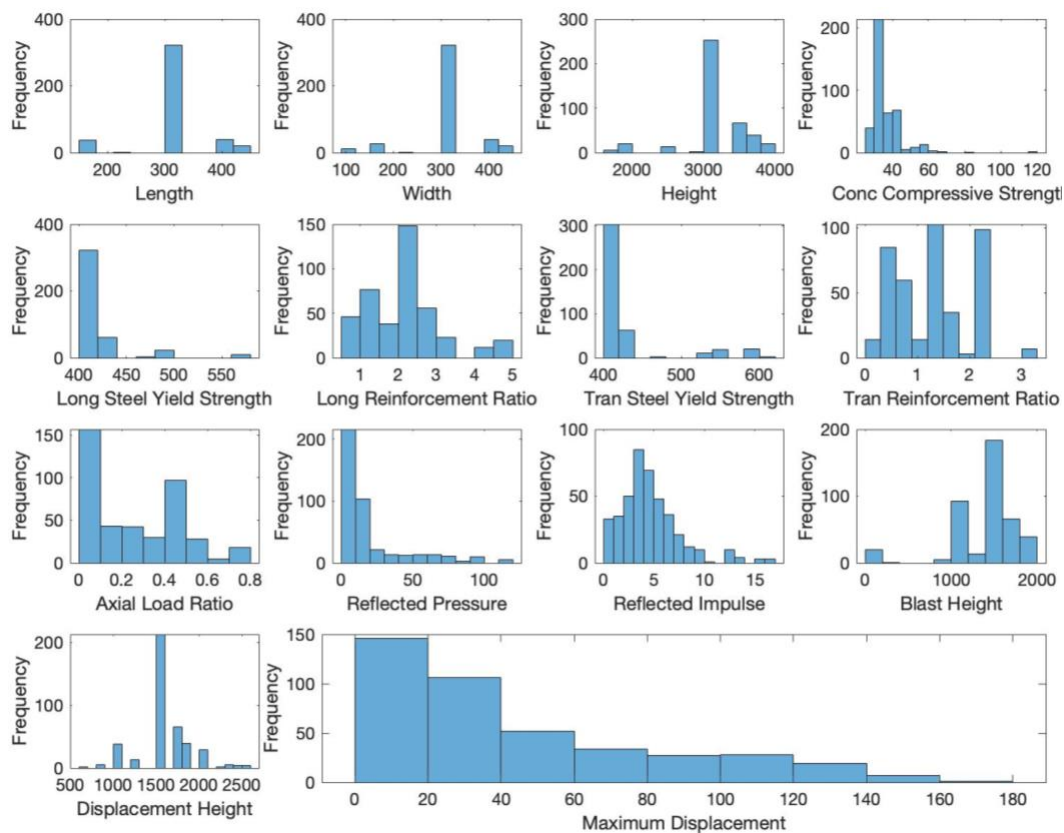


Figure 4-1. Distribution plots of features and output.

4.3 Model development

The algorithms used for the development of the prediction model and analysis of the application features were Gradient Boosted Regression Trees (GBRT) and Random Forests (RF), both being tree-based regression ensembles. The learning process and development

of each algorithm for the current chapter are discussed in the following sections. Additionally, the statistical performance measures adopted as well as their validation procedure are also provided. The development of the models in this study were done using Matlab's Statistics and Machine Learning Toolbox™ [20]

4.3.1 Gradient boosted regression trees

Gradient boosting is an approach for developing an accurate prediction model by combining multiple weak models to minimize a given loss function through a stage-wise procedure. The use of regression trees as a base model for applying gradient boosting produces a robust model that also incorporates the inherent qualities of decision trees [21]. The unique stage-wise learning procedure is illustrated in **Figure 4-2**. For GBRT, the first stage fits the data to a single regression tree and the model residuals are obtained and used to fit a new tree in the following stage. At every stage, the residuals of the overall model are computed and fit to a new tree which becomes added to the model of the subsequent stage and contributes to minimizing the loss function. To limit the contribution of each tree and avoid overfitting, a learning rate parameter is introduced into the model [22]. The process continues until the maximum number of iterations, or stages, is reached, and the resulting ensemble model produces an output as the sum of all the trees' output multiplied by the learning rate. Additional details on the procedure are provided in [22].

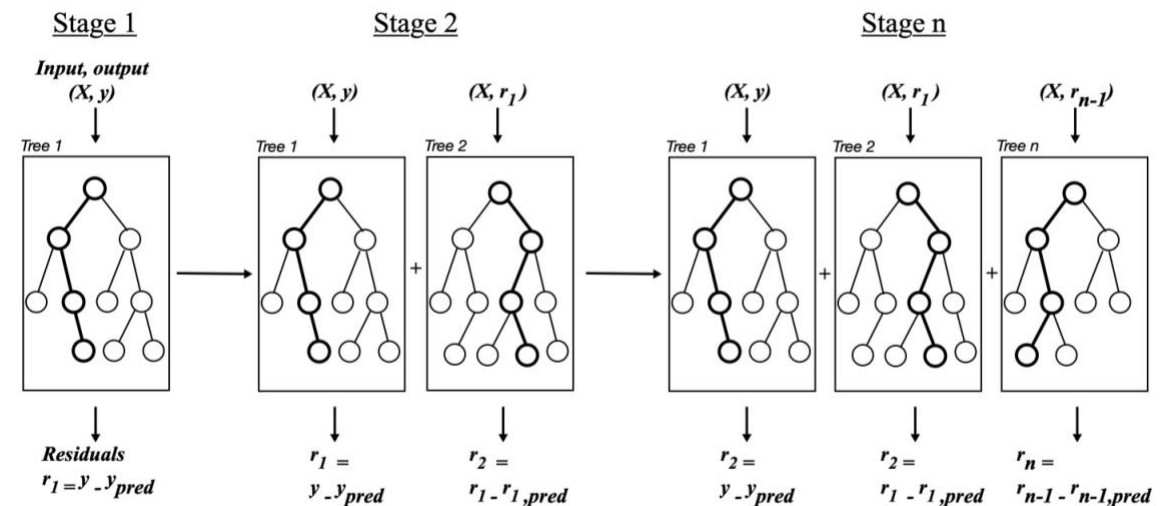


Figure 4-2. Stage-wise learning process of the gradient boosted regression trees algorithm.

The stability and predictive performance of a finalized GBRT model is highly dependent on the parameters of the gradient boosting process, being the number of stages and learning rate, and the parameters characterizing the added regression trees [21,22]. Therefore, a tuning process is required to identify the optimal parameter values that yields the highest performance for a given dataset. With respect to the current application, the tuned parameters of the GBRT model used in this chapter are number of learning cycles, learning rate, maximum number of branch splits, minimum leaf size, and number of variables to sample being 491, 0.18, 7, 2, and 13, respectively.

4.3.2 Random Forests and feature importance

In contrast to GBRT, the RF algorithm functions through forming an ensemble of decision trees in which each tree is trained on a random subset of training data. Furthermore, each tree is comprised of nodes with splitting criteria through which the input feature space is split into successively smaller regions with each node split along the decision tree. The process of region splitting is based on selective ranges of an input feature. It continues until a terminal node is reached and a decision is made [23-25]. The random nature of selecting subsets of training data for each decision tree allows the RF algorithm to produce generalized predictions while also avoiding overfitting of the data [25]. Also, approximately one-third of the randomly selected subset of data is left out of the training process for each tree. This allows each tree to possess an internal validation set which eliminates the necessity of a dedicated external validation set [25]. The decision output of the RF algorithm is produced differently from GBRT in that it is based on the average of individual predictions. For the RF model used in this chapter, a number of trees of 250 were used with the remaining parameters remaining as default values.

Tree-based ML algorithms are also capable of conducting feature importance analysis. The analysis is performed through an interaction-curvature test, which primarily depends on hypothesis testing as a node splitting criterion. For each node, the residuals of each prediction with respect to the weighted average of all predictions in that node are computed. This is followed by the partitioning of the values for a continuous feature into four quartiles, where the corresponding predictions of each quartile are counted, and the chi-square statistic and p -value are computed. The features which produce the smallest p -value in a

node will be selected to split the node, known as the curvature test. The interaction test adopts a similar methodology but considers a pair of features whose values are divided into four quadrants by splitting the value ranges into two halves at their median [20,26]. Additional details describing each test are provided in [26]. The presented statistical procedure of node splitting is used to estimate the unbiased importance of each feature by considering the summation of changes in the output due to node splits for each feature over the number of branched nodes [20]. Therefore, the interaction-curvature test was adopted herein for investigating the importance of features in the current application.

4.3.3 Performance measure

A robust machine learning model should be able to yield accurate predictions when provided with new test data previously unseen to the model. Therefore, significant efforts were made to train and test the model through numerous instances of testing and training data partitions based on cross-validation as well as data permutation. Through k -fold cross validation, the dataset is divided into k equally sized subsets such that the learning model is trained on $k-1$ subsets and tested on the remaining subset. The learning model's performance is then taken as the average of the performance measures resulting from k instances of training and testing. A k value of 10 is implemented in the current study where commonly selected k values are 5-fold and 10-fold cross-validation for assessing a learning model's performance.

Furthermore, applying cross-validation on multiple permuted instances of the dataset allows the final performance to account for significantly more combinations of training and testing. In the current study, 100 permuted iterations were taken considering cross-validation with the final performance measures taken as the average of all iterations. The statistical performance measures used for model evaluation are the mean absolute error (MAE), coefficient of determination R^2 , and the variance explained by cross-validation (VE_{cv}). MAE is a common error metric for evaluating the predictive accuracy of a model while being robust to outliers, but it is also unit dependent, such that comparisons can only be made for similar applications [27]. Additionally, the measure R^2 is an effective representation of the correlation between predicted values and actual values considering the entire dataset. A measure of the predictive accuracy of a model may be obtained through

$VEcv$, which considers the variation in the validation subset that is explained by the predicted values obtained by the model through cross-validation [27]. The formulation for each measure is given as follows:

$$MAE = \frac{1}{n} \sum_1^n |y_i - \hat{y}_i| \quad (1)$$

where \hat{y} is the predicted output, y is the actual output for every i th entry in the set, and where n is the number of datapoints in the set.

$$R^2 = \left(1 - \frac{\sum_1^n (y_i - \hat{y}_i)^2}{\sum_1^n (y_i - \bar{y})^2} \right) * 100\% \quad (2)$$

where \hat{y} is the predicted output, y is the actual output for every i th entry in the dataset, \bar{y} is the mean of the actual values, and n is the number of points in the dataset. The value of R^2 is always positive and ranges between 0 and 1.

$$VEcv = \left(1 - \frac{\sum_1^n (y_{CVi} - \hat{y}_i)^2}{\sum_1^n (y_{CVi} - \bar{y})^2} \right) * 100\% \quad (3)$$

where \hat{y} is the predicted output, y_{CV} is the actual output for every i th entry in the validation subset, \bar{y} is the mean of the actual values, and n is the number of items in the validation subset. It should also be noted that the value of $VEcv$ can be negative and has a maximum value of 100%, implying ideal accuracy [27].

4.4 Results and discussion

Using the features pertaining to the columns and blast load properties presented in **Table 4-1**, GBRT and RF models were developed for predicting the maximum displacement of blast loaded columns. The response prediction models were capable of accounting for a wide range of column designs, such as slender, short, conventionally reinforced, or seismically reinforced columns, while also covering both near-field and far-field blast applications. Furthermore, the models could predict the maximum displacement at varying heights along the column with a blast load having an angle of incidence of zero or different than zero. These diverse considerations of the application make the proposed model

effective for an extensive range of scenarios while minimizing limitations. To validate the models, statistical performance metrics were used to provide an unbiased representation of the model's predictive ability. Additionally, comparisons were made between predictions of the GBRT model and existing analytical and numerical models with respect to the available experimental data. Based on feature importance analyses conducted, the model was also assessed through its ability to capture the relation between the maximum displacement and various application parameters under separate blast loading categories. The following subsections provide details on the results of each validation approach.

4.4.1 Model validation through performance criteria

Predictions of the GBRT model resulted in a MAE of 3.63 ± 0.13 , an R^2 of $97.4\% \pm 0.3\%$, and VE_{cv} of $96.83\% \pm 1.6\%$ whereas the RF model yielded results of MAE of 6.7 ± 0.12 , an R^2 of $93\% \pm 0.3\%$, and VE_{cv} of $92\% \pm 3.9\%$. These results were based on the average values and standard deviations from undergoing 100 permuted instances of the dataset. The standard deviation of each measure shows that the model was highly capable of generalizing and producing stable and consistent results. Furthermore, the correlation between the predicted and actual values represented by the R^2 measure can be visualized in **Fig. 4-3** for the GBRT model and **Fig. 4-4** for the RF model. An error bound of 20% was also included in both figures to support the evaluation of the predictions' applicability. Additional error bounds were considered to provide better insight into the model's predictive ability for varying thresholds of error. For bounds of 5%, 10%, 20%, and 30% error, the average percentage of predicted points within each bound was 40.7%, 64.3%, 84.3%, and 92.5% for the GBRT model and 18.5%, 36.2%, 65.75%, and 80.4% for the RF model, respectively. Furthermore, for VE_{cv} values between 50% and 80%, the performance of a predictive model was considered to have good accuracy, while values greater than 80% demonstrate excellent accuracy [27].

As shown by the statistical performance measures, the GBRT model exhibited higher prediction capabilities than the RF model. This observation may also be visualized in **Figs. 4-3** and **4-4** which shows that fewer predictions are correlated to their actual values for the RF model than the GBRT model. The RF model is also observed in **Fig. 4-4** to overpredict several data points for the outputs ranging between 0 and 20 mm. Furthermore, the

percentage of predictions within lower error bounds were noticeably greater for the GBRT model than the RF model. Thus, although both models showed effective performance measures, the GBRT model exhibited strong predictive capability for this complex application and produced exceedingly acceptable results compared to the RF model. A similar observation was made between the RF and GBRT algorithms in a different study which employed such methods to predict the concrete compressive strength of ultra-high-performance concrete [24]. It can also be inferred that the GBRT algorithm, with properly tuned parameters, exceeds the performance of the RF algorithm.

Another noteworthy observation of model performance is the ability to account for both near-field and far-field blast cases in a single predictive model. Far-field blast loads produce a uniform load acting on a member whereas near-field blast loads are non-uniform and behave as a high-magnitude concentrated load, where each type similarly elicits different structural responses [28]. Thus, the ML model, namely the GBRT model, can interpret the advanced distinction in loading by implicitly identifying major variations within the given pressure and impulse information without being given any explicit label of near or far loading.

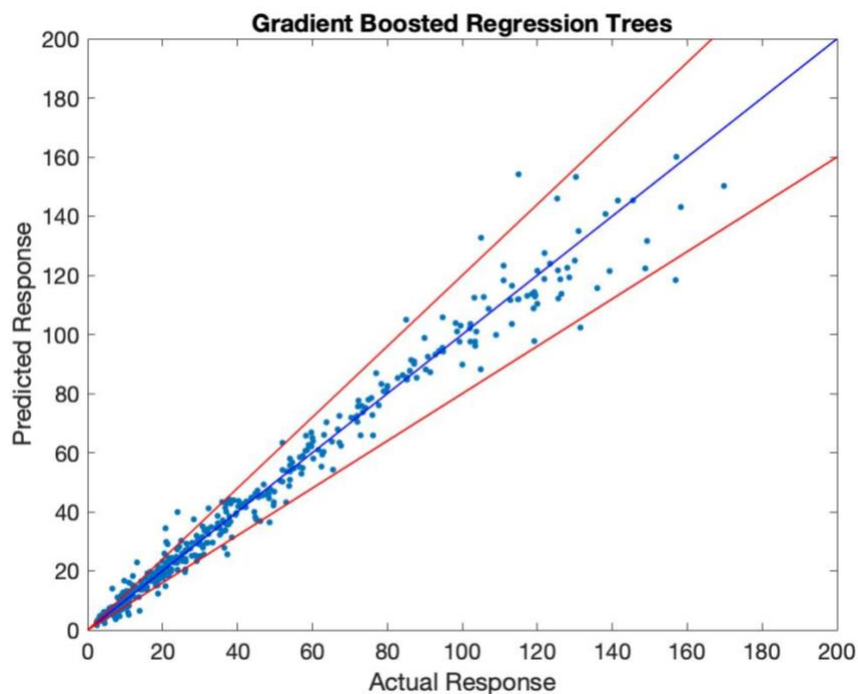


Figure 4-3. Actual versus predicted responses with a 20% error bound.

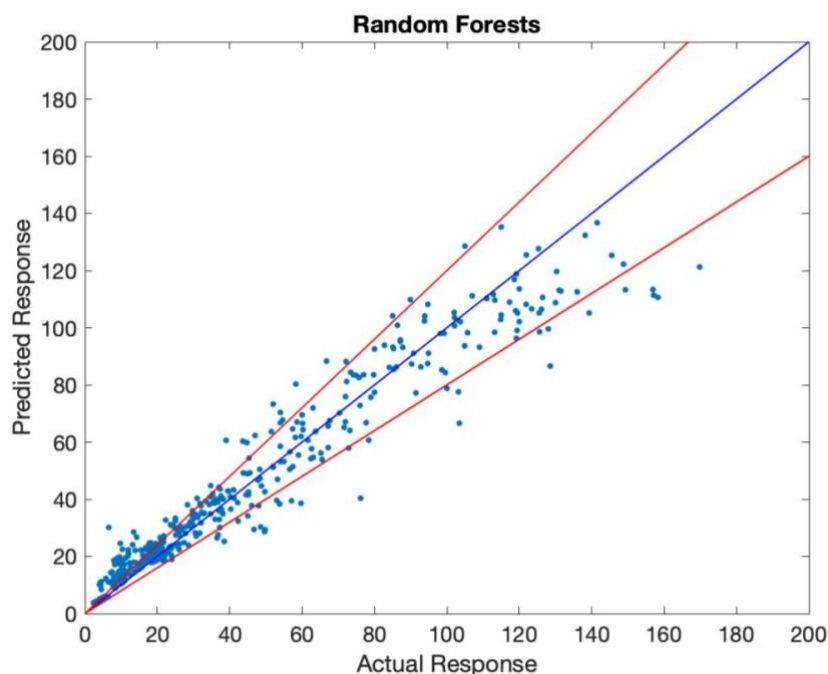


Figure 4-4. Actual versus predicted responses with a 20% error bound.

4.4.2 Model validation through comparisons of existing methods

In order to establish a comprehensive assessment of the proposed model, comparisons to existing analytical and numerical approaches were carried out with respect to the GBRT model which was shown to have a higher performance than the RF model. **Table 4-2** lists the recorded maximum displacement of 56 specimens from several experimental studies, along with its adopted prediction approach and resulting outputs. The 56 comparisons were divided into 7 sets where each set represents the source of the experimental data. Sets 1 to 4 were based on studies investigating RC columns subjected to far-field blasts, whereas sets 5 to 7 primarily studied near-field blasts for the same application. Furthermore, sets 1 to 5 adopted analytical prediction methods, while sets 6 to 7 implemented numerical modeling methods with results for varying mesh sizes provided.

The dynamic SDOF approach used in sets 1 to 5 is based on the average acceleration method described in UFC 3-340-02 [19]. Briefly described, the maximum displacement of a member is obtained through taking discrete time increments for velocity and acceleration and substituting them into an equation of motion in multiple iterations. The equation of

motion considers the member's resistance function as well as the load-mass transformation factor, which is the idealization of an equivalent lumped mass and concentrated load based on the member's shape function [19]. Although UFC 3-340-02 provided simplified resistance functions, improved results were obtained using nonlinear resistance functions based on section and member analyses [29]. This improved approach was adopted in the analytical analyses of sets 1 to 5 [1-4,15]. For the numerical models in sets 6 and 7, details on modeling, constitutive material parameters, and complete results are available at their respective sources.

For the experimental results of far-field blasts in sets 1 to 4, the ML model was able to accurately predict the actual displacements, while also proving to be more effective than the alternative analytical model throughout several comparisons. Also, there were a number of comparisons in which the ML model displayed less accurate results than the alternative analytical model, while still remaining close to the actual value. A notable observation is that a few predictions were overpredicted by the ML model as shown by comparisons 5, 8, 10, 14, 20, and 23 in set 1. This loss of accuracy was a result of the model's inability to capture the response of small displacement values caused by very low intensity blast loading and was only apparent in a limited number of comparisons. Additionally, for the experimental results of near-field blasts in sets 6 and 7, the ML model predictions indicated a highly acceptable relation to the actual values, while showing improved or similar accuracy to the alternative numerical models.

For the ML model displacement predictions of near-field blasts in set 5, the accuracy of results displayed lower performance compared to the previously described sets. This reduced accuracy is due to the minor variation of the axial load among the specimens. To further elaborate, the specimens for comparisons 5-4 to 5-9 all exhibit the same geometric, material, and blast properties and only vary slightly in their applied axial loading. As a result, the output prediction values of the ML model were remarkably similar for such comparisons. A similar description applies to comparisons 5-1 to 5-3 and 5-9 to 5-11. Therefore, the loss of accuracy was caused by the ML model's difficulty in capturing the slight changes in axial load among these specimens. Overall, the ML model was shown to

yield favorable results when compared to existing analytical and numerical methods, thus making it a strong contender for this application.

Table 4-2. Comparisons of the GBRT model to alternative models for near-field and far-field blast scenarios

Entry set	Source	Alternative model	Experimental result (mm)	Alt. model prediction (mm)	ML model prediction (mm)	Alt. model error (%)	ML Model Error (%)
1-1	[1]	Dynamic SDOF	13.9	14.2	14.47	2.16	4.1
1-2			20.8	18.7	12.42	10.1	40.29
1-3			24.2	28.5	14.81	17.77	38.8
1-4			15	15.6	14.5	4	3.33
1-5			7.5	13.4	12.26	78.67	63.47
1-6			13.5	15.1	13.75	11.85	1.85
1-7			18.2	19.8	19	8.79	4.4
1-8			3.5	11.3	13.1	222.86	274.29
1-9			19.4	25.4	20.05	30.93	3.35
1-10			5.1	8.4	11.9	64.71	133.33
1-11			22	18.2	19.55	17.27	11.14
1-12			15	13.3	19	11.33	26.67
1-13			24	21	20.4	12.5	15
1-14			2.2	6.7	11.4	204.55	418.18
1-15			16.8	18	19.7	7.14	17.26
1-16			14.4	10.7	13.6	25.69	5.56
1-17			10.8	8.5	10.1	21.3	6.48
1-18			21.4	17.3	22.1	19.16	3.27
1-19			18.4	11.5	18.47	37.5	0.38
1-20			9.6	13.1	17.8	36.46	85.42
1-21			18.8	18.7	17.46	0.53	7.13
1-22			30.2	24.4	24.74	19.21	18.08
1-23			5.5	8.7	12.66	58.18	130.18
1-24	20.8	34.3	34.4	64.9	65.38		
2-1	[2]	Dynamic SDOF	8.2	4.5	11.91	45.12	45.24
2-2			36.5	25.6	27.8	29.86	23.84
2-3			4.7	5.7	8.03	21.28	70.85
2-4			37.3	28.9	43.57	22.52	16.81

2-5			6.4	17.4	5.6	171.88	12.5
2-6			5.8	17.4	5.69	200	1.9
2-7			3.9	16.5	5.76	323.08	47.69
2-8			20	16.3	18.83	18.5	5.85
2-9			18.8	16	20.15	14.89	7.18
2-10			12.6	16.4	19.03	30.16	51.03
3-1	[15]	Dynamic SDOF	6.4	6.23	5.82	2.66	9.06
3-2			29.9	23.1	29.7	22.74	0.67
3-3			6.6	6.11	14	7.42	112.12
3-4			25	22.66	25.08	9.36	0.32
4-1	[3]	Dynamic SDOF	125.3	119.2	125.7	4.87	0.32
4-2			114.9	98.5	111.8	14.27	2.7
5-1	[4]	Dynamic SDOF	21.73	20.8	37.8	4.28	73.95
5-2			6.22	6	31.6	3.54	408.04
5-3			13.52	11.3	39.8	16.42	194.38
5-4			28.34	25	29.2	11.79	3.03
5-5			48.57	42.7	26.9	12.09	44.62
5-6			37.8	34.3	25.3	9.26	33.07
5-7			13.3	12	25.2	9.77	89.47
5-8			5.81	5.1	26.8	12.22	361.27
5-9			28.78	26.3	27.9	8.62	3.06
5-10			26.4	23.9	26.8	9.47	1.52
5-11			43.68	37.7	35.64	13.69	18.41
6-1	[8]	LS-DYNA 60mm mesh size	16.1	20.8	13.84	29.19	14.04
6-2		LS-DYNA 30mm mesh size	16.1	17.6	13.84	9.32	14.04
6-3		LS-DYNA 15mm mesh size	16.1	15.8	13.84	1.86	14.04
7-1	[14]	ANSYS 10mm mesh size	67.2	105.3	80.4	56.70	19.64
7-2			10.6	17.12	16.47	61.51	55.38

4.4.3 Feature importance analysis of near-field and far-field blast

Based on the model validation discussion in sections above, it was observed that the ML models displayed strong prediction capabilities with the GBRT model outperforming the RF model. The GBRT model also demonstrated similar or improved efficacy with respect to existing prediction methods. To further signify the aptitude of the ensemble models, feature importance analyses were conducted, measuring the effects of various parameters on the columns' maximum displacement. The first and second analysis considered the importance of features for the applications of near-field and far-field blast loading, respectively. A near-field blast is classified on having a scaled distance of less than $1.18 \text{ kg/m}^{1/3}$ whereas scaled distances exceeding this value are considered to produce far-field blasts [10]. The purpose of investigating separate loading scenarios originates from the considerable variations found in each application's structural response, as well as from their research significance [4,12,14,28]. Furthermore, each feature's importance obtained from the analysis of both applications was validated through existing parametric studies. The correlations between several features and maximum displacement from the literature are presented in **Figs. 4-6 to 4-10**. For each figure, apart from **Fig. 4-9**, every line is independent and based on a fixed scaled distance, while portraying variations of a selected feature and its consequent variation in maximum displacement, provided that all remaining features are kept constant. Additionally, each point on the line represents a single displacement output for a given feature value, while the slope between two consecutive points represents the effect of changing the feature's value. **Figure 4-9** follows a similar description, but primarily assesses correlations between the scaled distance and maximum displacement but does not consider any fixed scaled distances. Due to the availability of such parametric studies, only the features of concrete compressive strength, longitudinal reinforcement ratio, transverse reinforcement ratio, axial load ratio, reflected pressure, reflected impulse, and blast height could be validated by the literature and were thus considered in the analysis for each application. The importance measures of these features are presented in **Fig. 4-5**.

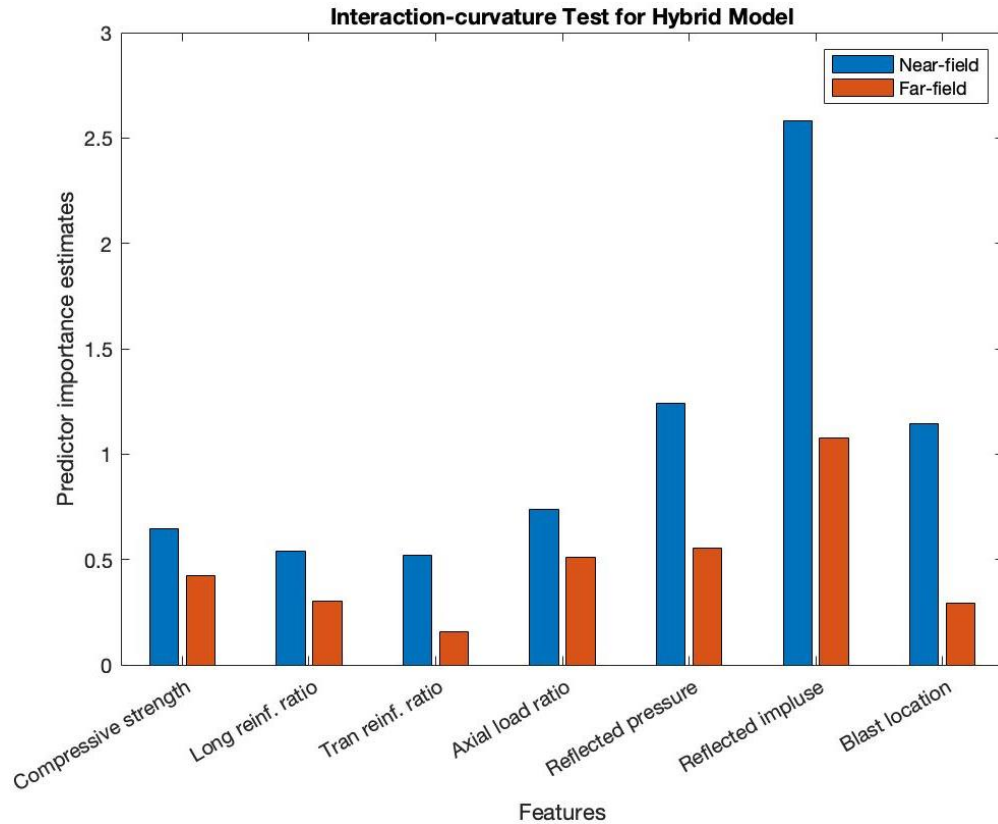


Figure 4-5. Feature importance estimates for selected features in near-field and far-field blasts.

4.4.4 Importance measure of column parameters

4.4.4.1 Concrete compressive strength

According to **Fig. 4-5**, the feature of concrete compressive strength was observed to have a greater effect on the maximum displacement of columns in near-field blasts than in far-field blasts. The observation is associated with the vulnerability of the column's compression zone undergoing blast loading. Initially, the compression zone of an axially loaded column is the entirety of its cross-section. For near-field blasts causing large lateral displacements, a significant drop in the axial load causes the column to behave similar to a beam having a cross-section primarily in tension, while inducing substantial flexural compression in the greatly reduced compression zone [1,2,3,12]. The described phenomenon would cause compression zones having lower compressive strengths to

exhibit very large strains or even complete crushing, both resulting in greater maximum displacement of the column [7]. This observation strongly corroborates the high importance of compressive strength in columns exposed to near-field blasts. However, for far-field blasts causing smaller lateral deflections, compression zones are less susceptible to high strains or crushing caused by a major shift in the neutral axis [12]. This also supports the reduced importance measure for compressive strength in columns subjected to far-field blasts. It is also hypothesized that if there existed a separate feature representing compression steel in the column, it would also exhibit higher importance in near-field blasts than far-field blasts. However, distinguishing between the effects of longitudinal reinforcement under compression and that under tension is beyond the scope of the current study due to the limitations of the current dataset, which only considers the longitudinal reinforcement of the entire cross-section. Additionally, there is very little experimental data that considers the effects of compression and tensile steel on axially loaded members subjected to blast loading. Therefore, a feature analysis of these two parameters through an ML model could not be validated by experimental data.

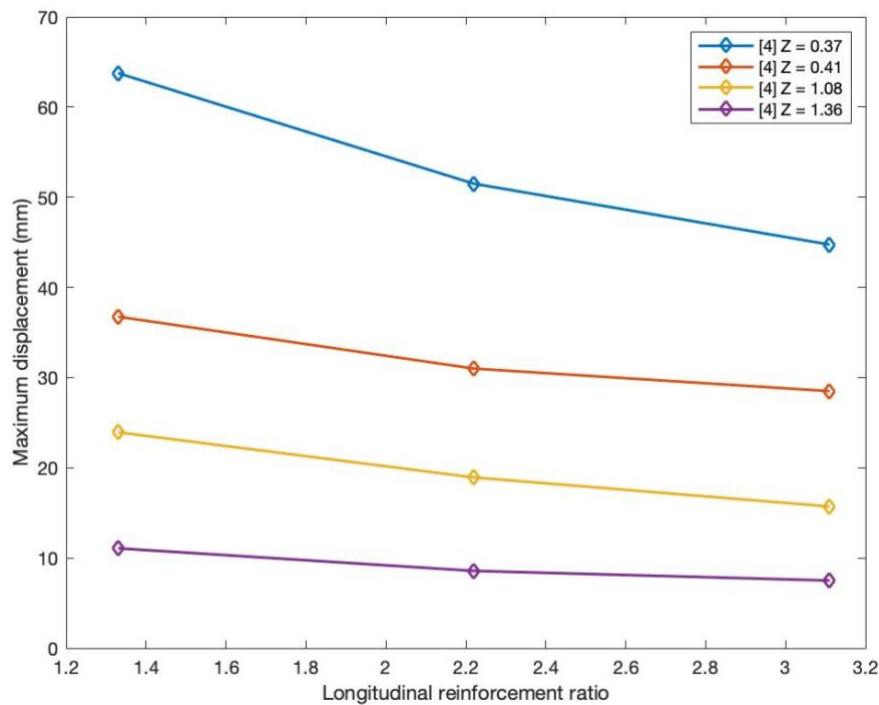


Figure 4-6. Effect of longitudinal reinforcement ratio on maximum displacement where Z has units of $m/kg^{1/3}$.

4.4.4.2 Longitudinal reinforcement ratio

Furthermore, the feature of the longitudinal reinforcement ratio was more pronounced in columns in near-field blasts than in far-field blasts as shown in **Fig. 4-5**. This observation is supported by the comprehensive parametric study conducted by Liu *et al.* [4], which found that the effect of varying the longitudinal reinforcement ratio on the maximum displacement became more noticeable as the blast's scaled distance decreased. Consequently, for larger scaled distances, a change in the longitudinal reinforcement yielded similar maximum displacements. The effect of the longitudinal reinforcement on the maximum displacement from a previous study is illustrated in **Fig. 4-6**. It can be observed that for the scaled distance of $0.37 \text{ m/kg}^{1/3}$, changes in the longitudinal reinforcement ratio resulted in a relatively large change in maximum displacement. In contrast, minimal changes in maximum displacement were produced for the same changes in longitudinal reinforcement ratio when subjected to a larger scaled distance of $1.36 \text{ m/kg}^{1/3}$. Such findings agree with the importance measure of the feature for far-field and near-field blasts.

4.4.4.3 Transverse reinforcement ratio

Figure 4-5 shows that for both near-field and far-field blasts, the feature of transverse reinforcement ratio carries a minimal effect on the resulting maximum displacement. The feature of transverse reinforcement ratio on the behavior of RC columns under blast loading has been widely investigated. For instance, Braimah and Siba [12] conducted a thorough experimental study on RC columns subjected to varying magnitudes of blast loading. They concluded that increasing the transverse reinforcement ratio improved the column's blast resistance for smaller scaled distances, whereas for larger scaled distances, the response of the column remained the same regardless of the transverse reinforcement ratio. Additional experimental, numerical, and analytical studies also found that the effect of the transverse reinforcement was only evident in high magnitude blast loads resulting from near-field blasts or low scaled distances, while the effect of the transverse reinforcement ratio was insignificant for far-field blasts or large scaled distances [1,4,7,8]. The results of these studies and the consequent effect of the transverse reinforcement on the maximum

displacement are shown in **Fig. 4-7**. It can be observed in **Figs. 4-7(a)** and **4-7(c)** that for equal changes in the transverse reinforcement ratio, slightly larger changes in maximum displacement were produced in near-field blasts than in far-field blasts. Similarly, it can be observed from **Fig. 4-7(b)** that larger changes in the transverse reinforcement ratio resulted in minimal changes of the maximum displacement in far-field blasts. Therefore, extensive literature strongly supports the results observed in **Fig. 4-5**, which indicates that the effect of the transverse reinforcement ratio was relatively minor although being more significant in near-field blasts than in far-field blasts.

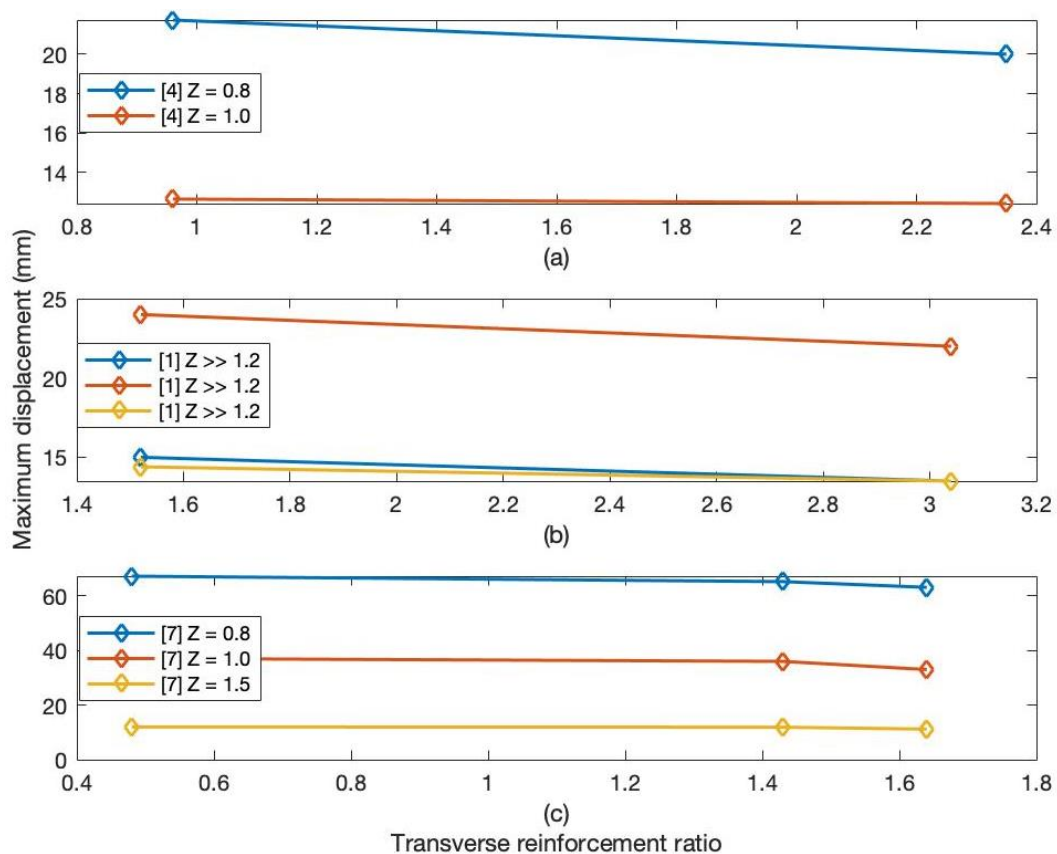


Figure 4-7. Effect of transverse reinforcement ratio on maximum displacement where Z has units of $m/kg^{1/3}$.

4.4.5 Axial load ratio

It can be observed in **Fig. 4-5** that the feature of ALR had a significant effect on both the far-field and near-field blasts, with the latter being more dominant. The ALR was

considered of high importance due to its variable influence on the column's structural response, which either magnifies or mitigates the P -delta effect induced on the column [4,16]. For far-field blasts, a greater ALR increased the stiffness of the column, resulting in lower maximum displacement. However, increasing the ALR for columns in near-field blasts introduced the risk of reducing a column's stiffness because of concrete crushing due to the increased flexure in the compression zone, as previously described [12]. Furthermore, a numerical parametric study showed that the effect of ALR was more pronounced in near-field blasts due to increased second-order moments, which consequently affected the resulting maximum displacement [6,30]. The resulting maximum displacements for various blast magnitudes and ALR are shown in **Fig. 4-8**. **Figure 4-8(a)** shows that minimal changes in the axial load ratio at very small scaled distances resulted in significant change of the maximum displacement. Conversely, **Fig. 4-8(b)** shows that relatively larger changes in the axial load ratio were required to cause substantial changes in the maximum displacement for greater values of scaled distance. These studies support the observation that the ALR was a pertinent feature for both of blast applications, while having greater influence in near-field blasts.

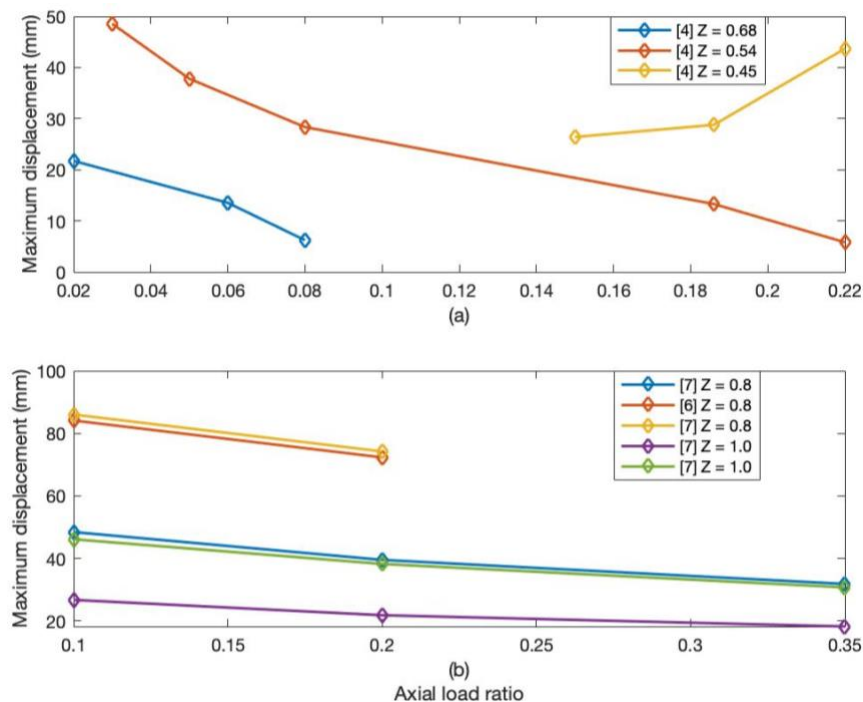


Figure 4-8. Effect of axial load ratio on maximum displacement where Z has units of $\text{m/kg}^{1/3}$.

4.4.6 Importance measure of blast parameters

4.4.6.1 Reflected pressure and reflected impulse

The features with highest importance for both near-field and far-field blasts were the reflected pressure and reflected impulse, as displayed in **Fig. 4-5**. Both features are a function of the blast's scaled distance, which is commonly used to represent the magnitude of the blast [19]. Furthermore, various studies have found that the maximum displacement of RC columns was strongly dependent on the blast's scaled distance, regardless of the column's dimensions or reinforcement ratios [4,8,12,31]. The extent to which the scaled distance affected the maximum displacement is visualized in **Fig. 4-9**. It can be observed in **Fig. 4-9(a)** that the maximum displacement was greatly affected by the scaled distance at lower ranges. A similar observation may be made in **Fig. 4-9(b)** where changes in the value of the scaled distance at lower ranges caused larger changes in the maximum displacement, while also showing that the effect of the scaled distance reduced as its range increased. A similar conclusion was drawn from a feature importance analysis on RC slabs in which blast parameters retained the highest feature importance measure [9]. Therefore, the importance measure of the blast parameters resulting from the analysis were consistent with existing studies.

For both near-field and far-field blasts, the reflected impulse had greater effect on the maximum displacement than the reflected pressure, as depicted in **Fig. 4-5**. Recent studies indicated that due to a near-field blast's period being relatively shorter than the natural period of a column or the time to reach a maximum response, such members should be analyzed based on reflected impulse [28,31]. Such reasoning clearly agrees with the observation in **Fig. 4-5** that the reflected impulse had greater effect on the maximum displacement than the reflected pressure in near-field blasts, while also being more pronounced in near-field blasts than far-field blasts. Furthermore, there exists more variability in the reflected impulse than reflected pressure for the same scaled distance. This is due to the reflected pressure being directly proportional to the scaled distance, while the reflected impulse being proportional to the scaled distance times $1/W^{1/3}$ where W is the weight of the charge [19,32]. Additionally, the effect of the blast's reflected impulse, and therefore its charge weight, on the maximum displacement is illustrated in **Fig. 4-10** based

on existing studies. It can be observed in both **Figs. 4-10(a)** and **4-10(b)** that for a fixed scaled distance, and therefore a fixed reflected pressure, the maximum displacement was significantly affected by the weight of the charge, which is directly correlated with the blast's reflected impulse. This shows that variations in maximum displacement subjected to constant scaled distances was primarily caused by the effect of the reflected impulse. Such observations further support that the effect of the reflected impulse was greater than the effect of reflected pressure, both for near-field or far-field blast loading, as shown in **Fig. 4-5**.

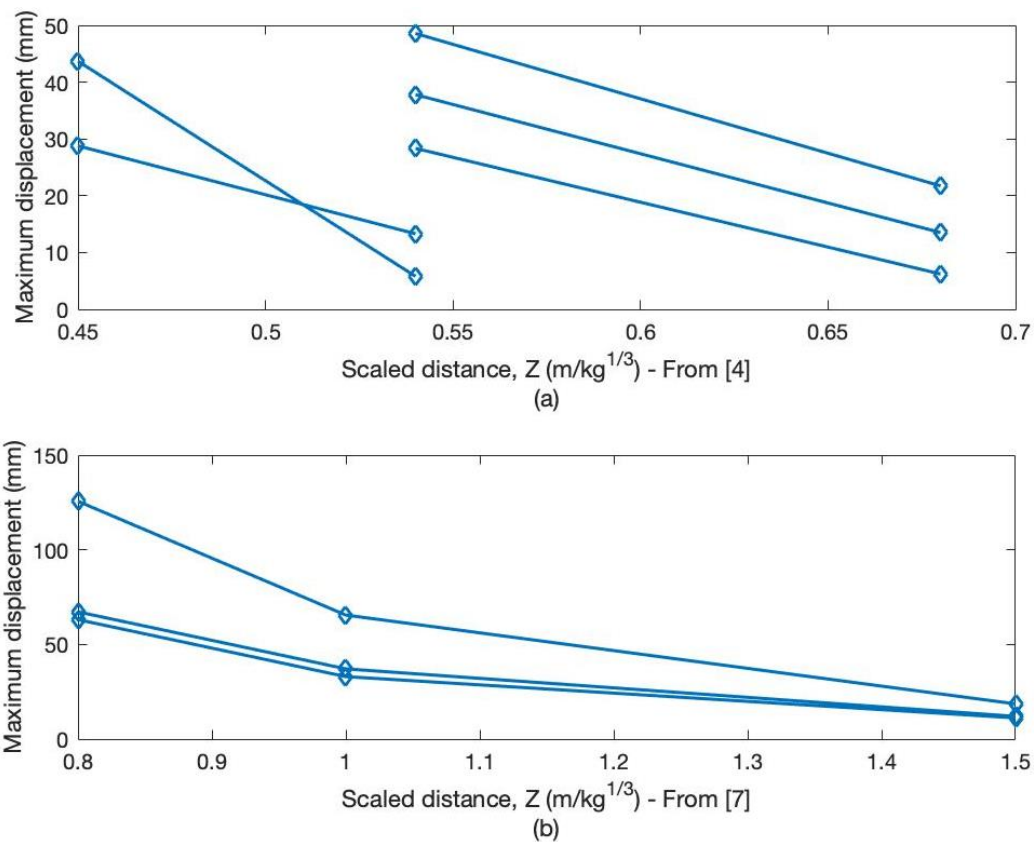


Figure 4-9. Effect of scaled distance on maximum displacement.

4.4.6.2 Blast height along the column

Figure 4-5 shows that the effect of the blast height on maximum displacement was greater in near-field blasts than in far-field blasts. Far-field blasts typically produced a uniform load on the face of the member in which the resulting maximum displacement was located at the member's mid-height. Additionally, when changing the height of the charge weight

along the column's height, there was only a minor change in the magnitude of blast parameters due to a trivial angle of incidence between the charge weight and the column's mid-height [19]. However, near-field blasts produced a non-uniform or concentrated load in which the greatest magnitude was applied to the location closest to the charge weight where the maximum displacement occurred [28]. Since the magnitude of the blast loading was uniform in far-field blasts, the maximum displacement occurred where the column's stiffness was lowest, being at mid-height. Conversely, the maximum displacement in near-field blasts occurred at the height of detonation in which a lower displacement was incurred as the blast moved closer to the supports where the stiffness of the column increased [33]. The described blast loading and column response phenomena for near-field and far-field blasts effectively support the observation made on the effect of the blast height on the maximum displacement.

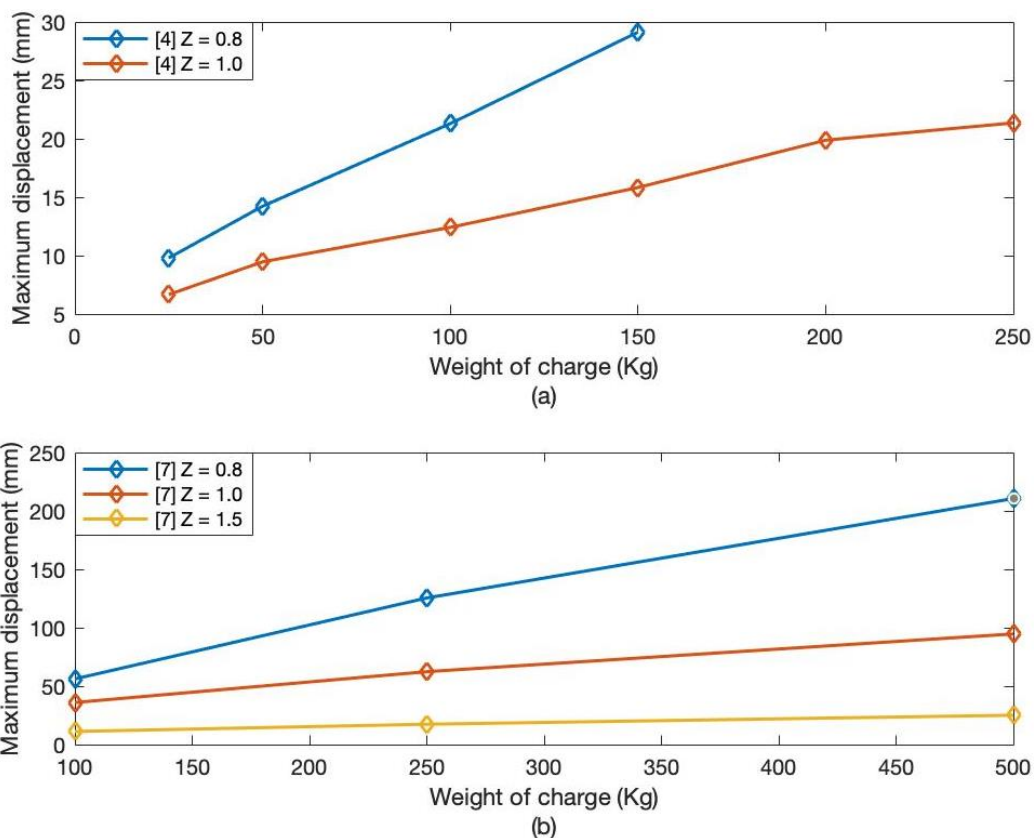


Figure 4-10. Effect of reflected impulse from changing charge weights on maximum displacement where Z has units of $m/kg^{1/3}$.

4.5 Practical implementation and model improvement considerations

The proposed ML models have been thoroughly validated based on its statistical performance, competence against existing prediction methods, and ability to capture complex relationships between pertinent features and their output. However, there were very few inconsistencies in predictions as stated in a previous section. The current section focuses on identifying limitations and discussing future improvements for the proposed model. Also, practical implementations of the proposed model are discussed and descriptions for supplementary models which encompass more detailed predictions of local and global structural responses pertinent to the application are provided.

4.5.1 Model improvement through added features

Although the features in **Table 4-1** were used to characterize the application of RC columns exposed to blast loading, additional features may be included to resolve the discrepancies found in the developed model and improve its predictive performance. The first improvement could be made within the parameter of transverse reinforcement ratio. In the current model development, although this feature was considered, it did not consider variable spacing, such as that implemented in seismic columns. Therefore, non-uniform transverse spacing could be considered in a future model improvement. Additionally, the feature of axial load ratio was proven to have a high effect on the output. However, variations in the column behavior due to the applied axial load were also a function of additional characteristics. These include the loss of axial load caused by large deformations, the magnification or mitigation of deflections caused by the *P*-delta effect, and the corresponding change in the cross-section's neutral axis. By quantifying these characteristics and including them as features, a future model would be able to better capture the complex behavior associated with axially loaded columns undergoing blast loading with greater accuracy than the current model. Moreover, numerical studies have shown that the column's behavior was greatly affected by its boundary conditions [16,17]. Consequently, a future model may consider a qualitative feature of alternative column boundary conditions as opposed to having primarily fixed boundary conditions as in the current model. The current model only accounted for square and rectangular columns.

Thus, considerations for circular columns could be included in a future model. Another consideration for model improvement is the inclusion of additional data that addresses specific model limitations. This would resolve the prediction discrepancies observed by the model in **Table 4-2**. In addition, there were minor inconsistencies in the training dataset primarily related to variations among the various numerical methods from which some data was collected.

4.5.2 Practical usage in accordance with code and future model development

Both the American and Canadian codes for blast design of structures provide displacement limits for flexural members in the form of maximum support rotations [10,11]. In order to maintain a repairable state for RC members subjected to blast loading, a maximum support rotation of 2° is required. However, a rotation of 6° may be used for less stringent demand of building protection such that element failure is not reached, and potential building collapse is avoided. The current model may be used to provide accurate preliminary displacement results, and therefore rotation results, while incorporating various essential RC column and blast parameters. It can also be used in the iterative design process of RC members where each iteration can provide an accurate response estimate by simply inputting trial parameters and receiving an immediate output. Therefore, the proposed model carries significant potential to help practicing blast engineers in improving the design process.

In further terms of practical usage, although the current model accounts for a variety of column and blast configurations as shown in **Table 4-1**, additional efforts are required to account for a wider range of feature values. Such efforts should be directed specifically towards the inclusion of more distinct and larger column cross-sections. Moreover, the response prediction of maximum displacement for the current application is practically effective for far-field and near-field blast-loaded columns. However, applications of the near-field variant also evaluate local responses and damage criteria. Thus, this study provides motivation for the development of future ML models towards capturing additional element responses of near-field blast applications and would strongly compliment the currently developed model.

4.6 Conclusions

A machine learning based structural response prediction model for RC columns subjected to blast loading was developed in the current chapter. Based on the available literature, a dataset of 420 test columns was compiled, considering both seismic and non-seismic columns, as well both near-field and far-field blast loads. The features used to characterize the complex application were the column dimensions, concrete compressive strength, steel yield strength for both transverse and longitudinal reinforcement, as well as their reinforcement ratios, axial load ratio, reflected pressure, reflected impulse, and the height of detonations and displacement along the column. The developed model was trained on ensemble tree-based algorithms, which considered dataset permutation, cross-validation, and feature importance. Based on this work the following conclusions can be drawn:

- Both the GBRT and RF algorithms were considered for model development in which the GBRT model presented a greater aptitude in modeling the application of blast-loaded RC columns
- Based on thorough investigation and validation, the proposed GBRT model was proven to provide accurate, generalized, and stable predictions of maximum displacement, as shown through its statistical performance measures of MAE , R^2 , and VE_{cv} with results of 3.63, 97.4%, and 96.83%, respectively.
- The GBRT model was also validated through direct comparison to existing prediction methods based on experimental benchmarks and was proven to outperform numerical and analytical methods in several cases.
- Predictions of the proposed model were made within seconds. They require minimal user intervention and little computational effort.
- Conversely, existing numerical methods are associated with high computational demand and require several minutes to several hours to yield results.
- Model validation was further conducted through comprehensive feature importance analyses, which confirmed the model's ability to capture and quantify the

relationships between design parameters and their output for both near-field and far-field blast scenarios.

- The features having the greatest effect on the maximum displacement were the reflected impulse, reflected pressure, blast height, axial load ratio, and concrete compressive strength. Results of feature importance analyses strongly correlated well with findings in the literature.
- The model was observed to outperform existing prediction methods in several cases.
- The model's performance based on accuracy, time, and complexity make it favorable for practical implementation in preliminary design processes.
- However, model improvements to mitigate minor prediction discrepancies are recommended and can be achieved via consideration of axial load changes, *P*-delta effects, changes to the neutral axis location throughout loading, along with consideration of the column's varying boundary conditions, alternative column geometry, and non-uniform tie spacing.
- Overall, the GBRT model achieved excellent performance offering a promising new approach to the field of blast engineering as a practically effective tool for preliminary design stages, while also motivating future complementary models.

4.7 Chapter references

- [1] Lloyd, A. (2010). Performance of reinforced concrete columns under shock tube induced shock wave loading (Master's thesis, University of Ottawa, Canada).
- [2] Lloyd, A. E. W. (2015). Blast retrofit of reinforced concrete columns (Doctoral dissertation, Université d'Ottawa/University of Ottawa).
- [3] Kadhom, B. (2016). Blast performance of reinforced concrete columns protected by FRP laminates (Doctoral dissertation, Université d'Ottawa/University of Ottawa).
- [4] Liu, Y., Yan, J., Li, Z., & Huang, F. (2019). Improved SDOF and numerical approach to study the dynamic response of reinforced concrete columns subjected to close-in blast loading. In *Structures* (Vol. 22, pp. 341-365).

- [5] LS-DYNA 971. Livermore Software Technology Corporation, Livermore, CA, USA; 2015.
- [6] Al-Bayti, A. (2017). Vulnerability of Reinforced Concrete Columns to External Blast Loading (Master's thesis, Université d'Ottawa/University of Ottawa).
- [7] Kyei, C., & Braimah, A. (2017). Effects of transverse reinforcement spacing on the response of reinforced concrete columns subjected to blast loading. *Engineering Structures*, 142, 148-164.
- [8] Abladey, L., & Braimah, A. (2014). Near-field explosion effects on the behaviour of reinforced concrete columns: a numerical investigation. *International Journal of Protective Structures*, 5(4), 475-499.
- [9] Almustafa, M. K., & Nehdi, M. L. (2020). Machine learning model for predicting structural response of RC slabs exposed to blast loading. *Engineering Structures*, 221, 111109.
- [10] ASCE. (2011). Blast protection of buildings: ASCE/SEI 59-11.
- [11] Canadian Standards Association. (2012). Design and assessment of buildings subjected to blast loads, CSA S850-12.
- [12] Braimah, A., & Siba, F. (2018). Near-field explosion effects on reinforced concrete columns: an experimental investigation. *Canadian Journal of Civil Engineering*, 45(4), 289-303.
- [13] Codina, R., Ambrosini, D., & de Borbón, F. (2016). Alternatives to prevent the failure of RC members under close-in blast loadings. *Engineering Failure Analysis*, 60, 96-106.
- [14] Codina, R., Ambrosini, D., & de Borbón, F. (2016). Experimental and numerical study of a RC member under a close-in blast loading. *Engineering Structures*, 127, 145-158.
- [15] Burrell, R. P., Aoude, H., & Saatcioglu, M. (2015). Response of SFRC columns under blast loads. *Journal of Structural Engineering*, 141(9), 04014209.
- [16] Astarlioglu, S., Krauthammer, T., Morency, D., & Tran, T. P. (2013). Behavior of reinforced concrete columns under combined effects of axial and blast-induced transverse loads. *Engineering Structures*, 55, 26-34.
- [17] Astarlioglu, S., & Krauthammer, T. (2014). Response of normal-strength and ultra-high-performance fiber-reinforced concrete columns to idealized blast loads. *Engineering structures*, 61, 1-12.
- [18] Canadian Standards Association. (2004). *Design of concrete structures*. Mississauga, Ont.: Canadian Standards Association.

- [19] USA Department of Defense. Structures to Resist the Effect of Accidental Explosions - Unified Facilities Criteria (UFC) 3-340-02. Department of Defense; 2008.
- [20] MathWorks, (2019). Statistics and Machine Learning Toolbox™: User's Guide (R2019a). Retrieved January 30, 2021 from https://www.mathworks.com/help/pdf_doc/stats/stats.pdf.
- [21] Elith, J., Leathwick, J. R., & Hastie, T. (2008). A working guide to boosted regression trees. *Journal of Animal Ecology*, 77(4), 802-813.
- [22] Friedman, J. H. (2001). Greedy function approximation: a gradient boosting machine. *Annals of statistics*, 1189-1232.
- [23] Han, Q., Gui, C., Xu, J., & Lacidogna, G. (2019). A generalized method to predict the compressive strength of high-performance concrete by improved random forest algorithm. *Construction and Building Materials*, 226, 734-742.
- [24] Marani, A., Jamali, A., & Nehdi, M. L. (2020). Predicting Ultra-High-Performance Concrete Compressive Strength Using Tabular Generative Adversarial Networks. *Materials*, 13(21), 4757.
- [25] Breiman, L. (2001). Random forests. *Machine learning*, 45(1), 5-32.
- [26] Loh, W. Y. (2002). Regression tress with unbiased variable selection and interaction detection. *Statistica sinica*, 361-386.
- [27] Li, J. (2016). Assessing spatial predictive models in the environmental sciences: Accuracy measures, data variation and variance explained. *Environmental Modelling & Software*, 80, 1-8.
- [28] Dua, A., & Braimah, A. (2016). State-of-the-art in near-field and contact explosion effects on reinforced concrete columns. *Canadian Society for Civil Engineering Annual Conference 2016: Resilient Infrastructure, London*.
- [29] Jacques, E., Lloyd, A., and Saatcioglu, M. (2012). "Predicting reinforced concrete response to blast." *Canadian Journal of Civil Engineering*, 39, 1-18.
- [30] Arowojolu, O., Rahman, M. K., & Hussain, B. M. (2017). Dynamic response of reinforced concrete bridge piers subjected to combined axial and blast loading. In *Structures Congress 2017* (pp. 98-109).
- [31] Abedini, M., Mutalib, A. A., Zhang, C., Mehrmashhadi, J., Raman, S. N., Alipour, R., & Mussa, M. H. (2020). Large deflection behavior effect in reinforced concrete columns exposed to extreme dynamic loads. *Frontiers of Structural and Civil Engineering*, 14(2), 532-553.

- [32] Shirbhate, P. A., & Goel, M. D. (2020). A Critical Review of Blast Wave Parameters and Approaches for Blast Load Mitigation. *Archives of Computational Methods in Engineering*. DOI: 10.1007/s11831-020-09436-y.
- [33] Wu, K. C., Li, B., & Tsai, K. C. (2011). Residual axial compression capacity of localized blast-damaged RC columns. *International journal of impact engineering*, 38(1), 29-40.

Chapter 5

5 Hybrid machine learning model for predicting structural response of RC beams under blast loading

5.1 Introduction and background

Being able to accurately predict the response of structural elements subjected to explosions and detonations is paramount for designing resilient and blast-resistant structures. Furthermore, prediction methods that can account for the properties of advanced materials such as high-strength concrete (HSC) and high-strength reinforcement (HSR) can improve the versatility of design practice. In recent years, substantial research efforts have been devoted to investigating the behavior of reinforced normal-strength concrete (NSC) and HSC beams under blast loading. Additionally, similar efforts have been made to develop response prediction models for such elements, including both analytical and numerical methods.

For instance, an experimental study by Guertin-Normoyle [1] investigated NSC, HSC, and ultra-high-performance concrete (UHPC) beams under simulated blast loads at the University of Ottawa's Shock-tube Simulator. The study indicated the extent to which HSC and UHPC can improve the blast performance of beams in comparison to beams made with NSC and normal-strength reinforcement (NSR). A dynamic single degree of freedom (SDOF) analytical model was evaluated based on maximum displacement predictions. When compared to experimental results, the SDOF model resulted in errors of 3.21% to 35.29% with an average of 19.41% considering 9 NSC beams. Similarly, Algassem [2] studied the behavior of high-strength fiber-reinforced concrete (HSFRC) beams along with HSC and NSC beams under the same simulated blast loading scheme. It was found that the addition of fibers improved the beam's blast performance by increasing its shear capacity, reducing fragmentation, and mitigating maximum and residual displacements. A SDOF

model was evaluated as an analytical prediction method based on maximum displacement and was found to yield prediction errors of 6.22% to 26.96% with an average of 13.58% considering 10 NSC and HSC beams.

Another experimental investigation on HSC beams under simulated blast loading was done by Charles [3], considering the effects of reinforcement detailing and steel fiber content. Results showed that the use of compression reinforcement led to improved blast resistance and controlled displacements, while steel fibers allowed for increased stirrup spacing without disrupting the beam's blast performance. The study also evaluated a SDOF model for maximum displacement predictions which produced errors between 10% and 28% with an average of 16.44% considering 9 HSC beams. Furthermore, Nassr *et al* [4] conducted an experimental study on the dynamic response of NSC beams under various ammonium nitrate-fuel oil (ANFO) charge weights. Using the recorded maximum displacement values as a reference, an analytical Timoshenko Beam Model (TBM) was evaluated and yielded errors of 0.75% to 21.45% with an average of 7.8% considering 6 NSC beams.

Along with analytical methods, numerical methods have also been widely adopted to model blast loaded NSC and HSC beams. For instance, Magnusson *et al.* [5] investigated different modelling considerations for NSC and HSC beams subjected to blast loading using Ansys Autodyn. These considerations included the use of linear concrete strain softening, strain rate effects for tensile reinforcement, and the effect of concrete-reinforcement bonding. Results of the numerical models were compared to experimental findings on corresponding specimens for both NSC and HSC beams through maximum displacement, which resulted in errors of 4.57% to 23%, with an average of 11% considering 6 comparisons. Moreover, an experimental study was conducted by Yao *et al* [6] on NSC beams of varying stirrup ratios exposed to different TNT charge weights. A corresponding numerical study using LS-DYNA was implemented to assess the simulated dynamic responses of the beam specimens considering perfect concrete-reinforcement bonding and strain-rate sensitive material models. Comparisons of maximum displacement were made and yielded errors of 2.9% to 8%, with average of 5% considering 4 comparisons. A similar numerical modelling configuration was implemented using ABAQUS in which two NSC beams subjected to

blast loading were evaluated against experimental displacements and resulted in errors of 6% and 9.25% [7].

Extensive literature survey shows that both analytical and numerical methods produced predictions of the behavior of NSC and HSC beams under blast loading with reasonable accuracy. However, each of these methods is generally associated with complex requirements for effective execution. For instance, analytical methods require dedicated background of the application to account for pertinent components within each method's derived formulations. Similarly, for numerical methods, a reliable understanding of material models, as well as competent modeling efforts and computational resources are required for producing accurate predictions. To potentially eliminate such complexities and demands of existing displacement prediction methods of blast-loaded structural elements, Almustafa and Nehdi [8] introduced a machine learning (ML) model for predicting the maximum displacement of reinforced concrete (RC) slabs under blast loading. The simplified model was assessed via statistical performance measures of mean absolute error (*MAE*), R^2 , and variance explained by cross-validation (*VE_{cv}*), achieving values of 4.38, 96.2%, and 94.4%, respectively. The model was also thoroughly validated against existing methods and was found to be a strong contender for the application.

In a complementary effort, the present chapter introduces a ML model to predict the maximum displacement of NSC and HSC beams reinforced with NSR or HSR subjected to blast loading. A hybrid gradient-boosted regression trees algorithm is implemented for the model's development while adopting a Henry Gas Solubility optimization algorithm for parameter tuning. The developed model was validated through the statistical performance measures *MAE*, R^2 , and *VE_{cv}*, while also being evaluated against existing analytical, numerical, and empirical models through direct output comparisons. The proposed model is also validated through its ability to identify the importance of each application feature via comparisons to experimental findings. Furthermore, this chapter introduces a classification model of blast loaded NSC and HSC beams, which is able to identify element failure modes, as well as crack pattern formations. The classification model is validated through measures of accuracy, precision, and recall, while being further corroborated with feature importance analysis supported by experimental studies. Lastly,

the elimination of modeling complexities is discussed for both models, along with highlighting their potential practical implementations.

5.2 Model development

5.2.1 Hybrid gradient-boosted regression trees

The maximum displacement prediction model development was based on a hybrid gradient-boosted regression trees (GBRT) algorithm. Traditional GBRT is an ensemble learning algorithm that takes advantage of many individual weak models to produce a robust prediction model. Towards this development, GBRT implements a stage-wise process of creating and incorporating single regression trees. Initially, a first regression tree is created which attempts to fit the data, albeit with large error. During the second stage, the residuals of the first tree are then fit onto a second tree as a means of mitigating the initially produced error. For every subsequent stage, a new tree is created to fit the errors of the previous tree and is added to the collection of existing trees. The process continues until a performance criterion with respect to a loss function is met or until a stopping criterion is reached [9]. The parameters that characterize the GBRT algorithm are the number of trees, the contribution of each tree through a learning rate, and the depth of each regression tree. Since the performance of the GBRT is highly dependent on its parameters, it becomes pertinent to identify the most optimal values. Thus, a novel optimization algorithm is implemented towards tuning the model parameters.

Henry Gas Solubility Optimization (HGSO) is a novel metaheuristic algorithm inspired by the behavior of gasses governed by Henry's Law. It states that the amount of a given gas that dissolves in a volume of liquid is directly proportion to the partial pressure of the gas in equilibrium with the liquid at constant temperature. For the HGSO algorithm, several gases (agent population size) are initialized and are divided into equal clusters. Each gas is a potential solution to the problem being optimized. At every time step, the gases are evaluated so that the best and worst candidates are collected. Afterwards, the parameters of the optimization process are updated to expand the gases' search. The updated parameters include the Henry's coefficient (H), which is a function of temperature,

solubility (S) being a function of pressure and H , and lastly, the position of the gas, which depends on S , the best gas of the previous time step, and a variable defining the quantification of gas interactions. Moreover, the position of the worst solution gases is drastically updated by introducing a random-valued variable. These mechanisms have been proven to be effective in updating the position of agents throughout a solution search to obtain a global optimum [10]. The HGSO algorithm was successfully integrated into the GBRT algorithm as a means of fine-tuning the model parameters.

Furthermore, the classification model developed herein implements a classification Random Forests algorithm RF. RF is composed of an ensemble of decision trees in which a random subset of training data is used to train each tree. The training process for each tree is achieved through successively splitting the input training data into smaller subsets of data by splitting criteria at each node. Once each node identifies the condition for splitting based on the ranges of input data, the training process is completed, and a prediction may be obtained by a terminal node. By utilizing numerous decision trees trained with random subsets of data, the RF algorithm can take advantage of the multiple node conditions of data splitting that produce a generalized and unbiased output [11]. The final output of the model is obtained through taking the majority vote of the discrete outputs produced by individual trees.

Moreover, the feature importance analysis used in this study is based on the node-splitting criterion of a random forests (RF) algorithm, known as the interaction-curvature test. It tests the null hypothesis that there is no interaction between a pair of input features and the output. Initially, the curvature test is conducted in which the residual value of each prediction in a node is computed with respect to the weighted average of all predictions in that node. Afterwards, the values of a continuous feature are partitioned into four quartiles for both positive and non-positive residuals, where the corresponding predictions of each quartile are counted. This forms a 2x4 contingency table in which the chi-square statistic and p -value are obtained. Consequently, the best input feature used to split a node is the one which minimizes the p -value with respect to curvature tests between each input feature of the node and the data point's output [12]. The approach for the curvature-interaction test uses a similar methodology, but instead computes statistics based on a pair of features

whose values are divided into four quadrants by splitting the value ranges into two halves at their median. Additional details describing each test are provided in [12]. The unbiased importance of each feature is obtained by considering the summation of changes in the output due to node splits for each feature over the number of branched nodes. Based on this procedure, the importance of each feature is obtained for the current application and is used for detailed investigation in subsequent sections of this chapter.

5.2.2 Performance measures and cross-validation

5.2.2.1 Cross-validation

Generally, a ML model requires a dataset to be able to learn information and correlations within a given application and produce practical predictions, while also requiring “unseen” data to measure its predictive performance. Therefore, by partitioning an available dataset into training and testing sets, a ML model can be objectively evaluated. A widely adopted data partitioning approach is the k -fold cross-validation (CV) in which the dataset is divided into k equally sized subsets in which the training process is done on $k - 1$ subsets, while the remaining subset is reserved for testing [8]. This allows for model performance to be evaluated as an average of k models, while accounting for standard deviation. When considering k to be the number of points in a dataset N , this becomes “Leave-One-Out” (LOO) CV, in which performance measures are based on n models having been trained on $N-1$ data points. Upon successful validation of a model using k -fold CV, LOO CV may be implemented to further evaluate a model’s performance when supplied with additional training data. Both LOO CV and 10-fold CV were considered in the current model development. In addition to CV, the dataset was permuted to achieve more generalized performance measures through additional combinations of training and testing.

5.2.2.2 Performance measures for displacement prediction model

The statistical performance measures used for evaluating the displacement prediction model are the mean absolute error (MAE), coefficient of determination R^2 , and the variance explained by cross-validation (VE_{cv}). MAE is a common error metric for evaluating the predictive accuracy of a regression model. While being robust to outliers, it is unit

dependent, such that comparisons can only be made for similar applications [13]. Additionally, the measure R^2 is an effective representation of the correlation between predicted values and actual values considering the entire dataset. A measure of the predictive accuracy of a model may be obtained through $VEcv$, which considers the variation in the validation subset that is explained by the predicted values obtained by the model through cross-validation [13]. It should be noted that $VEcv$ is applied only through k -fold CV in this study, and not LOO CV, whose validation set only consists of a single data point. The formulation for each measure is given as follows:

$$MAE = \frac{1}{n} \sum_1^n |y_i - \hat{y}_i| \quad (1)$$

$$R^2 = \left(1 - \frac{\sum_1^n (y_i - \hat{y}_i)^2}{\sum_1^n (y_i - \bar{y})^2}\right) * 100\% \quad (2)$$

$$VEcv = \left(1 - \frac{\sum_1^n (y_{CVi} - \hat{y}_i)^2}{\sum_1^n (y_{CVi} - \bar{y})^2}\right) * 100\% \quad (3)$$

where \hat{y} is the predicted output, y is the actual output for every i th entry in the dataset, \bar{y} is the mean of the actual values, n is the number of points in the dataset; and y_{CV} is the actual output for every i th entry in the validation subset. The value of R^2 is always positive and ranges between 0 and 1, while $VEcv$ can be negative and has a maximum value of 100%, implying ideal accuracy [13].

5.2.2.3 Performance measures for multi-class classification model

A classification model is fundamentally evaluated on its ability to label an output to its correct class, (true positive, TP), its ability to recognize that an output does not belong to other classes (true negative, TN), its tendency to label an output to an incorrect class (false positive, FP), and its tendency to mislabel an output for a given class (false negative, FN) [14,15]. The count of each classification scenario for a model may be conveniently visualized through a 2x2 confusion matrix for binary classification problems. For multi-class classification problems with k classes, a $k \times k$ confusion matrix may be adapted, as shown in **Fig. 5-1**.

		$C_0 \dots C_{k-1}$	C_k	$C_{k+1} \dots C_n$
		True Class	$C_{k-1} \dots C_0$	TN
C_k	FN		TP	FN
$C_n \dots C_{k+1}$	TN		FP	TN
		Predicted Class		

Figure 5-1. Confusion matrix representation for multi-class classification problems.

Through a confusion matrix, a classification model's *precision* and *recall* may be obtained through relations (4) and (5). The *precision* of a class expresses the degree to which the predicted output labels agree with the true class label, whereas the *recall* presents the effectiveness of a model in correctly labeling outputs for a particular class [15]. These two performance measures may be obtained for each class individually, or as an average for the entire model. A classification model can also be evaluated through its *accuracy*, or simply the number of correctly predicted outputs over the total number of outputs. Although *accuracy* is a suitable representation of a classification model's performance, it is sensitive to imbalanced data and can be biased towards the majority class. Therefore, two classification models may produce the same accuracy, yet demonstrate varying performances for different classes [16]. To mitigate such bias and achieve a more robust interpretation of the model, both *recall* and *precision* were used in the present chapter alongside *accuracy* to thoroughly evaluate the failure mode and cracking pattern classification model.

$$Precision = \frac{TP}{TP+FP} \quad (4)$$

$$Recall = \frac{TP}{TP+FN} \quad (5)$$

5.3 Data collection and description

The datasets for both models introduced in this chapter were compiled from numerous research articles and theses found in the literature. The development of both the displacement prediction model and the failure mode and crack pattern classification model were based on data from experimental studies that employed a blast simulation device, experimental studies that utilized explosive materials, and numerical studies verified by experiments. The following sections provide a detailed description of each model's dataset through its sources, statistics, distributions, and application considerations.

5.3.1 Feature descriptions

A total of eleven (11) features were considered for characterizing RC beams under blast loading. The selection of features was based on the availability of consistent data across the existing pertinent literature. Thus, the continuous features used to characterize the beam element are its height, width, length, concrete compressive strength, longitudinal steel yield strength, tension reinforcement area, compression reinforcement area, stirrup spacing, and a categorical feature labeling the beam's support conditions. Additionally, the features used to associate blast loading are the reflected pressure and reflected impulse. In cases where the explosive charge weight and standoff distance were provided instead of blast parameters, charts provided by UFC 3-340-02 [17] were utilized to obtain any required values. Therefore, values for both datasets were collected consistently across all features such that there were no instances of missing data.

5.3.2 Displacement prediction model

The dataset used for developing the displacement prediction model consisted of 150 data points of which 52 were from studies that utilized simulated blast loading [1-3,18-20], 33 were from studies that implemented explosive material detonations [4-6,21,22], and 65

were from numerical studies [6,23-25]. **Table 5-1** provides the mean, standard deviation, and range of features for the dataset, whereas **Fig. 5-2** presents their statistical distribution. While investigating the literature for relevant data, it was observed that blast-loaded RC columns with only corner reinforcement and no applied axial load strongly resembled blast-loaded RC beams. As a result, 49 numerical data points were obtained from such elements [24,25]. The compiled dataset considered NSC, HSC, NSR, and HSR beams subjected to both near-field and far-field blast loading, all of which contribute to creating a comprehensive dataset for the application. It should be noted that although a few of these studies had investigated additional types of beam specimens, only the ones relevant to the scope of this study were retained.

5.3.3 Failure mode and cracking pattern classification model

For the failure mode and cracking pattern classification model, a total of 108 data points was retrieved in which 70 were from studies that utilized simulated blast loading [1-3,18-20] and 38 were from studies that implemented explosive material detonations [4-6,21,22]. Similar considerations for NSC, HSC, NSR, and HSR beams under near-field and far-field blasts were included in the dataset. The mean, standard deviation, and range of features are listed in **Table 5-2**, while feature distributions are displayed in **Fig. 5-3**. Upon careful inspection of the compiled beam data and their respective state of damage, the beams were consistently categorized into four discrete classes. Two classes were concerned with crack pattern predictions for beams that did not reach failure, and two classes were allocated for predicting modes of failure. The four classes are labeled as flexural crack formation, bending failure, flexural-shear crack formation, and crushing failure, denoted as class 1, 2, 3, and 4, respectively. The beams resulting in flexural crack formation were associated with few to several hairline cracks perpendicular to the length of the beam. Beams identified with flexural-shear cracks developed both perpendicular cracks along the middle of the beam and 45° cracks towards the support. Bending failures were identified by the presence of large cracks at the beam's midspan associated with large plastic deformations, while crushing failures were primarily recognized by severe crushing of the compression zone. Post-blast images of each class can be found at the dataset's listed sources.

Table 5-1. Data statistics for displacement prediction dataset.

Feature/Output	Mean Count	Standard Deviation	Range Categories
Height (mm)	250.97	65.55	100 – 400
Width (mm)	205.83	81.53	100 – 300
Length (mm)	2402.19	555.46	1100 – 3000
Concrete compressive strength (MPa)	58.44	30.15	30 – 200
Steel yield strength (MPa)	473.19	156.61	235 – 929
Tension steel reinforcement ratio	1.43	0.66	0.36 – 4.1
Compression steel reinforcement ratio	0.65	0.58	0 – 1.4
Stirrup spacing (mm)	127.63	73.2	0 – 300
Reflected Pressure (MPa)	16.72	27.19	0.0198 – 95.55
Reflected Impulse (MPa-msec)	3.2	3.54	0.184 – 15.93
Support condition (simple / fixed)	80 / 70	-	2
Maximum displacement (mm)	35.85	33.7	3.01 – 210.6

Table 5-2. Data statistics for failure mode and crack pattern classification dataset.

Feature/Output	Mean Count	Standard Deviation	Range Categories
Height (mm)	238.7	61.50	100 – 250
Width (mm)	161.05	55.45	100 – 300
Length (mm)	2210	421.62	1100 – 2425
Concrete compressive strength (MPa)	66.27	30.67	30 – 160
Steel yield strength (MPa)	507.45	192.70	395 – 929
Tension steel reinforcement ratio	1.48	0.77	0.36 – 4.1
Compression steel reinforcement ratio	0.29	0.32	0 – 1.2
Stirrup spacing (mm)	116.5	56.59	0 – 200
Reflected Pressure (MPa)	11.6	22.90	0.0198 – 56.77
Reflected Impulse (MPa-msec)	20.4	2.78	0.0776 – 9.58
Maximum displacement (mm)	39.23	30.14	7-185.4
Failure mode or crack pattern (1,2,3,4)	40/17/29/22	-	4

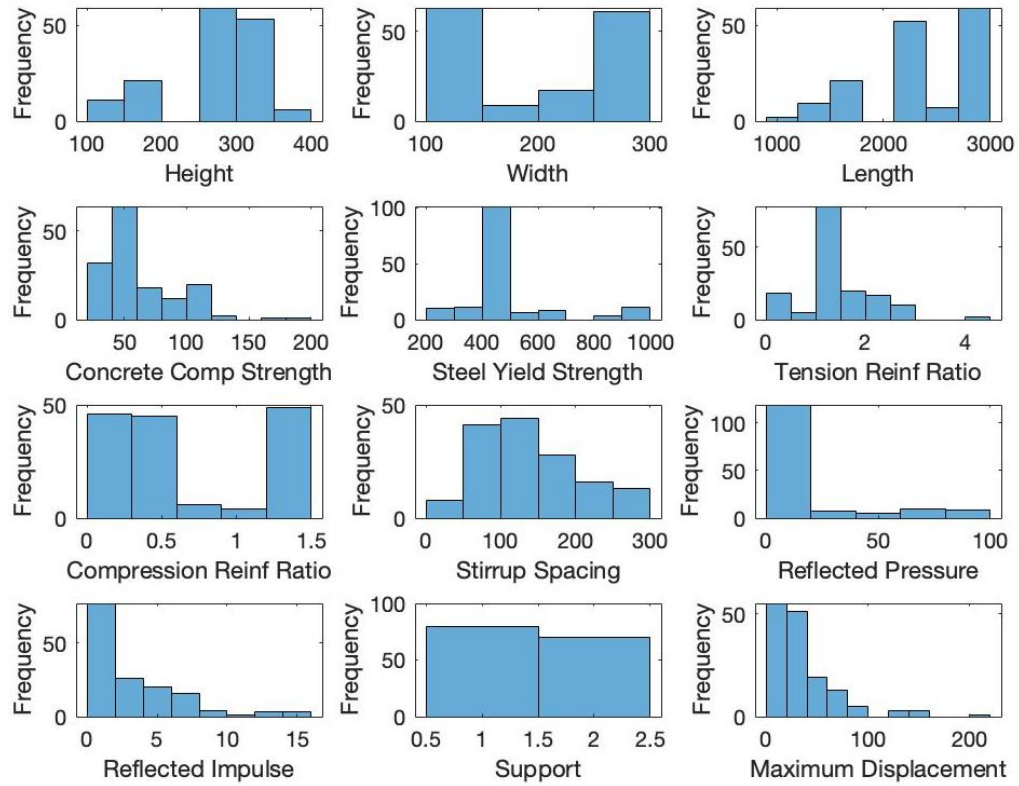


Figure 5-2. Histograms of features and output for displacement prediction dataset.

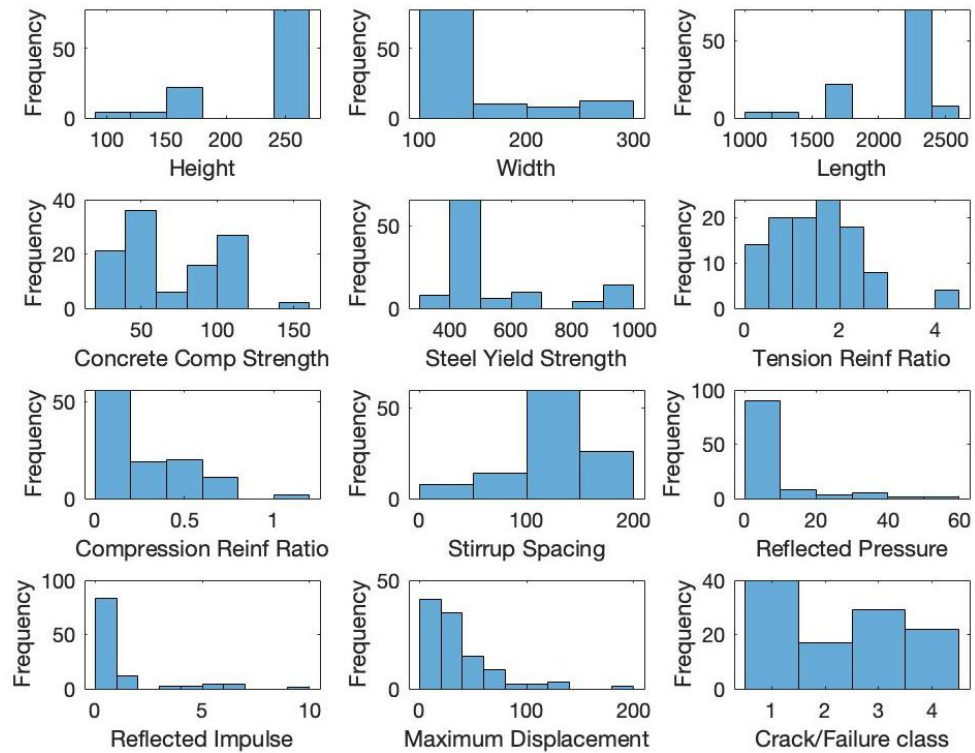


Figure 5-3. Histograms of features and output for classification dataset.

5.4 Displacement prediction model

The first model introduced in this chapter acts to produce maximum displacement predictions for blast-loaded RC beams. To conduct a detailed investigation on the effectiveness of the proposed model, various means of validation were employed. Initially, statistical performance measures were obtained by the ML model to assess the degree of correlation between actual and predicted values, as well as the overall magnitude of errors produced. Additionally, the proposed model was directly compared against several existing displacement prediction methods through output values found in the literature. Lastly, a feature importance analysis was conducted to evaluate the model's ability to capture relationships between input parameters and the predicted output.

5.4.1 Model validation through performance criteria

The optimized parameters for the number of trees, learning rate, and number of splits are 552, 0.43, and 63, respectively. Based on these values, the optimized HGBRT model for the displacement prediction model yielded a *MAE* of 5.3 ± 0.32 , R^2 of $92.1\% \pm 0.96\%$, and *VE_{cv}* of $88.1\% \pm 6.38\%$ when considering 10-fold CV. When considering LOO CV, the model produced *MAE* of 4.48 and R^2 of 93.4%. It has been reported that values for *VE_{cv}* of 50% to 80% are considered to have good accuracy, whereas values exceeding 80% signify excellent accuracy [13]. It can be observed from each measure's standard deviation that there was minimal variation among the results of each permuted instance, which strongly indicates the model's ability to generalize by providing stable results for different instances of training. The improved performance obtained through LOO CV is attributed to a larger dataset used to train the model as opposed to 10-fold CV. For both models, the correlation between the actual and predicted values with 20% error bounds are depicted in **Figs. 5-4** and **5-5** for 10-fold CV and LOO CV, respectively. It can be observed that the model expresses a strong agreement between actual and predicted values with LOO CV, reflecting improved performance measures. For further elaboration on the model's prediction capability, the average percentage of predictions within several thresholds of error bounds are provided in **Table 5-3**, which shows that nearly half of the predicted values were within a 10% error bound, with only few predictions exceeding the 30% error

bound. **Table 5-3** portrays the relatively improved performance obtained through LOO CV. As a result of these performance measures, the model demonstrated a strong aptitude for predicting maximum displacements within acceptable bounds.

**Table 5-3. Average percentage of predictions within different error bounds
respective of the dataset**

Error bound	10-fold CV	LOO CV
$\pm 5\%$	$22\% \pm 2.9\%$	26%
$\pm 10\%$	$47\% \pm 3.4\%$	50.7%
$\pm 20\%$	$71.56\% \pm 2.9\%$	78.66%
$\pm 30\%$	$86.7\% \pm 2.1\%$	93.3%

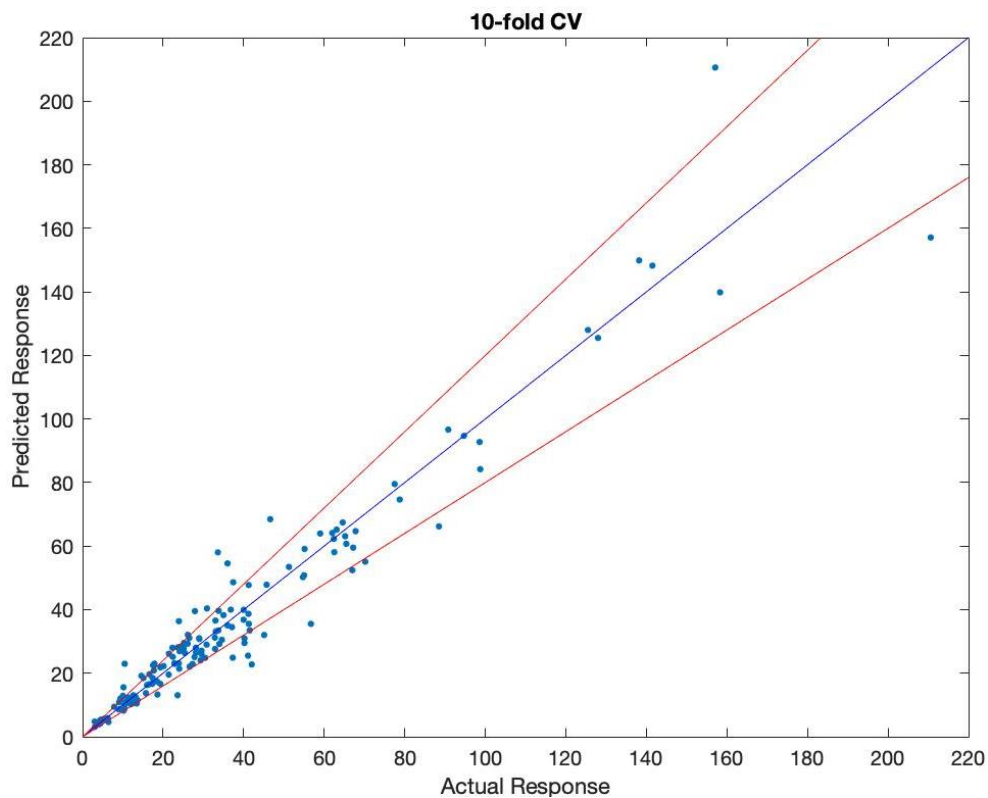


Figure 5-4. Actual versus predicted responses with a 20% error bound considering 10-fold CV.

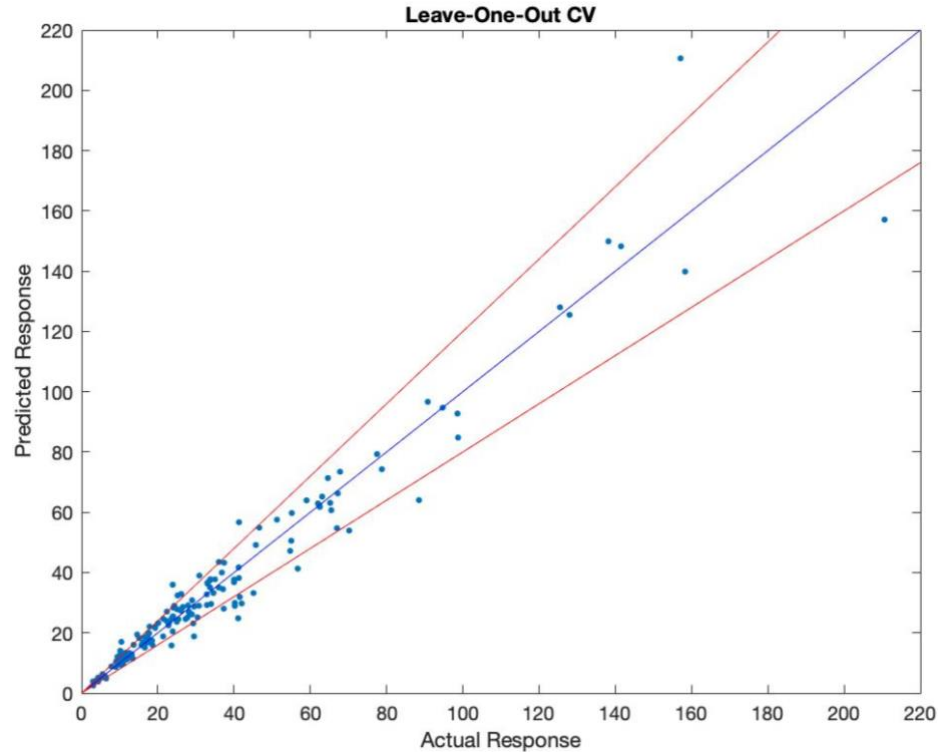


Figure 5-5. Actual versus predicted responses with a 20% error bound considering LOO CV.

5.4.2 Model validation through comparisons with existing methods

In addition to validation through model-specific performance measures, comparisons against predictions of alternative models were made to provide a more holistic evaluation of the proposed ML model. A total of 62 comparisons were made in which 48 were with analytical methods and 14 with numerical methods. The comparisons were divided into predictions for NSC beams and HSC beams, as given in **Tables 5-4** and **5-5**, respectively. Furthermore, each table provides the source, alternative model details, and errors resulting from the investigated models against experimental measurements. These comparisons not only show how well the ML model competes against existing models, but also underline its superior predictive capability for each beam type.

The different analytical models considered in this section include an equivalent SDOF model that applies an Acceleration Impulse Extrapolation Method through the program UOResistance [1] and an equivalent SDOF model that implements an Average Acceleration Numerical Integration Method using the program RCblast [26]. The two

methods for solving the equivalent SDOF equation of motion are outlined in UFC 3-340-02 [17]. An additional model used in the comparisons was the TBM, which explicitly incorporates the effects of shear deformation and rotational inertia, making it suitable for the current application [4].

Furthermore, the various numerical models considered accounted for material strain-rate effects, strain softening effects, and reinforcement bonding effects. The model used for each comparison entry is assigned in **Tables 5-4** and **5-5**, and additional information for each model can be found at their respective sources provided herein for each entry.

For displacement predictions of NSC beams in **Table 5-4**, the ML model demonstrated similar performance in a few instances (entries 1, 5, 14, 18, 21), while producing more accurate predictions in several other instances (entries 2, 4-7, 9, 10, 14-16, 18, 19, 22) when compared to analytical models. Similarly, the ML model achieved comparable accuracy to numerical methods in some instances (entries 31, 34, 37, 39), while attaining slightly less accurate results in other instances. It should be noted that most of the experimental measurements for entries 1-17 were collected from beam specimens that were subjected to repeated simulated blast loads, which has previously been reported to be a source of analytical prediction error [1-3]. Thus, it can be appropriately stated that although the ML provided mostly accurate predictions for these entries, the minor loss of accuracy for such entries can be attributed to the beams having already been subjected to loading. Additionally, the errors produced in entries 29 and 36 were inspected and found to be caused by marginal variations among features that could not completely be captured by the ML model. To clarify, the beams of entries 29 and 31 were from the same experimental study and possess identical beam and blast properties with only slightly varying stirrup spacings, which caused the model to predict the displacement of entry 29 to be similar to the prediction of entry 31. A similar discrepancy is observed in entries 27, 36, and 38 with respect to entries 26, 37, and 39. It should also be noted that entries 27, 29, 36, and 38 were not only observed to have highly similar features as beams within their respective study, but were also found to be outliers for several features. This contributed to the ML model's difficulty in distinguishing such beams and providing relatively inaccurate predictions. As a result of the displacement comparisons of models for NSC beams, the ML demonstrated

improved overall performance against several analytical models, while displaying comparable performance to some numerical models.

Likewise, **Table 5-5** presents displacement predictions for HSC beams with comparisons between alternative models and the proposed ML model. Based on these comparisons, the ML model predictions were highly capable of surpassing both analytical and numerical predictions (entries 1, 5, 7, 13, 14, 19, 22, 23), while also yielding predictions of similar accuracy (entries 3, 4, 16, 17, 21). Similar to the previously stated discrepancy, the ML model's prediction error for some instances can be attributed to the HSC beams being subjected to repeated loading. The results of these comparisons support the ML model's capability of accurately predicting maximum displacement for HSC beams.

In addition to both analytical and numerical models, the literature also includes empirical formulations for predicting the maximum displacement of blast-loaded RC beams. Upon conducting an experimental investigation on NSC beams under blast loading, Yao *et al.* [6] observed that the beam's stirrup reinforcement ratio (longitudinal cross-sectional area of stirrup steel to longitudinal cross-sectional area of the beam) highly influenced the resulting maximum displacement. In addition to experimental data, numerical models were developed to further examine the effect of the stirrup ratio. As a result, an empirical relationship to obtain the central deflection thickness ratio (δ/h) was fit using 4 experimental and 8 numerical data points as shown in Equation (6). It was reported that the relation was only suitable within the scaled distances of $0.44 \text{ m/kg}^{1/3} < Z < 0.5 \text{ m/kg}^{1/3}$ and stirrup ratios of $0.251\% < r < 1.51\%$, which adapts to 30 mm–180 mm stirrup spacing for a 125x125x1350 mm RC beams.

$$\frac{\delta}{h} = 0.064Z^{-1.717} \cdot r^{-0.75} \quad (6)$$

Table 5-4. Comparisons of ML model to alternative models for NSC beams.

Entry #	Source	Alternative model details	Experimental result (mm)	Alt. model prediction (mm)	ML model prediction (mm)	Alt. model error (%)	ML Model Error (%)
1	[1]	UOResistance	11.8	11.46	12.4	2.88	5.08
2	27.3		21.02	26.1	23	4.4	
3	10		10.5	12.62	5	26.2	

4			19.3	16.39	21.91	15.08	13.52
5			42	28.31	29.76	32.6	29.14
6			10.7	9.11	10.74	14.86	0.37
7			17.3	14.17	16.8	18.09	2.89
8			29.5	21.61	18.8	26.75	36.27
9	[2]	RCblast	12.65	14.96	12.3	18.26	2.77
10			29.53	33.12	28.7	12.16	2.81
11	[18]	RCblast	13.44	13.25	11.54	1.41	14.14
12			24.32	23.57	28.97	3.08	19.12
13			37.3	32.82	28.01	12.01	24.91
14	[19]	RCblast	11.5	13.7	13.38	19.13	16.35
15			11.6	12.3	11.18	6.03	3.62
16			22.8	25.2	22.46	10.53	1.49
17			41.5	41.7	31.9	0.48	23.13
18	[4]	TBM	28.15	29.15	26.9	3.55	4.44
19			24	29.15	25.5	21.46	6.25
20			16.02	15.9	16.68	0.75	4.12
21			15.74	15.9	15.89	1.02	0.95
22			67	62.39	54.74	6.88	18.3
23			55.14	62.39	59.76	13.15	8.38
24	[21]	SDOF using Average Acceleration Method	26.5	26.9	28.5	1.51	7.55
25			33.6	32.5	37.35	3.27	11.16
26			64.6	62.8	71.34	2.79	10.43
27			97.2	93.3	65.14	4.01	32.98
28	[6]	LS-DYNA 5mm mesh Perfect bonding	36	33	43.5	8.33	20.83
29			44	41.9	61.7	4.77	40.23
30			55	52.5	50.56	4.55	8.07
31			62	63.8	62.92	2.9	1.48
32	[27]	Autodyn 4mm mesh size Strain softening	17.5	16.5	20.07	5.71	14.69
33			17.5	16.7	20.07	4.57	14.69
34		Autodyn 4mm mesh size Bond-slip effect	17.5	14.1	20.07	19.43	14.69
35			17.5	16.3	20.07	6.86	14.69
36	[7]	Abaqus 5mm mesh size Perfect bonding	25	23.5	36.4	6	45.6
37			40	36.3	37.6	9.25	6
38	[28]	LS-DYNA 5mm mesh	9	9.83	33.3	9.2	270
39			40	44	37.6	10	6

Table 5-5. Comparisons of ML model to alternative models for HSC beams.

Entry #	Source	Alternative model details	Experimental result (mm)	Alt. model prediction (mm)	ML model prediction (mm)	Alt. model error (%)	ML Model Error (%)
1	[2]	RCblast	13.15	14.15	12.93	7.6	1.67
2			30.44	28.51	25.15	6.34	17.38
3			11.5	10.18	13.12	11.48	14.09
4			21.4	18.86	18.83	11.87	12.01
5			10.44	8.38	11.5	19.73	10.15
6			15.12	13.44	18.31	11.11	21.1
7			32.91	24.03	29.24	26.98	11.15
8	[18]	RCblast	10.17	13.46	14.06	32.35	38.25
9			22.39	25.87	27.05	15.54	20.81
10			33.78	34.85	37.75	3.17	11.75
11			9.08	9.35	10.49	2.97	15.53
12			17.72	18.46	19.88	4.18	12.19
13			10.91	8.39	10.1	23.1	7.42
14			16.59	13.21	18.5	20.37	11.51
15			26.15	20.8	32.9	20.46	25.81
16	[3]	RCblast	17.7	19.8	19.73	11.86	11.47
17			33.1	36.4	36.2	9.97	9.37
18			11.5	14.7	17.8	27.83	54.78
19			34.6	38.8	33.23	12.14	3.96
20			26.5	20.3	40.28	23.4	52
21			45.1	34.6	33.21	23.28	26.36
22	[27]	Autodyn 4mm mesh size Bond-slip effect	24.1	22.4	24.21	7.05	0.46
23			22.6	27.8	26.6	23.01	17.7

Similarly, Liu *et al.* [21] proposed an empirical expression to calculate the scaled maximum displacement ($2\delta/L$) of blast loaded NSC beams that accounts for the effect of charge mass and scaled distance using dimensional analysis. The proposed expression was fit to 4 experimental data points to obtain the relationship as shown in Equation (7), where M is the charge mass, and M_0 is taken as a benchmark of 0.4 kg. It was noted that the expression only applied to scaled distances of $0.5 \text{ m/kg}^{1/3} < Z < 0.68 \text{ m/kg}^{1/3}$ with standoff distances greater than or equal to 0.5 m.

$$\frac{2\delta}{L} = 0.01264Z^{-2.49} \cdot \left(\frac{\sqrt[3]{M}}{\sqrt[3]{M_0}}\right)^{2.56} \quad (7)$$

For both Equations (6) and (7), their respective studies have successfully validated the proficiency of the formulations within the limits of their specified range. However, the reported limiting ranges only account for a small number of application scenarios, beyond which the expressions become inaccurate. Also, the parameters that encompass the application of RC beams under blast loading exceed the ones accounted for in those empirical expressions. The following section provides a detailed analysis of the extent to which pertinent application parameters have on the response of a RC beams.

5.4.3 Model validation through feature importance

As previously stated, the displacement prediction model accounts for eleven features of the application to provide an accurate output as presented in **Table 5-1**. A feature importance analysis was conducted to evaluate the ML model's effectiveness in identifying the extent to which these input features influence the output. Furthermore, the importance estimate of input features was validated through evidence of correlations observed by experimental studies found in the literature. On account of the limitations of such studies, only the features of concrete compressive strength, steel yield strength, tension reinforcement ratio, compression reinforcement ratio, stirrup spacing, reflected pressure, and reflected impulse were considered in the current analysis.

Figure 5-6 depicts the feature importance estimates of the investigated input features. The estimates were acquired from the interaction-curvature test performed by means of the random forests algorithm as described in detail earlier. It can be observed in **Fig. 5-6** that

the two blast parameters had the highest effect on the output, followed by the steel yield strength, tension reinforcement ratio, concrete compressive strength, stirrup spacing, and compression steel reinforcement ratio. The following sections individually discuss each feature with supporting evidence from corresponding experimental correlations provided in **Tables 5-6 – 5-12**. The tables are arranged in increasing displacement order to obtain the percentage of increase and remain consistent among all comparisons. Additionally, comparisons between each two feature values were made while all other features remain constant.

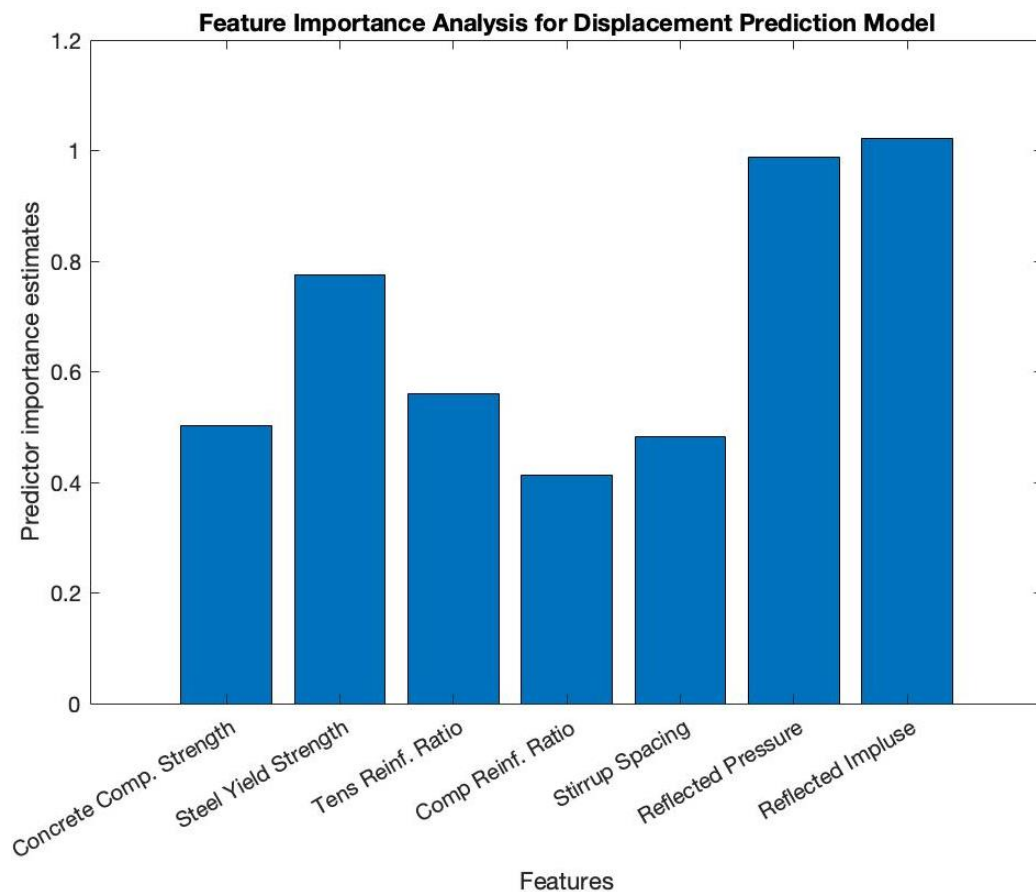


Figure 5-6. Feature importance estimates for selected features of the displacement prediction model.

5.4.3.1 Reflected pressure and reflected impulse

The two blast parameter features, i.e. reflected pressure and reflected impulse, are shown in **Fig. 5-6** to be the most significant when considering maximum displacement as the output. This observation has been widely concluded from numerous studies of both near-field and far-field blasts on RC beams [1-4, 21-23]. **Tables 5-6** and **5-7** list multiple instances of the two features from different studies, along with their corresponding maximum displacements. The percent of change in maximum displacement caused by the percent of change of each feature are also provided for each feature. It can be observed that there is a significant change in maximum displacement for relatively smaller changes in reflected pressure and impulse. Furthermore, smaller changes in both features cause a noticeably greater change in maximum displacement in near-field blasts, as shown in entry 4 in **Tables 5-6** and **5-7** compared to far-field blasts in entries 1-3. Therefore, the significance of both features on the output evidently supports the results obtained by the feature importance analysis. Moreover, when comparing the percent of change between the two features, it can be observed that a smaller change in reflected impulse is required to cause the same change in maximum displacement than the change in reflected pressure. This indicates that the resulting displacement is more sensitive to the reflected impulse than to pressure, which also strongly supports the difference in the features' importance measure depicted in **Fig. 5-7**.

5.4.3.2 Steel yield strength and concrete compressive strength

According to **Fig. 5-6**, the effect of steel yield strength on maximum displacement is observed to be greater than the effect of the concrete compressive strength. The corresponding experimental study that reflects on this comparison was conducted by Li [18] who investigated both HSC and HSR in beams subjected to simulated blast loading. **Tables 5-8** and **5-9** list the effects of both steel yield strength and concrete compressive strength on the maximum displacement. It can be interpreted that the rate of change for steel yield strength resulted in greater changes in maximum displacement when compared to the rate of change of concrete compressive strength. It was also reported from the experimental investigation [18] that the use of HSR led to significant improvement of blast

resistance and displacement reduction, whereas HSC was comparatively found to have a moderate effect [18]. A numerical investigation using LS-DYNA also found that the effect of steel yield strength was effective in improving the blast performance of HSC beams [29]. These observations corroborate the accuracy of the feature importance analysis, which deems the steel yield strength to be more influential than the concrete compressive strength.

Table 5-6. Effect of reflected pressure.

Source	Reflected Pressure (MPa)	Maximum Displacement (mm)	Change in Reflected Pressure (%)	Corr. Change in Max Disp. (%)
[1]	0.0198	10	Base	Base
	0.0353	19.3	78.3	93
	0.0515	42	160.1	320
[5]	0.68	8.7	Base	Base
	1.186	13.8	74.4	58.6
	1.907	26.6	180.4	205.7
[4]	0.077	16	Base	Base
	0.251	28.15	226	75.9
	0.348	67	351.9	318.8
[22]	23.16	9	Base	Base
	27.53	25	18.9	177.8
	40.1	40	73.1	344.4

Table 5-7. Effect of reflected impulse.

Source	Reflected Impulse (MPa msec)	Maximum Displacement (mm)	Change in Reflected Impulse (%)	Corr. Change in Max Disp. (%)
[1]	0.232	10	Base	Base
	0.354	19.3	52.6	93
	0.486	42	109.5	320
[5]	4.54	8.7	Base	Base
	6.83	13.8	50.4	58.6
	9.5	26.6	109.3	205.7
[4]	0.369	16	Base	Base
	0.558	28.15	51.2	75.9
	0.872	67	136.3	318.8
[22]	0.873	9	Base	Base
	1.05	25	20.3	177.8
	1.59	40	82.1	344.4

Table 5-8. Effect of steel yield strength.

Source	Steel yield strength (MPa)	Maximum Displacement (mm)	Change in Steel yield strength (%)	Corr. Change in Max Disp. (%)
[18] (a)	904	24.32	Base	Base
	449	29.53	50.3	21.4
[18] (b)	904	37.2	Base	Base
	449	47.96	50.3	28.9
[18] (c)	904	10.17	Base	Base
	449	13.15	50.3	29.3
[18] (d)	904	22.39	Base	Base
	449	30.44	50.3	36
[18] (e)	904	33.78	Base	Base
	449	44.53	50.3	31.8
[18] (f)	929	17.72	Base	Base
	471	21.4	49.3	20.8
[18] (g)	855	26.15	Base	Base
	460	32.19	46.2	23.1

Table 5-9. Effect of concrete compressive strength.

Source	Concrete Compressive Strength (MPa)	Maximum Displacement (mm)	Change in Concrete Compressive Strength (%)	Corr. Change in Max Disp. (%)
[18] (a)	96	10.17	Base	Base
	62	13.44	35.4	32.2
[18] (b)	96	22.39	Base	Base
	62	24.32	35.4	8.6
[18] (c)	96	33.78	Base	Base
	62	37.3	35.4	10.4
[18] (d)	96	52.74	Base	Base
	62	64.52	35.4	22.3

Additionally, a more detailed evaluation was made to further explain and support the high importance of steel yield strength depicted in **Fig. 5-6** and was expressed through material dynamic increase factors (DIF). A DIF for a material is used to identify its increased dynamic strength caused by high-rate loading such as blast or impact loads relative to the materials static strength [1-3]. In a sensitivity analysis conducted by Li [18] to investigate the discrepancy of SDOF model predictions for blast-loaded RC beams, various DIF for concrete and steel were analyzed. It was found that minor variations in the DIF of steel yield strength resulted in significant changes of analytical predictions when compared to the effect of variations caused by different DIF for concrete compressive strength. Thus, it was reported that the analytical predictions were more sensitive to the DIF of steel than to the DIF of concrete. In relation to the current ML model, the sensitive variations of DIF in steel yield strengths for various data points of both near-field and far-field blast loading rates for a range of different steel yield strengths were implicitly captured by the model as reflected through its high feature importance shown in **Fig. 5-6**. Moreover, the relatively less influential effect of concrete DIF was also implicitly obtained and portrayed through its corresponding importance estimate. Additional details on the model's implicit learning of the application is discussed in a subsequent section in this chapter. Overall, the experimental results describing the effect of both the steel yield strength and concrete compressive strength show a good relationship with the results of the feature importance analysis.

5.4.3.3 Tension and compression reinforcement ratios

As shown in **Fig. 5-6**, the model recognizes the tension reinforcement ratio to have a relatively high effect on maximum displacement, while having a greater influence than the compression reinforcement ratio. **Tables 5-10** and **5-11** provide the effects of both the tension and compression reinforcement ratios on the maximum displacement taken from their respective sources. It can be observed in **Table 5-10** that the tension reinforcement ratio has a considerably greater effect on the maximum displacement at smaller ratios, while having a seemingly minor effect at larger ratios. Accordingly, the feature of tension reinforcement ratio was found to have less effect than the steel yield strength as shown in **Table 5-8**. However, the rate of change of the tension reinforcement ratio still resulted in

higher corresponding changes in the maximum displacement than for the concrete compressive strength, as shown in **Table 5-9**. These experimental correlations agree with the ML model feature importance estimates for the tension reinforcement ratio with respect to the previously evaluated features. Furthermore, **Fig. 5-6** indicates that the feature of compression reinforcement ratio is the least influential when compared to all other features.

A similar observation may be inferred in **Table 5-11**, which depicts minor changes in maximum displacement for moderate changes in the feature, while also presenting the lowest changes in maximum displacement when compared to **Tables 5-6** to **5-9**. Therefore, it can be concluded that the feature importance of both tension and compression reinforcement ratios agree with experimental correlations.

Table 5-10. Effect of tension reinforcement ratio.

Source	Tension Reinf. Ratio (%)	Maximum Displacement (mm)	Change in Tension Reinf. Ratio (%)	Corr. Change in Max Disp. (%)
[1]	2.4	17.34	Base	Base
	1.5	19.32	37.5	11.4
	1	27.39	58.3	58
[2]	2.4	15.12	Base	Base
	1.5	21.4	37.5	41.5
	1	30.44	58.3	101.3
[18] (a)	2.4	16.59	Base	Base
	1.5	17.72	37.5	6.8
	1	22.39	58.3	35
[18] (b)	2.4	26.15	Base	Base
	1.5	26.77	37.5	2.4
	1	52.74	58.3	101.7
[5]	2.5	18.6	Base	Base
	1.12	22.9	55.2	23.1

Table 5-11. Effect of compression reinforcement ratio.

Source	Compression Reinf. Ratio (%)	Maximum Displacement (mm)	Change in Compression Reinf. Ratio (%)	Corr. Change in Max Disp. (%)
[3] (a)	0.8	12.1	Base	Base
	0.25	10.6	68.8	12.4
[3] (b)	0.8	37.4	Base	Base
	0.25	40.1	68.8	7.2

5.4.3.4 Stirrup spacing

Likewise, **Fig. 5-6** indicates moderate importance for the feature of stirrup spacing, while being comparable to the importance of concrete compressive strength. **Table 5-12** lists multiple experimental cases that consider both the effect of transverse reinforcement and varying the stirrup spacing. When compared to the change in maximum displacement caused by changing the tension reinforcement ratio in **Table 5-10**, the effect of changing stirrup spacings produces smaller changes in maximum displacement. This correlation agrees with the importance estimates of both features given in **Fig. 5-6**.

Table 5-12. Effect of stirrup spacing.

Source	Stirrup Spacing (mm)	Maximum Displacement (mm)	Change in Stirrup Spacing (%)	Corr. Change in Max Disp. (%)
[2] (a)	100	10.44	Base	Base
	None	12.55	-	20.2
[2] (b)	100	15.12	Base	Base
	None	19.31	-	27.7
[20] (a)	125	7.67	Base	Base
	None	9.03	-	17.7
[20] (b)	125	12.05	Base	Base
	None	17.85	-	48.1
[4]	125	55.14	Base	Base
	200	67	60	21.5
[6] (a)	60	36	Base	Base
	120	55	100	52.8
[6] (b)	60	44	Base	Base
	120	62	100	40.9

5.5 Failure mode and cracking pattern classification model

The second model introduced in this chapter was developed to classify crack patterns and failure modes of RC beams subjected to blast loading. The development of this model was based on classification RF, as opposed to the hybrid GBRT of the previous model. As previously mentioned, the classification model is tailored to distinguish between beams that have resulted in flexural crack formation, flexural-shear crack formation, bending failure, or crushing failure. This model also accounts for the maximum displacement of the beam as an input feature and may be considered an extension of the displacement prediction model. Similar to the displacement prediction model, the classification model was evaluated through several performance measures to assess both its strengths and weaknesses. A feature importance analysis was conducted to identify the most and least influential factors affecting the output. Limited experimental findings were further used to support and validate the model's evaluation of each input feature's significance.

5.5.1 Model validation through performance criteria

To conduct an in-depth evaluation of the classification model, a multi-class classification confusion matrix was developed through which measures of accuracy, precision, and recall were extracted, as shown in **Fig. 5-7**. A confusion matrix is a visual representation for the number of correctly predicted classes given by the matrix diagonal, and the class allocation of misclassified predictions [15]. The matrix was first assessed as a binary classifier in which the two classes for crack formation and two classes for failure modes were viewed as two distinct groups. The extracted accuracy for the binary classification should display the model's ability to classify whether a blast-loaded RC beam was within a state of cracking or has reached failure. The binary accuracy was computed as the sum of correctly classified outputs and incorrectly classified outputs, which were still within the same group (such as flexural cracks incorrectly classified as flexural shear cracks or bending failure incorrectly classified as crushing failure, and vice versa) over the total number of predictions. Afterwards, the multi-class classification accuracy was computed as the sum of correctly classified predictions, being the diagonal of the confusion matrix over the total number of predictions and expresses the model's ability to correctly classify the output as

one of the four classes. The resulting binary and multi-class classification accuracies were found to be $93.1\% \pm 0.6\%$ and $83.74\% \pm 0.9\%$, respectively.

		Predicted Class			
		Flexural Cracking	Bending Failure	Flexural-Shear Cracking	Crushing Failure
True Class	Flexural Cracking	34.14 ± 0.7	1.63 ± 0.48	3.23 ± 0.53	1 ± 0
	Bending Failure	1.01 ± 0.1	13.28 ± 0.47	0 ± 0	2.71 ± 0.45
	Flexural-Shear Cracking	2.17 ± 0.38	0 ± 0	25.83 ± 0.38	1 ± 0
	Crushing Failure	1 ± 0	2 ± 0	1.81 ± 0.39	17.19 ± 0.39

Figure 5-7. Multi-class confusion matrix for classification model.

In order to evaluate the classification capability for each class, the precision and recall for the four classes were computed using Equations (4) and (5), along with **Fig. 5-1** as a guide for each class. The precision for a class expresses the percentage of predictions for a given class belonging to its true class. For instance, the average total number of predictions for the class of flexural cracking was 38.32 ($34.14+1.01+2.17+1$) where 34.14 predictions belonged to its true class producing a precision of 89.1% for the class. Similarly, a class recall reports the percentage of correct class predictions with respect to the total items within the class. For example, an average of 34.14 correct predictions were made for the class of flexural cracking with respect to 40 true class items from the dataset, resulting in a recall of 85.35%. The precision and recall for each class, as well as for the overall model, are given in **Table 5-13**. It can be observed that the precision of the two crack formation

classes was higher than that of the two failure mode classes, with the class of flexural cracking exhibiting the highest precision. Similarly, the recall of the two crack formation classes was higher than the two failure mode classes, yet with the highest recall exhibited by the class of flexural-shear cracking. These comparisons indicate that the model was proficient in yielding correct predictions for the classes of crack formation, while having moderate capability in failure mode class predictions. Furthermore, **Fig. 5-7** shows that for all four classes, the majority of predictions that were not assigned to its true class were instead assigned to the alternative class of the same group, such that crack formation predictions remained in true crack formation classes and failure mode predictions remained in true failure mode classes. This observation supports the notion that the model exhibited an effective understanding of the application.

Table 5-13. Precision and recall for each class and overall model.

Class	Precision	Recall
Flexural Cracking	89.1% ± 1.82%	85.35% ± 1.75%
Bending Failure	78.5% ± 2.78%	78.1% ± 2.76%
Flexural-Shear Cracking	83.7% ± 1.23%	89.1 ± 1.31%
Crushing Failure	78.5% ± 1.78%	78.14% ± 1.77%
Overall Model	82.45% ± 1.9%	82.65% ± 1.9%

Similar to the displacement prediction model, a source of classification error resulted from RC beams that had undergone repeated loading. Such RC beams resulted in failure modes or crack patterns that were influenced by the plastic deformations incurred in previous simulated blasts. This form of discrepancy resulted in misclassification between the classes of flexural cracking and flexural-shear cracking. Additionally, a second source of prediction error was observed by a few RC beams that were subjected to near-field blasts of very low scaled distances, which caused misclassifications between the classes of flexural cracking and bending failure. Based on these two primary forms of classification discrepancies, an average of 17.56 incorrect predictions were observed from a total of 108

predictions. Overall, the classification model achieved good performance for predicting different crack and failure scenarios, while displaying limited misclassifications but within a shared response group.

5.5.1.1 Model validation through feature importance

A similar feature importance analysis was conducted on the classification model, which implemented the interaction-curvature test to obtain feature importance estimates. Unlike the continuous output of maximum displacement whose variations can be quantitatively discerned based on variations of input features, the effect of input features on the discrete outputs of crack formations and failure modes were only supported through qualitative experimental observations. The features considered for the importance analysis of the classification model were the same as those in the previous importance analysis and their estimates are provided in **Fig. 5-8**. It can be observed that the features of reflected pressure and reflected impulse had the highest influence on the discrete output. A similar observation was made in **Fig. 5-6**, which also deemed the features of blast parameters to have the highest effect on the maximum displacement model output. Furthermore, several experimental studies using far-field simulated blasts demonstrated clear variations in crack patterns and failure modes for varying blast parameters. Such variations were based on a variety of RC beams having NSC, HSC, NSR, and HSR [1-3,18]. Similar findings were obtained from near-field blasts of NSC beams in which failure modes were majorly affected by variations in the scaled distance, which correlates directly to reflected pressure and impulse [4]. Thus, the high feature importance estimate of the two blast parameters was strongly supported by a wide range of corresponding experimental outcomes. Moreover, the feature of tension reinforcement ratio was observed to greatly influence the resulting crack formation or failure mode of RC beams, as shown in **Fig. 5-8**. This was strongly corroborated by experimental studies in which varying the tension reinforcement ratio produced different RC beam responses under a range of far-field simulated blasts [1, 2, 18]. It was also reported that the effect of tension reinforcement was a primary factor for changes in the failure mode of NSC and HSC subjected to explosive materials [5].

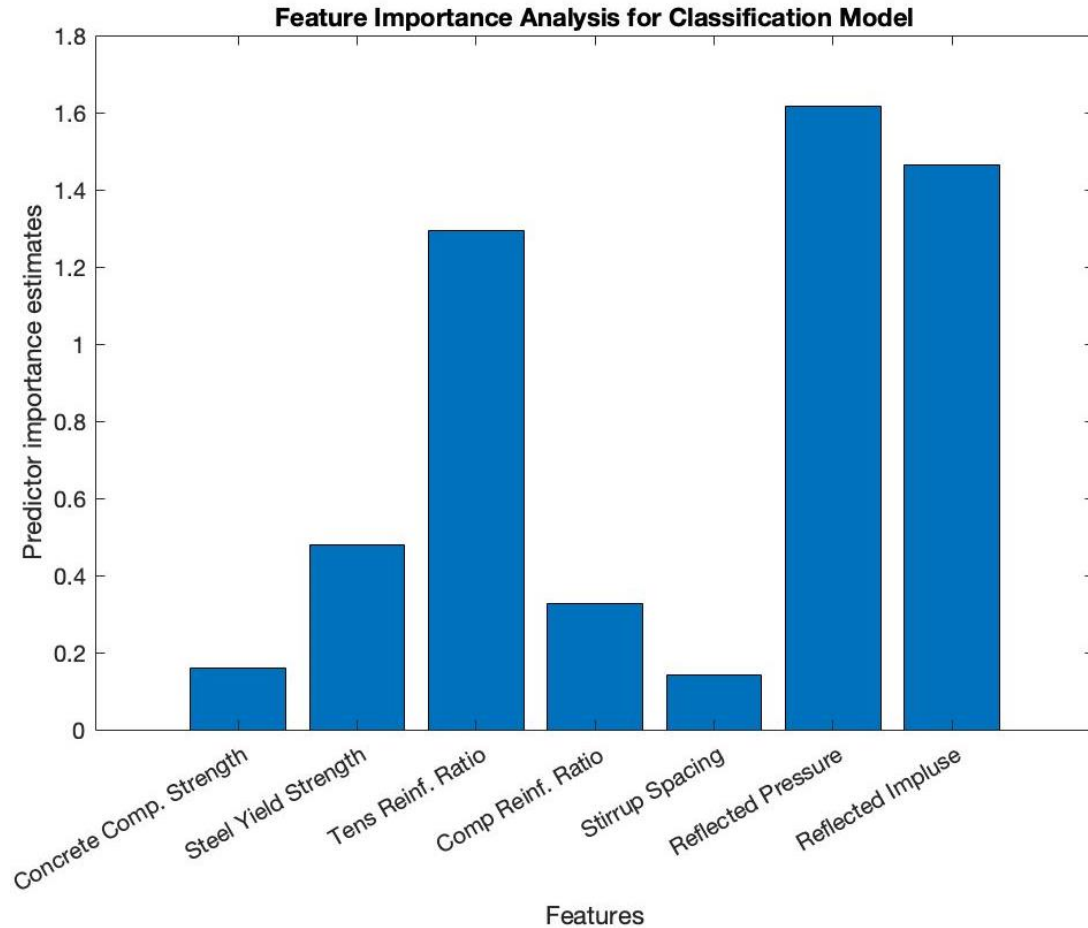


Figure 5-8. Feature importance estimates for selected features of the classification model.

Figure 5-8 further depicts that the features of steel yield strength and compression reinforcement ratio had limited influence on the output. The reduced effect of both features was apparent in corresponding experimental observations [3,18]. Under far-field simulated blasts, the effect of changing the steel yield strength produced changes in the output for larger tension reinforcement ratios and higher magnitudes of blast loading. However, at lower ratios of reinforcement and magnitudes of loading, the effect of steel yield strength attained insignificant changes in the output [18]. A similar trend was observed for the effect of compressive steel ratio, in which output variations were only reported at larger blast magnitudes, whereas no changes were recorded at lower magnitudes [3]. The limitations to the effect of both features reported from experiments correlate to their relatively low importance estimate.

The least influential features in **Fig. 5-8** are the concrete compressive strength and stirrup spacing. According to studies of both simulated and actual far-field blast loading, the effect of varying the concrete compressive strength achieved almost no change in the crack formation or failure mode of RC beams [2, 5, 18]. Moreover, the insignificant effect of stirrup spacing on the discrete outputs was demonstrated in studies of both far-field and near-field blasts [3,4]. Therefore, it can be concluded that the trivial estimates provided by the analysis correctly coincide with corresponding experimental results. For the seven features evaluated in **Fig. 5-8**, accurate correlations were investigated from existing studies, which evidently support the feature importance analysis conducted for the classification model. Overall, the thorough validation of the model both via performance measures and feature importance adequately delineate its predictive capability as well as its understanding of the application.

5.6 Implicit feature learning and elimination of modeling complexities

The two proposed models of displacement prediction and crack and failure classification demonstrated highly acceptable predictive capability for such a complex application of blast-loaded RC beams. In addition to measuring performances and identifying pertinent relationships, the extent to which the models implicitly learn features of the application was further investigated. The simplicity of the proposed models was reflected through the effect of the implicitly learned variations within the application. The models' implicit learning was expressed through material dynamic increase factors and constitutive material models as discussed in the subsequent sections.

5.6.1 Dynamic increase factors

The dynamic material properties of structural elements are greater than their static values when subjected to high strain rate, such as explosive or impact loading [1]. Thus, DIFs are applied to account for material strength improvements and are obtained through empirical methods. Guidelines such as the UFC-3-340-02 [17], CEB-FIP Code Model [30], and Saatcioglu *et al.* [31] provide DIF relationships for both concrete compressive strength and

steel yield strength (i.e. NSC and NSR). Additionally, a recent study was conducted to obtain DIF values for HSC [32]. To evaluate the discrepancy among the available DIF models for both concrete compressive strength and steel yield strength, several sensitivity analyses were conducted through analytical SDOF computations for RC beams [1,3,18]. The resulting variations for different combinations of material DIF models were assessed through the average ratio of predicted to actual displacements. When considering three separate combinations of DIFs varying in both steel and concrete, displacement ratios of 0.82, 0.86, and 0.99 were produced [1]. Furthermore, displacement ratios of 0.988, 1.007, and 1.01 were obtained from three different DIFs for concrete compressive strength, whereas displacement ratios of 0.988, 1.039, and 1.063 resulted when considering three DIFs for steel yield strength [18]. The presented variations in prediction accuracy for different DIF models of the same material demonstrate the influence of the feature for this application.

In the proposed ML displacement prediction model, the concrete compressive strength and steel yield strength were taken as their static values and presented in **Table 5-1**. However, when an attempt was made to develop the model using dynamic values, which accounted for material DIFs, the resulting performance metrics of *MAE*, *VE_{cv}*, and *R²* remained practically unchanged. This led to the conclusion that the model implicitly accounted for variations within the features of concrete compressive strength and steel yield strength. More specifically, the model identified differences among the effects of individual values through which the variations within the feature were implicitly learned. Moreover, this observation encourages simplicity of modeling in two ways. First, assessing multiple DIF models for different materials becomes irrelevant to the modeling process, and second, estimating material strain-rate values used in empirical formulations for DIFs would no longer be required. As a result, the ML model demonstrates ease of modeling without compromising accuracy and predictive capability.

5.6.2 Constitutive material models

Another aspect that is integrated into both analytical and numerical modeling methods is the use of constitutive material models. Minor variabilities in the structural response of numerical models due to different material models of blast-loaded RC elements have been

reported in the literature. Using LS-DYNA, Thiagarajan *et al.* [33] evaluated two different concrete models, the Winfrith Concrete Model (WCM) and the Concrete Damage Model Release 3 (CDMR3), on reinforced HSC and NSC slabs subjected to near-field blast loading. When compared to four experimental values of maximum displacement, the numerical model produced average errors of 12.8% using WCM and 37% using CDMR3, considering a 12.5 mm mesh size. Additional concrete material models that have been considered in modeling blast-loaded RC elements include the Continuous Surface Cap Model [24], the Brittle Damage Model [34], and the RHT Concrete Model [25, 27]. Similarly, the development of analytical SDOF models also require the definition of material models based on previously developed stress-strain models. The different concrete models used in previous studies [1-3, 18] include the Hognestad Model [35] for NSC, and the Popovics [36], Cusson and Paultre [37], and Mander *et al.* [38] models for HSC. As opposed to previous methods, the current ML models extract the relationships between the values of material properties without explicitly pre-defining the material's behavior. Although the use of different material models produced minimal discrepancy in both numerical and analytical methods, the elimination of this modeling component further supports the proposed approach in mitigating complexity for this application.

5.6.3 Practical implementation

The proposed ML models not only reduce the intricacies of modeling the application, but also present an ease of usage during execution. By inputting the desired element parameters and blast loading magnitudes, results of maximum displacement and crack patterns or failure modes are produced immediately. Previous sections have elaborated on the high accuracy of such instant results, which make the proposed models reliable for preliminary assessment. Furthermore, the datasets used to develop the present models are expansive in considerations, which account for both NSC and HSC beams reinforced with NSR or HSR. By implementing the proposed models in the preliminary iterative design process, results that satisfy blast design guidelines provided by ASCE 59-11 [39] and CSA S850-12 [40] may be obtained. These guidelines relate allowable rotation limits to the state of element damage in which a flexural element with a maximum support rotation of 2° remains in a repairable state, whereas a rotation limit of 6° would prevent element failure.

5.7 Conclusions

In order to develop a simplified model for the structural response of RC beams under blast loading, a hybrid machine learning model was developed to predict peak displacements. This model was developed using 150 data points from pertinent studies in the literature. It was evaluated using various performance measures, competitiveness with respect to existing numerical and analytical methods, and ability to capture relationships between input features and the output. Both NSC and HSC beams reinforced with NSR or HSR were considered in the model development. Furthermore, a classification model was developed to predict the post-blast crack pattern or failure mode of RC beams. The classification model was validated through a multi-class confusion matrix from which measures of accuracy, recall, and precision were extracted. It was also assessed via feature importance analysis, which correlated to qualitative experimental findings. The proposed models displayed favorable predictive capabilities and a constructive understanding of the application. The findings of this chapter further support the value of ML in advanced civil engineering applications to assist in paving the path for future innovation and automation. Based on this work, the following conclusions can be drawn:

- The use of the hybrid GBRT and classification RF models proved to be highly effective in modeling moderate sized datasets of a complex application.
- The displacement prediction model displayed a strong aptitude for peak displacement predictions with performance measures of $MAE = 4.56$, an $R^2 = 94.36\%$, and $VE_{cv} = 90.65\%$ using 10-fold CV, and $MAE = 4.24$ and $R^2 = 95.15\%$ using LOO CV.
- When compared to widely used analytical and numerical models, the displacement prediction model proved to be highly competitive, with minor discrepancies identified for future improvements.
- The feature importance analysis deemed the features of reflected impulse, reflected pressure, steel yield strength, and tension reinforcement ratio to have the highest

influence on peak displacement, which was corroborated by existing experimental studies.

- The classification model was proficient in classifying whether post-blast RC beams were in a state of cracking or failure, with a binary classification accuracy of 93.1%.
- The multi-class classification for identifying more detailed crack patterns and failure modes produced an acceptable accuracy of 83.74%, while yielding similar average model precision and recall values of 82.45% and 82.65%, respectively.
- For the classification model, the feature importance analysis was strongly supported by experimental findings. It was found that the features of reflected impulse, reflected pressure, and tension reinforcement ratio have the greatest effect on the discrete outputs, whereas the features of stirrup spacing and concrete compressive strength resulted in the least effect.
- Both models were found to implicitly account for material DIF, which highlights simultaneous sophistication and simplicity of the proposed models.
- Similarly, both models permitted the mitigation of modeling complexity by eliminating the explicit consideration of both material DIF and constitutive material models.

5.8 Chapter references

- [1] Guertin-Normoyle, C. (2018). *Blast Performance of Ultra-High-Performance Concrete Beams Tested Under Shock-Tube Induced Loads* (Master's thesis, Université d'Ottawa/University of Ottawa).
- [2] Algasse, O. (2016). *Parameters Affecting the Blast Performance of High Strength Fibre Reinforced Concrete Beams* (Doctoral dissertation, Université d'Ottawa/University of Ottawa).
- [3] Charles, C. J. (2019). *Effects of Detailing and Fibers on the Static and Blast Behaviour of High-Strength Concrete Beams*(Master's thesis, Université d'Ottawa/University of Ottawa).
- [4] Nassr, A. A., Razaqpur, A. G., & Campidelli, M. (2017). Effect of initial blast response on RC beams failure modes. *Nuclear Engineering and Design*, 320, 437-451.

- [5] Magnusson J and Hansson H .(2000). High Performance Concrete Beams Subjected to Shock Waves from Air Blast. Swedish Defense Research Agency (FOI), Tumba, FOA-R--OO-01586-311-SE.
- [6] Yao, S. J., Zhang, D., Lu, F. Y., Wang, W., & Chen, X. G. (2016). Damage features and dynamic response of RC beams under blast. *Engineering Failure Analysis*, 62, 103-111.
- [7] Temsah, Y., Jahami, A., Khatib, J., & Sonebi, M. (2018). Numerical analysis of a reinforced concrete beam under blast loading. In *MATEC Web of Conferences* (Vol. 149, p. 02063). EDP Sciences.
- [8] Almustafa, M. K., & Nehdi, M. L. (2020). Machine learning model for predicting structural response of RC slabs exposed to blast loading. *Engineering Structures*, 221, 111109.
- [9] Friedman, J. H. (2001). Greedy function approximation: a gradient boosting machine. *Annals of statistics*, 1189-1232.
- [10] Hashim, F. A., Houssein, E. H., Mabrouk, M. S., Al-Atabany, W., & Mirjalili, S. (2019). Henry gas solubility optimization: A novel physics-based algorithm. *Future Generation Computer Systems*, 101, 646-667.
- [11] Breiman, L. (2001). Random forests. *Machine learning*, 45(1), 5-32.
- [12] Loh, W. Y. (2002). Regression tress with unbiased variable selection and interaction detection. *Statistica sinica*, 361-386.
- [13] Li, J. (2016). Assessing spatial predictive models in the environmental sciences: Accuracy measures, data variation and variance explained. *Environmental Modelling & Software*, 80, 1-8.
- [14] Sokolova, M., & Lapalme, G. (2009). A systematic analysis of performance measures for classification tasks. *Information processing & management*, 45(4), 427-437.
- [15] Tharwat A. Classification assessment methods, *Applied Computing and Informatics*. 2018 [Online]. Available: <https://doi.org/10.1016/j.aci.2018.08.003>.
- [16] García, V., Mollineda, R. A., & Sanchez, J. S. (2010, August). Theoretical analysis of a performance measure for imbalanced data. In *2010 20th International Conference on Pattern Recognition* (pp. 617-620). IEEE.
- [17] USA Department of Defense. Structures to Resist the Effect of Accidental Explosions - Unified Facilities Criteria (UFC) 3-340-02. Department of Defense; 2008.

- [18] Li, Y. (2016). *Blast Performance of Reinforced Concrete Beams Constructed with High-Strength Concrete and High-Strength Reinforcement* (Master's thesis, University of Ottawa).
- [19] Castonguay, S. (2017). *Performance of Steel Fiber-Reinforced Concrete Beams Under Shock Tube Induced Blast Loading* (Master's thesis, Université d'Ottawa/University of Ottawa).
- [20] Lee, J. Y., Shin, H. O., Yoo, D. Y., & Yoon, Y. S. (2018). Structural response of steel-fiber-reinforced concrete beams under various loading rates. *Engineering Structures*, 156, 271-283.
- [21] Liu, Y., Yan, J. B., & Huang, F. L. (2018). Behavior of reinforced concrete beams and columns subjected to blast loading. *Defence Technology*, 14(5), 550-559.
- [22] Zhang, D., Yao, S., Lu, F., Chen, X., Lin, G., Wang, W., & Lin, Y. (2013). Experimental study on scaling of RC beams under close-in blast loading. *Engineering Failure Analysis*, 33, 497-504.
- [23] Zhang, X. H., Wu, Y. Y., & Wang, J. (2011). Numerical Simulation for Failure Modes of Reinforced Concrete Beams under Blast Loading. In *Advanced Materials Research* (Vol. 163, pp. 1359-1363). Trans Tech Publications Ltd.
- [24] Kyei, C., & Braimah, A. (2017). Effects of transverse reinforcement spacing on the response of reinforced concrete columns subjected to blast loading. *Engineering Structures*, 142, 148-164.
- [25] Abladey, L., & Braimah, A. (2014). Near-field explosion effects on the behaviour of reinforced concrete columns: a numerical investigation. *International Journal of Protective Structures*, 5(4), 475-499.
- [26] Jacques, E., Lloyd, A., & Saatcioglu, M. (2013). Predicting reinforced concrete response to blast loads. *Canadian Journal of Civil Engineering*, 40(5), 427-444.
- [27] Magnusson, J., Ansell, A., & Hansson, H. (2010). Air-blast-loaded, high-strength concrete beams. Part II: Numerical non-linear analysis. *Magazine of Concrete Research*, 62(4), 235-242.
- [28] Zhang, C., Gholipour, G., & Mousavi, A. A. (2019). Nonlinear dynamic behavior of simply-supported RC beams subjected to combined impact-blast loading. *Engineering Structures*, 181, 124-142.
- [29] Liao, Z., Li, Z. Z., Xue, Y. L., Shao, L. Z., Yang, D. P., & Tang, D. G. (2020). Study on Anti-Explosion Behavior of High-Strength Reinforced Concrete Beam Under Blast Loading. *Strength of Materials*, 1-13.

- [30] Comité euro-international du béton, & Fédération Internationale de la Précontrainte. (1993). CEB-FIP model code 1990: Design code (Vol. 1993). Thomas Telford Publishing.
- [31] Saatcioglu, M., Lloyd, A., Jaques, E., Braimah, A., & Doudak, G. (2011). Focused Research For Development of a CSA Standard on Design and Assessment of Buildings Subjected to Blast Loads. Ottawa: University of Ottawa; Hazard, Mitigation and Disaster Management Research Centre.
- [32] Guo, Y. B., Gao, G. F., Jing, L., & Shim, V. P. W. (2017). Response of high-strength concrete to dynamic compressive loading. *International Journal of Impact Engineering*, 108, 114-135.
- [33] Thiagarajan, G., Kadambi, A. V., Robert, S., & Johnson, C. F. (2015). Experimental and finite element analysis of doubly reinforced concrete slabs subjected to blast loads. *International Journal of Impact Engineering*, 75, 162-173.
- [34] Morales-Alonso, G., Cendón, D. A., Gálvez, F., Erice, B., & Sánchez-Gálvez, V. (2011). Blast response analysis of reinforced concrete slabs: experimental procedure and numerical simulation. *Journal of applied mechanics*, 78(5).
- [35] Hognestad, E. (1951). Study of combined bending and axial load in reinforced concrete members. University of Illinois - Engineering Experiment Station - Bulletin Series, Bul. 399, 128p.
- [36] Popovics, S. 1973. A numerical approach to the complete stress-strain curve of concrete. *Cement and Concrete Research*, 3(5): 583-599.
- [37] Cusson, D., & Paultre, P. (1995). Stress-strain model for confined high-strength concrete. *Journal of Structural Engineering*, 121(3), 468-477. doi:10.1061/(ASCE)0733-9445(1995)121:3(468)
- [38] Mander, J.B., Priestley, M.J., and Park, R. 1988. Theoretical stress-strain model for confined concrete. *Journal of structural engineering*, 114(8): 1804-1826.
- [39] ASCE. (2011). Blast protection of buildings: ASCE/SEI 59-11.
- [40] Canadian Standards Association. (2012). Design and assessment of buildings subjected to blast loads, CSA S850-12.

Chapter 6

6 Machine learning prediction for structural response of FRP retrofitted RC slabs subjected to blast loading

6.1 Introduction and background

Devastating events such as the August 4, 2020 explosion in Beirut, which killed more than 200 people, injured over 6500, and made another 300,000 homeless is a dreadful warning that civil infrastructure assets are vulnerable to accidental and deliberate blast loadings and explosion scenarios by stored chemicals, gas leaks, fuel tanks, and other material detonations. Thus, the requirement for protecting vulnerable structures carries paramount importance. Among the limited techniques of improving the resistance of reinforced concrete (RC) structures against blast loading, the use of fiber reinforced polymer (FRP) retrofits produces favorable results. Several experimental studies have demonstrated that FRP retrofits improved flexural capacity, increased strength and stiffness, reduced maximum displacements, and reduced steel reinforcement strains [1-4]. Furthermore, the presence of FRP retrofits acted to confine harmful fragments and debris resulting from blast loaded elements [4].

In order to model FRP retrofitted RC structures subjected to blast loading, both analytical and numerical models have previously been deployed. Jacques [1] conducted an extensive experimental study on RC slabs retrofitted with carbon fiber-reinforced polymer (CFRP) using a Shock Tube Testing Facility. A total of 13 different specimens exposed to sixty simulated explosions were investigated considering one-way and two-way elements, simple and fixed boundary conditions, and different fiber layout schemes. Additionally, the experimental data was used to validate an analytical single-degree-of-freedom (SDOF) method to predict the maximum displacement which resulted in a mean absolute error (*MAE*) of 9.93 and R^2 value of 86.5% based on 57 data points.

Likewise, Tolba [2] subjected eighteen two-way RC slabs, five being un-retrofitted control slabs and thirteen being retrofitted with either glass fiber-reinforced polymer (GFRP) or CFRP to 33.4 kg and 22.4 kg charges of ANFO (Ammonium Nitrate Fuel Oil). An analytical SDOF model was used to simulate the experimental program and the results of the maximum displacement for four slabs were compared with analytical results producing errors of 11.9%-40%. Similarly, Maazoun *et al* [3] investigated the blast response of one-way RC slabs retrofitted with varying numbers of CFRP strips. A total of five slabs were loaded via an explosive driven shock tube (EDST) with a detonation resulting from 40 g of C4. Analysis based on the SDOF method was done to predict the maximum displacement of each specimen and comparisons were made to the experimental results with errors ranging from 5% to 14% for retrofitted slabs.

In addition to using analytical approaches for predicting maximum displacements of FRP retrofitted RC slabs, some numerical approaches have also been implemented. For instance, Lin and Zhang [5] used the finite element modeling (FEM) software LS-DYNA to investigate the efficiency of retrofitting RC slabs with GFRP against blast loading. The numerical model was validated on two experimental data points which used GFRP retrofits, resulting in maximum displacement errors of 0.8% and 14.8%. The numerical model was further used to conduct a parametric study on GFRP retrofitted slabs considering factors such as top and bottom FRP layer thickness, standoff distance, and charge weight.

In another numerical study of FRP retrofits of RC slabs exposed to blast loading, Tanapornraweekit *et al.* [6] considered the effects of two different concrete material models, MAT 72R3 and MAT84, while exploring numerical models with and without strain rate effects using LS-DYNA. The developed model was used to study the behavior of GFRP and CFRP reinforced slabs subjected to two independent and consecutive blast loads. Numerical model predictions were compared to experimental data and the resulting differences in maximum displacement ranged from 2.6% to 44.5% considering six comparisons of slabs subjected to single blast before being loaded a second time. In a study by Nam *et al.* [7], a numerical model was developed using LS-DYNA for GFRP retrofitted RC slabs exposed to blast loading considering high strain-rate dependency as well as debonding failure. An existing experimental data point was used to validate the model

through maximum displacements as well as material strains for a GFRP retrofitted slab. The resulting difference in maximum displacement between numerical model and experimental data was 7.2%.

Using robust analyses for modelling the response of FRP retrofitted RC elements subjected to blast loading provides a unique opportunity to replace costly and hazardous structural blast experiments [7]. Currently, both analytical and numerical approaches have been used to model structures under blast loading. Although these approaches mitigate the associated cost and safety aspects of experimental blast loading, they require considerable theoretical competence, modelling effort, computational time, and continuous validation. Recently, a new approach introduced by Almustafa and Nehdi [8] implemented a machine learning model to predict the maximum displacement of RC slabs subjected to blast loading. The proposed model resulted in *MAE* of 4.38, an R^2 of 96.2%, and variance explained by cross-validation (*VEcv*) of 94.4%. Additionally, the model was compared to existing analytical and numerical results and found to be a strong contender. The use of such a model reduced the complexity of the application and eliminated the need for computationally costly modelling.

The current chapter develops a machine learning (ML) model to predict the maximum displacement of FRP retrofitted RC slabs subjected to blast loading. A detailed description of the dataset, selected features to model the application, and learning algorithm are provided. The use of synthetic data was investigated to improve model performance. Furthermore, a feature importance analysis using interaction-curvature tests was conducted, along with a comprehensive investigation of the importance of each feature. The model was also validated through error metrics including *MAE*, *MAPE*, and R^2 as well as through comparisons to existing analytical and numerical methods. Additionally, practical application with respect to design codes such as ASCE 59-11 [9] and CSA S850-12 [10] are described along with a discussion on model discrepancies.

6.2 Data collection and description

6.2.1 Feature description

The influential features used to model FRP retrofitted RC slabs under blast loading are categorized into three groups having a total of thirteen features. The first includes the features related to the slab specimen, namely the slab's length, width and thickness, concrete compressive strength, steel yield strength, steel reinforcement ratio, and a categorical feature distinguishing one-way and two-way slabs. The second considers the features associated with the FRP retrofit, including the fiber tensile strength, the bond strength between the retrofit and the concrete, the cross-sectional area of the retrofitted layer, and a categorical feature representing the arrangement of the FRP layer with respect to the slab.

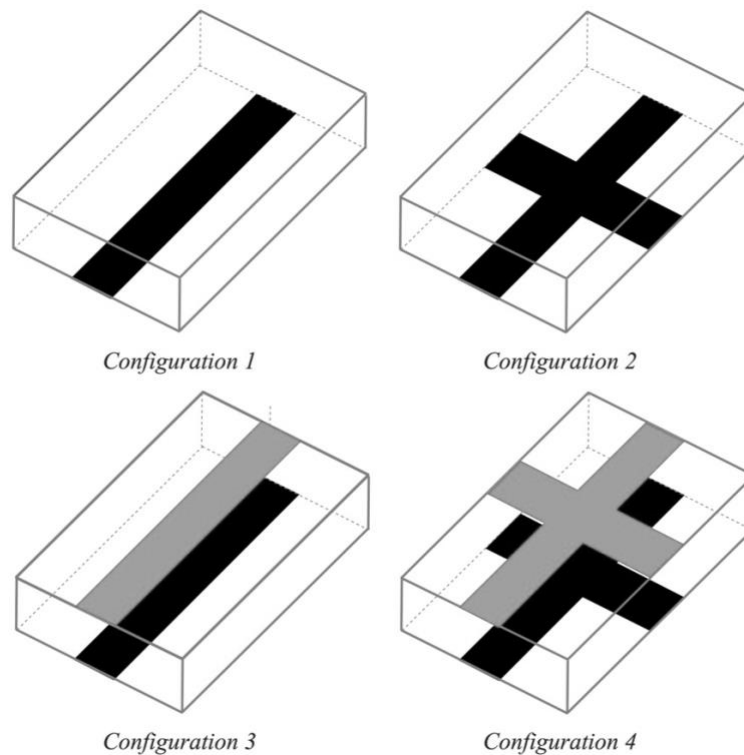


Figure 6-1. Configurations of FRP retrofit layers considered in the dataset.

The different configurations of FRP include retrofitting in one direction on the tensile side, retrofitting in two directions on the tensile side, retrofitting in one direction in both the

tensile side and blast side, and retrofitting in both directions on both sides, denoted by configurations 1, 2, 3 and 4, respectively. **Figure 6-1** illustrates the four configurations in which the black strips are placed on the tensile side, whereas the grey strips are placed on the blast side. The third group includes the features characterizing the blast load, which are given by the reflected pressure and reflected impulse. It should be noted that each data point used in this chapter contained all mentioned features without any missing values. The subsequent text describes the sources of data collection used to develop the dataset.

6.2.2 Experimental and numerical data

The dataset used in this chapter comprises data retrieved from several theses and articles available in the open literature. A total of 70 data points of various FRP retrofitted RC slabs exposed to blast loading were collected. The sources of data were based on experimental studies involving detonated charges [2,3,11-13], experimental programs using blast simulation facilities [1], and numerical models validated by experiments [7,14-16], yielding 18, 25, and 27 data points, respectively. The dataset covers both one-way and two-way slabs that were primarily simply supported with different types of FRP including CFRP, GFRP, and aramid fiber-reinforced polymer (AFRP). Furthermore, both near-field and far field blasts were considered in the dataset. The mean and standard deviation of each of the thirteen features along with the displacement output for non-synthetic data are given in **Table 6-1**, while their frequencies and distributions are shown in **Figure 6-2**.

Generally, experimental programs included preparing RC specimens through formwork, rebar placement along with strain gage installation, and concrete pouring and curing. Afterwards, the RC specimens were retrofitted with FRP laminates. A layer of primer coating was first applied to the cured concrete surface after being cleaned and lightly scratched and left to cure for thirty minutes. Subsequently, a layer of epoxy was applied to the surface via a roller, followed by full impregnation of the FRP sheets into the epoxy layer within the workable time of the epoxy (usually fifteen minutes). Lastly, after the epoxy and FRP sheet had cured, the surface was coated by a second layer of epoxy and left to cure. After specimens had been fully prepared, the appropriate instrumentation to capture the blast and response of the specimen was installed. The instrumented specimen

was then mounted on a durable support frame that simulates the required boundary conditions and was often constructed of steel.

Table 6-1. Mean, count, standard deviation, and range of features for real data.

Feature/Output	Mean/Count	Standard Deviation	Range/Categories
Slab Length (mm)	1822.9	489.05	1000-2640
Slab Width (mm)	1006.3	561.19	300-2640
Slab Depth (mm)	100.8	30.2	60-152
Concrete compressive strength	46.08	11.48	24-60
Steel yield strength (MPa)	512.3	81.6	356-580
Steel reinforcement ratio	0.008	0.0065	0.002-0.0317
Fiber tensile strength (MPa)	1540.8	910.3	560-3790
Bond strength (MPa)	46.69	18.6	5-72.4
Fiber cross section (mm ²)	538.4	447.38	15.4-1785.6
Reflected Pressure (MPa)	16.19	25.14	0.011-122.4
Reflected Impulse (MPa-msec)	1.46	1.29	0.0836-5.747
One-way / Two-way	49 / 21	-	2
FRP configuration (1, 2, 3, 4)	33 / 12 / 12 /	-	4
Maximum displacement (mm)	28.44	19.18	6-85.5

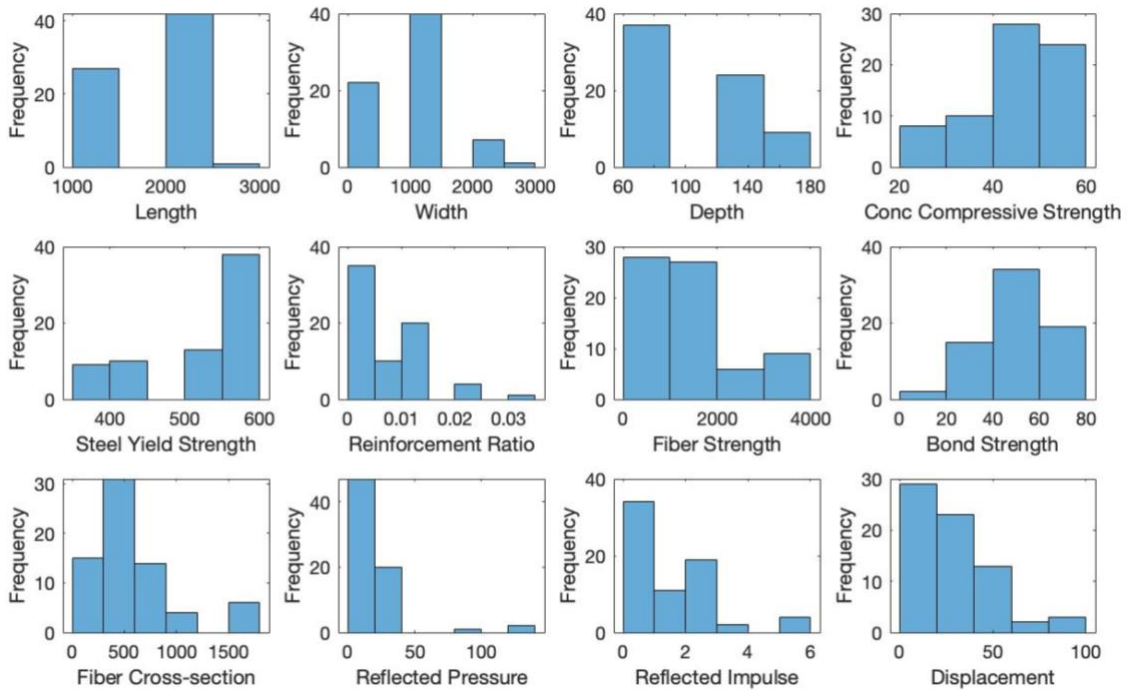


Figure 6-2. Distribution of features for real data.

6.2.3 Synthetic data

The acquisition of large experimental blast loading data is difficult due to the significant costs, stringent regulations, safety considerations, and extensive labor involved. Also, using numerical methods to generate numerous additional datapoints requires substantial computational time, modelling efforts, and continuous validation. Therefore, a novel method to generate synthetic data known as generative adversarial network (GAN) was adopted to create a larger and more robust dataset [17]. GAN operates by learning the probability distribution of inputs and outputs in a dataset and generating new samples of synthetic data, which are of similar quality to the real data. This is achieved through two opposing neural networks labeled as the generator and the discriminator. A brief workflow of a typical GAN is provided in **Figure 6-3**. The generator is tasked with implicitly identifying the original data's probability distribution and generating a new set of data, while the discriminator attempts to separate between the synthetic data and the real data. Additionally, the generator acts to minimize the variation between synthetic and real data, whereas the discriminator acts to maximize the probability of the generated data being real. Both networks compete back and forth until the discriminator is no longer able to distinguish between the generated data and the real data, implying that the generator has successfully matched the quality of the real dataset [17,18,19].

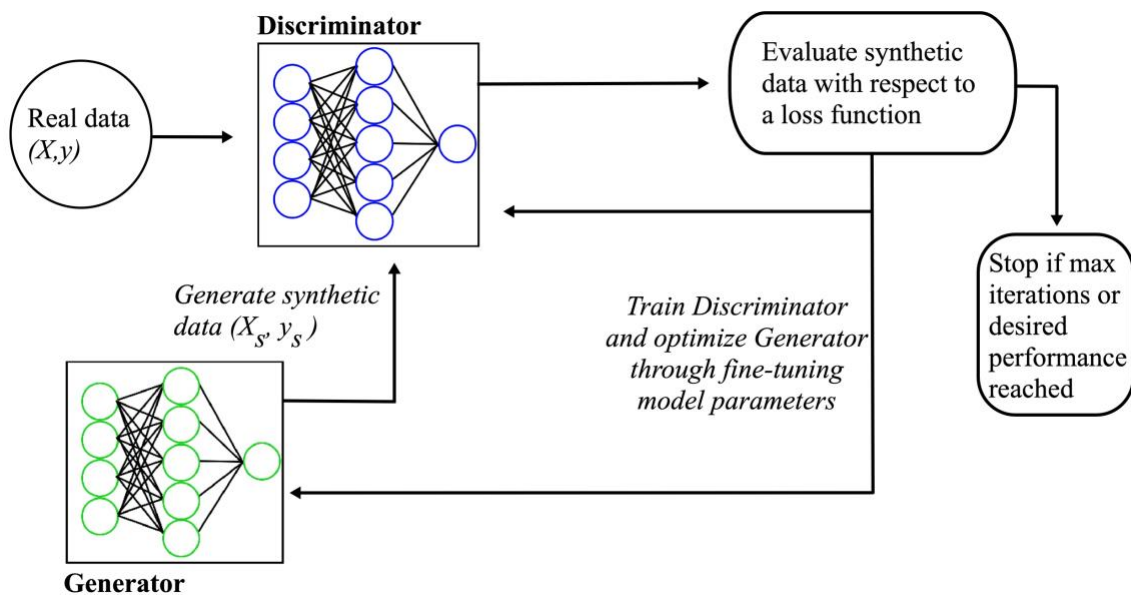


Figure 6-3. General workflow of a generative adversarial network.

A recently developed GAN, known as tabular GAN or TGAN, has been shown to successfully generate data based on continuous or discrete variables [19]. TGAN implements a long short-term memory (LSTM) network and multilayer perceptron (MLP) for the generator and discriminator, respectively. Additional details pertaining to each network's development, such as data transformation approaches and network loss functions can be found in [19]. The performance of TGAN has been thoroughly evaluated by existing tabular datasets available in the literature, which contained both discrete and continuous variables [19]. A recent implementation of TGAN was presented by Marani *et al.* [20] in which data for ultra-high-performance concrete mixture parameters was generated and used for the development of ML models. The study showed that the use of synthetic data to train ML models yielded performance that outperformed similar models that were only based on limited real data. Therefore, the current model development implemented TGAN through the TGAN library in python developed by Xu and Veeramachaneni [19].

A total of 200 synthetic data points was generated using the 70 data points accumulated from existing studies. **Table 6-2** presents the statistical description of the synthetic data, while each variable's frequency distribution is given in **Fig. 6-4**. From the fourteen variables of the dataset, two were discrete variables, with the remaining being continuous variables. However, during the data synthesis process, the continuous variables of concrete compressive strength, steel yield strength, fiber tensile strength, and bond strength were considered discrete to account for practical and commercially available values of each material. Additional considerations were made to the generated continuous variables such that they remained true to the application and within acceptable ranges. These considerations include keeping the L/W ratio of the slab greater or equal to one, keeping the reinforcement ratio greater than the minimum allowable ratio given by CSA A23.3-14 [21], and avoiding unreasonably small or large values of reflected pressure and impulse.

Table 6-2. Mean, count, standard deviation, and range of features for synthetic data.

Feature/Output	Mean/Count	Standard Deviation	Range/Categories
Slab Length (mm)	1845.79	447.21	670 – 2580
Slab Width (mm)	720.12	235.18	14 – 1230
Slab Depth (mm)	127	34.83	66.61 – 205.4
Concrete compressive strength (MPa)	46.35	11.55	24.36 – 75.71
Steel yield strength (MPa)	573.85	61.48	430.93 – 766
Steel reinforcement ratio	0.0117	0.0077	0.0033 – 0.0329
Fiber tensile strength (MPa)	1684.91	760.17	529.67 – 5308
Bond strength (MPa)	55.02	10.37	4.92 – 90.82
Fiber cross section (mm ²)	732.74	387.99	7.82 – 3400
Reflected Pressure (MPa)	22.87	24.09	0.52 – 185.15
Reflected Impulse (MPa-msec)	1.26	0.88	0.01 – 5.74
One-way / Two-way	122 / 78	-	2
FRP configuration (1, 2, 3, 4)	79 / 40 / 34 / 47	-	4
Maximum displacement (mm)	22.62	8.5	4.57 – 53.12

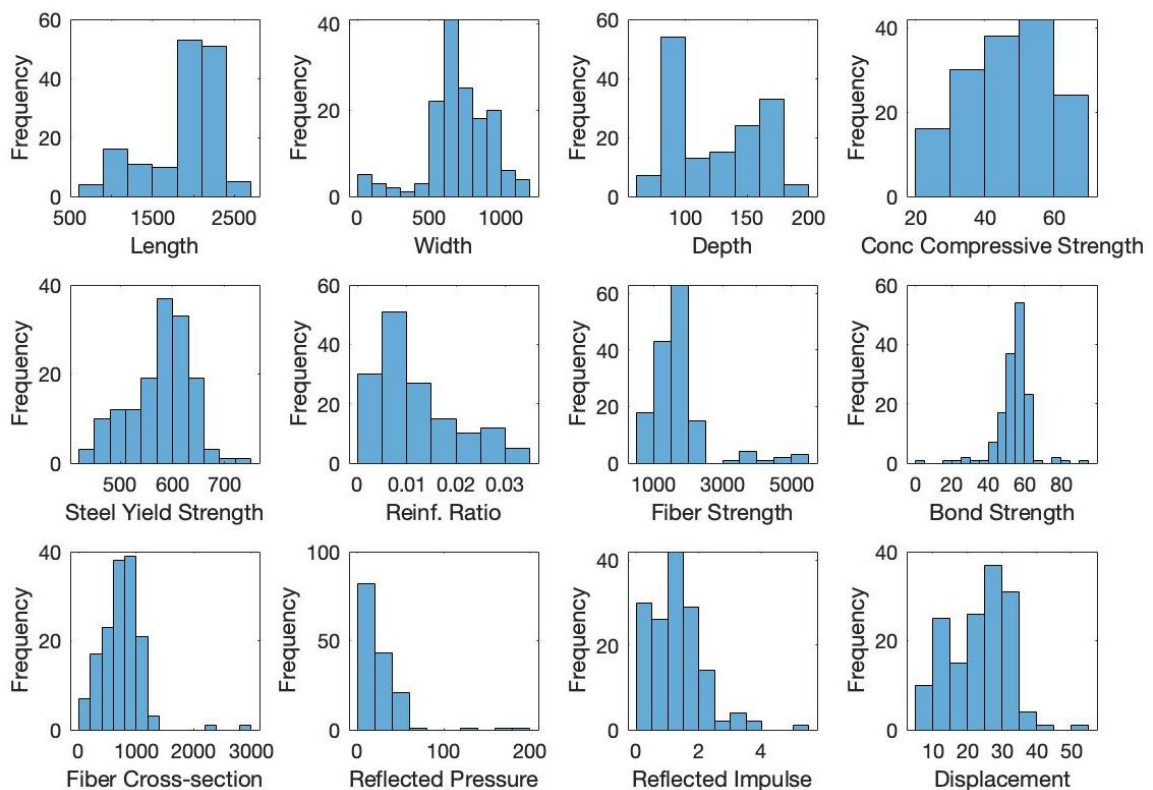


Figure 6-4. Distribution of features for synthetic data.

6.3 Model development and assessment

6.3.1 Gaussian process regression

Gaussian process regression is a probabilistic ML model developed based on a joint distribution of a Gaussian process (prior) and an application dataset. By definition, a Gaussian process (GP) is a set of random variables such that any finite collection of which can be expressed as a Gaussian distribution [22]. A GP is defined by its mean function $m(x)$ and a covariance function $k(x, x')$ and may be expressed as per Eq. (1). When considered independently, a GP (prior) may be used to draw output samples for a given subset. However, with a broadly defined mean value and covariance, such samples would simply be random [23].

$$f(x) \sim GP(m(x), k(x, x')) \quad (1)$$

To incorporate “domain knowledge” of a given application such that meaningful sampling may be achieved, a joint distribution between known inputs, X , and outputs, y , is formed considering the prior. The resulting joint multivariate Gaussian distribution is presented in Eq. (1), where $K(X, X)$, $K(X, X_*)$, $K(X_*, X)$, and $K(X_*, X_*)$ are the covariance matrices between all training and testing input pairs, and f is the desired sampling output variable [22,23]. The inherent noise present within the known dataset may be modeled as a Gaussian distribution having a mean of zero and a variance of σ_n^2 and is also assumed to be additive independent.

$$\begin{bmatrix} y \\ f \end{bmatrix} \sim \mathcal{N} \left(\begin{bmatrix} m(X) \\ m(X_*) \end{bmatrix}, \begin{bmatrix} K(X, X) + \sigma_n^2 I & K(X, X_*) \\ K(X_*, X) & K(X_*, X_*) \end{bmatrix} \right) \quad (2)$$

By conditioning the joint multivariate distribution on the inputs and outputs of a given dataset X, y , as well as the desired inputs, X_* , a predictive multivariate Gaussian distribution may be developed. The resulting distribution is given by Eq. (3) and is characterized by a predictive mean, \bar{f} , and covariance [22].

$$f|X, y, X_* \sim \mathcal{N}(\bar{f}, cov(f)) \quad (3)$$

The expressions for the predictive mean and variance are obtained based on fundamentals of multivariate conditioning properties and are expressed in Eqs. (4) and (5). These outputs make up the resulting GP regression model considering an application-specific dataset [22].

$$\bar{f} = m(X_*) + K(X_*, X)[K(X, X) + \sigma_n^2 I]^{-1}(y - m(X)) \quad (4)$$

$$cov(f) = K(X_*, X_*) - K(X_*, X)[K(X, X) + \sigma_n^2 I]^{-1}K(X, X_*) \quad (5)$$

The variations of a GP regression model are brought forth based on the initially selected mean function and covariance function. In some cases, a mean function may be taken as zero or kept as a constant value. However, a fixed valued mean may not always correctly represent the application's predictive distribution and it may appear more convenient to allow multiple mean values. Such an implementation may be achieved using a fixed basis function $H(X)\beta$ and $H(X*)\beta$ for both known input data and testing input data, where β is a set of tuning parameters that is estimated based on the given dataset [22,23]. Moreover, there exists a wide range of covariance functions to develop the GP model, such as Squared Exponential and Rational Quadratic [24,25]. The covariance acts to quantify the extent of similarity between the input value data based on the selected covariance functions. For n number of test inputs, each covariance matrix term in Eq. (2) is an n -by- n matrix whose evaluation may be represented by Eq. (6). Subsequently, each term in the covariance matrix is given by the covariance of any two inputs such that the matrix diagonal is always 1 [22].

$$K(X_*, X_*) = \begin{bmatrix} k(x_1^*, x_1^*) & k(x_1^*, x_2^*) & \cdots & k(x_1^*, x_n^*) \\ k(x_2^*, x_1^*) & k(x_2^*, x_2^*) & \cdots & k(x_2^*, x_n^*) \\ \vdots & \vdots & \ddots & \vdots \\ k(x_n^*, x_1^*) & k(x_n^*, x_2^*) & \cdots & k(x_n^*, x_n^*) \end{bmatrix} \quad (6)$$

For the current model, a non-isotropic exponential covariance function was implemented based on an exploration of multiple selections. The non-isotropic nature of the function designates a characteristic length scale, σ_m , for each feature m up to d features of the input data. Conversely, an isotropic function would define only a single length scale for the entire input data. The non-isotropic exponential covariance function is provided in Eq. (7), where

θ is a $d+1$ hyperparameter vector comprised of the d length scales and the signal standard deviation, σ_f [22].

$$k(x, x' | \theta) = \sigma_f^2 e^{-r} ; r = \sqrt{\sum_{m=1}^d \frac{(x_m - x'_m)^2}{\sigma_m^2}} \quad (7)$$

Upon appropriate selection of a mean and covariance functions, the GP regression model acts to optimize the model hyperparameters being the noise variance, σ_n , the coefficients of the basis functions, β , and the covariance function hyperparameters θ . This is achieved through maximizing the log marginal likelihood of the model, as shown in Eq. (8), where K symbolizes $K(X, X)$ [22,24,25].

$$\log P(y|X, \sigma_n, \beta, \theta) = -\frac{1}{2} (y - H\beta)^T [K + \sigma_n^2 I]^{-1} (y - H\beta) - \frac{1}{2} \log |K + \sigma_n^2 I| - \frac{n}{2} \log 2\pi \quad (8)$$

It can be observed that the optimization of the model hyperparameters only depends on the training input data. A quasi-Newton optimization is used to obtain the hyperparameter values based on Eq. (8) [26]. Upon the completion of model development, output predictions may be sampled based on new input data considering Eqs. (4) and (5).

6.3.2 Performance criteria and cross-validation

An effective ML model should be able to produce accurate results for new inputs not used in the learning dataset, and thus unfamiliar to the model. Therefore, data should be partitioned such that a portion is used to train the model, while the remaining data is used to test and validate the learning model. Using k-fold cross-validation (CV), the data is partitioned into k equally sized subsets and the learning model is trained on $k-1$ subsets and tested on the remaining subset. The training and testing processes conclude when each subset is used for testing once with the model's performance taken as the average of k evaluations [27,28]. The current model adopts a k value equal to the number of points in the dataset, n , also known as the Leave-One-Out (LOO) CV. The final performance measures are computed by taking the average value produced from n evaluated models. Furthermore, an alternative training and testing method is adopted, which acts to train on

synthetically produced data and test on real data. Both approaches are compatible with the evaluation of a ML model considering a small dataset [20].

The statistical performance metrics used to assess the developed model are the mean absolute error (*MAE*), mean absolute percent error (*MAPE*), and the coefficient of determination R^2 . The use of *MAE* is a common error metric for evaluating the predictive accuracy of models, but is known to be unit dependent, so comparisons can be made only for similar applications [29]. Unlike *MAE*, the metric of *MAPE* provides a scale-independent performance measure that is easily interpreted between 0 and 100%. Also, R^2 is a commonly used measure to assess the correlation between predicted and actual values considering the entire dataset. The formulation for each measure is given as follows:

$$MAE = \frac{1}{n} \sum_1^n |y_i - \hat{y}_i| \quad (9)$$

$$MAPE = \frac{1}{n} \sum_1^n \left| \frac{y_i - \hat{y}_i}{y_i} \right| * 100\% \quad (10)$$

$$R^2 = \left(1 - \frac{\sum_1^n (y_i - \hat{y}_i)^2}{\sum_1^n (y_i - \bar{y})^2} \right) * 100\% \quad (11)$$

where \hat{y} is the predicted output, y is the actual output for every i th entry in the dataset, \bar{y} is the mean of the actual values, and n is the number of points in the dataset. The value of R^2 is always positive and ranges between 0 and 1.

6.3.3 Feature importance using Interaction Test

In addition to evaluating a model's performance through error metrics, it is also important to assess the effect which each feature has on the model's output. With the understanding of each feature's importance, it would be possible to know the extent to which a model will change with alterations to different features. Furthermore, this assessment would be able to identify unimportant features that may be discarded without affecting the model's performance. A common feature importance measure is *Permutation Feature Importance (PFI)*, which operates by randomly permuting a single feature and obtaining the model's new error metrics. The difference in the model's performance before and after permutation would be the measure of importance for the permuted feature. The feature importance

measure would be obtained for every feature in the model, with greater values implying a larger effect on the model [30].

Another approach to measure feature importance is through an *Interaction Test*, which implements hypothesis testing as a node splitting criterion as part of the Random Forests Algorithm and is used as an unbiased feature importance measure. Briefly explained, for a given node in a decision tree, the residuals of each prediction with respect to the weighted average of all predictions in that node are computed. The values of a continuous feature in the node are partitioned into four quartiles, where the corresponding predictions for each quartile are counted and the chi-square statistic and its p -value are computed. The smallest p -value resulting from the considered features in a node will be selected to split the node. This is known as the curvature test. The interaction test follows the same approach, but considers a pair of variables, which are divided into four quadrants by splitting the range of each variable into two halves at their median [31, 32]. A detailed explanation of each test can be found in [31]. The node splitting criterion presented is used to assess the importance of each feature by considering the summation of changes in the output due to node splits for each feature over the number of branched nodes [32]. This feature importance measure is used herein to assess the model features in the current chapter.

6.4 Displacement behavior prediction model

The model developed in this chapter acts to predict the maximum displacement of FRP retrofitted RC slabs when subjected to blast loading, while considering the continuous and categorical features listed in **Table 6-1**. The proposed model's performance measures, feature importance, and comparisons to existing methods are discussed. Furthermore, a comprehensive investigation on the effects of input features on the displacement of normal RC slabs versus retrofitted RC slabs was conducted.

6.4.1 Model validation through performance criteria

The performance metrics of the behavior prediction model considered two approaches for training the GP regression model; the first using only real data (GPR), and the second adopting both real and synthetic data for training, while testing on real data (GPR-Syn).

Furthermore, for each approach, a moving average filter implementation was considered to sequentially smooth the resulting predictive distributions. **Table 6-3** shows the *MAE*, *MAPE*, and R^2 , for each approach considered. It should be noted that the evaluation of the performance metrics considered only real data (70 data points) in the testing sets for all cases.

Table 6-3. Performance metrics for various model considerations.

Model	<i>MAE</i> (mm)	<i>MAPE</i> (%)	R^2 (%)
GPR	3.63	19.82	92.6
GPR Smooth	2.28	14.26	97.8
GPR-Syn	3.5	18.4	94.1
GPR-Syn Smooth	2.28	13.2	97.7

It can be observed from **Table 6-3** that the performance metrics of the model were improved when the additional synthetic data generated by TGAN are considered in the training process. Moreover, when analyzing the predictive distributions based on **Figure 6-5**, the adoption of synthetic data significantly improved the stability of the predictive variance presented through the 95% confidence intervals. When considering the effect of smoothing the predictive distributions, the observed noise was mitigated, and the resulting predictive mean and variance were enhanced. Similarly, the incorporation of synthetic data acted to improve the predictive variance but attained minimal contribution towards the predictive mean.

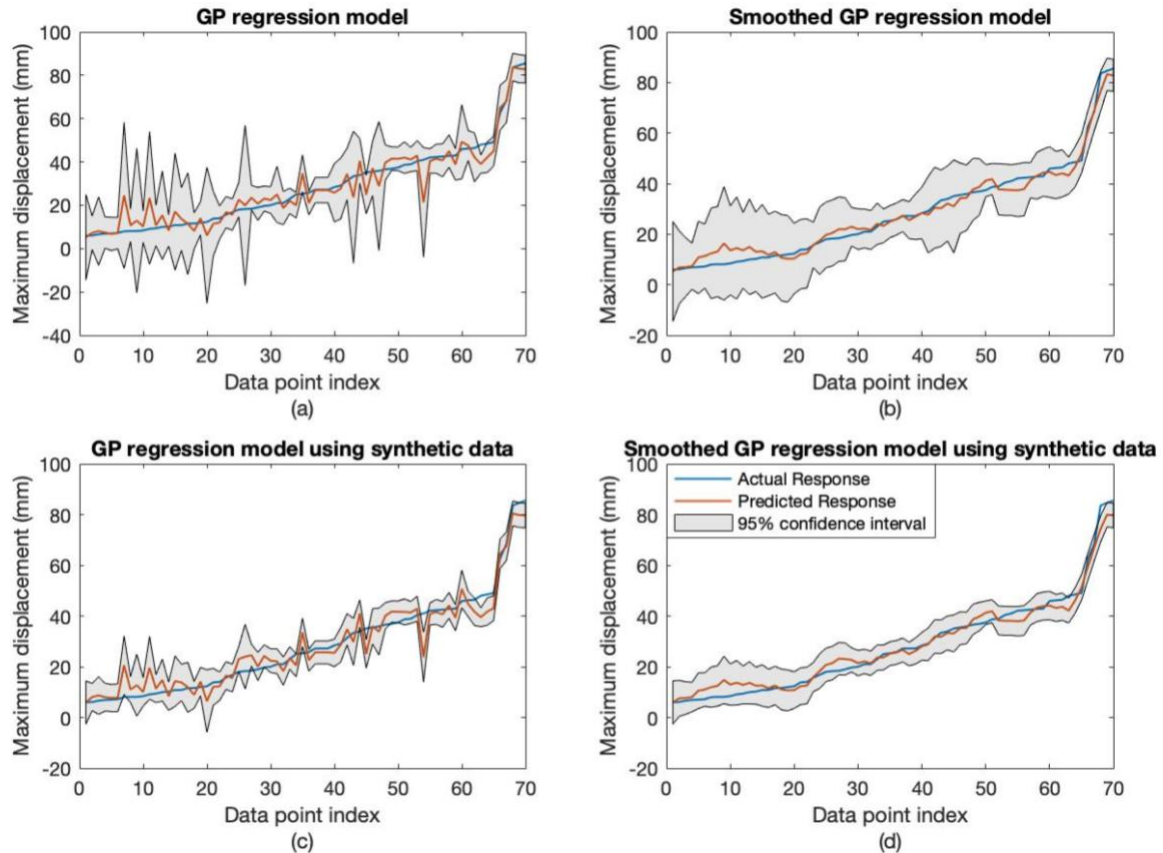


Figure 6-5. Actual versus prediction response plots for different model considerations.

In addition to the performance metrics, **Table 6-4** presents the percentage and number of data points that were predicted within several error bounds based on a total of 70 predictions. The resulting accuracies for each approach were consistent in that the implementation of smoothing improved the model's accuracy, yet the use of synthetic data was shown to be less effective. With the smoothed GPR-Syn approach yielding the highest overall performance, a visual representation of the predicted versus actual values for the model approach is also depicted in **Figure 6-6** considering 10% and 20% error bounds.

Overall, the effect of incorporating synthetic data in the current model's development assisted in developing a more focused confidence interval, while minimally supporting the resulting predictive mean. On the other hand, the application of smoothing the predictive distribution successfully improves the model's performance through both the resulting

mean and variance. Thus, the performance criteria presented show that the model can produce superior predictive results.

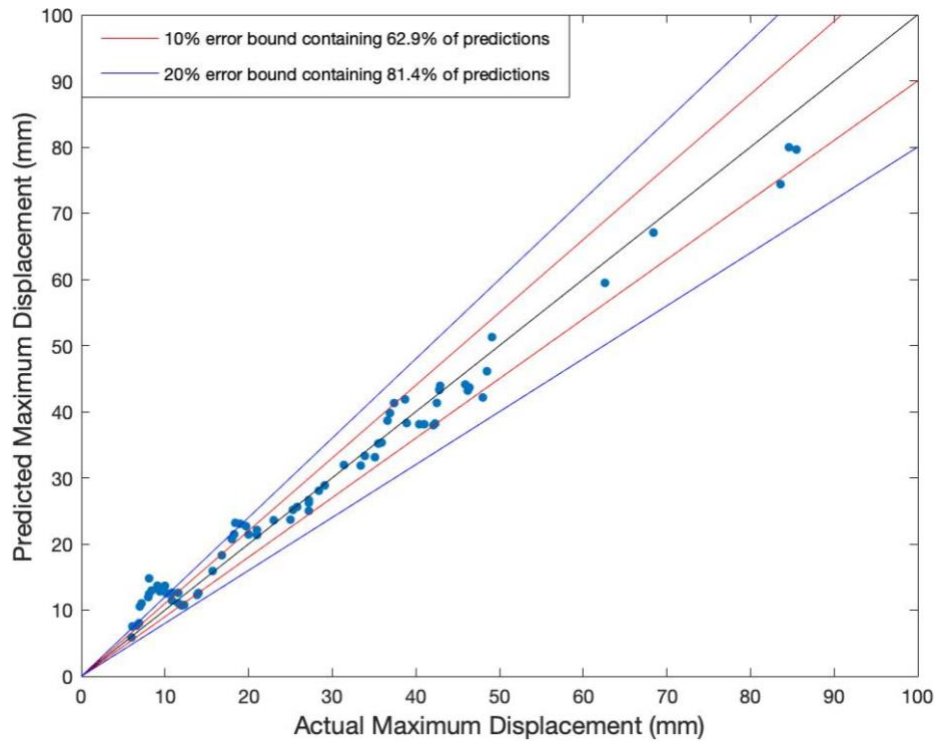


Figure 6-6. Actual response versus predicted scatter plot with error bounds.

Table 6-4. Percent and number of data points within each error bound for various considerations of training data and cross-validation

Error bound	GPR	GPR Smooth	GPR-Syn	GPR-Syn Smooth
$\pm 5\%$	25.7% (18)	35.7% (25)	18.6% (13)	34.3% (24)
$\pm 10\%$	48.6% (34)	61.4% (43)	42.8% (30)	62.9% (44)
$\pm 20\%$	74.3% (52)	84.28% (59)	71.4% (50)	81.4% (57)
$\pm 30\%$	87.1% (61)	87.1% (61)	81.4% (57)	87.1% (61)

6.4.2 Model Validation through comparisons of existing methods

A common analytical method to assess the behavior of structural members under blast loading is the dynamic SDOF approach based on an average acceleration method [33]. The

maximum displacement of a member is obtained through taking discrete time increments for velocity and acceleration and substituting them into a single-degree-of-freedom equation of motion to calculate displacement at each increment until a maximum is reached. Furthermore, the approach considers a mass factor, which converts a member with distributed mass into an equivalent lumped mass based on the member's shape function. It also implements a load factor, which transforms the total load on the member into an equivalent concentrated load by further considering the member's shape function [33].

Table 6-5 reports comparisons of predicted displacement values by SDOF versus the proposed machine learning model. It also compares predictions of the proposed model to that of a more detailed dynamic SDOF analysis used in [2]. Based on these comparisons, it can be observed that the model developed in this chapter yielded predictions that are more accurate than or similar in accuracy to existing analytical models. Furthermore, the reduced accuracy of the results from [1] in **Table 6-5** may have been due to the multiple loading scheme of specimens, which was not captured by the analytical model. However, the results of the ML model showed accurate predictions, despite the multiple load scheme, which suggests that implicit patterns were identified by the model beyond the explicit feature data provided. Such ML qualities further inspire the use of ML in complex engineering applications.

Based on the predictions shown in **Table 6-5**, the ML model was proven to outperform the analytical model through multiple comparisons (entries 3-6, 8, 9, 13-16, 20, 22-27), while producing similar accuracy in few other cases (entries 7, 18). Although direct comparisons to numerical methods were not feasible due to limited pertinent literature or missing information, indirect comparisons were stated instead. When using numerical methods to predict the structural response of FRP retrofitted slabs, the current literature has investigated modelling aspects, such as varying concrete material models [6], material strain rate dependency [6, 7], retrofit bonding failure [7], and perfect FRP bonding [5]. The numerical models developed in these studies were verified with experimental results and found differences in maximum displacement of 0.8% and 14.8% in [5], 2.6%, 4.2%, 7.5%, 11.75%, 23.9%, and 44.5% in [6], and 7.2% in [7]. When compared to the errors of numerical models, the developed ML model attained comparable accuracy.

Table 6-5. Comparison of displacement prediction model and analytical methods.

Entry #	Source	Alternative Model Detail	Experimental result (mm)	Alt. Model Prediction (mm)	ML model prediction (mm)	Alt. Model Error (%)	ML Model Error (%)
1	[1]	Dynamic SDOF	11.6	11.2	11.03	3.45	4.91
2			8.1	9.36	12.4	15.56	53.09
3			42.5	51.7	41.3	21.65	2.82
4			40.4	62.8	38.1	55.45	5.69
5			62.6	75.9	59.45	21.25	5.03
6			84.6	94.3	80	11.47	5.44
7			9.4	13	12.8	38.30	36.17
8			42.3	53.4	38.43	26.24	9.15
9			68.4	83.2	67.1	21.64	1.9
10			83.6	82.4	74.4	1.44	11
11			85.5	88	79.62	2.92	6.88
12			7	5.7	10.5	18.57	50
13			31.4	34.2	31.9	8.92	1.59
14			42.9	38.6	43.9	10.02	2.33
15			6.1	10	7.5	63.93	22.95
16			29.1	30.2	28.86	3.78	0.82
17			38.7	37.9	41.86	2.07	8.17
18			45.9	44.7	44.11	2.61	3.9
19			6	7.3	5.87	21.67	2.17
20			6.6	9.31	7.66	41.06	16.06
21			10	13.6	13.62	36	36.2
22			33.4	41	31.84	22.75	4.67
23			35.1	40.5	33.11	15.38	5.67
24			35.9	25	35.32	30.36	1.62
25			25.3	13.8	25.15	45.45	0.59
26	[2]	Dynamic SDOF	11.58	10.85	12.6	6.3	8.81
27			13.85	10.85	12.3	21.6	11.19

6.4.3 Model validation through feature importance

After assessing the model's performance measures and comparing its prediction accuracy to existing methods, the evaluation of each model feature importance is discussed. The relevance of conducting a feature importance analysis for a machine learning model is that it can be compared to existing experimental or numerical parametric analyses to further evaluate the model's overall ability to assess a given application.

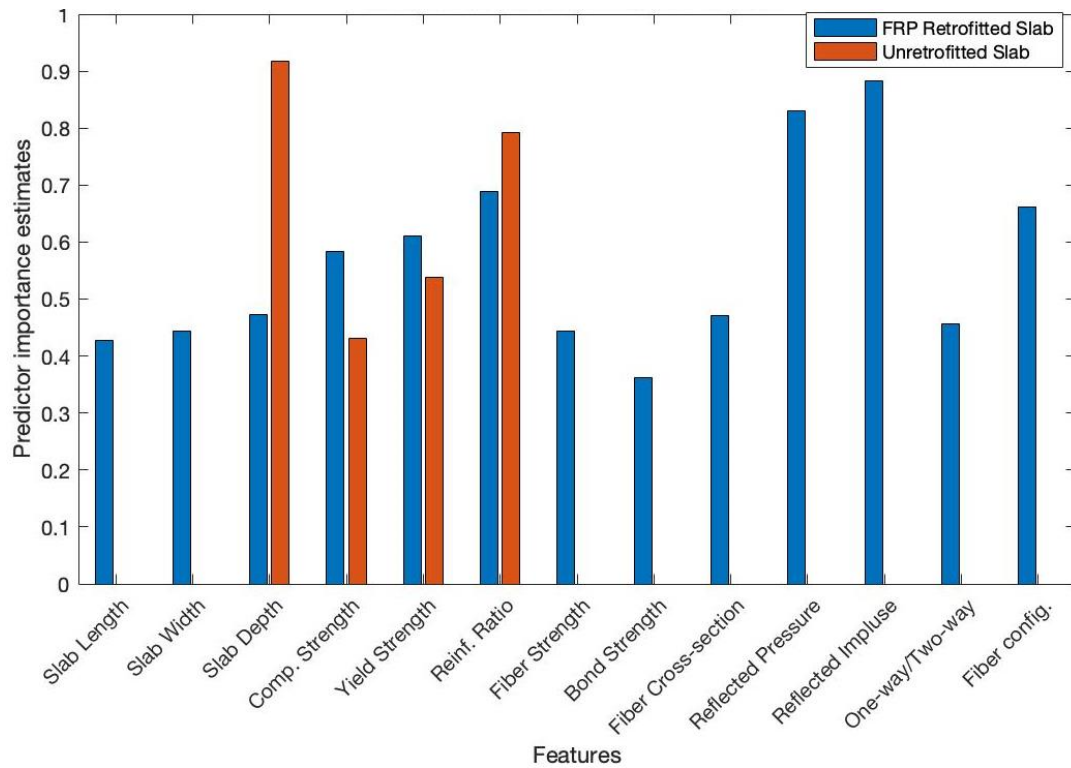


Figure 6-7. Feature importance estimates for FRP retrofitted slabs and conventional slabs.

In order to provide a benchmark on which discussions are based, the current application's feature importance is compared to the feature importance of normal RC slabs exposed to blast loading, which has already been thoroughly validated by experimental results [8]. Consequently, this will not only assess the importance of each feature for FRP retrofitted slabs exposed to blast loads but will also assess how the addition of FRP retrofits affects the relevant features of a normal RC slab for the same application. Lastly, the comparisons made will be explained via existing experimental results. The bar chart in **Figure 6-7** depicts the importance of each feature for retrofitted slabs and the importance of slab depth, concrete compressive strength, yield strength, and reinforcement ratio for conventional slabs exposed to blast loading.

6.4.3.1 Features of slab properties

6.4.3.1.1 Slab depth

As shown in **Fig. 6-7**, the effect of the slab depth on FRP retrofitted slabs is considerably less significant than that on a conventional RC slab. This is supported by the rates of changing depths and their corresponding change in displacements for retrofitted and conventional slabs in experimental and numerical studies. Pantelides *et al* [11] investigated fiber-reinforced concrete, FRP bars, and fiber laminates as damage mitigation techniques for two-way RC slabs, which were subjected to bursts of C4 or ANFO. Among the tested slabs, three were retrofitted with GFRP laminates having depths of 14" (356 mm), 10" (254 mm), and 6" (152 mm). The corresponding recorded maximum displacement for each slab was 45.47 mm, 37.54 mm, and 35.48 mm, respectively. Therefore, a decrease of 28.65% and 57.2% in the slab's depth resulted in 5.8% and 28.15% increase in the maximum displacement, respectively. Also, in the experimental study by Jacques [1], CFRP retrofitted one-way slabs having depths of 120 mm and 80 mm were subjected to simulated blasts. For two separate magnitudes of loading, the 120 mm slab resulted in deflections of 31.4 mm and 42.9 mm, whereas the 80 mm slab resulted in deflections of 42.4 mm and 62.6 mm. Consequently, for a 33.3% decrease in the slab depth, the corresponding increase in displacements was 35% and 46%. In terms of conventional slabs, a numerical parametric study by Lin *et al.* [34] showed that for a 10% and 25% increase in the slab depth, the increase in displacements was 27.4% and 169%, respectively. In another parametric study for conventional slabs conducted by Oesterle [35], it was found that a decrease of 28.65% and 57.2% in the slab depth resulted in an increase of 46.4% and 166.1% in maximum displacement, respectively. Based on these findings, it can be inferred that the rate of change for displacements for changing depths was greater in conventional slabs than in FRP retrofitted slabs. Therefore, the reduced feature importance of slab depth for FRP retrofitted slabs compared with conventional slabs agreed with the experimental and numerical comparisons.

6.4.3.1.2 Concrete compressive strength and steel yield strength

For the features of concrete compressive strength and steel yield strength, **Fig. 6-7** shows that the displacement for FRP retrofitted slabs were slightly more affected than that of conventional slabs. Evidence of this observation may be obtained by analyzing the strain rates of concrete and steel for retrofitted and conventional slabs. The value of a material's strain rate is correlated to its compressive or yield strength through a dynamic increase factor (DIF). In the experimental study by Jacques [1], two cases were observed for steel strain rates of FRP retrofitted slabs compared to conventional slabs. In some specimens, steel strain rates were lower for the retrofitted slabs than in conventional slabs, while in other specimens, they were found to be greater. In the first case, conventional slab specimens were found to have mid-span tension steel strain rates of 0.023 s^{-1} , 0.051 s^{-1} , and 0.062 s^{-1} , while the corresponding FRP retrofitted slabs recorded strain rates of 0.005 s^{-1} , 0.022 s^{-1} , and 0.033 s^{-1} , respectively. Conversely, for the second case, the steel strain rates of conventional slabs were 0.016 s^{-1} and 0.045 s^{-1} , while the FRP retrofitted slabs recorded values of 0.047 s^{-1} and 0.067 s^{-1} , respectively.

It was also observed that the steel strain rates for retrofitted slabs were larger than that for conventional slabs when the L/W ratio was greater than 1; and smaller than that of conventional slabs when the L/W ratio was equal to 1 [1]. Similar variations in the steel strain rate could also be observed in the experimental results of Guo *et al.* [12]. Their results showed that the central steel strain rates of a conventional slab in both direction were 0.1563 s^{-1} and 0.1652 s^{-1} , while the strain rates for retrofitted slabs were 0.1072 s^{-1} and 0.1073 s^{-1} for one specimen; and 0.121 s^{-1} and 0.148 s^{-1} for a second specimen. All comparisons were made under the same magnitude of near-field blast loading in which the L/W ratio of the slabs was 1 [12]. These values further support the variation in steel strain rates between conventional and retrofitted slabs. Similarly, central concrete strain rates for FRP retrofitted slabs were observed to be less than those of conventional slabs. In the same study [12], central concrete strain rates in both directions for FRP retrofitted slabs were recorded as 0.01875 s^{-1} and 0.03 s^{-1} , while the strain rate values for the corresponding conventional slab were 0.05 s^{-1} and 0.044 s^{-1} .

The variations in compressive strength and yield strength of conventional and FRP retrofitted slabs under blast loading are due to the relation between strain rate and concrete compressive strength and steel yield strength through dynamic increase factors (DIF). The DIF for concrete and steel is the ratio between the dynamic stress and the static stress, while being nonlinearly related to the material's strain rate [33]. Also, the dynamic concrete compressive strength and steel yield strength are given by their static value multiplied by the material's DIF in which greater strain rates yield greater DIF values. Therefore, variations between FRP retrofitted slabs and conventional slabs are presented through strain rates of both steel and concrete. This implies that there were variations in their DIF and consequently in their compressive and yield strengths, which are reflected in the feature importance analysis.

6.4.3.1.3 Steel reinforcement ratio

The last feature relating to the slab properties is the steel reinforcement ratio. **Fig. 6-7** indicates that the FRP retrofitted slabs were less affected by variations in the reinforcement ratio than conventional slabs. This reduced effect of the reinforcement ratio has been observed in experimental studies [12]. It can be shown through experimentally recorded steel strains, that the steel reinforcement of retrofitted slabs was less engaged than in conventional slabs. In CFRP retrofitted slabs tested by Ha *et al.* [13], the recorded maximum tension steel strains were 9683 $\mu\epsilon$ and 7434 $\mu\epsilon$, whereas the conventional slabs produced strains of 15998 $\mu\epsilon$ and greater than 28113 $\mu\epsilon$. Furthermore, experiments by Guo *et al.* [12] indicated that GFRP retrofitted slabs produced strains of 1150 $\mu\epsilon$ and 2155 $\mu\epsilon$, while corresponding conventional slabs resulted in strains of 1595 $\mu\epsilon$ and 2532 $\mu\epsilon$. Lastly, tension steel strain values of 80 $\mu\epsilon$, 1800 $\mu\epsilon$, 400 $\mu\epsilon$, and 590 $\mu\epsilon$ were obtained from CFRP retrofitted slabs in the experimental study of Jacques [1], where conventional slabs yielded values of 900 $\mu\epsilon$, 1900 $\mu\epsilon$, 1020 $\mu\epsilon$, and 1800 $\mu\epsilon$, respectively. It should be noted that all comparisons between retrofitted slabs and their corresponding conventional slabs were made under similar detonated blast loads or simulated blast loads. Based on these results of strain comparisons, the conclusions drawn via comparison of feature importance were further supported by experimental results. As demonstrated, the use of feature importance

analysis for machine learning models can accurately capture the extent of meaningful relationships between features and the output for a given dataset.

6.4.3.2 Features of FRP properties

6.4.3.2.1 FRP tensile strength

Feature importance analysis was also conducted on the FRP properties, namely its tensile strength, bonding strength, and cross-section, as shown in **Fig. 6-7**. The effects of these features on the displacement were compared to the corresponding observed effects in experimental and numerical studies. The feature of FRP tensile strength had low effect. Variations in the feature produced small variations in output compared to features with greater significance. Similar conclusion can be drawn from the numerical parametric study of Kong *et al.* [14]. For AFRP and CFRP retrofitted slabs, the maximum displacements were 36.9 mm and 33.9 mm, respectively, which indicates a reduction of only 8.1% when the tensile strength decreased by 28.5% from 2083 MPa (CFRP) to 1490 MPa (AFRP) [14]. Additionally, in the experimental study by Tolba [2], both CFRP and GFRP were used as slab retrofits to resist blast loading. It was concluded that both materials provided similar resistance and that the preferred material should be chosen based on cost. These conclusions support the low effect of the FRP tensile strength obtained by the feature analysis of the ML model.

6.4.3.2.2 Bond strength

Similarly, the bond strength between the FRP retrofit and the concrete surface was shown to have relatively low effect on the maximum displacement (**Fig. 6-7**). Through numerical parametric study, bond strengths of 5 MPa and 10 MPa had large effect on the displacement, whereas bond strengths of 30 MPa and 50 MPa produced nearly the same results. It was concluded that for a given magnitude of blast load, values of bond strength beyond the required strength to prevent debonding will have little to no effect on the output [14]. It should be noted that practical values of bond strength range between 30 MPa and 75 MPa. Furthermore, for the numerical model presented by Nam *et al.* [7], a strain rate dependent GFRP failure model with perfect bonding yielded a displacement of 10.23 mm, while a similar model with debonding yielded a comparable displacement of 10.56 mm.

This comparison further supports that with enough bond strength, the displacement was unaffected by further increasing the bond strength. Numerical results support the results of the ML model feature importance analysis, which indicate that variations in bond strength produced small variations in displacement.

6.4.3.2.3 FRP cross-sectional area

The feature effect of the FRP cross-section (displayed in **Fig. 6-7**) can be discussed based on the number of FRP layers or layer thickness, as well as the width of the FRP retrofit. In a numerical parametric study [14], 1, 2, 4, and 5 AFRP layers yielded displacements of 48 mm, 42.1 mm, 37.4 mm, and 36.9 mm, respectively. These results show that increasing the thickness of the retrofit by increasing AFRP layers provided only slight reduction in the displacement, and this beneficial effect decreased with increasing AFRP layers. Moreover, an experimental study conducted by Maazon *et al* [3] tested one-way slabs with varying number of CFRP strips, which can also be perceived as varying width of retrofit. The different cases considered were slabs having 1, 2, or 4 strips of CFRP, which corresponds to 15 mm, 30 mm, and 60 mm width with resulting displacements of 21 mm, 20 mm, and 18 mm, respectively. It is to be noted that the conventional control slab recorded a maximum displacement of 34.2 mm [3]. Although the response of the slab was significantly improved by the retrofitting material, increasing the strips or width of the material produced little benefit [3]. Both the numerical and experimental conclusions on the FRP thickness and width support the results of the feature analysis of the ML model, which indicated that the FRP cross-section has relatively low effect.

Therefore, the investigation of features relating to FRP properties were accurately reflected in the limited numerical and experimental results found in the open literature. For both slab properties and FRP properties, the feature importance analysis was able to capture the influence of each feature and how it relates to the output of the application.

6.5 Practical implementation and recommendations

6.5.1 Prediction model for displacement

The model developed in this chapter uses features related to the RC slab, FRP properties, and blast properties to predict the slab's resulting maximum displacement. When compared to existing approaches for the same application, the current model has minimal complexity and computes more accurate results at trivial computational cost. Therefore, by providing a reliable preliminary prediction of the retrofitted slab behavior under blast load, it could assist in the iterative design process for selecting appropriate parameters with respect to imposed limits on displacement. A more involved analysis may be conducted thereafter for finalizing designs. Imposed design limits set forth by ASCE 59-11 [9] and CSA S850-12 [10] state maximum allowable support rotations for different degrees of element damage. Both codes state that for the life safety level of protection of flexural elements, a maximum allowable support rotation of 2° should be considered, whereas a collapse prevention level of protection requires a maximum support rotation of 8° . Additionally, it should be noted that the dataset only considered maximum displacements in the direction of loading and did not consider rebounding deflection, which is a pertinent design consideration for FRP retrofitted flexural elements. Therefore, an additional model that predicts maximum rebounding displacements should be coupled with the proposed model.

6.5.2 Dataset discrepancies

The model developed in the present chapter were based on the most comprehensive dataset that could be retrieved from state-of-the art open literature. However, this dataset included a few minor discrepancies that could be eliminated with further research to generate a more comprehensive, future database. First, the FRP debonding phenomenon was not considered in any analysis and data points that exhibited large debonding failure modes were not included in the model. The current dataset of 70 points contains 12 points that displayed minor debonding, but no feature(s) was allocated for this behavior. Additionally, the dataset did not consider cases of retrofitting schemes with unique strip spacing, which were instead simplified into a single strip for each relevant direction. Fewer than 10 points contained such retrofitting schemes. These aspects may be considered as causes of the

minor errors measured. Although the dataset included these minor simplifications, the developed model achieved adequate accuracy.

6.6 Conclusions

The present chapter introduced a machine learning model for predicting the behavior of FRP retrofitted reinforced concrete slabs exposed to blast loading. The developed model was trained and tested using a GP regression algorithm and a dataset of 70 real points retrieved from the open literature, along with 200 synthetic data points obtained using a state-of-the-art tabular GAN. LOO CV was implemented in evaluating the model in which the training process was considered, once with only real data, and once with real and synthetic data. Model validation included statistical performance metrics, direct and indirect prediction comparisons to existing analytical and numerical methods, and feature importance analysis supported by both experimental and numerical studies. Lastly, practical implementations were discussed and suggestions for improved models based on the discrepancies of the current dataset were made. The main conclusions drawn from the current chapter are as follows:

- The displacement prediction model yielded *MAE*, *MAPE*, and R^2 of 2.28, 13.4%, and 97.7%, respectively, considering real and synthetic data.
- When compared to existing SDOF model predictions, the ML model was able to predict the maximum displacement more accurately and with significantly fewer technical considerations.
- The prediction errors of the ML model were well correlated with numerical model errors through indirect comparisons of maximum displacement, while demonstrating considerably less computational cost.
- The feature importance analysis through an interaction-curvature test evidently displayed the proposed model's ability in recognizing and identifying critical slab, FRP, and blast load features and their correlation to the output.

- The importance of features of RC slab properties for both FRP retrofitted and conventional slabs were thoroughly investigated, and pertinent quantitative comparisons were provided.
- The practical implementation of the proposed models is characterized by favorable accuracy, simplified use, and trivial computational demand.

6.7 Chapter references

- [1] Jacques, E. (2011). *Blast retrofit of reinforced concrete walls and slabs* (Master's Thesis, Université d'Ottawa/University of Ottawa).
- [2] Tolba, A. F. F. (2002). *Response of FRP-Retrofitted Reinforced concrete panels to Blast loading* (Doctoral dissertation, Carleton University).
- [3] Maazoun, A., Belkassem, B., Reymen, B., Matthys, S., Vantomme, J., & Lecompte, D. (2018). Blast response of RC slabs with externally bonded reinforcement: Experimental and analytical verification. *Composite Structures*, 200, 246-257.
- [4] Malvar, L. J., Crawford, J. E., & Morrill, K. B. (2007). Use of composites to resist blast. *Journal of Composites for Construction*, 11(6), 601-610.
- [5] Lin, X., & Zhang, Y. X. (2016). Nonlinear finite element analysis of FRP-strengthened reinforced concrete panels under blast loads. *International Journal of Computational Methods*, 13(04), 1641002.
- [6] Tanapornraweeakit, G., Haritos, N., Mendis, P., & Ngo, T. (2010). Finite element simulation of FRP strengthened reinforced concrete slabs under two independent air blasts. *International Journal of Protective Structures*, 1(4), 469-488.
- [7] Nam, J. W., Kim, H. J., Kim, S. B., Yi, N. H., & Kim, J. H. J. (2010). Numerical evaluation of the retrofit effectiveness for GFRP retrofitted concrete slab subjected to blast pressure. *Composite Structures*, 92(5), 1212-1222.
- [8] Almustafa, M. K., & Nehdi, M. L. (2020). Machine learning model for predicting structural response of RC slabs exposed to blast loading. *Engineering Structures*, 221, 111109.
- [9] ASCE. (2011). Blast protection of buildings: ASCE/SEI 59-11.
- [10] Canadian Standards Association. (2012). *Design and assessment of buildings subjected to blast loads*. CSA S850-12.

- [11] Pantelides, C. P., Garfield, T. T., Richins, W. D., Larson, T. K., & Blakeley, J. E. (2012). Behavior of concrete panels reinforced with synthetic fibers, mild steel, and GFRP composites subjected to blasts. In Structures Congress 2012 (pp. 23-34).
- [12] Guo, Z., Xu, Z., Chen, C., Zhang, B., Lehman, D. E., & Cao, S. (2017). Behavior of GFRP retrofitted reinforced concrete slabs subjected to conventional explosive blast. *Materials and Structures*, 50(6), 236.
- [13] Ha, J. H., Yi, N. H., Choi, J. K., & Kim, J. H. J. (2011). Experimental study on hybrid CFRP-PU strengthening effect on RC panels under blast loading. *Composite Structures*, 93(8), 2070-2082.
- [14] Kong, X., Qi, X., Gu, Y., Lawan, I. A., & Qu, Y. (2018). Numerical evaluation of blast resistance of RC slab strengthened with AFRP. *Construction and Building Materials*, 178, 244-253.
- [15] Tanapornraweekit, G., Haritos, N., Mendis, P., & Ngo, T. (2006). Full-Scale Blast Test and Non-linear Finite Element Analysis on Conventional Steel and CFRP Retrofitted Reinforced Concrete Panels. Proceedings of the MDCMS 1 - Vietnam First International Conference on Modern Design, Construction and Maintenance of Structures. Construction Publishing House. Hanoi, Vietnam.
- [16] Mosalam, K. M., & Mosallam, A. S. (2001). Nonlinear transient analysis of reinforced concrete slabs subjected to blast loading and retrofitted with CFRP composites. *Composites Part B: Engineering*, 32(8), 623-636.
- [17] Goodfellow, I., Pouget-Abadie, J., Mirza, M., Xu, B., Warde-Farley, D., Ozair, S., Courville, A., & Bengio, Y. (2014). Generative adversarial nets. In *Advances in neural information processing systems* (pp. 2672-2680).
- [18] Park, N., Mohammadi, M., Gorde, K., Jajodia, S., Park, H., & Kim, Y. (2018). Data synthesis based on generative adversarial networks. *arXiv preprint arXiv:1806.03384*.
- [19] Xu, L., & Veeramachaneni, K. (2018). Synthesizing tabular data using generative adversarial networks. *arXiv preprint arXiv:1811.11264*.
- [20] Marani, A., Jamali, A., & Nehdi, M. L. (2020). Predicting Ultra-High-Performance Concrete Compressive Strength Using Tabular Generative Adversarial Networks. *Materials*, 13(21), 4757.
- [21] CSA Group. (2014). Design of Concrete Structures (CSA A23. 3-14). *Canadian Standards Association, Toronto, ON, Canada*.
- [22] Rasmussen CE, Williams CKI. (2006). Gaussian processes for machine learning. The MIT Press, Cambridge

- [23] Schulz, E., Speekenbrink, M., & Krause, A. (2018). A tutorial on Gaussian process regression: Modelling, exploring, and exploiting functions. *Journal of Mathematical Psychology*, 85, 1-16.
- [24] Arthur, C. K., Temeng, V. A., & Ziggah, Y. Y. (2020). Novel approach to predicting blast-induced ground vibration using Gaussian process regression. *Engineering with Computers*, 36(1), 29-42.
- [25] Momeni, E., Dowlatshahi, M. B., Omidinasab, F., Maizir, H., & Armaghani, D. J. (2020). Gaussian process regression technique to estimate the pile bearing capacity. *Arabian Journal for Science and Engineering*, 45(10), 8255-8267.
- [26] Nocedal, J. and S. J. Wright. *Numerical Optimization*, Second Edition. Springer Series in Operations Research, Springer Verlag, 2006, 139-141.
- [27] T. Hastie, R. Tibshirani, J. Friedman J. (2009). *The elements of statistical learning: data mining, inference, and prediction*, New York, USA: 2nd edition, Springer.
- [28] Fushiki, T. (2011). Estimation of prediction error by using K-fold cross-validation. *Statistics and Computing*, 21(2), 137-146.
- [29] Li, J. (2016). Assessing spatial predictive models in the environmental sciences: Accuracy measures, data variation and variance explained. *Environmental Modelling & Software*, 80, 1-8.
- [30] Strobl C, Boulesteix AL, Kneib T, Augustin T, Zeileis A. (2008). Conditional variable importance for random forests. *BMC Bioinf.* 9(1):307.
- [31] Loh, W. Y. (2002). Regression trees with unbiased variable selection and interaction detection. *Statistica Sinica*, vol. 12, 361-386.
- [32] MathWorks, (2019). *Statistics and Machine Learning Toolbox™: User's Guide (R2019a)*. Retrieved August 1, 2020 from https://www.mathworks.com/help/pdf_doc/stats/stats.pdf
- [33] USA Department of Defense. (2008). "Structures to Resist the Effect of Accidental Explosions - Unified Facilities Criteria (UFC) 3-340-02", Department of Defense.
- [34] Lin, X., Zhang, Y. X., & Hazell, P. J. (2014). Modelling the response of reinforced concrete panels under blast loading. *Materials & Design (1980-2015)*, 56, 620-628.
- [35] Oesterle, M. G. (2009). *Blast simulator wall tests: experimental methods and mitigation strategies for reinforced concrete and concrete masonry* (Doctoral dissertation, UC San Diego).

Chapter 7

7 Machine learning prediction of structural response for steel fiber-reinforced concrete beams subjected to far-field blast loading

7.1 Introduction and background

The use of steel fiber-reinforced concrete (SFRC) for developing protective structures has become exceptionally favorable owing to its unique engineering properties. In compression, SFRC is characterized by the improved performance of its post-peak behavior, which induces ductility to the brittle cement-based materials. For instance, in high strength concrete (HSC), which exhibits a markedly brittle post-peak response, the inclusion of steel fibers significantly improves ductility [1]. Moreover, SFRC achieves much enhanced tensile strength both in direct tension testing [2] and splitting tensile testing [3] when compared to conventional concrete. The behavior of SFRC under dynamic loading has also been thoroughly investigated. Under high strain rates, SFRC exhibits increased compressive strength and greater ductile response. Similarly, an increase in the steel fiber content results in a higher peak compressive strength [4,5].

Recently, several experimental studies have been devoted to investigating the response of SFRC beams under far-field blast loading simulated using a Shock-Tube Facility. Guertin-Normoyle [6] studied various configurations of ultra-high-performance fiber reinforced concrete (UHPFRC) beams having high strength reinforcement (HSR). Two different types of steel fiber contents at dosages of 1%, 2%, and 3% by volume fraction were considered. Using UHPFRC and HSR were both found effective in mitigating maximum and residual displacements and minimizing member debris. However, using UHPFRC with normal strength reinforcement caused the failure mode to shift from the concrete crushing

observed for normal strength concrete (NSC), to tensile rebar rupture. Moreover, the usage of fibers reduced cracking and displacement, especially for fibers with greater aspect ratio.

Similarly, Algassem [7] explored the effects of two different steel fiber types and contents in high strength fiber-reinforced concrete (HSFRC) beams. HSFRC beams achieved greater control of damage and displacement compared to HSC beams. In several cases, HSFRC beams with 1% fiber content prevented shear failure and induced a ductile response despite the absence of stirrups. The blast performance of HSFRC beams with stirrups did not improve with increasing fiber content and insignificant variations were observed beyond 0.5% fiber content. Moreover, at the same fiber volume, shorter steel fibers performed better than the longer ones. The effect of steel fibers in HSC beams with HSR was studied by Li [8] using one fiber type at 1% fiber content. The steel fibers significantly improved the blast performance of HSC beams reinforced with HSR.

Castonguay [9] assessed NSC beams without stirrups having normal strength reinforcement (NSR), while considering three different types of steel fibers at various fiber contents. The inclusion of steel fibers prompted an enhanced blast performance, reducing the overall damage and displacements, while maintaining effective control of crack development. Using 1% fiber content was adequate in replacing stirrups and preventing shear failure. The beneficial effect of fiber addition was observed to be limited to 1% fiber content, with minimal improvements observed beyond this threshold level. Larger aspect ratio steel fibers led to greater increase in the performance of SFRC beams.

In contrast to the experimental studies above, Charles [10] examined the effects of the reinforcement detailing in HSFRC beams. Using 0.75% steel fiber content with a stirrup spacing of half the beam's depth better improved the blast performance than using a stirrup spacing of a quarter of the beam's depth without steel fibers. Therefore, it was posited that reduced stirrup spacing in design may be adopted in the presence of steel fibers. It was also observed that increasing the tension reinforcement in HSFRC beams improved blast performance, yet exceeding certain limitations resulted in loss of ductility and overall reduced performance under blast loading.

The properties of the steel fibers used in the above studies are given in **Table 7-1**. It can be observed that the use of steel fibers generally improved blast resistance and structural response of beams subjected to far-field blast loading. However, when inspecting the effect of fiber content on structural response, discrepancies were observed throughout the literature. Guertin-Normoyle [6] reported that no discernable maximum displacement trend was observed for fiber contents between 1% and 3% in UHPFRC beams. Furthermore, while using 1% steel fiber content in HSFRC beams with stirrups reduced the maximum displacement, no clear correlation could be obtained when using 0.5% fiber content [7]. Therefore, various studies have identified the need for further investigation on the effect of the fiber content on SFRC beams under far-field blast loading [6,7,8] and for elucidating the effect of the various steel fiber types [6,8].

Table 7-1. Steel fiber properties.

ID	Reference	Fiber Name	Length (mm)	Diameter (mm)	Aspect Ratio (mm/mm)	Tensile Strength (MPa)
F1	[6][10]	OL 13/.20	13	0.2	65	2750
F2	[6]	BELM-0.3/13-3150	13	0.3	43	3150
F3	[9]	BP-80/30	30	0.38	79	2300
F4	[7][8][9][10]	ZP 305	30	0.55	55	1350
F5	[7][9]	5D	60	0.92	65	2350

For each of the experimental studies surveyed herein, a dynamic single degree of freedom (SDOF) model was developed to analytically predict the displacement under blast load results for the respective beam configuration. The material models, dynamic increase factor (DIF) models, and analysis procedure for each SDOF model were appropriately implemented and may be found in the respective sources discussed above. The results from each analytical study based on the maximum displacement produced a mean absolute error of 16.2% considering 41 comparisons [6], 13.6% considering 20 comparisons [7], 9.7% considering 12 comparisons [8], 20% considering 25 comparisons [9], and 10.6%

considering 8 comparisons [10]. It should be noted that these values only consider the response prediction of beam specimens that incorporate steel fibers. Additional discussion on these comparisons is provided in subsequent sections. Although the analytical models yield acceptable results, dedicated DIF models for UHPFRC, and DIF tension models for HSFRC and HSR have yet to be developed. Moreover, there is need for simplified and robust predictive methods which can effectively produce structural responses for such members under blast loading [6,7,8].

We stand on the brink of a fourth industrial revolution, where automated design, building information modeling, additive manufacturing and smart materials and structures could dominate future infrastructure developments. Resilience to blast loading could become part of this automated process. Given the available experimental data and existing numerical simulations, developing intelligent and simplified models for blast loading have become increasingly conceivable. Therefore, the present chapter develops a machine learning (ML) model to predict the maximum displacement of various SFRC beam configurations under far-field blast loading. Using both intelligently generated synthetic data and gaussian process regression modeling, the developed model is evaluated through numerous statistical performance measures. Furthermore, an in-depth comparison between the proposed model and existing predictive methods is provided. The simplicity of the proposed model is elaborated through its ability to implicitly account for complex application considerations as well as eliminating complex technical and computational demand. After thorough development and validation, the proposed model is used to develop comprehensive trends for varying steel fiber contents and types across several pertinent SFRC beam configurations presented in the literature.

7.2 Model development

7.2.1 Gaussian process regression

A Gaussian Process (GP) is defined as a set of random variables, from which any finite subset exhibits a joint (multivariate) Gaussian distribution. A GP is also considered a distribution over functions and is characterized by a mean function $m(x)$ and a covariance

function $k(x, x')$ [12]. The mean function $m(x)$ defines the expected function value at input x given by Eq. (1) and represents the average of every function evaluated at input x within the distribution. The covariance function $k(x, x')$ signifies the dependence between the function values at every input pair (x, x') and is given by Eq. (2). As a result, a GP, $f(x)$, is represented in Eq. (3) [12].

$$m(x) = \mathbb{E}[f(x)] \quad (1)$$

$$k(x, x') = \mathbb{E}[(f(x) - m(x))(f(x') - m(x')))] \quad (2)$$

$$f(x) \sim GP(m(x), k(x, x')) \quad (3)$$

Sampling output values of $f(x)$ given a finite subset $X^* = \{x_1^*, x_2^*, \dots, x_n^*\}$ from a GP is achieved through sampling from a multivariate Gaussian distribution. For an assumed mean function $m(x) = 0$, and a covariance function $K(X^*, X^*)$, $f(x)$ is represented by Eq. (4), where computing $K(X^*, X^*)$ is given by Eq. (5) [13].

$$f(x) \sim \mathcal{N}(0, K(X^*, X^*)) \quad (4)$$

$$K(X^*, X^*) = \begin{bmatrix} k(x_1^*, x_1^*) & k(x_1^*, x_2^*) & \cdots & k(x_1^*, x_n^*) \\ k(x_2^*, x_1^*) & k(x_2^*, x_2^*) & \cdots & k(x_2^*, x_n^*) \\ \vdots & \vdots & \ddots & \vdots \\ k(x_n^*, x_1^*) & k(x_n^*, x_2^*) & \cdots & k(x_n^*, x_n^*) \end{bmatrix} \quad (5)$$

When a training dataset having X inputs and y outputs is introduced with the desire of sampling predictions f for new (test) inputs X^* , the joint distribution of the training outputs y and the sampled outputs f with respect to the prior is represented in Eq. (6). Furthermore, to model the inherent noise (ε) of the training dataset, the noise is assumed to be additive independent having a gaussian distribution with a mean of zero and a variance of σ_n^2 denoted by $\varepsilon \sim \mathcal{N}(0, \sigma_n^2)$. Thus, the covariance of the training inputs $K(X, X)$ becomes $K(X, X) + \sigma_n^2 I$ as considered in Eq. (6), where I is an identity matrix (having ones in the diagonal and zeros everywhere else) [12].

$$\begin{bmatrix} y \\ f \end{bmatrix} \sim \mathcal{N} \left(\begin{bmatrix} m(X) \\ m(X^*) \end{bmatrix}, \begin{bmatrix} K(X, X) + \sigma_n^2 I & K(X, X^*) \\ K(X^*, X) & K(X^*, X^*) \end{bmatrix} \right) \quad (6)$$

The terms $K(X,X)$, $K(X, X^*)$, $K(X^*, X)$, and $K(X^*, X^*)$ are the covariance matrices between training inputs, training and testing inputs, and testing inputs, respectively, and are similarly represented by Eq. (5). Since the goal of GP regression is to obtain samples of f given the training dataset and the testing inputs, then the joint Gaussian distribution is conditioned on X , y , and X^* to formulate the predictive distribution, as shown in Eq. (7). The predictive mean, \bar{f} , and covariance of the distribution are presented in Equations (8) and (9) [12,14]. A step-by-step example of how a single test point is predicted using a GP regression model is provided in [13].

$$f|X, y, X_* \sim \mathcal{N}(\bar{f}, cov(f)) \quad (7)$$

$$\bar{f} = m(X_*) + K(X_*, X)[K(X, X) + \sigma_n^2 I]^{-1}(y - m(X)) \quad (8)$$

$$cov(f) = K(X_*, X_*) - K(X_*, X)[K(X, X) + \sigma_n^2 I]^{-1}K(X, X_*) \quad (9)$$

In some cases, the mean function is specified as a fixed value, however, introducing a basis function to represent a mean at every observation becomes more convenient in modeling a given application. The fixed basis function with coefficients β , given as $H(X)\beta$, provides a value for every observation in which β is hyperparameter vector whose values are inferred from the data. Similarly, $H(X^*)\beta$ represents the mean values for the set of new observations [12]. A constant basis function is adopted in this chapter and is incorporated into Eq. (8).

Furthermore, the choice of covariance (kernel) function is pertinent in developing an efficient GP regression model. As previously described, the covariance function measures the dependency between output values as a function of their input values. In other words, the extent to which input values are similar indicates the similarity of their expected output values. In such context, *similarity* is commonly expressed through the distance between input values. Several different kernel functions are available in the literature, such as the Squared Exponential Kernel, Rational Quadratic Kernel, Matern class of kernels, etc. [14]. Upon thorough investigation, the Rational Quadratic Kernel was selected to model the GP regression model in this chapter and is represented in Eq. (10), where θ represents the hyperparameters of characteristic length scale, σ_l , positive-valued scale-mixture parameter, α , and the signal standard deviation, σ_f [12].

$$k(x, x' | \theta) = \sigma_f^2 \left(1 + \frac{(x-x')^T(x-x')}{2\alpha\sigma_l^2} \right)^{-\alpha} \quad (10)$$

The development of the GP regression model has been shown to depend on the noise variance, σ_n , the coefficients of the basis functions, β , and the kernel hyperparameters $\theta = \{\sigma_l, \alpha, \sigma_f\}$. Towards identifying their optimal values, a commonly adopted approach is through the maximization of the log marginal likelihood of the model presented in Eq (11), which only considers information from the training dataset [12,13]. It should be noted that $K(X,X)$ is denoted as K in Eq. (11).

$$\log P(y|X, \sigma_n, \beta, \theta) = -\frac{1}{2}(y - H\beta)^T [K + \sigma_n^2 I]^{-1} (y - H\beta) - \frac{1}{2} \log |K + \sigma_n^2 I| - \frac{n}{2} \log 2\pi \quad (11)$$

The optimization of Eq. (11) is achieved using a quasi-Newton optimizer [15], which is conveniently integrated into MATLAB's Statistics and Machine Learning Toolbox [16]. Once the optimized hyper parameters of the GP regression model are achieved for a given dataset, Eqs. (8) and (9) are utilized for predicting the mean output value for new data points along with its variance.

7.2.2 Generative adversarial networks

Due to the labor, high cost, and safety concerns associated with experimental studies of structural blast loading, the possibility of establishing a large-scale comprehensive dataset is rather limited. Accordingly, implementing state-of-the-art synthetic data generators can provide a novel means to develop larger and improved synthetic datasets without depreciating the original application. This can be achieved for instance using generative adversarial networks (GAN) [17]. By learning the complex distribution of a dataset, GAN can generate synthetic data, while retaining the quality of the real data. The development of a GAN is based on two neural networks, the generator, and the discriminator, in which one acts to generate synthetic data, while the other attempts to distinguish between the real and generated data. As the generator feeds data into the discriminator, its objective is to minimize the variation between the real and generated data. Conversely, the discriminator's target is to maximize the probability that the synthetic data is real. Once the generator is

capable of synthesizing data that the discriminator is unable to distinguish as real or synthetic, the GAN is successfully developed and may be used to generate quality data [17,18]. In the present chapter, a novel conditional tabular GAN (CTGAN) is implemented. It introduces an improved method for representing continuous data having complex distributions, while accounting for imbalance of discrete data [18]. CTGAN was based on the development of tabular GAN (TGAN) [17], which adopts the use of long short-term memory (LSTM) neural network for GAN development, whereas CTGAN is implemented based on fully connected neural networks. The network architecture, loss functions, and benchmark performances for each GAN are detailed in their respective sources.

7.2.3 Statistical performance measures

The evaluation of the proposed model is based on two different training approaches. The first approach considers k -fold cross validation, where the data is divided into k equal subsets in which the model is tested on every subset having been trained on the remaining $k-1$ subsets. Model performance is then taken as the average performance measure of each training and testing set to obtain a reliable evaluation of the model, where the number of folds currently taken is 10. The second approach implements a “train on synthetic data, test on real data” method, which utilizes synthetic data to obtain the required hyperparameters leading to the development of the model, after which performance measures are acquired with respect to the real data. The performance measures considered for each approach of model evaluation are the mean absolute error (MAE), mean squared error (MSE), mean absolute percent error ($MAPE$), and the coefficient of determination (R^2) as presented in Eqs. (12)-(15) below.

$$MAE = \frac{1}{n} \sum_1^n |y_i - \hat{y}_i| \quad (12)$$

$$MSE = \frac{1}{n} \sum_1^n (y_i - \hat{y}_i)^2 \quad (13)$$

$$MAPE = \frac{1}{n} \sum_1^n \left| \frac{y_i - \hat{y}_i}{y_i} \right| * 100\% \quad (14)$$

$$R^2 = \left(1 - \frac{\sum_1^n (y_i - \hat{y}_i)^2}{\sum_1^n (y_i - \bar{y})^2} \right) * 100\% \quad (15)$$

where \hat{y} is the predicted output, y is the actual output for every i th entry in the dataset, \bar{y} is the mean of the actual values, and n is the number of points in the dataset. Both *MAE* and *MSE* are widely used for measuring model performance in which *MSE* is more sensitive to outlier predictions than *MAE* [19]. Furthermore, *MAPE* is a popular scale-independent measure, which is easily interpreted between 0 and 100%. It should be noted, however, that *MAPE* is inappropriate for datasets having zero or near-zero outputs since this results in infinite or undefined *MAPE* [20]. Lastly, the measure of a model's R^2 provides an indication of how well predictions correlate to actual values [21]. The statistical performance measures are therefore reported for each of the training approaches.

7.3 Data collection

This section provides details on the sources of the dataset used throughout this chapter, along with a brief description of their respective experimental programs. Details of the dataset are provided along with a discussion on the choice of the features selected. Similarly, the data synthesis process using CTGAN is described and details of the synthetic dataset are provided.

7.3.1 Description of shock wave simulation device

The original data used in this chapter was retrieved from six extensive experimental programs conducted at the University of Ottawa Shock Tube Facility (UOST). These studies investigated various parameters of SFRC beams subjected to far field blast loading as briefly discussed earlier in the introductory section. The UOST Facility can simulate a wide range of far-field blast loads of high explosives. The main components of the device are a variable-length driver, spool section, and expansion chamber. The driver section generates the source of the shock wave in which varying driver pressures will result in varying magnitudes of reflected pressures, whereas the alternative driver section lengths control the duration of the shock wave. The spool section consists of two aluminum diaphragms and is pressurized such that the pressure differential between the spool section and the driver section is less than the rupture strength of the diaphragms. Once the desired pressure in the driver is reached, the pressure in the spool section is released causing the

diaphragms to rupture and generating a shock wave in the expansion section. Additional technical details pertaining to the operation of the device are available in [22]. When considering a driver length of 2743-mm, the average generated shock wave parameters for a selection of driver pressures are provided in **Table 7-2** where the equivalent scaled distance assumes a standoff distance of 50-m.

7.3.2 Data from UOST and feature description

A total of 117 data points was collected from [6-11], which accounts for SFRC beams with configurations of NSC, HSC, UHPC, NSR, and HSR. Also, five different steel fiber types as displayed in **Table 7-1** at six alternative fiber contents (0.5%, 0.75%, 1%, 1.5%, 2%, 3%) were considered within the dataset. Additionally, 50 data points of non-fiber beams having similar design properties were collected from the same sources. All the tested specimens adhered to the design criteria set forth by CSA A23.3-14 [24]. The limiting design characteristics throughout the dataset are the beam dimensions (all of which were 250 x 150 x 2440 mm with a shear span of 740 mm) and the absence of compression steel. Although there exists a limit to beam dimension considerations, the importance of this dataset is apparent through its holistic consideration of a multitude types of concrete, reinforcement, and fibers, while the effect of dimension is beyond the current scope.

After careful investigation, the dataset was developed considering the features of fiber content, fiber aspect ratio, fiber tensile strength, concrete compressive strength, steel yield strength, tension reinforcement ratio, transverse reinforcement ratio, reflected pressure, and reflected impulse. **Table 7-3** provides the mean, standard deviation, and range of each feature in the dataset, while **Figure 7-1** depicts their distributions.

Table 7-2. Average shock wave parameters produced by UOST Facility.

Blast ID	Driver Pressure (kPa)	Reflected Pressure (kPa)	Reflected Impulse (kPa msec)	Scaled Distance (m/kg^{1/3})	Equivalent Charge Weight (kg)
B-1	207	41	379.7	8.4	212
B-2	276	49.6	461.8	7.4	304
B-3	345	57.7	547.8	6.8	399
B-4	483	75.9	744.4	5.8	635
B-5	621	79.4	891.4	5.7	683
B-6	690	84.5	921.1	5.5	755

Table 7-3. Statistics of real data.

Feature	Mean	Standard Deviation	Range
Fiber content (%)	0.887	0.791	0 - 3
Fiber aspect ratio	41.294	27.531	0 - 78.95
Fiber tensile strength (MPa)	1400.602	1102.380	0 - 3150
Concrete compressive strength (MPa)	91.386	39.454	34 - 160
Steel yield strength (MPa)	568.078	188.699	430 - 929
Tension reinforcement ratio (%)	1.808	0.599	1 - 4.1
Transverse reinforcement ratio (%)	0.147	0.130	0 – 0.458
Reflected pressure (MPa)	0.045	0.017	0.0198 - 0.0942
Reflected impulse (MPa msec)	0.422	0.194	0.184 - 1.313
Maximum displacement (mm)	21.240	11.948	4.55 - 54.7

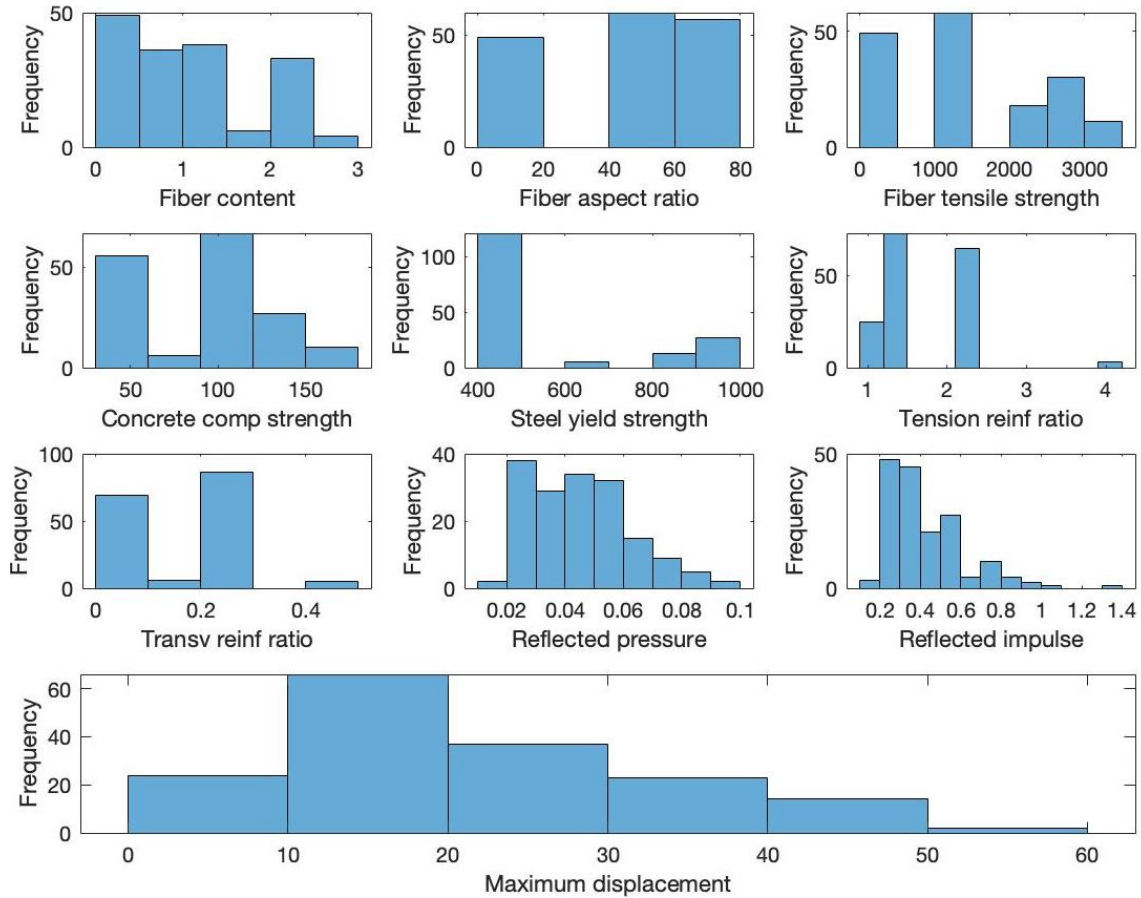


Figure 7-1. Distribution of features for real data.

The transverse reinforcement ratio was taken as the steel stirrup area over the area of the shear span and beam height. This allows for easier interpretation where lower ratio implies less reinforcement, with absence of reinforcement at zero. This contrasts with using stirrup spacings, which leads to more reinforcement at smaller values, but eliminating reinforcement at zero. It should be noted that the experimental studies conducted at UOST tested beam specimens under repeated blast loads. Therefore, during the data collection process, specimens that were reported to have reached element failure because of accumulated damage from multiple consecutive blast loading were discounted from the dataset. Additionally, specimens exhibiting behavioral anomalies that were reportedly due to issues with fiber concrete mixing were also disregarded.

7.3.3 Data from CTGAN

The 117 data points of SFRC beams and 50 data points of non-fiber RC beams were used to generate 300 synthetic data points using CTGAN. Each feature was considered continuous, which allowed for new feature values to be introduced, while remaining within an acceptable range of the original feature. Also, efforts were made towards maintaining consistency between the reflected pressure and reflected impulse pairs such that the shock wave parameters of the synthetic data resembled realistic pairs resulting from the UOST device. The mean, standard deviation, and range of the synthetic data are presented in **Table 7-4** along with their distributions shown in **Figure 7-2**. From a preliminary statistical assessment, it can be observed that both the real and synthetic data exhibit similar distributions with respect to their mean and standard deviation. Further evaluations of implementing synthetic data for ML model development are discussed in subsequent sections.

Table 7-4. Statistics of synthetic data.

Feature	Mean	Standard deviation	range
Fiber content (%)	1.173	0.749	0 - 2.86
Fiber aspect ratio	56.4	31.59	0-133
Fiber tensile strength (MPa)	1452.3	938.35	15-5105
Concrete compressive strength (MPa)	116.1	43.42	35-234
Steel yield strength (MPa)	595.2	218.64	68 - 1184
Tension reinforcement ratio (%)	2.04	0.918	0 - 5
Transverse reinforcement ratio (%)	0.23	0.187	0 – 0.786
Reflected pressure (MPa)	0.048	0.017	0.013 - 0.107
Reflected impulse (MPa msec)	0.468	0.16	0.152 - 1.025
Maximum displacement (mm)	24.1	11.04	2.6 - 62.8

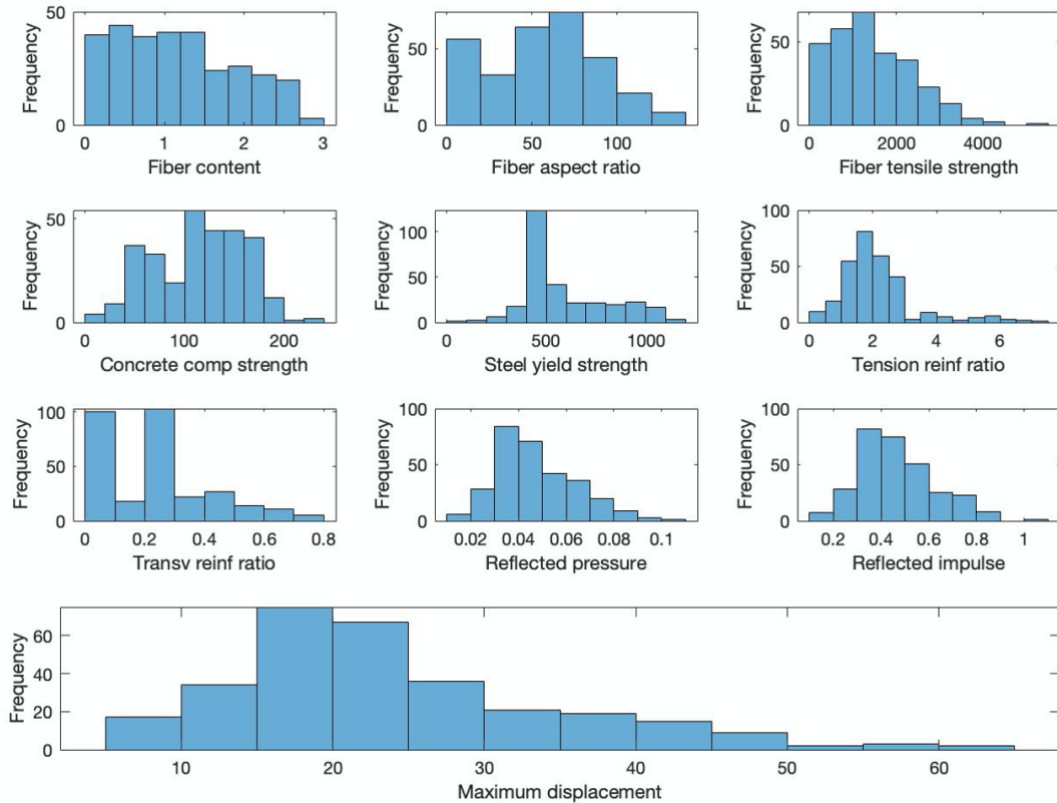


Figure 7-2. Distribution of features for synthetic data.

7.4 Results and discussion of model validation

This section explores the performance of the proposed model considering the different aforementioned training approaches using both graphical representations and statistical measures. Furthermore, the proposed model's implicit consideration of pertinent application parameters is reflected through constitutive material modeling and dynamic increase factor modeling. Lastly, a thorough comparison between the performance of existing analytical models and the proposed ML model is investigated.

7.4.1 Evaluation of model performance

The performance of the GP regression model was evaluated based on *MAE*, *MSE*, *MAPE*, and R^2 considering the training approach of cross-validation on only real data (GPR-CV), in addition to the approach of training on synthetic data and testing on real data (GPR-Syn). The response predictions were observed to exhibit a degree of noise. Accordingly, a

moving average smoothing approach was implemented [25]. **Figure 7-3** compares the actual and predicted responses (mean and variance) of the 117 data points pertaining to only those specimens incorporating steel fibers for the different modeling considerations. Similarly, **Table 7-5** reports the performance measures of each model consideration. Upon initial inspection, it can be observed that an overall acceptable fit of predicted values to the corresponding actual values is produced throughout the various considerations.

The effect of implementing smoothing is observed when comparing **Fig. 7-3(a)** and **Fig. 7-3(b)** as well as **Fig. 7-3(c)** and **Fig. 7-3(d)** in which relative outliers are mitigated, which resulted in improved model performance. The performance measures shown in **Table 7-5** also indicate significant reduction in the prediction error when smoothing was applied to both the GPR-CV and GPR-Syn models. It should be noted that predictions of new data points considering the smoothed model response were made with respect to the existing testing dataset. Therefore, every new data point prediction also requires predicting the existing test set, which is noted to be computationally trivial.

Table 7-5. Performance measures for different model considerations.

Model	MAE (mm)	MSE (mm)	MAPE (%)	R² (%)
GPR-CV	3.26	20.7	16.47	87.06
GPR-CV Smooth	2.29	9.72	10.58	93.9
GPR-Syn	2.75	15.5	13.8	90.32
GPR-Syn Smooth	1.87	6.74	8.71	95.8

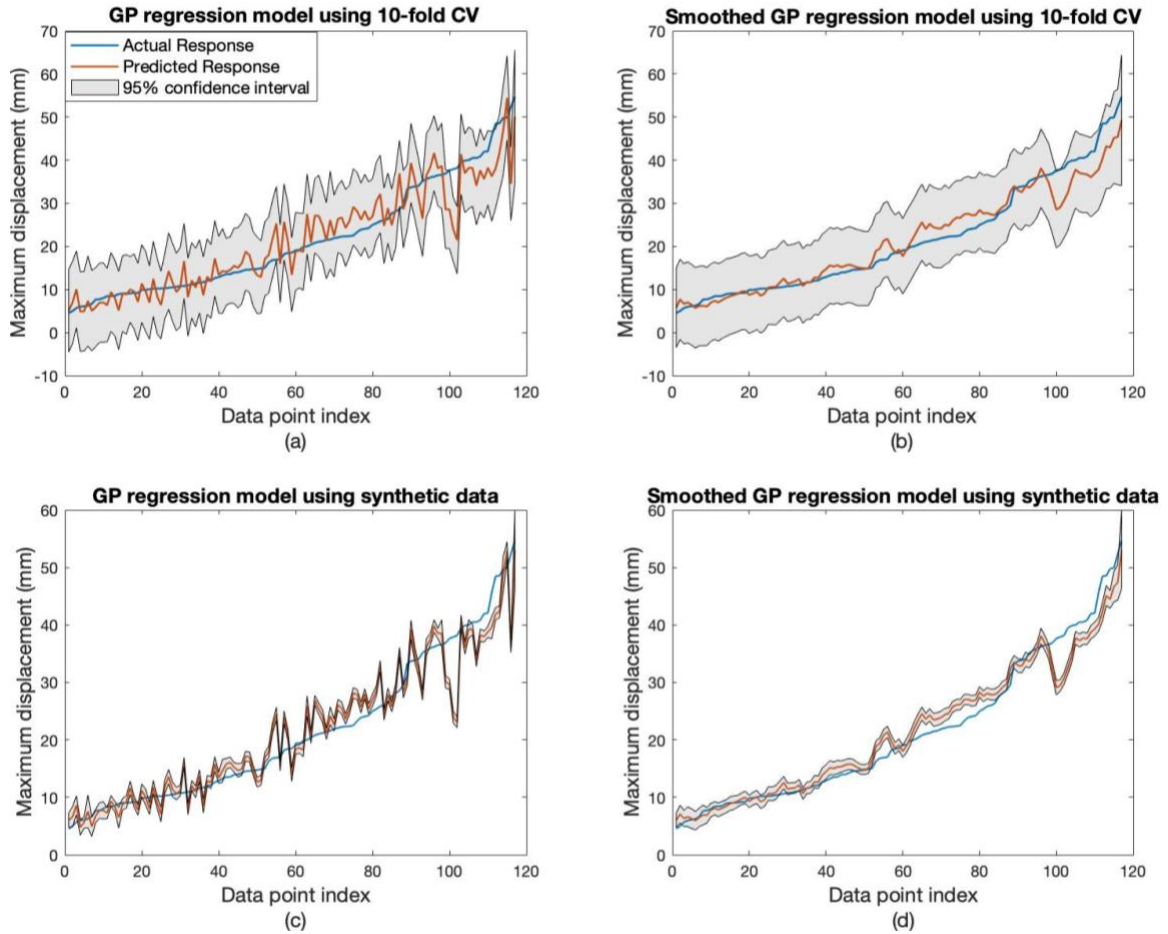


Figure 7-3. Actual versus prediction response plots for different model considerations.

Additionally, the effect of adopting synthetic data for model training, while testing on real data, as opposed to using traditional CV on only real data is depicted in **Fig. 7-3(a)** and **Fig. 7-3(c)**, as well as **Fig. 7-3(b)** and **Fig. 7-3(d)**. Synthetic data is not only shown to improve model performance, but also to reduce prediction variance. This improvement is also quantitatively represented in **Table 7-5** in which an increased correlation between actual and predicted responses through R^2 and reduced prediction errors through MAE , MSE , $MAPE$ are observed. The approach of the GPR-Syn model is remarkably practical for developing ML models using smaller datasets due to the independence of model development (training) from the real testing data, without sacrificing model performance, as demonstrated herein as well as in other studies [26,27].

The use of smoothing as well synthetic data both led to improved model performance when considered either independently or collectively. The best model performance was achieved by the GPR-Syn Smooth model, which attained superior predictive performance with minimal variance. To illustrate the aptitude of the GPR-Syn Smooth model, a scatter plot of actual and predicted values considering two error bounds is presented in **Fig. 7-4**. The figure shows that 64.1% (75) of the 117 data points were predicted within 10% error, while nearly 95% (111) of predictions were within a 20% error bound. Overall, the performance of the smoothed GP regression model trained with synthetic data was proven to effectively produce accurate predictions considering the complexity of the application.

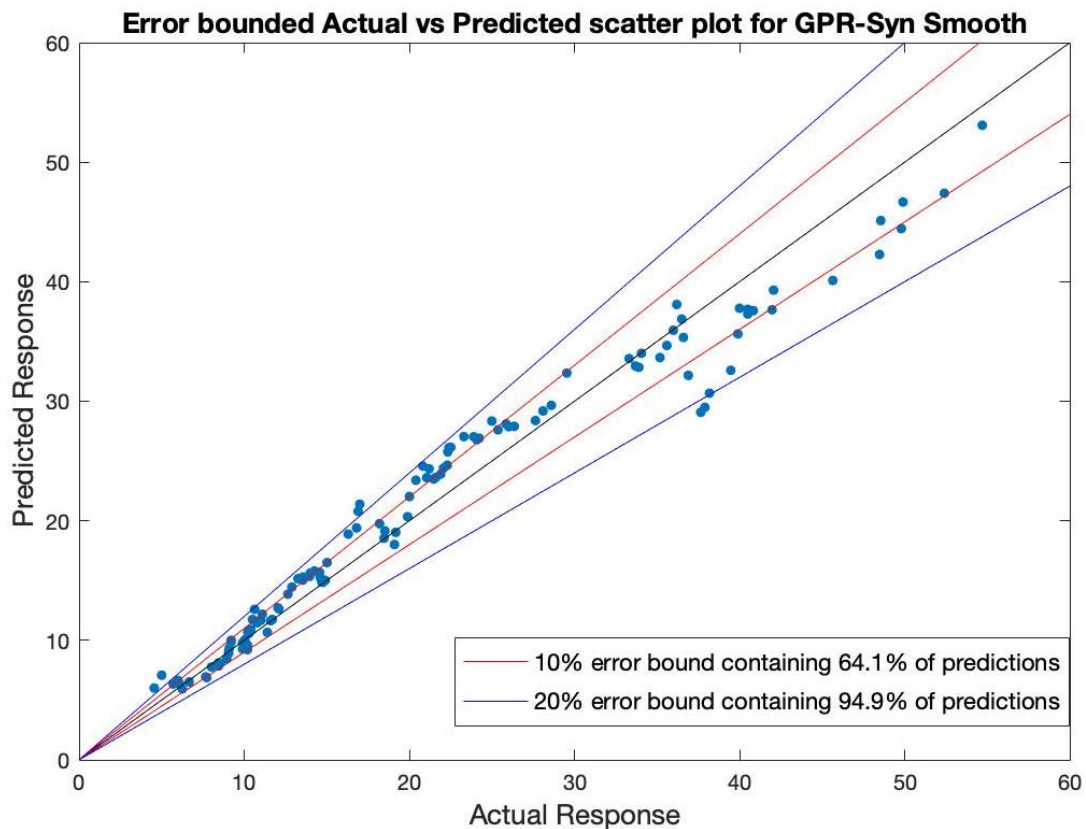


Figure 7-4. Actual versus prediction scatter plot with 10% and 20% error bounds.

7.4.2 Implicit application considerations

One of the most notable characteristics of the proposed model is its ability to capture implicit patterns of the application with respect to the limited explicitly defined features provided. The extent of these implicit patterns for the current application are primarily described through the static and dynamic behaviors of the materials considered in the dataset. As previously stated, the dataset is comprised of SFRC, HSFRC, and UHPFRC, which are characterized solely by their corresponding concrete compressive strength, steel fiber content, fiber aspect ratio, and tensile strength. Such information would be remarkably insufficient for predicting the behavior of these materials under blast loading by the diverse pertinent models that exist in the open literature. This is highlighted in the subsequent section in this text, which provides a brief description of empirically derived compression and tension material models that represent the behavior of SFRC, HSRFC, and UHPFRC, as well as strain-rate dependent models that characterize the dynamic behavior of such materials.

7.4.2.1 Compressive and tensile behavior of steel fiber concrete

A simplified compressive strength model for SFRC was developed by Ou *et al.* [28]. It was adapted from an existing stress-strain model for plain unconfined concrete as shown in Eq. (16), in which σ_c and ε_c are the stress and strain of SFRC, f'_c and ε_{co} are the compressive strength and strain at peak stress of plain concrete, and β is a material property [29]. The compressive strength model introduces a reinforcing index RI_v which accounts for the volumetric fiber content, fiber length, and fiber diameter as given by V_f , φ , and l in Eq. (17), respectively. Hence, f'_{cf} , ε_{cf} , and β were empirically defined as functions of RI_v as provided by Eqs. (18)-(16). The empirical model was developed based on forty cylindrical test specimens with an f'_c in the range of 36 to 47 MPa and RI_v in the range of 0 to 1.7.

$$\frac{\sigma_c}{f'_{cf}} = \frac{\beta \left(\frac{\varepsilon_{co}}{\varepsilon_{cf}} \right)}{\beta - 1 + \left(\frac{\varepsilon_{co}}{\varepsilon_{cf}} \right)^\beta} \quad (16)$$

$$RI_v = V_f(l/\varphi) \quad (17)$$

$$f'_{cf} = f'_c + 2.35(RI_v) \quad (18)$$

$$\varepsilon_{cf} = \varepsilon_{co} + 0.0007(RI_v) \quad (19)$$

$$\beta = 0.71(RI_v)^2 - 2(RI_v) + 3.05 \quad (20)$$

Similarly, an experimental study by Mansur *et al.* [1] investigated the compressive behavior of HSFRC for the characterization of a stress-strain model. The compressive strength of the cylindrical specimens considered were between 70 and 120 MPa, with steel fiber contents of 0.5% or 1%. The developed stress-strain model was a modified version of Eq. (16) and introduced two correction factors k_1 and k_2 which are valued at 1 for the ascending branch, but account for the influence of fiber parameters affecting the descending branch. The empirical expression for k_1 and k_2 is presented in Eq. (22), where RI_v is the same expression shown in Eq. (17). Also, the material property β is given by Eq. (23) in which E_t is the tangent modulus estimated by Eq. (24).

$$\frac{\sigma_c}{f'_c} = \frac{k_1 \beta \left(\frac{\varepsilon}{\varepsilon_o}\right)}{k_1 \beta - 1 + \left(\frac{\varepsilon}{\varepsilon_o}\right)^{k_2 \beta}} \quad (21)$$

$$k_1 = \left(\frac{50}{f'_c}\right)^3 [1 + 2.5(RI_v)^{2.5}] ; k_2 = \left(\frac{50}{f'_c}\right)^{1.3} [1 - 0.11(RI_v)^{-1.1}] \quad (22)$$

$$\beta = \frac{1}{1 - \frac{f'_c}{\varepsilon_o E_t}} \quad (23)$$

$$E_t = (10300 - 400V_f) f'_c{}^{0.33} \quad (24)$$

Furthermore, Hosinieh *et al.* developed a simplified quadrilinear stress-strain model to describe the unconfined compressive behavior of UHPFRC [30]. A limited number of cylindrical specimens were tested having a steel fiber content of 2.5% and producing compressive strengths between 124.6 and 137.8 MPa. The quadrilinear model defines four principle stress and strain values in which each strain expression is given in Eqs. (25)-(28). The ascending branch of the model reaches the first principal stress, $\sigma_1 = f'_c$, with a predefined modulus of elasticity, E_c , of 50 GPa. A constant stress branch is observed between ε_1 and ε_2 , after which a descending branch leads to ε_3 with a corresponding stress

value of $\sigma_3 = 0.5f'_c$. The incorporation of the steel fiber properties V_f , φ , and l in the model is observed in the final descending branch leading towards ε_4 with a stress value of zero.

$$\varepsilon_1 = f'_c/E_c \quad (25)$$

$$\varepsilon_2 = \varepsilon_1 + 0.002 \quad (26)$$

$$\varepsilon_3 = \varepsilon_2 + 0.002 \quad (27)$$

$$\varepsilon_4 = \varepsilon_3 + 0.00007(V_f l/\varphi) \quad (28)$$

Moreover, a trilinear stress-strain model for representing the tensile behavior of SFRC was developed by Lok and Pei [31]. The model accounts for the pre-cracking and post-cracking stages of SFRC in which the pre-cracking stage exhibits the same slope or elastic modulus in compression until the cracking stress, f'_{ct} , is reached. Upon cracking, the behavior is represented by two descending branches. The first branch decreases to a stress value of f_2^* with a corresponding strain of ε_2^* , followed by a second branch decreasing to a stress of zero with an approximated strain of 0.02 mm/mm. The value of f'_{ct} is estimated by Eq. (29) where σ_2^* and ε_2^* are given by Eqs. (30) and (31) in which τ_d is the dynamic bond stress assumed to be 3.5 MPa and E_{fp} is the elastic modulus of the steel fiber.

$$f'_{ct} = 0.33\sqrt{f'_c} \quad (29)$$

$$\sigma_2^* = \frac{1}{2} V_f \tau_d \frac{l}{\varphi} \quad (30)$$

$$\varepsilon_2^* = \tau_d \frac{l}{\varphi} \frac{1}{E_{fp}} \quad (31)$$

7.4.2.2 Strain-rate dependent behavior of steel fiber concretes

The rate at which the material is loaded, either in tension or compression, is a significant factor that affects measured material strengths. To account for such effects, dynamic increase factors (DIF) are employed alongside static strengths to determine a materials respective dynamic strength [4]. Multiple experimental studies have reported the strain-

rate sensitivity of SFRC in both tension and compression [4, 32]. Consequently, comprehensive DIF models have been developed to accommodate such loading.

A recent study by Yang *et al.* [32] established a well-rounded compression DIF (CDIF) model for SFRC considering static compressive strengths between 120 and 165 MPa, steel fiber contents between 0.5% and 6%, and diverse fiber shapes. The analytical formulation for the model is shown in Eq. (32). The values of δ and β are given by Eq. (33), where K is a constant representing the fiber shape, f_c is the static compressive strength of concrete, and f_{co} is 10 MPa. Also, $\dot{\epsilon}_s$ is the static strain rate being $3 \times 10^{-5} \text{ s}^{-1}$, $\dot{\epsilon}_t$ is the transition strain rate, and i is a factor representing the fiber content.

$$CDIF = \begin{cases} \left(\frac{\dot{\epsilon}}{\dot{\epsilon}_s}\right)^{1.026\delta} & , \dot{\epsilon} < \dot{\epsilon}_t \\ 0.6608\beta\left(\frac{\dot{\epsilon}}{\dot{\epsilon}_s}\right)^{\frac{1+0.05i}{3}} & , \dot{\epsilon} \geq \dot{\epsilon}_t \end{cases} \quad (32)$$

$$\delta = \frac{1}{5+9\frac{f_c}{f_{co}}} ; \log\beta = 6.156K\delta - 2.33 \quad (33)$$

Within the same study [32], an equivalent tension DIF (TDIF) model was developed for SFRC, which accounts for specimens having static compressive strengths between 56 and 190 MPa, steel fiber contents between 1% and 3%, and varying fiber shapes. The resulting analytical formulation is presented in Eq. (34), with corresponding expressions of δ and β given by Eq. (35). The value for $\dot{\epsilon}_s$ is given as $1 \times 10^{-6} \text{ s}^{-1}$ and m is a factor representing the fiber content.

$$TDIF = \begin{cases} \left(\frac{\dot{\epsilon}}{\dot{\epsilon}_s}\right)^{K\delta} & , \dot{\epsilon} \leq \dot{\epsilon}_t \\ m\beta\left(\frac{\dot{\epsilon}}{\dot{\epsilon}_s}\right)^{\frac{1}{3}} & , \dot{\epsilon} > \dot{\epsilon}_t \end{cases} \quad (34)$$

$$\delta = \frac{1}{1+8\frac{f_c}{f_{co}}} ; \log\beta = 7K\delta - 2.141 \quad (35)$$

Based on the material models and DIF models presented above, which characterize the complex behavior of steel fiber concretes, it can be notably realized that, in the absence of such analytical behavior representations, the proposed ML model was still able to

accurately incorporate such materials in blast load applications. This indicates an underlying capacity of ML models to learn implicit correlations within a given dataset of explicitly defined features. As a result, this quality strongly motivates the implementation of ML in modeling highly complicated applications.

To further support such motivation, a recent study by Yang *et al.* [33] used a novel ML approach to model the CDIF and TDIF of SFRC, as opposed to developing an analytical formula. A Random Forests algorithm was implemented in developing each model, in which model hyperparameters were optimized using the Firefly Algorithm, which is a well-known metaheuristic algorithm. Using 193 and 314 data points for developing the CDIF and TDIF models, the resulting R^2 values were 87.4% and 90%, respectively. The noteworthy performance of the models considered the features of fiber content, fiber aspect ratio, fiber tensile strength, fiber shape, concrete compressive strength, and strain rate. The range of each feature along with details on model development are available in [33].

Additionally, a more recent study developed an ML model to predict the maximum displacement of RC slabs subjected to both near-field and far-field blast loading [34]. Considering ten application features and 150 data points compiled from the literature, a classification-regression Random Forests model was developed yielding an R^2 value of 96.2%. The model was proven to be highly proficient in recognizing the importance of features which correlated well to experimental findings. The predictive performance of the model was also found to be competitive with the performance of several existing analytical and numerical models. The limitations and discrepancies of the model were also investigated, which identified opportunities for further improvements.

7.4.3 Comparisons to existing prediction methods

To appraise the performance of the proposed model with respect to existing prediction methods, this section compiles the predictions of several alternative models in the literature. Comparisons of consistent data points between the ML model and the alternative models are made with respect to experimental results and are divided into seven sets (Sets A-G). The different alternative models considered are various dynamic SDOF models and a 2D numerical model using the finite element software VecTor2 [35]. Each comparison

set is shown in **Table 7-6**, which lists the alternative model, number of predictions compared, and the respective model reference. Additionally, the beam material types (concrete; reinforcement) and fiber details (type; content) used by each model are provided in which the fiber types are based on **Table 7-1**. It should be noted that Sets F and G use the same comparison data as Sets B and C but consider different prediction models.

Table 7-6. Comparisons between the ML model and alternative prediction models.

Set	Alt. Model	# of tests	Beam details	Fiber type & content	Alt. model <i>MAPE</i> (%)	ML model <i>MAPE</i> (%)	Alt. model R^2	ML model R^2
A	[6] SDOF	41	UHPSFRC; NSR,HSR	F1, F2; 1%, 2%, 3%	16.24	9.92	91.88	97.33
B	[7] SDOF	20	HSFRC; NSR	F4, F5; 0.5%, 1%	13.65	6.61	96.1	98.14
C	[8] SDOF	12	HSFRC; HSR	F4; 1%	9.76	7.96	95.85	90.68
D	[9] SDOF	25	SFRC; NSR	F3,F4,F5;0.5%,0.75%, 1%, 1.5%	19.97	9.51	75.08	94.49
E	[10] SDOF	8	HSFRC; NSR	F1, F4; 0.75%	10.62	5.53	96.94	99.52
F	[36] SDOF with AD	20	HSFRC; NSR	F4, F5; 0.5%, 1%	9.64	6.61	96.8	98.14
G	[23] VecTor2	12	HSFRC; HSR	F4; 1%	7.82	7.96	97.3	90.68

Based on the results of the comparisons for Sets A-E in **Table 7-6**, it can be observed that the ML model outperformed the dynamic SDOF model in both *MAPE* and R^2 for all comparison sets except Set C. Although the ML model produced better *MAPE* than Set C, the lower R^2 value indicated a reduced correlation between the prediction and experimental values, which was due to Set C having fewer outliers in this case. It can also be observed that the SDOF model displayed favorable performance when limited fiber variations are considered, as shown for Sets B, C, and E. Conversely, the SDOF model attained lower performance for Sets A and D, likely because of a relatively larger range of fiber variations. Moreover, the alternative prediction model in Set F utilized an improved SDOF, which accounted for the accumulated damage (AD) imposed on the test specimens [36]. The

extent of this improvement is observed when comparing Sets F and B in which a lower *MAPE* and higher R^2 are produced. Similarly, Set G implements a numerical prediction model, VecTor2, which led to more favorable prediction when compared to the SDOF model in Set C for the same data. In Set F, the ML model was shown to yield better results than the improved SDOF model, whereas in Set G the ML model produced similar *MAPE* but lower R^2 value, which was similarly observed in Set C.

A graphical representation for the comparisons of Sets A-G considering the correlation coefficient, *RMSE*, and standard deviation for each set is provided by the Taylor Diagram depicted in **Fig. 7-5** generated using the tool in [37]. It can be observed in **Fig. 7-5** that the proposed ML model produces more accurate predictions (lower *RMSE*) and higher correlation to the actual experimental data than the alternative models for almost all the considered datasets, while performing comparably to the numerical model of Set G.

It is noteworthy that the ML model was more competent in considering different fiber types and fiber contents, which is a product of implicitly learning the underlying effects of such features through the provided dataset. It should also be noted that this flexibility in accounting for the features of the application may only be achieved given the availability of sufficiently reliable data. In the current model, the entire dataset was sourced from the same testing facility, which allowed for reduced variability due to consistent workmanship, experimental procedure, and data collection strategy, thereby improving the quality of the dataset. However, since the dataset is comprised of several different materials with significantly varying behaviors, the observed error of the ML mode is primarily caused by the degree of its inability to capture certain application behaviors. A solution for this discrepancy would be to identify these behavioral gaps from the existing dataset and obtaining new authentic data explaining such gaps, thus reducing the degree of error. Nonetheless, the proposed ML outperformed existing models despite that it only relies on simplified inputs, while eliminating the high degree of modeling complexity associated with SDOF or finite element based existing models.

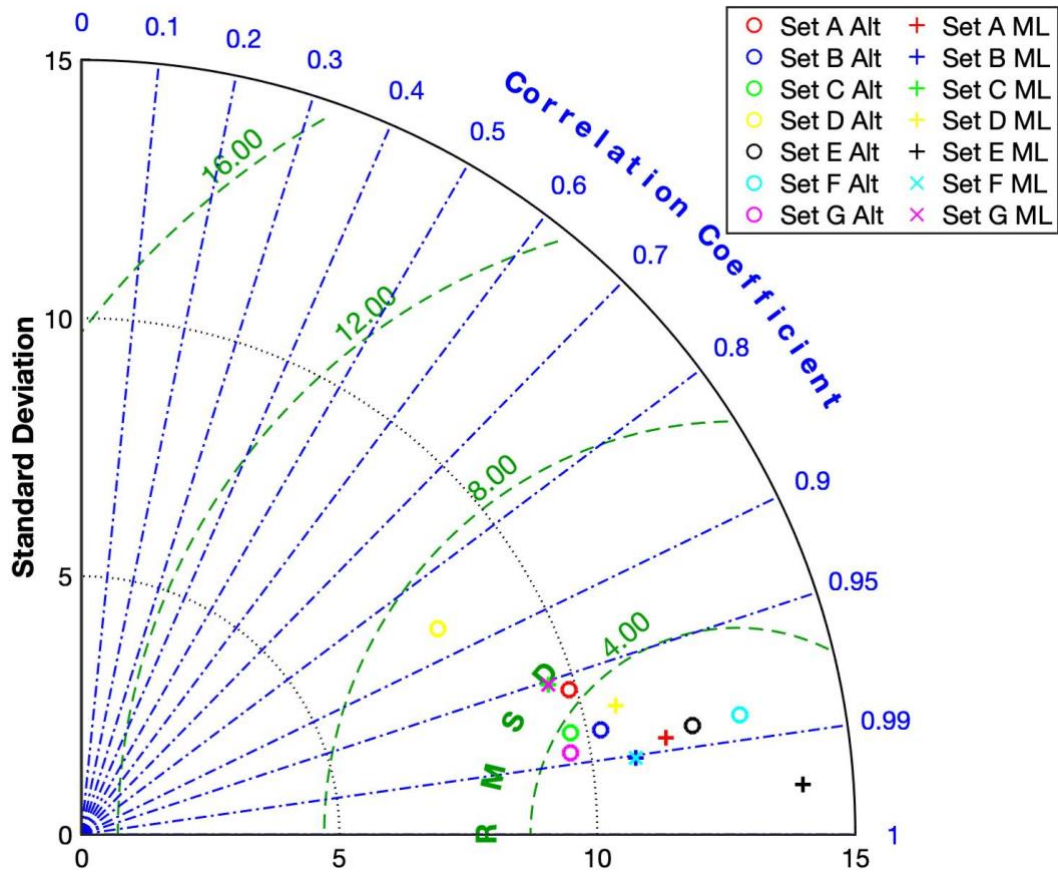


Figure 7-5. Taylor Diagram representing model comparisons for Sets A-G.

7.5 Parametric analysis

It was demonstrated above that the developed ML model attained highly acceptable results, while acquiring a favorable comprehension of the relevant application parameters. Model predictions were made without any predefinition of complex material models or strain-rate sensitive DIFs. Instead, the model learned correlations between and interactions of features resulting from experimental findings. Thus, an extensive parametric analysis is conducted to elucidate the behavior of steel fiber-reinforced concrete behavior subjected to far-field blast loading.

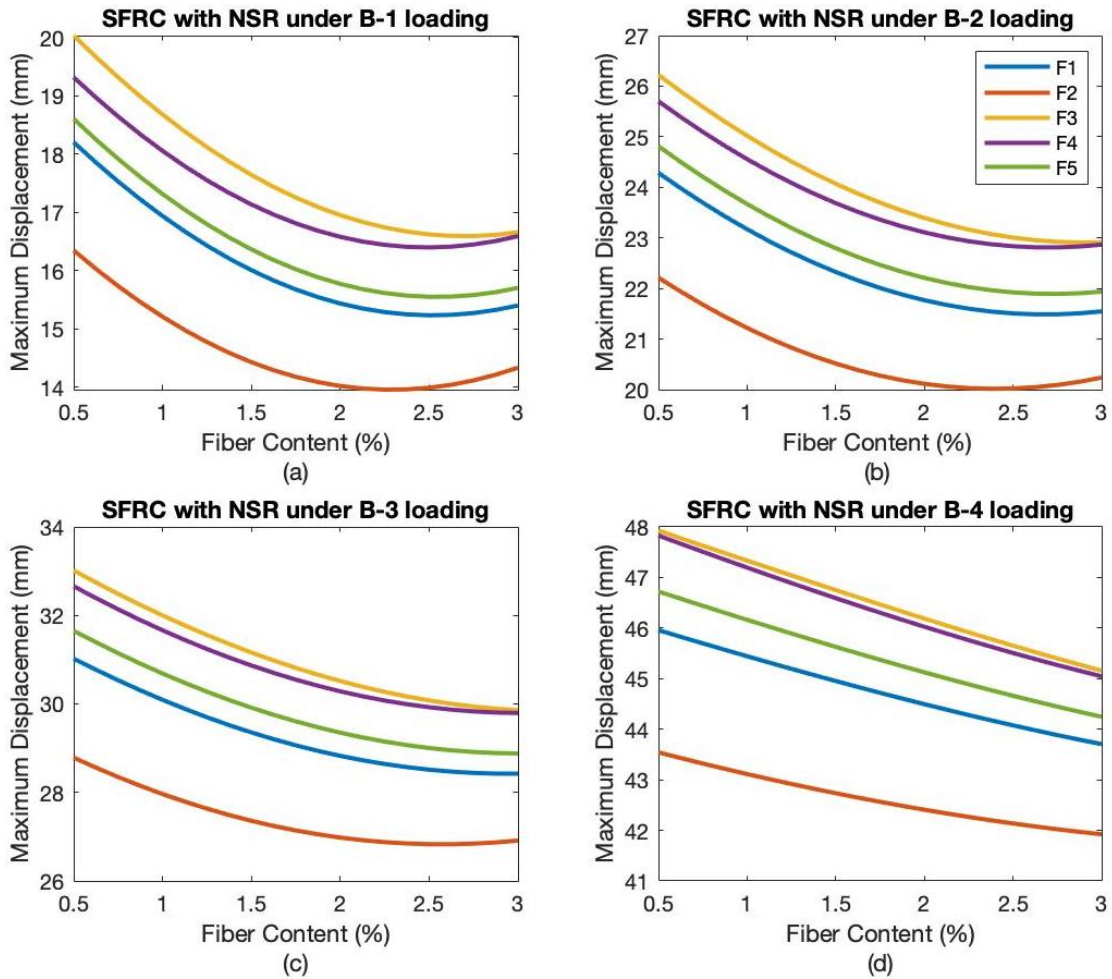


Figure 7-6. Effect of fiber parameters on maximum displacement of SFRC beams with NSR.

The parametric analysis primarily investigates the effects of different fiber types at varying contents for beams of SFRC with NSR, UHPFRC with NSR, and UHPFRC with HSR. The compressive strengths of SFRC and UHPFRC are taken as 40 MPa and 150 MPa, while the steel yield strengths of NSR and HSR are taken as 420 MPa and 900 MPa, respectively. The different fiber types considered are listed in **Table 7-1** and fiber contents range from 0.5% to 3%. The tension and transverse reinforcement ratios for all cases remained constant at 2.4% (two 20M bars) and 0.244% (equivalent to stirrup spacing of 100 mm), respectively. **Figures 7-6 to 7-8** represent each beam type and are divided into parts (a) to (d), which refer to different magnitudes of far-field blast loading (B-1, B-2, B-3, and B-4) corresponding to **Table 7-2**.

The first parametric evaluation considers SFRC beams with NSR, as shown in **Fig. 7-6**. It can be observed that an increase in the fiber content produces a reduction in the maximum displacement for all loading cases. However, a clearly limiting effect is noted for lower and intermediate magnitudes of loading as shown in **Figs. 7-6(a) to 7-6(c)**, which indicates no further enhancement beyond 2% fiber content. An alternative response is shown in **Fig. 7-6(d)**, which suggests that at higher magnitudes of blast loading, an increase in the fiber content enhance performance under blast loading. Similar response was observed in [9] where a limiting fiber content was reported when considering 0.5%, 0.75%, 1%, and 1.5% fiber contents at lower and intermediate blast magnitudes using the UOST Facility. For higher blast magnitudes, a decrease in maximum displacement at higher fiber contents was also observed, but a clear trend was hindered by element failures, which were reportedly caused by issues in concrete mixing and placement. Additionally, the study considered different fiber types (F3, F4, F5) where F5 produced the lowest displacement in multiple instances, whereas F3 and F4 resulted in the lowest displacement in fewer instances. This comparison of fiber types coincides with the response shown in **Fig. 7-6**, which also indicates that fiber type F5 achieved greatest performance. Using the same testing facility, a second study which utilized fiber contents of 0.5% and 1% for SFRC beams reinforced with NSR also concluded that increased structural performance was directly related to an increase in fiber content [11]. These supporting studies indicate that **Fig. 7-6** accurately captures the responses for the given beam type. Although using steel fibers improves the blast performance of SFRC beams, a crucial complementary analysis is the identification of the corresponding failure mode. While such analyses are beyond the scope of current study, a brief pertinent discussion is provided below.

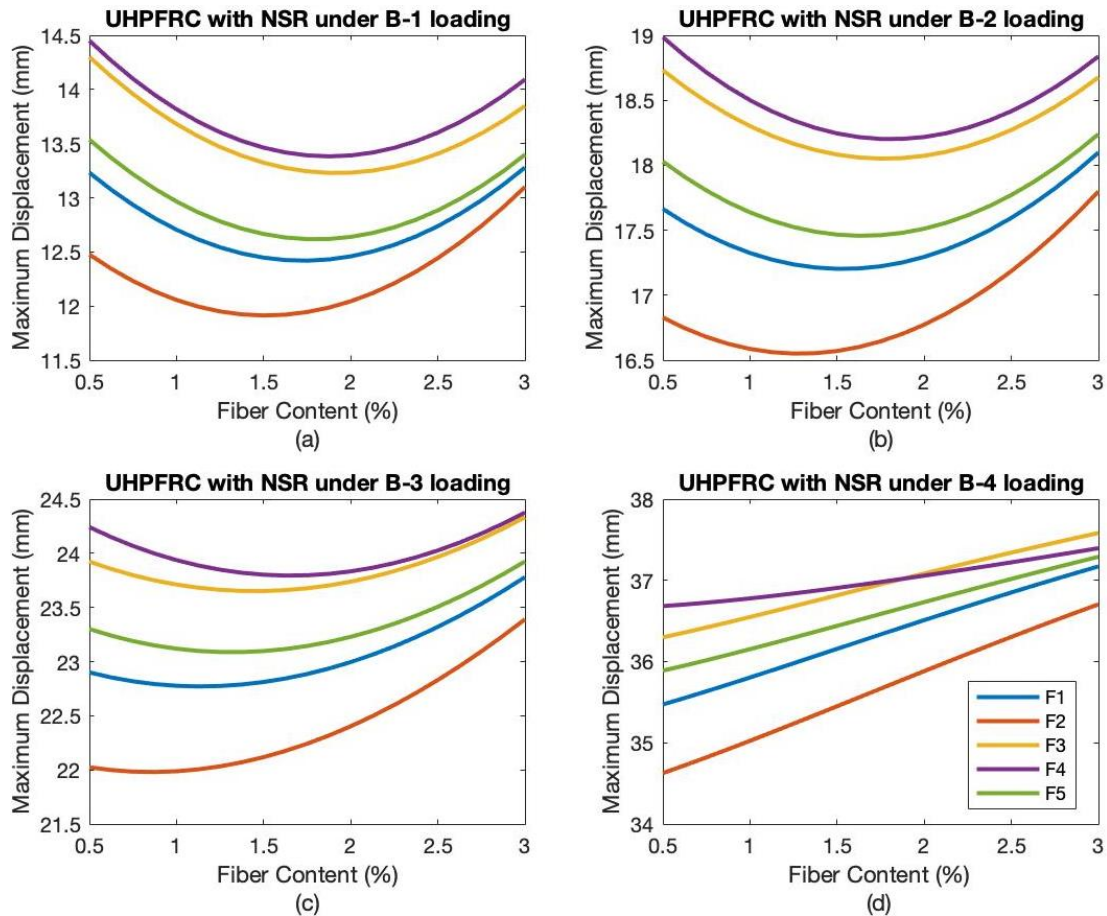


Figure 7-7. Effect of fiber parameters on maximum displacement of UHPFRC beams with NSR.

For UHPFRC beams with NSR, **Fig. 7-7** depicts significantly different behaviors than the previously evaluated for SFRC beams. It can be observed from **Figs. 7-7(a) to 7-7(c)** that the maximum displacement follows a U-shaped trend with an optimal fiber content that decreases with increased blast magnitude. This implies that the addition of steel fibers improves the structural performance of UHPFRC with NSR until a certain threshold limit, after which a reduction in performance occurs with added fibers. It can also be observed in **Fig. 7-7(d)** that at a higher blast magnitude, the provision of steel fibers produces an adverse effect, which results in greater maximum displacements.

Limited experimental findings suggest that a similar response was observed when testing a similar beam type with 1%, 2%, and 3% fiber content (although without stirrups) using the UOST facility [6]. For several blast magnitudes, an increase in maximum displacement

resulted from 2% fiber content compared to using 1%; however, using 3% fiber content resulted in a reduction of displacement. This result is partially inconsistent with the responses shown in **Fig. 7-7**. An additional study at the same facility considered fiber contents of 0.5% and 1% for HSFRC (100 MPa) with NSR [7]. For all instances of comparison at high blast magnitudes, incorporating greater fiber content resulted in a greater maximum displacement, which concurs with the trends provided in **Fig. 7-7**.

To further support the trends in **Fig. 7-7**, additional context for fiber-reinforced concrete and additional experimental findings are provided. A unique material property of high-performance fiber-reinforced concrete is its ability to induce a deflection-hardening behavior, resulting in the production of multiple cracks, which translates into higher energy dissipation. This is observed upon the development of the first crack and continues until the maximum post-cracking stress is applied. Exceeding this stress value produces a critical crack that signifies the onset of crack localization, where additional deformation will no longer produce new cracks, but instead will widen the critical crack. The widening of the critical crack is then characterized by a deflection-softening behavior [38]. For high-performance fiber-reinforced concrete under dynamic loading, a similar behavior is observed [39]. Conversely, normal fiber-reinforced concrete exhibits crack localization and thereby deflection-softening behavior upon reaching the first crack [38]. Furthermore, for SFRC beams reinforced with NSR, the crack localization has recently been experimentally investigated and found to be more pronounced at larger fiber contents [40]. In another study, UHPFRC beams were tested under flexure and it was reported that beams which exhibited crack localization induced localized deformation on the tension reinforcement. This resulted in significantly higher stresses of the tension bars and resulted in rebar rupture (at smaller reinforcement ratio of 0.94% and 1.5%) [41].

Accordingly, it could be posited that increased fiber content may result in more dominant localized crack, which in turn induces greater stress (and therefore strain) on the tension bars at greater blast magnitudes. Provided that sufficient tension reinforcement is in place and rebar rupture does not occur, the induced localized strain would develop into increased maximum displacement during blast loading. This would ultimately result in a fiber pullout failure mode due to the increasing width of the localized crack. Such a failure mode was

evidently reported by blast loaded UHPFRC and HSFRC beams at more significant blast magnitudes with varying fiber contents in [6] and [7]. Based on this overall discussion of material properties, observed behaviors, and experimental findings, it can be stated that the behavior observed in **Fig. 7-7** depicts acceptable trends.

Figure 7-8 illustrates the behavior of UHPFRC beams made with HSR considering various blast magnitudes. Similar to the previous section, the behavior with respect to fiber content follows a U-shaped trend. However, considering the material property of HSR having a notably greater yield strength than NSR, strains due to crack localization of UHPFRC would result in less displacement. This reduced effect of fiber content on maximum displacement can be observed in **Figs. 7-8(a) to 7-8(d)** when compared to **Figs. 7-7(a) to 7-7(d)**. Another major variation between the two beam types is that under higher magnitudes of blast load, the failure mode of UHPFRC with HSR would result in rebar rupture instead of fiber pullout, which was also observed in [6]. This failure mode is further supported by the strains, where HSR ruptures at 0.06 mm/mm strain, while NSR ruptures at 0.17 mm/mm [6]. Thus, the behavior of this beam type expands on the previous section and is appropriately depicted in **Fig. 7-8**.

Considering the overall effect of fiber types among different beam types in **Figs. 7-6 to 7-8**, it can be observed that the fibers having shortest length, F1 and F2, attained the highest blast performance. Considering fibers F1 and F2 alone, a similar conclusion was reached in [6]. Although using alternative fiber types, another study [9] reported that higher blast performance resulted from using larger aspect ratio fibers. Similarly, the use of shorter steel fibers led to enhanced blast resistance than longer fibers in [7]. Therefore, it can be concluded that both greater aspect ratio and shorter steel fibers provide highest performance with respect to both experimental studies as well as the parametric study.

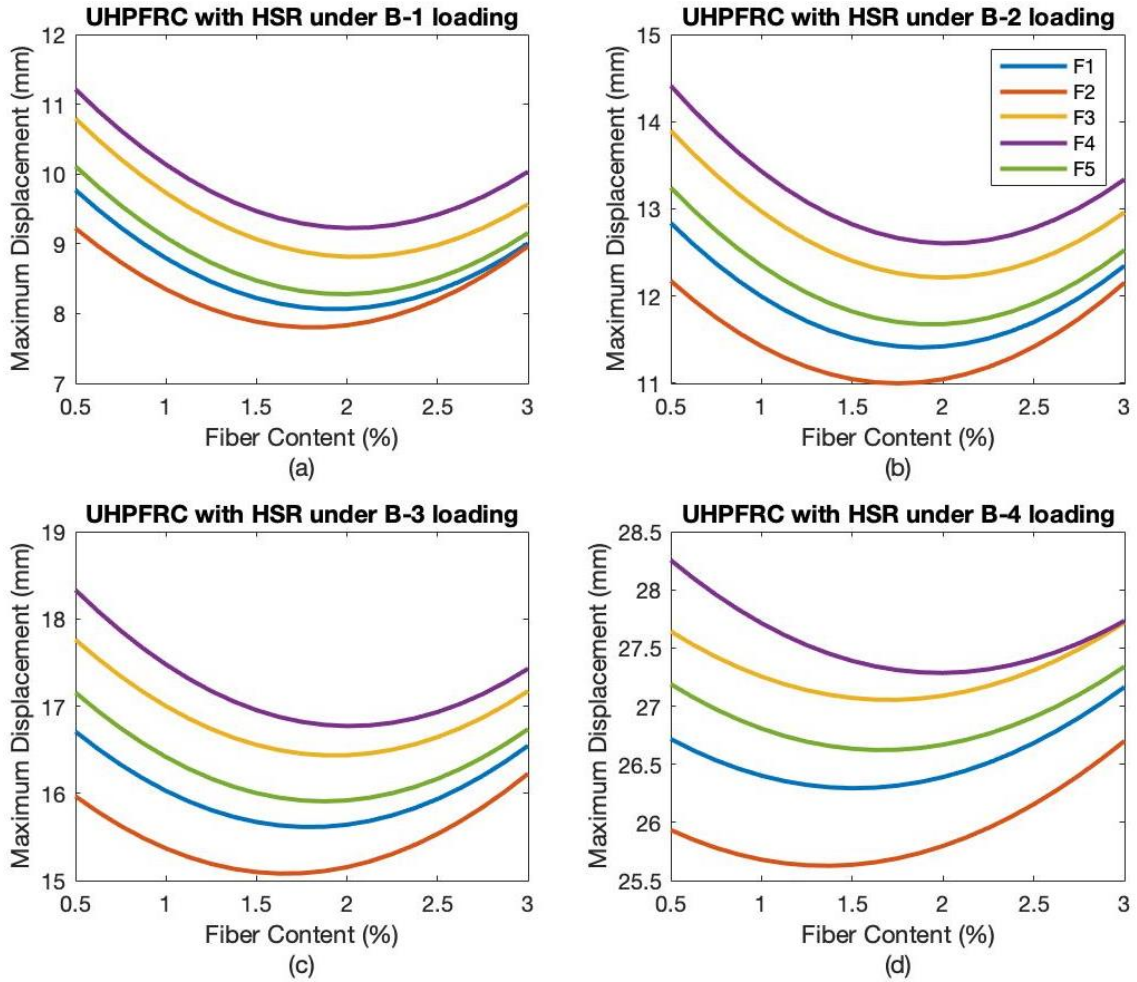


Figure 7-8. The effect of fiber parameters on UHPFRC beams with HSR.

The proposed ML model predicts only the global maximum displacement of beams in the current application. However, to better capture the response of such beam types, a complementary local damage prediction model is required. As a result, additional considerations have been made as part of an ongoing study for developing a classification model to predict the local damage response of steel fiber-reinforced concrete subjected to blast loading. This failure mode classification model, paired with the currently developed displacement prediction model, would provide exceedingly simplified and meaningful response predictions of steel fiber-reinforced concrete beams under blast loading.

7.6 Conclusions

The present chapter develops a simplified machine learning model to predict the maximum displacement of SFRC, HSFRC, and UHPFRC beams subjected to far-field blast loading. A GP regression model was implemented alongside CTGAN and considered the features of fiber content, fiber aspect ratio, fiber tensile strength, concrete compressive strength, steel yield strength, tension reinforcement ratio, transverse reinforcement ratio, reflected pressure, and reflected impulse. Multiple performance measures were used to assess the proposed model, which was trained considering either real data or synthetic CTGAN data. Both static and dynamic material models for each SFRC were provided and used to reflect on the proposed model's implicit considerations. Lastly, a comprehensive parametric study was conducted, which considered the effect of varying fiber types and contents for the different beam configurations considered in this chapter. The following conclusions can be drawn:

- The use of GP regression was highly appropriate in modeling this complex application despite the limited data available. The model attained higher performance when synthetic CTGAN generated data was used for model training, while the entire real dataset is used for model testing.
- The statistical performance metrics for the proposed model resulted in a *MAE* of 1.87, a *MSE* of 6.74, an R^2 of 95.8%, and a *MAPE* of 8.71%.
- The proposed model was highly competent in capturing variations among different steel fiber-reinforced concretes and steel reinforcement types, while not requiring the provision of material models or DIF models.
- When compared to existing analytical models, the proposed model effectively produced more accurate predictions, while achieving similar performance to a numerical predictive model.
- Based on the parametric analysis, it was observed that the performance of SFRC beams with NSR increased with increasing fiber content at higher magnitudes of blast loading.

- For UHPFRC concrete beams with NSR, the increase of the fiber content produced a lower blast performance at higher blast magnitudes, while producing a limiting effect at lower magnitudes.
- For UHPFRC concrete beams with HSR, an enhanced blast performance was observed with an increase in the fiber content until a critical threshold content was reached. Exceeding this critical content resulted in reduced blast performance.
- In terms of fiber types, the use of shorter steel fibers with larger aspect ratio was most effective in improving blast resistance.
- Overall, the proposed model effectively captures both the behavior of various fiber-reinforced concrete beams subjected to blast loading and yielded favorable accuracy in predicting their maximum displacements.
- Future development of a failure mode classification model, paired with the currently developed displacement prediction model, would provide a highly simplified response prediction model for steel fiber-reinforced concrete beams under blast loading.

7.7 Chapter references

- [1] Mansur, M. A., Chin, M. S., & Wee, T. H. (1999). Stress-strain relationship of high-strength fiber concrete in compression. *Journal of materials in civil engineering*, 11(1), 21-29.
- [2] Kwan, A. K. H., & Chu, S. H. (2018). Direct tension behaviour of steel fibre reinforced concrete measured by a new test method. *Engineering Structures*, 176, 324-336.
- [3] Song, P. S., & Hwang, S. (2004). Mechanical properties of high-strength steel fiber-reinforced concrete. *Construction and Building Materials*, 18(9), 669-673.
- [4] Wang, Z. L., Shi, Z. M., & Wang, J. G. (2011). On the strength and toughness properties of SFRC under static-dynamic compression. *Composites Part B: Engineering*, 42(5), 1285-1290.
- [5] Yoo, D. Y., & Banthia, N. (2017). Mechanical and structural behaviors of ultra-high-performance fiber-reinforced concrete subjected to impact and blast. *Construction and building materials*, 149, 416-431.

- [6] Guertin-Normoyle, C. (2018). *Blast Performance of Ultra-High Performance Concrete Beams Tested Under Shock-Tube Induced Loads* (Master's Thesis, Université d'Ottawa/University of Ottawa).
- [7] Algasseem, O. (2016). *Parameters Affecting the Blast Performance of High Strength Fibre Reinforced Concrete Beams* (Master's Thesis, Université d'Ottawa/University of Ottawa).
- [8] Li, Y. (2016). *Blast Performance of Reinforced Concrete Beams Constructed with High-Strength Concrete and High-Strength Reinforcement* (Master's Thesis, University of Ottawa).
- [9] Castonguay, S. (2017). *Performance of Steel Fiber-Reinforced Concrete Beams Under Shock Tube Induced Blast Loading* (Master's Thesis, Université d'Ottawa/University of Ottawa).
- [10] Charles, C. J. (2019). *Effects of Detailing and Fibers on the Static and Blast Behavior of High-Strength Concrete Beams* (Master's Thesis, Université d'Ottawa/University of Ottawa).
- [11] Lee, J. Y., Shin, H. O., Yoo, D. Y., & Yoon, Y. S. (2018). Structural response of steel-fiber-reinforced concrete beams under various loading rates. *Engineering Structures*, 156, 271-283.
- [12] Rasmussen CE, Williams CKI. (2006). Gaussian processes for machine learning. The MIT Press, Cambridge
- [13] Schulz, E., Speekenbrink, M., & Krause, A. (2018). A tutorial on Gaussian process regression: Modelling, exploring, and exploiting functions. *Journal of Mathematical Psychology*, 85, 1-16.
- [14] Arthur, C. K., Temeng, V. A., & Ziggah, Y. Y. (2020). Novel approach to predicting blast-induced ground vibration using Gaussian process regression. *Engineering with Computers*, 36(1), 29-42.
- [15] Nocedal, J. and S. J. Wright. *Numerical Optimization*, Second Edition. Springer Series in Operations Research, Springer Verlag, 2006, 139-141.
- [16] MathWorks, (2020). *Statistics and Machine Learning Toolbox™: User's Guide (R2020b)*. Retrieved March 4, 2021 from https://www.mathworks.com/help/pdf_doc/stats/stats.pdf
- [17] Xu, L., & Veeramachaneni, K. (2018). Synthesizing tabular data using generative adversarial networks. *arXiv preprint arXiv:1811.11264*.
- [18] Xu, L., Skoularidou, M., Cuesta-Infante, A., & Veeramachaneni, K. (2019). Modeling tabular data using conditional gan. *arXiv preprint arXiv:1907.00503*.

- [19] Hyndman, R. J., & Koehler, A. B. (2006). Another look at measures of forecast accuracy. *International journal of forecasting*, 22(4), 679-688.
- [20] Kim, S., & Kim, H. (2016). A new metric of absolute percentage error for intermittent demand forecasts. *International Journal of Forecasting*, 32(3), 669-679.
- [21] Nakagawa, S., & Schielzeth, H. (2013). A general and simple method for obtaining R² from generalized linear mixed-effects models. *Methods in ecology and evolution*, 4(2), 133-142.
- [22] Lloyd, A., Jacques, E., Saatcioglu, M., Palermo, D., Nistor, I., & Tikka, T. (2011). Capabilities and effectiveness of using a shock tube to simulate blast loading on structures and structural components. *Behavior of Concrete Structures Subjected to Blast and Impact Loadings, ACI-SP*, 281.
- [23] Li, Y., & Aoude, H. (2020). Influence of steel fibers on the static and blast response of beams built with high-strength concrete and high-strength reinforcement. *Engineering Structures*, 221, 111031.
- [24] Canadian Standards Association. (2014). Design of Concrete Structures (CSA A23.3-14). *CSA Group, Mississauga, ON, Canada*.
- [25] MathWorks, (2020). *Curve Fitting Toolbox™: User's Guide (R2020b)*. Retrieved March 4, 2021 from https://www.mathworks.com/help/pdf_doc/stats/stats.pdf
- [26] Marani, A., Jamali, A., & Nehdi, M. L. (2020). Predicting Ultra-High-Performance Concrete Compressive Strength Using Tabular Generative Adversarial Networks. *Materials*, 13(21), 4757.
- [27] Chaabene, W. B., & Nehdi, M. L. (2021). Genetic programming based symbolic regression for shear capacity prediction of SFRC beams. *Construction and Building Materials*, 280, 122523.
- [28] Ou, Y. C., Tsai, M. S., Liu, K. Y., & Chang, K. C. (2012). Compressive behavior of steel-fiber-reinforced concrete with a high reinforcing index. *Journal of Materials in Civil Engineering*, 24(2), 207-215.
- [29] Carreira, D. J., & Chu, K. H. (1985, November). Stress-strain relationship for plain concrete in compression. In *Journal Proceedings* (Vol. 82, No. 6, pp. 797-804).
- [30] Hosinieh, M. M., Aoude, H., Cook, W. D., & Mitchell, D. (2015). Behavior of ultra-high performance fiber reinforced concrete columns under pure axial loading. *Engineering Structures*, 99, 388-401.
- [31] Lok, T. S., & Pei, J. S. (1998). Flexural behavior of steel fiber reinforced concrete. *Journal of materials in civil engineering*, 10(2), 86-97.

- [32] Yang, L., Lin, X., & Gravina, R. J. (2018). Evaluation of dynamic increase factor models for steel fibre reinforced concrete. *Construction and building materials*, 190, 632-644.
- [33] Yang, L., Qi, C., Lin, X., Li, J., & Dong, X. (2019). Prediction of dynamic increase factor for steel fibre reinforced concrete using a hybrid artificial intelligence model. *Engineering Structures*, 189, 309-318.
- [34] Almustafa, M. K., & Nehdi, M. L. (2020). Machine learning model for predicting structural response of RC slabs exposed to blast loading. *Engineering Structures*, 221, 111109.
- [35] Wong, P. S., Vecchio, F. J., & Trommels, H. (2013). Vector2 & Formworks user's manual second edition. *University of Toronto, Canada*.
- [36] Algassem, O., Li, Y., & Aoude, H. (2019). Ability of steel fibers to enhance the shear and flexural behavior of high-strength concrete beams subjected to blast loads. *Engineering Structures*, 199, 109611.
- [37] Peter Rochford (2021). PeterRochford/SkillMetricsToolbox (<https://github.com/PeterRochford/SkillMetricsToolbox>), GitHub. Retrieved March 4, 2021.
- [38] Shi, C., & Mo, Y. L. (Eds.). (2008). *High-performance construction materials: science and applications* (Vol. 1), 91-97.
- [39] Wille, K., Xu, M., El-Tawil, S., & Naaman, A. E. (2016). Dynamic impact factors of strain hardening UHP-FRC under direct tensile loading at low strain rates. *Materials and Structures*, 49(4), 1351-1365.
- [40] Karinski, Y. S., & Dancygier, A. N. (2018). Effect of Fibers Amount on the Cracking Localization Phenomenon in Tensile Bars—An Experimental Study. In *High Tech Concrete: Where Technology and Engineering Meet* (pp. 390-395). Springer, Cham.
- [41] Yoo, D. Y., & Yoon, Y. S. (2015). Structural performance of ultra-high-performance concrete beams with different steel fibers. *Engineering Structures*, 102, 409-423.

Chapter 8

8 Conclusions and future research

8.1 Summary and conclusions

Extensive research was carried out in this study focusing on integrating various machine learning (ML) algorithms in the field of structural blast engineering. The main objective was to investigate the feasibility of developing state-of-the-art response prediction models for reinforced concrete (RC) structural members under blast loading. The motivation of this goal stems from the need to develop simple, reliable, and accurate predictive models that are competitive with the existing more complex and computationally costly methods. The contributions and summary of each thesis chapter are outlined below.

The second chapter provided a comprehensive review of the literature on the blast phenomena and pertinent blast parameters. Empirical relations for obtaining blast parameter values were presented along with corresponding graphical solutions. Furthermore, an overview of existing behavior prediction methods was provided including the equivalent single degree of freedom (SDOF) models as well as numerical models. Subsequently, several existing studies for conventional RC members under blast loading were listed along with discussion of the structural blast mitigation strategies. Lastly, recent studies that incorporated ML in various structural engineering applications were described.

The third chapter investigated the development of a ML model for predicting the maximum displacement of RC slabs under blast loading. Development of the model was based on a hybrid classification-regression random forests algorithm considering 150 data points. The ten (10) features defining the application were the length, width, and thickness of the slab, concrete compressive strength, reinforcing steel yield strength, steel reinforcement ratio, the blast's scaled distance, the blast's reflected impulse, type of slab, and slab support. The

following conclusions of this chapter were reached considering multiple analyses of the proposed model:

- Performance measures of the RC slab displacement prediction model were presented through the mean absolute error (*MAE*), variance explained by cross-validation (*VEcv*), and coefficient of determination (R^2) producing results of 4.38, 94.4%, and 96.2%, respectively.
- Twenty-five direct comparisons to existing analytical and numerical models were made based on references of experimental results in which the ML model was proven to outperform the alternative models in several instances, while producing comparable results in other instances.
- A feature importance analysis was conducted through permutation feature importance (*PFI*). It was observed that the features pertaining to the blast load exhibited the highest influence, followed by the slab's thickness and reinforcement ratio. The results of the analysis were corroborated with several experimental results.
- Overall, the developed model achieved very promising results for its specific application where existing discrepancies within the model's dataset were thoroughly explored.

The fourth chapter explored the development of a ML model for predicting the maximum displacement of RC columns under blast loading. The gradient boosted regression trees (GBRT) ML algorithm was adopted for model development. A dataset consisting of 420 columns was collected from the open literature based on experimental studies and numerical and analytical models validated by experiments. Towards developing the ML model, thirteen (13) application features were defined being the column's length, width, height, concrete compressive strength, longitudinal steel yield strength, longitudinal steel reinforcement ratio, transverse steel yield strength, transverse steel volumetric reinforcement ratio, axial load ratio (ALR), reflected pressure, reflected impulse, height of the blast along the column, and height of the recorded maximum displacement.

Considering several different analyses conducted as a means of model validation, the resulting conclusions of this chapter are as follows:

- The resulting performance measures of the proposed RC column displacement prediction model yielded values of *MAE*, *VE_{cv}*, and *R*² of 3.63, 96.83%, and 97.4%, respectively.
- A total of fifty-six direct comparisons to existing prediction methods were made based on experimental references in which the proposed model exhibited highly acceptable performance.
- A small number of comparative discrepancies were observed, and the sources of error were clearly identified with respect to certain application variations existing in the data.
- A comprehensive feature importance analysis was conducted through an interaction-curvature test (ICT) in which the most prominent features were those related to blast parameters (reflected impulse and reflected pressure).
- Furthermore, the most influential column parameters were observed to be the applied axial load ratio and the concrete compressive strength, followed by the longitudinal reinforcement ratio. The results of the feature importance analysis were strongly supported by available experimental correlations.
- Overall, the ML model displayed competent predictive ability as well as a strong aptitude for capturing the extent to which different application features affected the application.

The fifth chapter investigated the applicability of developing a maximum displacement prediction model for RC beams using ML methods. The model development was built on a hybrid GBRT algorithm that employed a novel Henry Gas Solubility Optimization algorithm for hyperparameter tuning. A total of 150 data points were collected from the available literature in which eleven (11) features were selected to characterize the application including the beam height, width, length, concrete compressive strength,

longitudinal steel yield strength, tension reinforcement area, compression reinforcement area, stirrup spacing, support conditions, reflected pressure and reflected impulse. The conclusions drawn from various analyses and model developments in this chapter are presented:

- The statistical performance metrics of the RC beam displacement prediction model resulted in *MAE* of 5.3, *VEcv* of 88.1%, and R^2 of 92.1%.
- When direct comparisons to existing methods were made, two alternative sets were defined. The first consisted of thirty-nine comparisons and considered normal-strength concrete beams, while the second considered high-strength concrete beams and captured twenty-three comparisons. The proposed model achieved satisfactory performance compared to that of existing methods for both comparison sets.
- A feature importance analysis was conducted based on ICT in which the parameters of reflected pressure and reflected impulse had the highest influence, followed by the beam parameters including steel yield strength, tension reinforcement ratio, and concrete compressive strength.
- A secondary ML model was developed within the chapter, which focused on the classification of failure modes and crack patterns for blast-loaded RC beams. The various class outputs considered were flexural cracking, bending failure, flexural-shear cracking, and crushing failure.
- The proposed classification model presented a binary classification accuracy of 93.1% and a multi-class classification accuracy of 83.74%. Using the same feature importance analysis, the features of reflected impulse, reflected pressure, and tension reinforcement ratio were found to have the greatest effect on the resulting qualitative behavior.
- Consequently, the overall performance of both ML models for RC beams was favorable in which both local and global member response predictions were demonstrated.

The sixth chapter investigated the development of a ML model considering fiber-reinforced polymer (FRP) retrofitting as a blast mitigation strategy. The developed model aimed to predict the maximum displacement of FRP retrofitted RC slabs under blast loading and adopted a Gaussian process (GP) regression algorithm with a non-isotropic exponential kernel function. Additionally, a Tabular Generative Adversarial Network (TGAN) was considered to generate synthetic data. The model development considered a total of 70 real and 200 synthetic data points having thirteen (13) features of slab length, width, thickness, concrete compressive strength, steel yield strength, steel reinforcement ratio, slab type, FRP tensile strength, surface bond strength, FRP cross-sectional area, FRP configuration, reflected pressure, and reflected impulse. Based on a number of model investigations within this chapter, the following conclusions were reached:

- The performance metrics of mean absolute percent error (*MAPE*), *MAE*, and R^2 were utilized to evaluate the FRP retrofitted RC slab displacement prediction model yielding values of 13.2%, 2.28, and 97.7%, respectively.
- Twenty-seven direct comparisons to existing analytical models were performed in which the ML model achieved superior performance. Similarly, indirect comparisons were made with respect to nine predictions of numerical models in which comparable predictive capabilities were remarked.
- Based on ICT, the most influential features were observed to be the reflected pressure, reflected impulse, FRP configuration, and the steel reinforcement ratio.
- A comparative feature analysis was also made with respect to non-retrofitted RC slabs for the features of slab depth, concrete compressive strength, steel yield strength, and reinforcement ratio. Based on these features, variations between FRP retrofitted and non-retrofitted RC slabs were investigated.
- Considering the overall model evaluation, the proposed ML model attained highly acceptable predictive performance and was proven to be a strong competitor for displacement prediction of composite FRP retrofitted members.

The seventh chapter evaluated the feasibility of developing a ML model considering the blast mitigation strategy of incorporating steel fibers. Towards such development, a ML model was designed and evaluated to predict the maximum displacement of steel fiber-reinforced concrete (SFRC) beams of varying strengths under blast loading. A GP regression algorithm was implemented considering an isotropic rational quadratic kernel function, while implementing a conditional TGAN for generating synthetic data. A total of 117 real and 300 synthetic data points were used, which considered nine (9) features including the fiber content, fiber aspect ratio, fiber tensile strength, concrete compressive strength, steel yield strength, tension reinforcement ratio, transverse reinforcement ratio, reflected pressure, and reflected impulse. The following conclusions were obtained with respect to thorough model evaluations and further analyses conducted in this chapter:

- The statistical performance measures used to evaluate the SFRC beam displacement prediction model were mean squared error (*MSE*), *MAE*, *MAPE*, and R^2 , which yielded values of 6.74, 1.87, 8.71%, and 95.8%, respectively.
- Implicit application considerations were thoroughly discussed with respect to static and dynamic material models for materials of SFRC, HSFRC, and UHPFRC.
- Considering seven independent sets of comparison, the ML model was evaluated with respect to 138 instances of both analytical and numerical model predictions and was observed to produce superior performance for nearly all comparative sets.
- A parametric analysis was conducted to evaluate the effects of the fiber content and fiber type on the maximum displacement of SFRC under varying magnitudes of blast loading. The different types of SFRC beams considered were SFRC with normal strength steel reinforcement (NSR), ultra-high performance SFRC (UHPFRC) with NSR, and UHPFRC with high strength steel reinforcement (HSR).
- From the parametric study, it was observed that for both SFRC with NSR and UHPFRC with HSR, an increase in the fiber content resulted in an increase in the blast performance. However, for UHPFRC with NSR, an increase in the fiber content resulted in reduced blast performance at higher blast magnitudes.

- Also, it was inferred from the parametric study that shorter steel fibers having larger aspect ratio produced the highest blast resistance. This observation was also found to concur with experimental findings.
- Overall, the proposed model achieved an exceptional predictive performance with a proficient comprehension of the application parameters. Considerations for an extended local response prediction model for SFRC beams were also proposed.

8.2 Future research

Based on the limited model discrepancies identified within each of the proposed models, it can be inferred that a source of predictive error resulted from the model's lacking ability to form ideal associations among features. This may either result from the quality or quantity of the data. As a result, a primary extension of this work is to identify the gaps in each model's performance by conducting a detailed analysis of the data used for model development. Such an analysis would also identify the feature space in which the model is weak, such that efforts can be made to reinforce the dataset. Furthermore, although the developed models considered a wide range of features (some more than others), it is also pertinent to identify the extent to which such ranges are practical. This may refer to member dimension sizes, reinforcement ratios, and the inclusion of additional design features. Once investigated, the dataset may be augmented with new data that accounts for practical use. Towards this end, new data may be considered with respect to experimental work, or numerical models validated by experiment. It should be noted that such investigations are considered to be non-trivial tasks.

Another consideration for future research is the development of analytical expressions that signify the proposed models. This should be considered only after the aforementioned investigation is conducted. The availability of accurate analytical expressions with generalizing capabilities would eliminate both the ML interface and the "black-box" predictions. However, such expressions would need to be carefully developed such that accuracy is not sacrificed from the original ML model.

Although most of the developed models throughout this thesis deal with the global member behavior of maximum displacement, an attempt to investigate local behaviors was made through the failure mode and crack pattern classification model in Chapter Five. The classification model was shown to produce good accuracy, while capturing the influence of application parameters. Thus, possible extensions for the models in Chapters Three and Four would be the development of models which can predict the local condition of each member. Similarly, more complex extensions may be adapted for Chapters Six and Seven to capture the local behavior considering the respective blast-mitigation strategy.

Curriculum Vitae

Name: Monjee Almustafa

Post-secondary Education and Degrees: Prince Sultan University
Riyadh, Saudi Arabia
2016-2019 B.Sc. in Construction Engineering Management

Western University
London, Ontario, Canada
2019-2021 M.E.Sc in Structural Engineering

Honors and Awards: Undergraduate Academic Scholarship
2016-2019

Undergraduate Research Award
2019

Related Work Experience Graduate Teaching Assistant
Western University
Fall 2020, Winter 2021.

Publications:

Ibrahim, Y. E., & **Almustafa, M.** (2020). Mitigation of blast load risk on reinforced concrete structures considering different design alternatives. *Archives of Civil Engineering*. 66(3): 225-238.

Almustafa, M. K., & Nehdi, M. L. (2020). Machine learning model for predicting structural response of RC slabs exposed to blast loading. *Engineering Structures*, 221, 111109.